

DISSERTATION
SUBMITTED TO THE
COMBINED FACULTY OF
NATURAL SCIENCES AND MATHEMATICS
OF THE
RUPERTO-CAROLA-UNIVERSITY OF HEIDELBERG,
GERMANY
FOR THE DEGREE OF
DOCTOR OF NATURAL SCIENCES

PUT FORWARD BY

ERIK BERTRAM, M.SC.
BORN IN: KIRN, GERMANY

ORAL EXAMINATION: FEBRUARY 3RD, 2016

THE ROLE OF TURBULENCE IN
THE PROCESS OF STAR FORMATION

REFEREES:

PROF. DR. RALF S. KLESSEN

PROF. DR. HENRIK BEUTHER

*“When I meet God, I am going to ask him two questions:
Why relativity? And why turbulence?
I really believe he will have an answer for the first.”*

- Werner Heisenberg

Zusammenfassung

In dieser Arbeit studieren wir den Einfluss von interstellarer Turbulenz auf den Sternentstehungsprozess. Wir zeigen, dass supersonische Turbulenz verschiedene Eigenschaften des interstellaren Mediums (ISM) signifikant beeinflusst. Dazu rechnen wir numerische Simulationen von typischen Molekülwolken in verschiedenen Umgebungen. Wir analysieren im besonderen typische Gaswolken, die man in der Scheibe der Milchstraße findet, sowie solche, die in extremeren Regionen unserer Galaxis vorkommen, z.B. in der zentralen Molekularzone (CMZ) in der Nähe des galaktischen Zentrums. Zusätzlich rechnen wir einen Strahlungstransport in verschiedenen Feinstrukturlinien und vergleichen unsere Ergebnisse mit Beobachtungen. Wir untersuchen den Einfluss der Turbulenz auf unterschiedliche Observable, z.B. auf die Strukturfunktionen, die Δ -Varianz, die Energiespektren sowie die Sternentstehungseffizienzen. Weiterhin analysieren wir die Wirkung der Turbulenz auf die Chemie und die verschiedenen Phasen des ISM. Unsere Studien der Gaswolken in der Milchstraßenscheibe zeigen, dass die statistischen Eigenschaften der Turbulenz signifikant durch den verwendeten Gas-Tracer beeinflusst werden. Des Weiteren demonstrieren wir anhand unserer Studien der Gaswolken im galaktischen Zentrum, dass starke Turbulenz die Sternentstehung signifikant dämpfen, jedoch nicht blockieren kann. Schließlich zeigen wir, dass atomare Gas-Tracer zahlreiche Eigenschaften des H_2 - sowie des gesamten Gases der Wolke gut reproduzieren und dass sie eine nützliche Alternative zu molekularen Linien bei Studien des ISM in der CMZ bieten.

Abstract

The aim of this thesis is to study the role of interstellar turbulence in the process of star formation. We demonstrate that supersonic turbulent motions significantly affect various properties of the interstellar medium (ISM). Therefore, we run numerical simulations of molecular clouds in different environments. In particular, we study typical clouds located in the Milky Way disk as well as clouds which can be found in more extreme regions in our Galaxy, e.g. in the Central Molecular Zone (CMZ) near the Galactic Center. In addition, we perform radiative transfer calculations of numerous diagnostic fine structure lines and compare our results with observational measurements. Furthermore, we analyze the influence of the turbulence on different observables, e.g. on the structure functions, the Δ -variance, the power spectra as well as the star formation efficiencies. We also study the impact of turbulent motions on the chemistry and the different phases of the ISM. Our studies about Milky Way disk clouds show that the statistical properties of the turbulence are significantly influenced by the individual gas tracers. Moreover, our investigations about CMZ-like clouds show that high levels of turbulence can significantly suppress, but never inhibit star formation, owing to local compression of gas by turbulent shocks. Finally, we show that various atomic tracers accurately reflect most of the physical properties of both the H_2 and the total gas of the cloud and that they provide a very useful alternative to common molecular lines when we study the ISM in the CMZ.

List of publications

(* = These publications are partially or fully presented in this thesis)

1. * **Bertram, E.**; Glover, S. C. O.; Clark, P. C.; Ragan, S. and Klessen, R. S. (2015), *Synthetic observations of molecular clouds in a galactic center environment: II. Analyzing the internal cloud kinematics*, will soon be submitted to Mon. Not. R. Astron. Soc.
2. * **Bertram, E.**; Glover, S. C. O.; Clark, P. C.; Ragan, S. and Klessen, R. S. (2015), *Synthetic observations of molecular clouds in a galactic center environment: I. Studying maps of column density and integrated intensity*, published in Mon. Not. R. Astron. Soc., Volume 455, Issue 4, p.3763-3778 (arXiv:1509.06649)
3. * **Bertram, E.**; Glover, S. C. O.; Clark, P. C. and Klessen, R. S. (2015), *Star formation efficiencies of molecular clouds in a galactic centre environment*, published in Mon. Not. R. Astron. Soc., Volume 451, Issue 4, p.3679-3692 (arXiv:1505.04403)
4. * **Bertram, E.**; Klessen, R. S. and Glover, S. C. O. (2015), *Structure analysis of simulated molecular clouds with the Δ -variance*, published in Mon. Not. R. Astron. Soc., Volume 451, Issue 1, p.196-209 (arXiv:1504.07137)
5. * **Bertram, E.**; Konstandin, L.; Shetty, R.; Glover, S. C. O. and Klessen, R. S. (2015), *Centroid velocity statistics of molecular clouds*, published in Mon. Not. R. Astron. Soc., Volume 446, Issue 4, p.3777-3787 (arXiv:1410.6508)
6. **Bertram, E.**; Shetty, R.; Glover, S. C. O.; Klessen, R. S.; Roman-Duval, J. and Federrath, C. (2014), *Principal component analysis of molecular clouds: can CO reveal the dynamics?*, published in Mon. Not. R. Astron. Soc., Volume 440, Issue 1, p.465-475 (arXiv:1402.2101)
7. **Bertram, E.**; Federrath, C.; Banerjee, R. and Klessen R. S. (2012), *Statistical analysis of the mass-to-flux ratio in turbulent cores: effects of magnetic field reversals and dynamo amplification*, published in Mon. Not. R. Astron. Soc., Volume 420, Issue 4, pp. 3163-3173 (arXiv:1111.5539)
8. Young, M. D., **Bertram, E.**; Moeckel, N. and Clarke, C. J. (2012), *Reliable estimation of the column density in smoothed particle hydrodynamic simulations*, published in Mon. Not. R. Astron. Soc., Volume 426, Issue 2, pp. 1061-1072 (arXiv:1207.6513)

Contents

1	Introduction	17
1.1	The process of star formation	17
1.2	Motivation of this work	20
1.3	Objectives of the thesis	22
1.4	Observable properties of molecular clouds	24
1.5	Turbulent properties of the interstellar medium	27
1.5.1	Mass-density distribution within clouds	29
1.5.2	Filamentary structure of the ISM	30
1.5.3	The star formation rate and efficiency	31
1.5.4	The stellar initial mass function	32
1.6	Star formation in extreme regions: the CMZ and the Galactic Center	33
1.7	Numerical implementation of the simulations	36
1.8	Outline of the thesis	38
1.9	General remarks and how to read this work	40
2	Theory of Hydrodynamics	41
2.1	Introduction to special relativity	42
2.2	Equations of Hydrodynamics	43
2.2.1	Assumptions and limitations	43
2.2.2	The Eulerian and the Lagrangian viewpoint	43
2.2.3	The collision-less Boltzmann equation	44
2.2.4	Deriving the continuity equation	45
2.2.5	The relativistic energy-momentum tensor	46
2.2.6	Continuity equation for energy and momentum	47
2.2.7	Euler's equation of motion	47
2.2.8	Viscosity effects in Euler's equation: the Navier-Stokes equation	48
2.2.9	Characterizing turbulent flows with the Reynolds number . . .	49
2.2.10	Energy budget equation for a fluid	50
2.2.11	Introducing gravity via the Poisson equation	50
2.2.12	Perturbation theory and sound waves	51
2.2.13	The ideal gas law and the polytropic equation of state	52
2.2.14	Homogeneous functions and the scalar virial theorem	53

2.2.15	The Rankine-Hugoniot shock jump conditions and shock waves	54
2.2.16	Gravitational stability analysis and the Jeans quantities	55
2.2.17	Typical timescales in star formation theory	56
2.2.18	Summary of the hydrodynamic equations	58
2.3	Equations of Magneto-Hydrodynamics	58
2.3.1	Assumptions and limitations	58
2.3.2	Introducing the relativistic Maxwell equations	58
2.3.3	The induction equation and the evolution of magnetic fields .	60
2.3.4	Euler's equation of motion with magnetic fields	61
2.3.5	Magnetic advection and diffusion processes	61
2.3.6	Generating magnetic fields via the battery mechanism	62
2.3.7	Ambipolar diffusion in a magnetized fluid	63
2.3.8	Alfvén waves and the Alfvén velocity	64
3	Radiative transfer	65
3.1	Basic quantities of radiative transfer	65
3.2	Interaction of radiation with matter	66
3.3	Blackbody radiation and the Stefan-Boltzmann law	68
3.4	The Planck spectrum, Wien's law and the Rayleigh-Jeans limit	69
3.5	Absorption and emission processes: the Einstein coefficients	71
3.6	Atomic excitation and deexcitation by collisions	73
3.7	The Lorentz profile of line emission	74
3.8	The Doppler profile of thermally moving atoms	76
3.9	Convolving the Lorentz and the Doppler profile: the Voigt profile . .	77
3.10	Other processes responsible for line broadening	78
3.11	Heating and cooling processes in the ISM	78
3.12	Theoretical background of fine structure lines	79
3.13	Measuring velocities with the Doppler shift	81
4	Turbulence theory	83
4.1	Motivation of turbulence theory	83
4.2	Symmetry groups of turbulence theory	85
4.3	Energy cascades in an ideal fluid	86
4.4	A statistical view at the ergodic theorem	87
4.5	Kolmogorov axioms of incompressible turbulence	88
4.6	Introduction to structure functions	89
4.7	Phenomenology of the Kolmogorov theory	89
4.8	Burger's turbulence of a compressible fluid	92
4.9	Correction to the Kolmogorov theory: the She-Levèque model	92
4.10	The Dubrulle and Boldyrev model	95
4.11	Deviation from log-normal: effects of intermittency	95
4.12	Another correction to the Kolmogorov theory: the β -model	96

5	Centroid Velocity Statistics of Molecular Clouds	99
5.1	Introduction	99
5.2	Methods and simulations	101
5.2.1	MHD and chemistry simulations	101
5.2.2	Radiative transfer	102
5.2.3	Centroid velocity increments	103
5.2.4	Structure functions of the CVI	103
5.2.5	Fourier and power spectra	104
5.2.6	Theoretical relations for the SF slopes	105
5.3	Results	106
5.3.1	Analysis of the CVISF	106
5.3.2	Analysis of the Fourier spectra	109
5.3.3	Variation of the abundance of ^{13}CO	109
5.4	Discussion	112
5.4.1	Slopes of the CVISF	112
5.4.2	Slopes of the Fourier spectra	113
5.4.3	Projection effects	114
5.4.4	Connection to the fractal dimension	114
5.4.5	Limitations of the models	115
5.5	Summary and Conclusions	115
6	Structure analysis of simulated MCs with the Δ-variance	117
6.1	Introduction	117
6.2	Methods and simulations	119
6.2.1	Computational method	119
6.2.2	Radiative transfer post-processing	120
6.2.3	Centroid velocity, integrated intensity and column density maps	121
6.2.4	The Δ -variance method	122
6.3	Results	124
6.3.1	Δ -variance analysis of the CV maps	128
6.3.2	Δ -variance analysis of the intensity and column density maps	130
6.3.3	Variation of the abundance of ^{13}CO	132
6.4	Discussion	133
6.4.1	Interpreting the Δ -variance spectra of the CV maps	133
6.4.2	Interpreting the spectra of intensity and column density maps	134
6.4.3	Comparison of the Δ -variance to other statistical tools	135
6.4.4	Previous studies of CV maps	136
6.4.5	Previous studies of intensity and column density maps	136
6.4.6	Model limitations	137
6.5	Summary and Conclusions	138
7	Star formation efficiencies of MCs in a galactic center environment	141
7.1	Introduction	142

7.2	Methods and simulations	143
7.2.1	Computational method	143
7.2.2	Sink particles	144
7.2.3	Important quantities	145
7.2.4	Initial conditions and model parameters	146
7.3	Results	148
7.3.1	Analysis of the model clouds	148
7.3.2	Analysis of the volume, temperature and column density PDF	155
7.3.3	Sink particle formation	156
7.4	Discussion	158
7.4.1	Comparison to star formation in the GC	158
7.4.2	Comparison to previous studies of unbound clouds	160
7.4.3	Suppressing star formation	160
7.4.4	Limitations of the model	162
7.5	Summary and Conclusions	162
8	Synthetic observations of MCs in a galactic center environment:	
	I. Studying maps of column density and integrated intensity	165
8.1	Introduction	166
8.2	Methods	167
8.2.1	Hydrodynamical and chemical model	167
8.2.2	Model parameters	169
8.2.3	Radiative transfer	170
8.3	Results	171
8.3.1	Thermal state of the clouds	171
8.3.2	Tracing the shape of the MC	172
8.3.3	Estimating the effective cloud radii	177
8.3.4	Tracing the total and H ₂ column density	178
8.3.5	Mass fraction traced by the emission	182
8.3.6	Estimating the CO-to-H ₂ conversion factor	184
8.4	Summary and Conclusions	186
9	Synthetic observations of MCs in a galactic center environment:	
	II. Analyzing the internal cloud kinematics	189
9.1	Introduction	190
9.2	Methods	191
9.2.1	Hydrodynamical and chemical model	191
9.2.2	Radiative transfer calculation	193
9.2.3	Model parameters	193
9.3	Results	194
9.3.1	Column density and velocity-integrated intensity maps	194
9.3.2	Estimating the velocity dispersion of the total cloud mass	196
9.3.3	Estimating the velocity dispersions of the different tracers	200
9.3.4	Computing spectra and the FWHM of the different tracers	202

9.3.5	Evolution of the virial parameter in the simulations	204
9.3.6	Estimating the virial state of the cloud	205
9.4	Summary and Conclusions	207
10	Discussion and outlook	209
10.1	Summary of this thesis	209
10.2	Idea for further investigations and some open questions	212
10.3	Closing remarks	215
	Appendix	217
A	Centroid Velocity Statistics of Molecular Clouds	219
A.1	Resolution study	219
B	Structure analysis of simulated MCs with the Δ-variance	223
B.1	Resolution study	223
B.2	Comparison of spectra with different filter functions	225
C	Star formation efficiencies of MCs in a galactic center environment	227
C.1	Simulations with a different random seed	227
D	Synthetic observations of MCs in a galactic center environment:	
I.	Studying maps of column density and integrated intensity	229
D.1	Radiative transfer post-processing: influence of grid resolution	229
D.2	Dependence on viewing angle	231
D.3	Influence of the CO abundance on the line emission of [CII] and [OI]	232
E	Tables of constants and unit systems	235
F	Tables of symbols, physical definitions and nomenclature	237
G	Lists	243
G.1	List of Figures	243
G.2	List of Tables	252
H	Acknowledgements	257
I	Bibliography	259

Introduction

1.1 The process of star formation

Stars play an important role in the Universe. They bring the light into our world and are responsible for all the life on the earth. Without stars everything would be dark and cold. We would not have any idea of where we are, where we come from and where we might going to. Stars are candles in the Universe.

Nearly all chemical elements heavier than hydrogen and helium are produced in stars and play a crucial role in the evolution of molecular clouds (MCs), since they influence heating and cooling processes of the interstellar medium (ISM) and thus affect the thermodynamic properties as well as the chemistry (Hollenbach & Tielens, 1997; van Dishoeck & Blake, 1998; Tielens, 2010). These heavy elements are called *metals*¹ and they are mainly produced in fusion processes in the interior of stars or in supernova events of massive stars. Today, we find a lot of heavier elements on earth. Silver, gold or and many more metals were produced in stars a long time ago. Studying the formation of stars is therefore also crucial to understand the process of planet and even galaxy formation.

Star formation is a multiscale process. It ranges over more than 8 orders of magnitude in space and over more than 20 orders of magnitude in density. To understand how a star can form out of a diffuse molecular cloud on parsec scales with low densities of several $\sim 100 \text{ cm}^{-3}$ and temperatures of some $\sim 10 \text{ K}$ (see, e.g. Shu et al., 1987; Lada, 2005; Hennebelle & Falgarone, 2012) we require a long-ranged force that can account for such a condensation process over time. The only of the four fundamental forces in nature, which can achieve this, is gravity. Thus, gravitational contraction will certainly play the chief part in a star formation theory (see, e.g. Larson, 1981; Shu et al., 1987; Larson, 2003; McKee & Ostriker, 2007).

The condensation of matter is initiated by gravitational instabilities in the ISM, which trigger the formation of dense clumps in the cloud. The further compression

¹In the astrophysical terminology, metals are all elements heavier than hydrogen.



Figure 1.1:

The Pleiades are an example of an open star cluster in the Milky Way, containing middle-aged hot B-type stars. The cluster is made up of ~ 3.000 stars at a distance of ~ 120 pc from Earth in the constellation of Taurus. In the picture we can also still see the diffuse gas out of which the stars formed. Image credit (07/12/2015): NASA, ESA and AURA/Caltech, D. Soderblom and E. Nelan (STScI), F. Benedict and B. Arthur (University of Texas), and B. Jones (Lick Observatory).

of the gas depends on the amplitude of a number of physical processes. For example, magnetic fields can delay or even inhibit core collapse (see, e.g. Zeldovich et al., 1983; Shu et al., 1987; Price & Bate, 2007, 2008; Seifried et al., 2011). In an ambipolar diffusion process, charged particles are frozen into the magnetic field, while neutral particles can move freely with respect to the field lines (Mouschovias, 1991; Tassis & Mouschovias, 2004; Mouschovias et al., 2006; Vázquez-Semadeni et al., 2011). Moreover, heating and cooling mechanisms are crucial for the ongoing evolution of the cloud. If the temperature in the cloud is too high (e.g. when nearby stars provide enough radiation to heat the gas), the collapse can be decelerated or even stopped, since the Jeans mass M_J scales with the cloud's temperature to the power of $3/2$, i.e. $M_J \propto T^{3/2}$ (Jeans, 1902). Conversely, cooling processes (mostly triggered by collisional excitations of gas and dust and following emission of photons) can support core collapse and lead to denser clumps. Furthermore, if the cloud rotates, angular momentum can act against the condensation process (Larson, 1972).

Generally, stars do not form individually, but in clusters, which typically contain thousands of stars of the same age (King, 1962, 1966; Bate et al., 2003; Tan et al., 2006; Zwart et al., 2010). In Fig. 1.1 we show an example of an open star cluster, the Pleiades, where we can also still see the diffuse gas out of which the stars formed². To arrive at such a clustered structure in the early evolution, the cloud must fragment into subregions, which can then collapse separately (Evans, 1999; Klessen, 2001).

²Image credit: <http://hubblesite.org/newscenter/archive/releases/2004/20/image/a/>

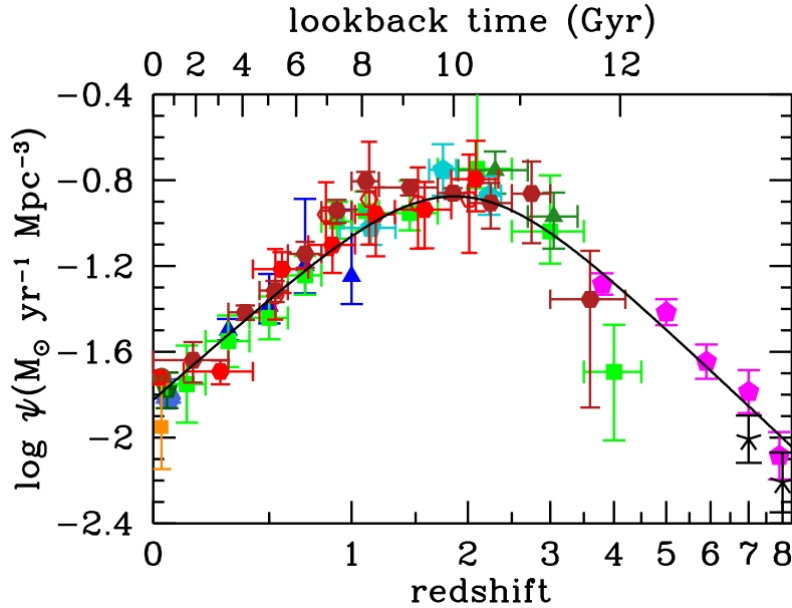


Figure 1.2:

Cosmic star formation history as a function of look-back time and redshift. Shown are both far-UV and infrared measurements of the cosmic star formation rate (SFR) density ψ . We observe a maximum SFR density at $z \approx 2$. Today, the SFR density decreases continuously (taken from Madau & Dickinson, 2014).

How can a star condense out of a diffuse ISM? This process can be divided into several phases. In the first phase of gravitational collapse, overdense regions in the MC contract until individual clumps become optically thick at some point and heat up again, because photons cannot escape anymore. This leads to a hydrostatic equilibrium in the inner core region, which halts the collapse for a while. However, due to the gravitational attraction of the core, the envelope around it falls freely onto the clump and forms an even denser region, a *protostellar core*, which primarily consists of molecular hydrogen. With this gain of mass, the contraction can proceed. The inner region heats up further, which stabilizes the core again.

The next and second phase of collapse starts at a temperature of $T \approx 10^3$ K when the molecular hydrogen dissociates into atomic hydrogen. This is because the H_2 dissociation requires a significant amount of thermal energy, which is taken away from the core. Thus, the temperature can decrease, which supports the collapse. The contraction then proceeds until a new hydrostatic equilibrium is reached. All hydrogen is now in the atomic form. We call this object a *protostar*. Still, mass is flowing onto the central core from the accretion disk around it (Cassen & Moosman, 1981; Tan & McKee, 2004; Krumholz et al., 2009). The temperature in the interior grows as mass continuously falls onto the protostar. When the envelope becomes optically thin, radiation can escape the core for the first time. The contraction process then continues until the hydrogen is fully ionized, which occurs at temperatures of $T \approx 10^5$ K. However, this temperature is still too low for the first fusion processes,

which require temperatures of $T \approx 10^7$ K. The transport of heat out of the protostar at this point is mainly dominated by convection, which is very effective.

After some time, the protostar then reaches the Hayashi line (Hayashi, 1961), the first equilibrium line in the Hertzsprung-Russel diagram. It can then continue to heat up in the interior. Finally, the protostar reaches the main sequence and nuclear fusion begins. A new star is born.

For stars with masses $0.25 \lesssim M/M_\odot \lesssim 1.5$ the fusion process in the central region is mainly dominated by fusion of hydrogen into helium, the so-called p-p chain. For masses $M/M_\odot \gtrsim 1.5$, fusion is dominated by the CNO cycle. Stars with $0.08 \lesssim M/M_\odot \lesssim 0.25$ only exhibit a very small region in the center where the temperature is high enough for hydrogen burning. If $M/M_\odot \lesssim 0.08$, the temperature is not expected to be high enough for fusion processes. These objects are called brown dwarfs (Basri, 2000; Burrows et al., 2001).

Stars are common objects in galaxies (Grebel, 2000). The most important quantity characterizing a star is its mass, from which we can estimate the radius, the spectral type and the (effective) temperature. In our own Galaxy, we find about $\sim 10^{11}$ stars (Gilmore et al., 1989; Majewski, 1993; Freeman & Bland-Hawthorn, 2002) with different masses, that range from a few until tens of solar masses (Kroupa, 2002). They form with a rate of $\sim 3 - 5 M_\odot \text{ yr}^{-1}$ (Murray, 2011; Krumholz et al., 2012). However, observational measurements have revealed that the cosmic star formation rate strongly varied over the time. In Fig. 1.2, we show the cosmic star formation history as a function of look-back time and redshift. We see that the star formation rate density continuously grew in the past and peaked approximately 3.5 Gyr after the Big Bang at redshift $z \approx 2$ (Madau et al., 1996; Bouwens et al., 2011; Madau & Dickinson, 2014). Afterwards, the rate declined exponentially, which means that we are living in a post-era of very active star formation activity today.

The age of stars vary strongly, ranging from a few million years for the most massive stars to a few billion years for lower mass stars. The condensation process described above approximately proceeds within a free-fall time,

$$\tau = \sqrt{\frac{3\pi}{32G\rho}} = 140 \text{ Myr} \left(\frac{n}{0.1 \text{ cm}^{-3}} \right)^{-1/2}, \quad (1.1)$$

where ρ and n are the mass and particle number density of the cloud and G the gravitational constant, respectively (Jeans, 1902). Hence, in a human life (order ~ 100 yr) we are only able to observe the current state in the very long evolution of a star. Though, the question is: How can we get deeper insights into whole the star formation process, when the cosmic timescales are so long?

1.2 Motivation of this work

There are essentially two routes to answer this question: one through the analysis of observations and the other via numerical simulations. If we observe a large number of stars, we can hope to find enough objects in different evolutionary stages for a

statistical analysis. Conversely, we could also use super-computers to run numerical simulations and adopt different initial conditions for a given situation to analyze in detail how magnetic fields, the density and the velocity field, radiative transport, feedback processes, the chemical composition of the gas and other effects influence the formation of stars (Kennicutt, 1998a; Larson, 2003; Lada, 2005).

In this thesis, we focus on the latter and perform numerical simulations of MCs to analyze how different properties of the turbulence affect star formation. The ISM is known to be turbulent on a supersonic scale (Mac Low & Klessen, 2004). These turbulent motions are triggered by jets, stellar winds, magnetorotational and gravitational instabilities as well as by supernova explosions at the end of the lifetime of stars (see, e.g. Mac Low & Klessen, 2004; Scalo & Elmegreen, 2004; Elmegreen & Scalo, 2004; McKee & Ostriker, 2007; Hennebelle & Falgarone, 2012). They influence a huge number of observables (e.g. the star formation rate and the initial mass function, as we will discuss below) and are thus highly important for the process of star formation. However, turbulent motions play a dual role: On one hand, they can support MCs against gravitational collapse. On the other hand, turbulent shocks can create overdense regions on small scales, which in turn may collapse and form stars and clusters (Mac Low & Klessen 2004; Bertram et al. 2015c).

In particular, our studies of turbulence focus on two regions in the Galaxy:

- *Disk.* We perform numerical simulations of local solar neighbourhood MCs using the ZEUS-MP magnetohydrodynamical code (Norman, 2000; Hayes et al., 2006). These MCs have properties which are typical for clouds found in the disk of our Galaxy. Examples are the Orion and the eagle nebula or NGC 3372, also known as the Carina nebula (Hillenbrand, 1997; Pound, 1998; Palla & Stahler, 1999; Smith et al., 2000). The mean number densities range from several $\sim 10 - 100 \text{ cm}^{-3}$, the velocity dispersions are of the order of a few km s^{-1} , while typical gas temperatures are $\sim 20 \text{ K}$ (see, e.g. Larson, 1981; Shu et al., 1987; Solomon et al., 1987; Dame et al., 2001). The studies which belong to clouds located this region are presented in chapters 5 and 6.
- *Galactic Center.* The galactic center is a more active region compared to the rest of the Galaxy. We perform numerical simulations of clouds located near the center of the Milky Way in the *Central Molecular Zone (CMZ)* using the moving mesh code AREPO (Springel, 2010). The CMZ is a region which is rich in molecular and very dense gas with number densities of several 10^3 cm^{-3} (Longmore et al., 2013) and which extends a few hundred parsecs around the center. It is supposed to be highly turbulent with velocity dispersions of the order of several 10 km s^{-1} (Oka et al., 1998, 2001; Shetty et al., 2012; Tsuboi & Miyazaki, 2012). Furthermore, the interstellar radiation field and the cosmic-ray flux in the CMZ seem to be enhanced by a factor of $\sim 100 - 1000$ (Yusef-Zadeh et al., 2007; Clark et al., 2013; Indriolo et al., 2015; Ginsburg et al., 2015) compared to the canonical value (Habing, 1968; Draine, 1978; Mathis et al., 1983). Examples of typical clouds in the CMZ are G0.253+0.016, also known as “The Brick” (Güsten et al., 1981; Lis et al., 1994; Lis & Menten, 1998;

Lis et al., 2001; Molinari et al., 2011; Immer et al., 2012; Longmore et al., 2012; Kauffmann et al., 2013; Clark et al., 2013; Johnston et al., 2014; Rathborne et al., 2014; Kruijssen et al., 2015; Pillai et al., 2015), or Sgr B2, a giant molecular cloud located ~ 120 pc away from the galactic center (Cummins et al., 1986; Goldsmith et al., 1990; Takagi et al., 2002). The studies which belong to this region are presented in chapters 7, 8 and 9.

In particular, we are also interested in how turbulent motions can be measured by an observer. In this context, we want to close a gap between previous studies of turbulent star formation, which often only analyze the numerical domain without connecting the results to the observable world, and observational measurements. Therefore, we do not only study the impact of the turbulence on various physical properties themselves (e.g. the star formation efficiency, the power spectrum, etc.), but also focus on comparing our theoretical results to observations. Therefore, we perform radiative transfer calculations using the tool RADMC-3D (Dullemond, 2012), whenever this is meaningful and possible.

1.3 Objectives of the thesis

In this section, we give an overview of the objectives of this thesis. Here, we only present a few of the most important aspects of our work. In particular, we aim to answer the following ten questions:

1. What role do optical depth effects play in the observations of turbulent motions?

It is known that radiation from different cloud tracers (e.g. ^{12}CO or ^{13}CO) have different optical properties. While ^{12}CO is usually optically thick, ^{13}CO is established to be an optically thin tracer. However, it is still unclear which role these different optical effects play in the observable determination of statistical properties of the turbulence field. How do different tracers affect the statistics of e.g. structure functions, PCA or the Δ -variance analysis?

2. How do the linewidth-size relations for different cloud tracers compare with each other?

Several years ago, Larson has established that the internal velocity dispersion δv of MCs is proportional to the corresponding scale ℓ to the power of a specific slope index p , $\delta v \propto \ell^p$. This empirical law is known as the linewidth-size relation. However, the determination of p strongly depends on the tracer, because optical depth effects significantly affect the observations. How do the different cloud tracers influence these turbulent slopes?

3. Is there a critical density threshold below which CO fails as a gas tracer of turbulence?

Since ^{12}CO is optically thick, it saturates above a specific column density

threshold and subsequently lose its ability to accurately trace very dense gas regions. Furthermore, it is known as a tracer which only works in compact cloud regions and which fails in diffuse regions. However, the question then is: Is there a critical density threshold below which ^{12}CO fails as a gas tracer?

4. What are the advantages and disadvantages of the different statistical methods?

There exist a lot of different methods to characterize the turbulence in MCs, e.g. structure functions, PCA or the Δ -variance. Clearly, some of them have advantages and disadvantages in terms of computational cost, accuracy and theoretical meaning. How do these methods compare with each other and which provide the most information on the physics of the cloud?

5. How do our theoretical models compare to observational measurements?

Theoretical models alone are useless unless they are linked to the observable world. How do our theoretical models compare with existing observational measurements?

6. Could a high level of turbulence suppress star formation?

Star formation is very efficient if the MC is in virial equilibrium. This can be characterized through the virial parameter, $\alpha = E_{\text{kin}}/|E_{\text{pot}}|$, defined as the ratio of kinetic and potential energy of the system. For virialized clouds we have $\alpha = 0.5$. But what about unbound clouds with $\alpha > 1.0$? Then, the turbulent kinetic energy dominates the potential energy and one would expect that the star formation efficiency significantly decreases. Can star formation occur even in clouds which are highly unbound, e.g. with values $\alpha \geq 8.0$?

7. Could a high external radiation field suppress (or even inhibit) star formation?

We can ask the same question if the cloud is exposed to a very high external radiation field. The higher the interstellar radiation field, the larger the radiation pressure, because $p = u/3$ for isotropic radiation, with u being the energy density of the photon field. How does an extreme interstellar radiation field affect the star formation efficiencies?

8. How does the star formation efficiency depend on the environmental volume density?

The empirical Schmidt-Kennicutt law relates the star formation rate surface density to the gas surface density. This means that the star formation efficiency should also depend on the environmental volume density of the cloud. How are they related? Can we quantify this?

9. Which tracers other than CO can we use to gain information about the properties of clouds in an extreme CMZ-like environment?

In an extreme CMZ-like environment we find a very high interstellar radiation

Cloud Type	A_V [mag]	n_{tot} [cm^{-3}]	L [pc]	T [K]	M [M_{\odot}]	Examples
Diffuse	1	500	3	50	50	ζ Ophiuchi
Giant Molecular Cloud	2	100	50	15	10^5	Orion
Dark Clouds						
Complexes	5	500	10	10	10^4	Taurus-Auriga
Individual	10	10^3	2	10	30	B1
Dense Cores	10	10^4	0.1	10	10	TMC-1/B335

Table 1.1:

Different observable properties of various molecular cloud types and some famous examples, taken from Stahler & Palla (2006).

field, which can photodissociate molecular CO. Thus, we would expect that it could be complicated to use such a molecular tracer to infer information about the cloud properties (e.g. the effective radius, internal velocities, etc.). Which other tracers could be used?

10. How does the X_{CO} -factor of clouds in a CMZ-like environment compare with the canonical value?

The X_{CO} -factor is defined as the ratio of H_2 column density and integrated intensity of ^{12}CO , $X_{\text{CO}} = N_{\text{H}_2}/W_{\text{CO}}$. The canonical value of the X_{CO} -factor is $X_{\text{CO}} \approx 2 - 4 \times 10^{20} \text{ cm}^{-2} \text{ K}^{-1} \text{ km}^{-1} \text{ s}$, primarily valid for MCs in the Milky way disk. It is still unclear whether its value is the same for a cloud located in an extreme environment like the CMZ or for ULIRGs³. Do we find the same or a larger/smaller value of X_{CO} for these systems?

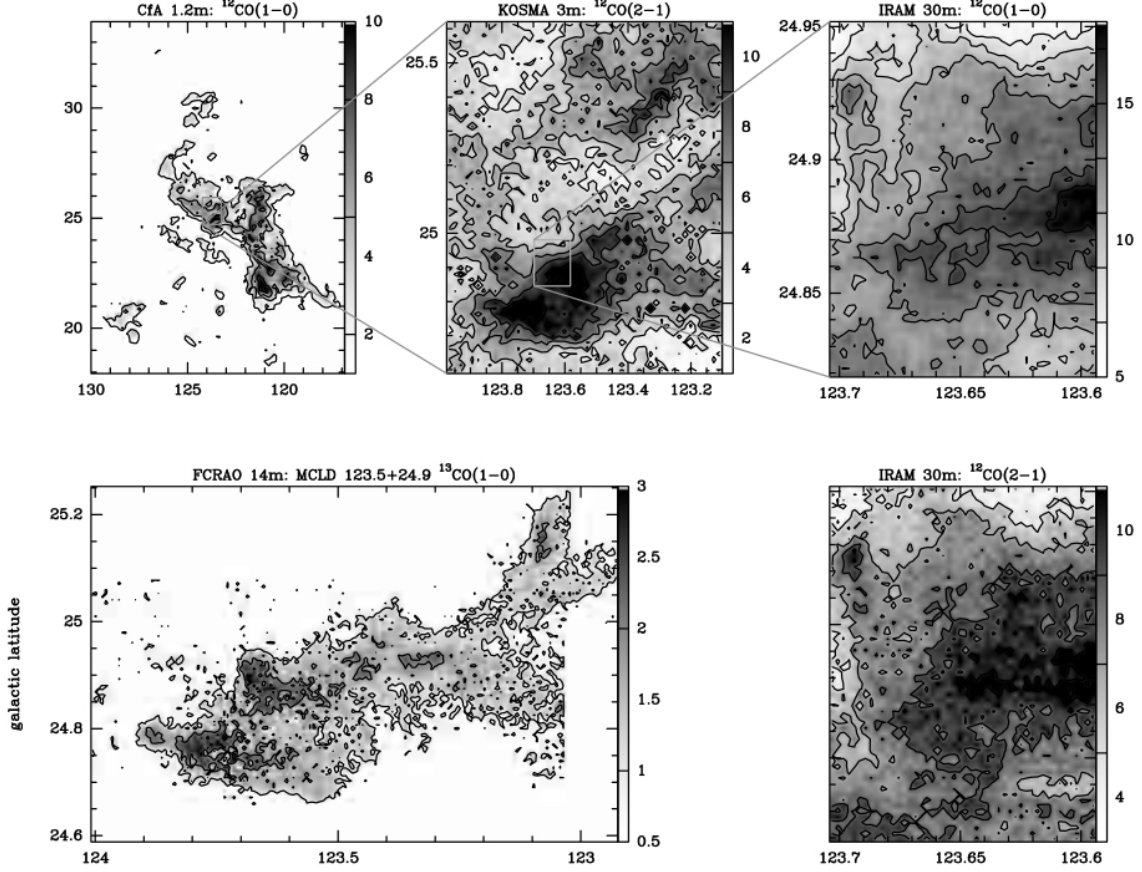
In the following, we shortly review some important aspects of molecular clouds and turbulence, which are necessary to properly understand the chapters of this thesis.

1.4 Observable properties of molecular clouds

Molecular clouds play a fundamental role in the process of star formation. They are stellar nurseries (Lada & Lada, 2003) and mainly consist of molecular hydrogen, H_2 , which is unobservable at typical cloud temperatures of $T \approx 10 - 50 \text{ K}$, since it has no permanent dipole moment. Furthermore, its rotational and vibrational modes are too energetic to be excited by collisions in such a cold environment. The second most abundant molecule is carbon monoxide⁴, ^{12}CO or ^{13}CO . It is often used as a tracer to gain information about the underlying distribution of H_2 . Fortunately, CO is bright enough to be easily observed in MCs and so observers rely on measurements of the $J = 1 \rightarrow 0$, $J = 2 \rightarrow 1$ or other fine structure lines of these tracers (see, e.g. Stutzki et al., 1988; Beuther et al., 2014; Ragan et al., 2015; Cormier et al., 2015).

³Ultra luminous infrared galaxies

⁴In the following we will simply write CO instead of ^{12}CO .

**Figure 1.3:**

Velocity integrated spectral line maps of the rotational transition $^{12}\text{CO } J = 1 \rightarrow 0$, $^{12}\text{CO } J = 2 \rightarrow 1$ and $^{13}\text{CO } J = 1 \rightarrow 0$, observed towards the Polaris Flare, and one of its cores, MCLD 123.5+24.9. The transition and the telescope are indicated at the top of each panel. The line intensity is given in main beam brightness temperature, T_{mb} . Iso-intensity levels are shown from 2 to 8 in steps of 2 (CfA map), 1 to 11 by 2 (KOSMA), 1 to 4 by 1 (FCRAO), 5 to 17 by 2 (IRAM, $^{12}\text{CO } J = 1 \rightarrow 0$), 3 to 11 by 2 (IRAM, $^{12}\text{CO } J = 2 \rightarrow 1$), in units of K km s^{-1} . This Figure is taken from Bensch et al. (2001).

Other molecular tracers that are commonly used, for example, are HCN, NH_3 or CS (Ziurys & Turner, 1986; Schilke et al., 2000; Beuther et al., 2004; Juvela et al., 2012). However, the problem is that the optical properties of some tracers make observations often complicated. For example, ^{12}CO is optically thick and saturates in denser cloud regions, while ^{13}CO is known to be optically thin (see, e.g. Glover et al. 2010, Shetty et al. 2011a). Furthermore, CO freezes out in the very dense cloud regions (Alves et al., 1999). Hence, any observation always relies on a combination of numerous tracers to get an idea of the physics in the cloud's interior.

The H_2 column density can be inferred using the X_{CO} factor, which relates the velocity-integrated intensity of carbon monoxide, W_{CO} , to the H_2 column density N_{H_2} , defined as $X_{\text{CO}} = N_{\text{H}_2}/W_{\text{CO}}$ (see, e.g. Solomon et al., 1987; Polk et al., 1988; Young & Scoville, 1991; Dame et al., 2001; Liszt et al., 2010; Leroy et al., 2011;

Glover & Mac Low, 2011; Bolatto et al., 2013; Narayanan & Hopkins, 2013; Clark & Glover, 2015). This ratio is thought to be remarkably constant in the Galaxy and thus provides a possibility to estimate the column density of molecular hydrogen in MCs. However, concerns have been raised that the X_{CO} -factor may be significantly different from the canonical value in clouds in the galactic center or in distant starburst galaxies. Furthermore, there is considerable observational evidence that X_{CO} is smaller in ULIRGs than in normal spiral galaxies (see e.g. the detailed discussion in Bolatto et al., 2013).

Another observable gas tracer in MCs is dust. It consists of silicates and graphites with a bit of ice (Ossenkopf et al., 1992; Ossenkopf & Henning, 1994). Dust forms in SN explosions or in AGB stars and provides a surface for complex astrochemical processes, such as for H_2 formation. It also plays an important role for the heating and cooling mechanisms in clouds. For example, dust grains can collide with thermal gas particles, which transfer a fraction of their kinetic and internal energy to the dust particles, which then radiate the energy away and support the cooling of the cloud (Ostriker & Silk, 1973; Whitworth et al., 1998; Williams, 2005). Vice versa, it also supports the net heating due to the photoelectric effect (Weingartner & Draine, 2001). The dust mass only provides about $\sim 1\%$ of the total gas mass and is thus insignificant compared to the mass of hydrogen. However, dust extinction measurements are proportional to the optical depth and thus can be used to estimate the gas content of a cloud (Lada et al., 1994; Alves et al., 1998). Thereby, a gas-to-dust ratio of ~ 100 seems to hold throughout most clouds (Lilley, 1955). The dust emission is continuous, because it can be described by a quasi-blackbody spectrum. The emission lies in the infrared, although the spectral shape strongly depends on the detailed grain composition (Draine 2003a,b). Observations show that the optical depth is related to the frequency via

$$\tau_\nu = \tau_0 \left(\frac{\nu}{\nu_0} \right)^\beta, \quad (1.2)$$

where β is the spectral index and τ_ν and ν the optical depth as well as the frequency of the continuous dust emission, respectively. The suggested value for β lies in the range $1 < \beta < 2$ (see, e.g. Draine & Lee, 1984). The larger the frequency (the lower the wavelength), the higher is the optical depth seen by the dust emission.

The typical size of MCs is on a parsec scale, although Giant Molecular Clouds (GMCs) can have sizes of the order of $L \approx 50$ pc, while dense cores can typically be found on sub-parsec scales down to $L \approx 0.1$ pc (Bergin & Tafalla, 2007). Their masses range from $M \approx 10 M_\odot$ for diffuse MCs to $M \approx 10^5 M_\odot$ for GMCs, while typical number densities are a few $\sim 100 \text{ cm}^{-3}$ for diffuse MCs up to several $\sim 10^4 \text{ cm}^{-3}$. Moreover, typical lifetimes of MCs are of the order $\sim 20 - 40$ Myr (see, e.g. Blitz & Shu, 1980; Fukui & Kawamura, 2010; Meidt et al., 2015). In Fig. 1.3, we show an example of a typical MC observed towards the Polaris Flare in $^{12}\text{CO } J = 1 \rightarrow 0$, $^{12}\text{CO } J = 2 \rightarrow 1$ and $^{13}\text{CO } J = 1 \rightarrow 0$ (Bensch et al., 2001). It shows a filamentary, hierarchical and self-similar structure, which is typical for MCs. Table 1.1 shows different MCs with some interesting properties (Stahler & Palla, 2006).

Importance	Driving mechanism	Injected energy $\dot{\epsilon}$ [erg cm ⁻³ s ⁻¹]
1	Supernovae	3×10^{-26}
2	Protostellar outflows	2×10^{-28}
3	Ionizing radiation	5×10^{-29}
4	Gravitational instability	4×10^{-29}
5	Magnetorotational instability	3×10^{-29}

Table 1.2:

Examples of possible driving mechanisms in MCs together with a magnitude estimate of the injected energy $\dot{\epsilon}$. For further discussions, see the review by Mac Low & Klessen (2004).

1.5 Turbulent properties of the interstellar medium

In Fig. 1.3 we can see that the internal structure of a molecular cloud is highly hierarchical and strongly affected by turbulent motions. This hierarchy was characterized by Larson (1981), who found the empirical result that the CO linewidth δv measured by the Doppler shift scales with the typical size ℓ of the cloud,

$$\frac{\delta v}{\delta v_0} = \left(\frac{\ell}{\ell_0} \right)^p, \quad (1.3)$$

where p is the scaling exponent of the power-law characterizing the turbulent hierarchy. This equation is called *Larson's law*. In particular, Larson (1981) measured $p \approx 0.4$ and $\delta v_0 \approx 1 \text{ km s}^{-1}$. Later studies (e.g. by Solomon et al., 1987) found a slightly steeper relationship, namely $\delta v \propto \ell^{0.5}$. Furthermore, several studies revealed that MCs in other galaxies (e.g. Bolatto et al., 2008) and in the ISM in the Galactic center (e.g. Oka et al., 2001; Shetty et al., 2012) also follow a similar relationship. During the last decades, this linewidth-size relationship has been the focus of a large number of studies (see, e.g. Ossenkopf & Mac Low, 2002; Heyer & Brunt, 2004; Heyer et al., 2009; Roman-Duval et al., 2011; Ballesteros-Paredes et al., 2011).

The basis of turbulent star formation was initially set by the theoretical framework developed by Kolmogorov (1941). In his phenomenological models, Kolmogorov (1941) assumed a hierarchical energy cascade, while the statistical properties are completely defined by means of the wavenumber and the energy dissipation rate. Comparing to Larson's law, Kolmogorov (1941) found a value $p = 1/3$, which does not quite seem to fit into the observable range of power-law slopes with $p \approx 0.4 - 0.8$ (Heyer & Schloerb, 1997; Brunt et al., 2003; Heyer & Brunt, 2004; Federrath et al., 2010; Roman-Duval et al., 2011). The problem is that the theory assumes subsonic and incompressible turbulence, while the turbulent motions found in MCs are highly supersonic and compressible with sonic Mach numbers (much) larger than unity, $\mathcal{M}_s = v_{\text{turb}}/c_s > 1$ (Padoan, 1995; Padoan et al., 1997, 1999; Boldyrev et al., 2002; Mac Low & Klessen, 2004; Federrath et al., 2010), where v_{turb} is the turbulent velocity dispersion and c_s the sound speed. Typical values for the velocity dispersions

in clouds are of the order of several km s^{-1} . Thus, the Kolmogorov (1941) theory cannot be the final description for the dynamics of the ISM.

Later, the Kolmogorov (1941) theory was modified by Burgers (1948), who assumed shock-dominated turbulence, for which he found a theoretical value of $p = 1/2$. This value fits much better into the range of observed values. Thus, in MCs we generally would expect to find steeper slopes than the one proposed by Kolmogorov (1941). Moreover, turbulent motions in clouds can also be quantified in terms of the virial α parameter, defined as the kinetic over the potential energy, $\alpha = E_{\text{kin}}/|E_{\text{pot}}|$ (McKee & Zweibel, 1992). Thus, if we assume that the cloud is virialized ($\alpha = 0.5$), we can also estimate the cloud's mass, since $\alpha \approx \sigma^2 R / (2GM)$. However, the assumption of virialization is probably not exact, since other terms of the virial law could alter this law significantly (Ballesteros-Paredes et al., 1999).

Turbulent motions are created by a large number of different physical processes. The most important ones are listed in Table 1.2 (taken from Mac Low & Klessen, 2004). If we compare the values with each other, we find that supernova feedback is supposed to contribute by far the most energy to the turbulent driving (McKee, 1989; Cappellaro et al., 1999), followed by protostellar outflows (Lizano et al., 1988; McKee, 1989). Other effects are ionizing radiation as well as gravitational (Wada et al., 2002) and magnetorotational instabilities (Balbus & Hawley, 1991, 1998).

Observations show that most of these processes excite a considerable amount of compressive velocity modes, which are responsible for the formation of stars. According to the Helmholtz decomposition, we can split up each vector field $\mathbf{f}(\mathbf{r})$ into a rotational and a divergence part. A pure rotational vector field is divergence-free, $\nabla \cdot \mathbf{f} = 0$, while a pure divergent vector field is rotational-free, $\nabla \times \mathbf{f} = 0$. The first is the solenoidal, the latter the compressible case. A good approximation for the ISM and MCs in numerical simulations is a natural 2:1 mixture of solenoidal to compressive modes (Padoan et al., 1997; Klessen et al., 2000; Klessen, 2001; Heitsch et al., 2001; Elmegreen & Scalo, 2004; Pan et al., 2015). Thus, a forcing routine embedded in a numerical scheme has to account for the correct driving mechanism.

Turbulence also plays a crucial role in the evolution of interstellar magnetic fields. Many molecular clouds are observed to be roughly trans-Alfvénic, with Alfvén Mach numbers of the order $\mathcal{M}_A = v_{\text{turb}}/v_A \sim 1$ (Crutcher, 1999), where v_A is the Alfvén velocity. In magnetized clouds, the magnetic field can grow due to the turbulent dynamo. Thereby, kinetic energy is converted into magnetic energy, which leads to an increase of the field strength (Brandenburg & Subramanian, 2005; Schober et al., 2012; Brandenburg et al., 2012). Typical magnetic field strengths that are observed in MCs are of the order of several μG (Crutcher, 2012). However, there is also observational evidence that magnetic fields are significantly stronger in massive and dense cores than in low-mass cores and can reach values of several $100 \mu\text{G}$ up to a few mG (Crutcher, 1999; Beuther et al., 2010; Crutcher et al., 2010).

The magnetic field strength can be measured via Faraday rotation (Crutcher & Troland, 2008), by studying synchrotron emission or via Zeeman splitting (Crutcher et al., 1993, 1999). The latter is a common method used by observers and relies on the linear coupling of the magnetic field to the magnetic dipole moment of the

electron in the Hamilton operator, which induces a small shift in the spectral lines. By measuring this energy difference, we can compute the strength of the magnetic field in the cloud. In a similar fashion, the Faraday rotation describes the rotation of the polarization plane of electromagnetic waves due to an external magnetic field and synchrotron emission is radiated by relativistic electrons accelerated by a B-field.

So far, we have seen that turbulent motions are an important ingredient for star formation. Turbulence affects a vast number of observable properties of which we will present and discuss just a few of the most important aspects in the following.

1.5.1 Mass-density distribution within clouds

In the past years, various studies have established that the mass-density PDF of isothermal turbulent clouds can be well approximated by a log-normal distribution (see, e.g. the studies and the references in Padoan et al., 1997; Padoan & Nordlund, 2002; Federrath et al., 2010; Konstandin et al., 2012). This PDF can be measured in supersonic turbulent gas, where we can observe a mixture of dense, diffuse and void regions with a high density contrast. Following Padoan & Nordlund (2002), we can characterize this mass distribution by introducing a new variable s , defined as the natural logarithm of density ρ and mean density $\langle \rho \rangle$,

$$s \equiv \ln \frac{\rho}{\langle \rho \rangle}. \quad (1.4)$$

This new variable seems to describe a log-normal distribution, which can be characterized by the following Gauss function:

$$p(s)ds = \frac{1}{\sqrt{2\pi\sigma_s^2}} \exp\left[-\frac{(s - \langle s \rangle)^2}{2\sigma_s^2}\right] ds. \quad (1.5)$$

In this equation, σ_s is the standard deviation of our new s -variable. This relation yields a fairly well approximation for the mass-density distribution caused by turbulent motions. However, it is known that in real clouds small deviations from this log-normal shape caused by so-called intermittency effects exist (see, e.g. Batchelor & Townsend, 1949; Anselmet et al., 1984). We will study these effects later in chapter 4 when we discuss turbulence theory.

Furthermore, various studies have shown that σ_s also depends on the sonic rms Mach number \mathcal{M} of the turbulent medium. In particular, σ_s can be characterized by means of the following relation:

$$\sigma_s^2 = \ln(1 + b^2 \mathcal{M}^2). \quad (1.6)$$

Here, b is a dimension-less number, which also depends on the forcing routine (Federrath et al., 2010). We see that the dispersion of s grows with increasing sonic Mach number. This makes sense because we would naively expect that larger turbulent motions immediately lead to a broader distribution of the cloud's density.

Thus, we can learn something about the nature of turbulence if we study the width of the PDF in more detail. In particular, Padoan et al. (1997) found $b \approx 0.5$ from 3D MHD simulations of turbulence, which seems to be a reliable estimate of this parameter. However, as noted by Federrath et al. (2010), b also strongly depends on the turbulent driving. From isothermal MHD simulations, they find $b \approx 1/3$ for fully solenoidal and $b \approx 1$ for fully compressive turbulent driving.

1.5.2 Filamentary structure of the ISM

The structure of MCs is filamentary, as revealed by a large number of previous studies (see, e.g. Schneider & Elmegreen, 1979; Bally et al., 1987; Nutter et al., 2008; André et al., 2010; Arzoumanian et al., 2011; Schneider et al., 2012; Kirk et al., 2013; Zernickel et al., 2013; Smith et al., 2015). An observational example for the internal structure of a cloud is shown in Fig. 1.3, where we can see filaments of different sizes and on different spatial scales. Further examples will be presented in chapters 5, 6 and 7.

Filaments are important structures in MCs. Their shapes are strongly influenced by turbulent motions. The story behind filaments is the following: Prestellar cores form along filaments, which by themselves are again embedded in a larger network of filaments. It is assumed that gas in clouds is first assembled along the filament, which then fragments into individual dense cores. This fragmentation occurs due to gravitational instability and there have been attempts also to estimate a critical density threshold above which this process happens (André et al., 2010). The theoretical background for this collapse along the filament was first given by Inutsuka & Miyama (1992), who showed that in an unmagnetized isothermal filament a critical line threshold exist, which is unstable to axisymmetric perturbations if the critical line mass is greater than the number $M_{\text{line}}^{\text{crit}} = 2c_s^2/G$, with c_s being the (isothermal) sound speed and G the gravitational constant. Interestingly, this threshold only depends on the temperature of the medium. For a gas with $T \approx 10$ K we can estimate this value to be $\sim 16 M_\odot/\text{pc}$, which translates into a column density threshold of $\sim 160 M_\odot/\text{pc}^2$ or a volume density threshold of $\sim 1600 M_\odot/\text{pc}^3$.

Furthermore, an important observational result is one first noted by (Arzoumanian et al., 2011), who found a characteristic width of ~ 0.1 pc for filaments in the Herschel Gould Belt survey. In their study, (Arzoumanian et al., 2011) describe their filaments by a Plummer profile function,

$$\rho(r) = \frac{\rho_c}{[1 + (r/R)^2]^{p/2}} \quad (1.7)$$

where ρ_c is the density in the center of the filament, R is the characteristic radius of the flat inner portion of the density profile and p is a constant. In particular, they find a value $p = 2$. Moreover, it has been noted that ~ 0.1 pc is also the size scale that marks a transition to coherence between the turbulent and the quiescent gas in a cloud (Goodman et al., 1998; Pineda et al., 2010). However, it is still under

an active debate what the role of turbulence together with magnetic fields and self-gravity is and how they affect other observable properties, e.g. the IMF or the star formation rate.

1.5.3 The star formation rate and efficiency

Star formation is supposed to be inefficient, even if we average over a larger sample of clouds in the Galaxy. Only a small fraction of the gas in a cloud is converted to stars. The star formation rate (SFR) in the Milky Way was estimated to be $\sim 3 - 5 M_{\odot} \text{ yr}^{-1}$, corresponding to a star formation efficiency (SFE) per free-fall time of roughly $\sim 1\%$ (Murray, 2011; Krumholz et al., 2012). It is obvious that the SFR is directly affected by the conditions of turbulence in a cloud. However, how can we get such a connection between the SFR and supersonic turbulence? Or in other words: Can we get a predictive theory of star formation from the underlying turbulence statistics? Such a theory has to account for the fact that local processes can significantly influence the SFR. Such processes are e.g. radiation, stellar winds, magnetic fields as well as outflows and jets (see, e.g. Dale et al., 2005; Banerjee & Pudritz, 2006; Krumholz et al., 2007; Peters et al., 2010; Seifried et al., 2012). Moreover, in a recent study, Federrath (2015a) found that only models including turbulence, magnetic fields and feedback can produce a realistic SFR.

Several studies tried to analyze the dependence of the turbulence on the SFR. In an effort to quantify this, Krumholz & McKee (2005) introduced an analytic expression to compute the SFR per free-fall time, which reads

$$\text{SFR}_{\text{ff}} = \frac{\epsilon_{\text{ff}}}{\phi_t} \int_{x_{\text{crit}}}^{\infty} x p(x) dx, \quad (1.8)$$

where ϵ_{ff} is the fraction of mass which reaches the collapsing core phase, ϕ_t is a factor which might influence the free-fall timescale t_{ff} , e.g. due to the presence of magnetic fields, x is the density normalized by the mean density and $p(x)$ the PDF of the gas density. In particular, Krumholz & McKee (2005) adopt a value of $\epsilon_{\text{ff}} \approx 0.5$, although we note that the exact value strongly depends on the environmental conditions. What does this integral tell us? First, it computes the fraction of total mass above a critical value x_{crit} which is in an unstable phase. The value of x_{crit} is motivated by the fact that the thermal sound speed is of the order of the turbulent fluctuations at the collapse scale (for further details see the discussion in Krumholz & McKee, 2005). Second, additional prefactors guarantee that the SFR can be significantly affected by jets, outflows, magnetic fields, and so on. We can then also translate the dimension-less quantity SFR_{ff} into a real SFR by using

$$\dot{M} = \text{SFR}_{\text{ff}} \frac{M_{\text{cloud}}}{\phi_t t_{\text{ff}}}, \quad (1.9)$$

where ϕ_t is expected to be of the order unity, $\phi_t \sim 1$. In particular, (Krumholz & McKee, 2005) find $\phi_t \approx 1.91$ through a Levenberg-Marquardt fit for the numerical simulations which are discussed in a study by Vázquez-Semadeni et al. (2003).

Using the SFR above, we can also define a SFE per free-fall time,

$$\epsilon_{\text{ff}} = t_{\text{ff}} \cdot \frac{\dot{M}_*}{M_{\text{cloud}}}, \quad (1.10)$$

where \dot{M}_* is the star formation rate averaged over t_{ff} (Krumholz & McKee, 2005; Krumholz & Tan, 2007; Murray, 2011). We will estimate this quantity later in simulations of star formation in the CMZ near the galactic center.

1.5.4 The stellar initial mass function

Another important observable property which is also significantly affected by turbulence is the stellar initial mass function (IMF) and the initial core mass function (CMF), which characterize the mass distribution of stars (cores). Although we do not study the IMF in this thesis explicitly, we nevertheless want to briefly discuss some key properties of the IMF because of the high importance of it in response to turbulent motions.

If dN is the infinitesimal number of objects per unit mass bin dM , the distribution of stars in the Galaxy is given by the empirical power-law

$$dN \propto M^{-\alpha} dM, \quad (1.11)$$

where α is a dimension-less exponent. It was first characterized in a famous paper by Salpeter (1955), who proposed a value $\alpha \approx 2.35$ for stars in a range of $0.4 - 10$ solar masses. That means that low mass stars are much more common in the Universe than high mass stars. Later on, Kroupa (2001) suggested a broken power-law with $\alpha \approx 2.35$ above half a solar mass as well as $\alpha \approx 1.3$ between $0.08 - 0.5 M_{\odot}$ and $\alpha \approx 0.3$ below $0.08 M_{\odot}$. This steeply decreasing tail at higher masses was also supported in a study by Chabrier (2003). However, the exact relation between the CMF and the IMF is still a highly debated topic (see, e.g. the studies and the references in Alves et al., 2007; Goodwin et al., 2008). The easiest approach is to assume that both CMF and IMF only differ by some constant factors.

The interesting question is how turbulent motions affect the shape of the IMF (see, e.g. the reviews by Mac Low & Klessen, 2004; Elmegreen & Scalo, 2004). Since turbulence seems to be a probabilistic theory, the distribution of stars within a cloud will also be probabilistic to some degree. Hence, we should in principle be able to connect the statistics of the IMF to statistical measures of the turbulent gas, although there is no precise theoretical description yet. However, some attempts have already been made. For example, in an approach by Hennebelle & Chabrier (2008), they derive an analytical theory of the IMF based on a Press-Schechter statistical formalism and on models of supersonic turbulence. Their mass spectrum reproduces the observed IMF well. Moreover, Padoan & Nordlund (2002) studied how supersonic turbulent motions fragment MCs and how this process leads to the observed IMF. However, although most studies agree that turbulence plays a key role for the mass distribution of stars, a comprehensive theoretical description requires further simulations that rule out the role of the initial conditions on the IMF.

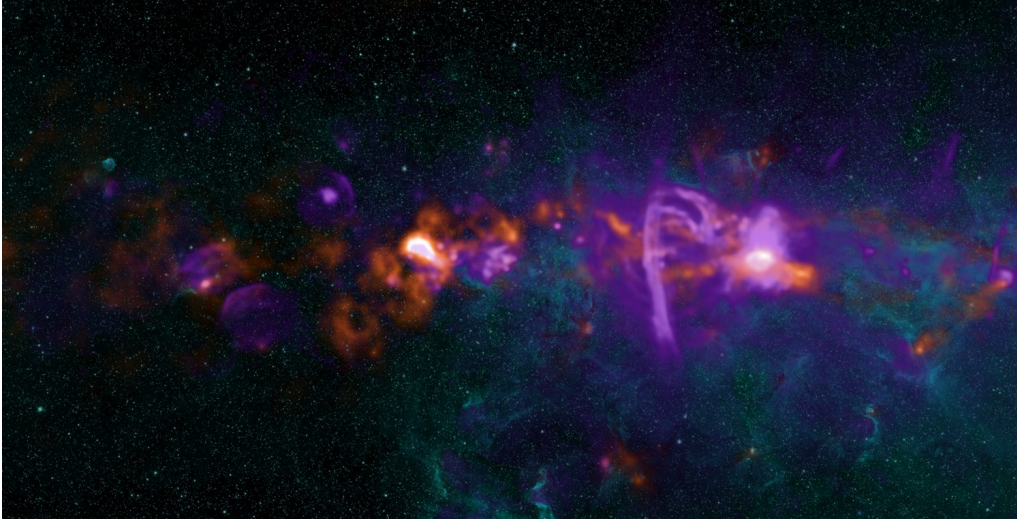


Figure 1.4:

The Galactic Center with its surrounding Central Molecular Zone (CMZ). This image was taken with the NRAO Very Large Array at 20 cm (purple) and with the Caltech Submillimeter Observatory at 1.1 mm (orange). The purple regions are HII regions which are illuminated by supernovae remnants and hot massive stars. The orange regions are cold dust regions of molecular gas with temperatures of 20 – 30 K. The scale of the CMZ is about ~ 200 pc in radius. The investigators are Adam Ginsburg and John Bally (University of Colorado, Boulder) and Farhad Yusef-Zadeh (Northwestern University).

1.6 Star formation in extreme regions: the CMZ and the Galactic Center

The Galactic Center (GC) in our Milky Way is a fascinating region for many reasons. It is located 8.33 ± 0.35 kpc from the earth (Gillessen et al., 2009; Eisenhauer et al., 2005, 2003) in the directions of Sagittarius and Scorpius and provides an accessible laboratory for studying physical processes under extreme conditions. Such extreme conditions are e.g. the high interstellar radiation field and the high cosmic-ray flux (which can be larger by a factor $\sim 100 - 1000$ than the solar neighbourhood value; see, e.g. Yusef-Zadeh et al., 2007; Clark et al., 2013; Ginsburg et al., 2015; Indriolo et al., 2015), high internal velocity dispersions (which can be of the order of several 10 km s^{-1} ; see, e.g. the studies by Genzel & Townes, 1987; Morris & Serabyn, 1996a; Johnston et al., 2014), high densities (of the order of $> 10^4 \text{ cm}^{-3}$ in some clouds; see, e.g. Longmore et al., 2012; Kauffmann et al., 2013) or high magnetic fields (typically also enhanced by a factor of ~ 1000 ; see, e.g. Morris, 2014; Pillai et al., 2015) and occur in molecular clouds found in the *Central Molecular Zone* (CMZ) around the GC. In Fig. 1.4 we present an image of the GC with its surrounding CMZ⁵, which extends outwards to ~ 200 pc in radius. In Tab. 1.3 we compare

⁵Image credit (07/12/2015): <http://images.nrao.edu/664>

some important physical quantities measured in the solar neighbourhood with those observed in the CMZ. We see that most observables are enhanced by a factor of $\sim 100 - 1000$ compared to local cloud values.

In the CMZ itself one can identify three clusters of young massive stars (see, e.g. Tambllyn et al., 1996; Genzel et al., 1996; Paumard et al., 2001, 2006; Tanner et al., 2006): the Arches cluster (~ 30 pc away from the GC with $M > 10^4 M_\odot$), the Quintuplet cluster (~ 30 pc from the GC with $M \approx 10^4 M_\odot$) and a cluster around the central black hole (Figer et al., 1999). These three clusters contain hundreds of main sequence O-stars, tens of Wolf-Rayet stars and a few blue variable stars. Most stars are not distributed randomly but rather lie in one or two disks around the center that are strongly inclined to each other. In projection on the plane of the sky the inner disk appears to rotate clock-wise and the outer one counter-clockwise (see e.g. the review by Alexander, 2005; Genzel et al., 2010).

An important heating source in CMZ clouds are cosmic rays. They most notably consist of protons, but also of electrons and ionized atoms. The distribution $F(E)$ of the cosmic ray particles per unit time, unit area and energy interval can be characterized by the following power law:

$$F(E) \propto E^{-\gamma}. \quad (1.12)$$

Here, γ is the power law slope, while observations show that $2.7 \lesssim \gamma \lesssim 3.0$ holds (see, e.g. Nagano et al., 1992; Abraham et al., 2008). Typically, those particles have energies in the range of $10^{15} - 10^{20}$ eV. They are supposed to be produced in AGNs, cosmic jets of magnetized neutron stars and black holes or in shocks of supernova explosions (Hillas, 1984). Cosmic rays can significantly ionize the ISM (in particular the hydrogen) and also heat up the gas in the deep interior of clouds, preventing dense cores from gravitational collapse, as we will see later.

The GC contains a bright HII region (*Sgr A West*) and the densest star clusters in our Galaxy. At the center we expect a supermassive black hole, named *Sgr A**, with a mass of about $3 - 4 \times 10^6 M_\odot$ (Schödel et al., 2002; Ghez et al., 2003), which can be inferred e.g. by the orbital period of the S2 star. *Sgr A** is a compact radio source whose formation history is not known yet. It is supposed to have a diameter of $\sim 4.4 \times 10^7$ km (Doeleman et al., 2008), which is slightly less than the distance from Mercury to the sun at its perihelion. The GC itself cannot be observed directly in the visible spectrum due to gas and dust along the line-of-sight. The available information comes from gamma ray, infrared or radio wavelength observations. The very central region is at ~ 1.5 pc surrounded by a torus of very dense gas, called the *circum nuclear disk* (Genzel, 1989; Christopher et al., 2005).

The conversion of gas into stars is a fundamental process in astrophysics. Stars form in regions of dense gas by collapse of dense clumps (see, e.g., the reviews by Mac Low & Klessen, 2004; McKee & Ostriker, 2007). Previous studies by Krumholz & McKee (2005), Bigiel et al. (2008), Padoan & Nordlund (2011) and others showed that the number of stars formed per unit time (referred to as the star formation rate, or shortly SFR) is proportional to the amount of gas in the star-forming region (see

	Solar neighbourhood	Central Molecular Zone
Densities	$\sim 100 \text{ cm}^{-3}$	$> 10^4 \text{ cm}^{-3}$
Temperatures	$\sim 20 \text{ K}$	$\sim 70 \text{ K}$
Velocities	a few km s^{-1}	a few 10 km s^{-1}
Magnetic fields	a few μG	a few mG
Interstellar radiation field	$G_0 = 1$	$G_0 = 100 - 1000$
Cosmic-ray flux	$3 \times 10^{-17} \text{ s}^{-1}$	$10^{-14} - 10^{-15} \text{ s}^{-1}$

Table 1.3:

Comparison of some important physical properties measured in solar neighbourhood clouds and in clouds located in the Central Molecular Zone (CMZ).

e.g., Schmidt, 1959; Kennicutt, 1998b). That means that the SFR surface density Σ_{SFR} shows a power-law dependence on the gas surface density Σ_{gas} , and we can quantify this relation via

$$\Sigma_{\text{SFR}} \propto (\Sigma_{\text{gas}})^n, \quad (1.13)$$

where n is a power-law slope index. Kennicutt (1998b) found a value $n = 1.4 \pm 0.15$, while Schmidt (1959) estimated a value $n \approx 2$. This is known as the Schmidt-Kennicutt relation and is an important empirical result in star formation theory. It appears to hold in the disk of our Milky Way and also in distant galaxies (Kennicutt & Evans, 2012). However, there is still some debate about whether a universal relationship holds for all galaxies or not and whether this relation also yields reliable estimates for the SFR in an extreme environment like the CMZ (see, e.g. Shetty et al., 2013, 2014). Furthermore, there is observational evidence that the SFR in the CMZ lies significantly below the Schmidt-Kennicutt relation (Longmore et al. 2013a). Thereby, the measured SFR seems to be suppressed by a factor of at least $\gtrsim 10$. Hence, an unresolved question still is: What regulates star formation in the central few hundred parsecs of the Galaxy?

Several studies have tried to solve this problem of star formation in such an extreme environment, which challenges current star formation theories. For example, Kruijssen et al. (2014) studied the impact of several mechanisms on the SFR on different physical scales, e.g. the very strong radiation field, magnetic fields, turbulent pressure, galactic tides or feedback. They argue that star formation could be episodic due to a gradual build-up of dense gas by spiral instabilities or that variations in the rates of gas flows into the CMZ might significantly alter the star formation process. Longmore et al. (2013a) state, for example, that the order of magnitude higher internal velocity dispersion could disrupt compact regions before they are able to go into gravitational collapse. However, the question which physical processes are most important for regulating the SFR in the CMZ still remains unsolved. The most likely scenario at the moment is that a combination of various strong physical processes might be able to regulate the SFR in this region. However, since the conditions in the CMZ are so extreme, studies which account for all these processes are rare and numerically very challenging, as we will see next.

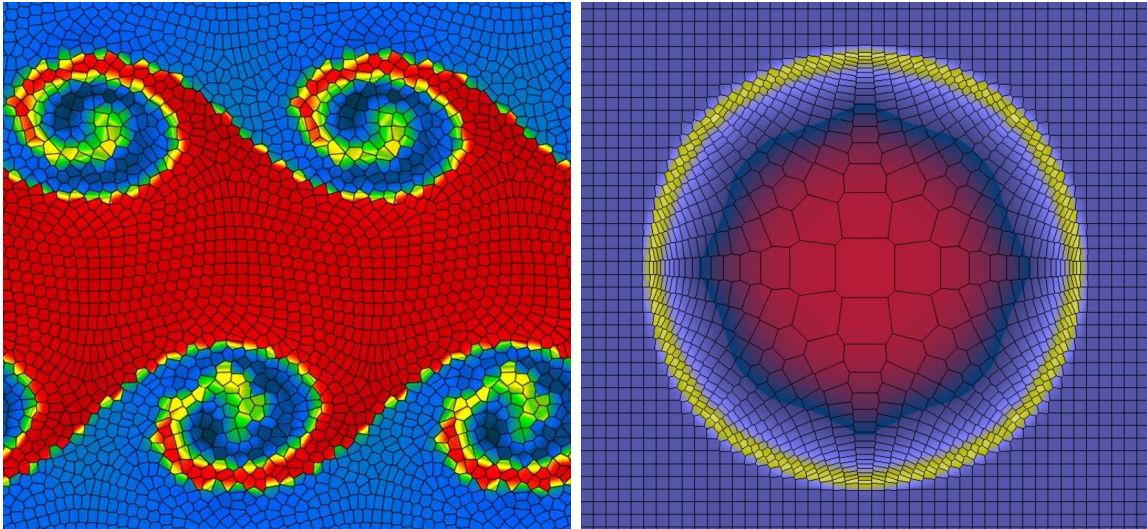


Figure 1.5:

Prominent examples of applications using the moving mesh code AREPO. The left plot shows a Kelvin-Helmholtz instability, while the right plot illustrates a Sedov-Taylor expansion in a low resolution calculation, most notably used to study the dynamics of supernova explosions. Each plot shows the density field overlaid with the Voronoi tessellation in black. We directly see the big advantage of the unstructured and moving mesh, which allows us to accurately track the flows in the simulations with high precision.

1.7 Numerical implementation of the simulations

In this work, we run high-resolution three-dimensional simulations of turbulent interstellar gas. Our simulations that we describe in chapters 5 and 6 are modeled using a modified version of the ZEUS-MP magnetohydrodynamical code (Norman, 2000; Hayes et al., 2006). ZEUS-MP is a multiphysics (MP) code for astrophysical fluid dynamics, implemented in Fortran 77 and parallelized using MPI⁶. It uses an Eulerian grid and incorporates four main code modules: a hydrodynamical and magneto-hydrodynamical module as well as a module for radiation transport and self-gravity, exclusively written for 3D astrophysical simulations. The code was developed at the Laboratory for Computational Astrophysics (LCA) of the National Center for Supercomputing Applications (NCSA) at the University of Illinois.

The simulations that we present in chapters 7, 8 and 9 are modeled using the novel AREPO code (Springel, 2010), an improved version of the successful GADGET-2 code (Springel, 2005). It is written in C++ and also parallelized using the MPI. AREPO is a moving mesh code, which makes use of an unstructured mesh, the so-called Voronoi tessellation. The aim of AREPO is to eliminate the disadvantages of older codes, that means codes which use either a Lagrangian or Eulerian scheme. In this context, it unifies the power of both methods, which makes it fully Galilean invariant. Furthermore, it incorporates an adaptive mesh refinement (AMR) method

⁶Message Passing Interface

to follow the evolution of high-density regions in the clouds as well as an accurate treatment of self-gravity for the gas. Thus, the code can be used to solve complex numerical problems with a very high accuracy. In Fig. 1.5, we show two prominent examples of applications using the moving mesh code AREPO: a Kelvin-Helmholtz instability as well as a Sedov-Taylor explosion⁷. We directly see the big advantage of the unstructured and moving mesh, which allows us to accurately track the flows in the simulations with high precision.

In both codes, we have embedded a detailed atomic and molecular cooling function, described in detail in Glover et al. (2010) and Glover & Clark (2012), which allows us to run non-isothermal simulations and to study the properties of the ISM very close to reality. Furthermore, we make use of a simplified treatment of the molecular chemistry of the gas. Our chemical treatment is based on the work of Nelson & Langer (1999) and Glover & Mac Low (2007), and allows us to follow the formation and destruction of H₂ and CO self-consistently within our simulations. The chemical network tracks the abundances of 9 species and follows 30 chemical reactions. Full details of the chemical model can be found in Glover & Clark (2012).

For each numerical experiment, we also study the dependence of our results on the specific choice of resolution. The corresponding studies are presented at the end of this thesis in the Appendix.

Furthermore, the codes have to guarantee numerical stability. An important number in this context is the *Courant-Friedrichs-Lewy (CFL) number*, which is used to numerically discretize time-dependent partial differential equations. In particular, it gives a computational measure for the numerical stability of the code. For example, if we assume a wave which propagates through the computational domain with velocity u , then the spatial and temporal steps Δx and Δt of the numerical scheme have to be chosen such that the wave can still be resolved. To quantify this, we can define the CFL number c as the ratio of the two velocities, that means

$$c = \frac{u}{\Delta x / \Delta t} = \frac{u \Delta t}{\Delta x}. \quad (1.14)$$

If $c \lesssim 1$, the scheme is supposed to be numerically stable (see, e.g. the introduction into numerical methods by Toro, 2009). Typically, in the presented simulations we adopt values $c \simeq 0.4 - 0.8$ (Springel, 2010). This condition directly leads to the CFL timestep $\Delta t = c \Delta x / u$, which determines the maximum allowed timestep for cells.

During our simulations, the code refinement accounts for very dense and collapsing gas regions. However, these regions strongly affect the integration times Δt of the Riemann solver, making the runs more and more computationally expensive. Therefore, we have embedded a sink particle algorithm, which accounts for the sub-grid physics (see, e.g. Bate et al., 1995; Jappsen et al., 2005; Greif et al., 2011). If the Jeans length cannot be resolved anymore, the compact gas region is put into a Lagrangian particle, which only interacts gravitationally with the surrounding medium. Therefore, various checks have to be fulfilled before a dense region is considered as a sink. More details about the algorithm will be given in chapter 7.

⁷Image credit (07/12/2015): <http://wwwmpa.mpa-garching.mpg.de/~volker/arepo/>

1.8 Outline of the thesis

The aim of this thesis is to better understand the role of turbulence in the process of star formation. Therefore, we start with an introduction to the theoretical principles of hydrodynamics in chapter 2. Since we try to derive the most important equations in a relativistic form, we start with a short overview of the structure of spacetime and consider the theory of special relativity in Section 2.1. In the next Section 2.2, we then explain that our approach of hydrodynamics is only valid in the case where the mean free path of the fluid particles λ is much smaller than the typical length scale L of the system, $\lambda \ll L$. It follows a derivation of the collision-less Boltzmann equation in phase-space, which we then use to derive the continuity equation. We continue with a review on the full set of important equations of hydrodynamics. These are Euler's equation of motion, the Navier-Stokes equation, the energy equation as well as Poisson's equation and a closure equation to relate the pressure to the density field. Furthermore, we also describe the physics of sound and shock waves, gravitational instabilities and introduce the scalar virial theorem. These are necessary to understand the following chapters of this thesis. In Section 2.3 we continue our analysis by including magnetic fields into our hydrodynamic equations. We shortly review Maxwell's equations and then explain the induction equation, which allows us to extend Euler's equation of motion by a magnetic force term. At the end of Section 2.3 we deal with the generation of magnetic fields as well as their evolution in advection and diffusion processes. We end this chapter with a theoretical treatment of ambipolar diffusion.

In chapter 3, we deal with the concepts of radiative transfer, which we need to understand the basics of the radiative transfer post-processing that we perform later on. Therefore, we first introduce basic physical quantities and move on to describe the interaction process of light with matter. We explain the concepts of black-body radiation and derive the Stefan-Boltzmann law, the Planck spectrum as well as Wien's law and the Rayleigh-Jeans law. In the ISM, absorption and emission processes are crucial and thus we also explain the idea behind the Einstein coefficients, which describe absorption as well as spontaneous and stimulated emission. Afterwards, we continue with a treatment of atomic collisional excitation and de-excitation, derive the Lorentz, the Doppler and the Voigt profile of lines and discuss other sources of line broadening. We then give an overview of important heating and cooling processes in the ISM. At the end of chapter 3, we describe the physics of fine structure line emission and how to measure velocity dispersions using the Doppler shift.

In chapter 4, we explain the basics of turbulence theory. We start with an introduction of symmetry groups and continue with a broad introduction into Kolmogorov's theory. This includes its phenomenology as well as a proper treatment of the turbulent energy cascade. However, Kolmogorov's theory is only valid in the limit of incompressible and subsonic turbulence. This is a problem since turbulent motions in the ISM are highly supersonic and compressible. Thus, modifications

are needed in order to better describe the situation given in MCs. This is why we explain Burger’s turbulence of compressible fluids. Furthermore, there is considerable evidence that intermittency effects play an important role for the higher order structure functions. Thus, corrections to Kolmogorov’s theory are applied in the model from She and Levèque, which account for such intermittent deviations off the log-normal. We finish this section by looking at two other turbulence models, the Dubrulle and Boldyrev model as well as the β -model, which is historically important.

In chapter 5 and 6, we then apply our knowledge and compute structure functions, Fourier spectra and Δ -variances of 2D centroid velocity (CV) maps in order to study the turbulent gas dynamics of typical molecular clouds (MCs) in numerical simulations. These various statistical methods are widely used in the astronomical community and are often applied to obtain information about the underlying velocity field. However, the open question still is how the turbulence statistics is measured by observers (e.g. by observing the intensity of the CO emission) and how this translates into statistical quantities of the total or the H₂ density. We therefore compute statistical averages for the total density, H₂ number density, ¹²CO number density as well as the integrated intensity of ¹²CO ($J = 1 \rightarrow 0$) and ¹³CO ($J = 1 \rightarrow 0$) and compare the results with each other. We show that optical depth effects can significantly affect all statistical measures, which also leads to different scaling properties. Finally, we present a correction factor and describe how one can get the statistical measures of the total or H₂ gas by means of the integrated CO intensity.

We then turn to more extreme regions in our Galaxy and consider star formation in the Central Molecular Zone (CMZ) near the galactic center in chapter 7. We model the evolution of MCs numerically by using the moving mesh code AREPO. All clouds are exposed to a harsh environment similar to that found in the CMZ, in an effort to understand why the star formation efficiency (SFE) of clouds in this environment is so small. The turbulent kinetic energy is regulated by the virial α parameter, expressing the ratio of kinetic to potential energy in the simulation domain. Despite the harsh environment and the large turbulent velocity dispersions adopted, we find that all of the simulated clouds form stars within less than a gravitational free-fall time. However, even in our most unbound clouds, the SFE remains higher than that inferred for real CMZ clouds.

In chapter 8 and 9, we analyze the chemical state of the CMZ clouds from above, since our code also accounts for a simplified treatment of time-dependent chemistry. We use the radiative transfer code RADMC-3D to compute synthetic images in various diagnostic lines. These are [CII] at 158 μm , [OI] (145 μm), [OI] (63 μm), ¹²CO ($J = 1 \rightarrow 0$) and ¹³CO ($J = 1 \rightarrow 0$) at 2600 μm and 2720 μm , respectively. We show that the atomic tracers accurately reflect most of the physical properties of both the H₂ and the total gas of the cloud and that they provide a useful alternative to molecular lines when studying the ISM in the Central Molecular Zone.

We broadly summarize and discuss our main results in chapter 10. Moreover, we provide an outlook of open questions and think of other projects that could help us to expand our knowledge on the role of turbulence in the star formation process.

1.9 General remarks and how to read this work

This PhD thesis contains work which was developed in the years 2014/2015 mainly at the Institute for Theoretical Astrophysics (ITA) in Heidelberg. All material in chapters 5, 6, 7, 8 and 9 was recently also published in MNRAS⁸ and was only slightly modified to guarantee an adequate presentation in this thesis. The full details of the publications including names of all co-authors can be found in the publication list at the very beginning of this work. Furthermore, most of the theoretical concepts and equations are adopted from popular textbooks. Therefore, we usually present a list of well-known books at the beginning of each chapter that can be used to study the different physical effects in more detail. Nevertheless, we also try to provide a broad overview of the various topics that are analyzed in this thesis. All important equations which are used later are also put in a box in the corresponding section.

How should one read this work? We strongly recommend to generally read chapters 1 and 2, because they provide the conceptual and theoretical background to understand most of the presented studies. Both chapters 5 and 6 also require the content from chapter 3 and 4, while for a basic understanding of chapter 7 it is still sufficient to only read chapter 2. For the last two chapters 8 and 9 it is sufficient to study chapter 3.

⁸Monthly Notices of the Royal Astronomical Society

Theory of Hydrodynamics

In the following sections, we introduce the most important equations that are necessary to understand the basic concepts and idea of this thesis. A lot of the derivations start with a fully relativistic approach. This is necessary to understand how the equations follow in the non-relativistic limit, $\beta = v/c \ll 1$. That is why we first summarize some equations of special relativity in the following (Section 2.1), which we will use later on to derive the full set of hydrodynamical equations. Before we start with the detailed analysis of mathematics for our fluid theory, we always start with a focus on the assumptions and limitations. This is important because both hydrodynamics and magneto-hydrodynamics only work for a limited range of physical problems. Furthermore, we only focus on equilibrium states. This is however enough to understand the basic concepts presented in this work.

We then continue with the theory of hydrodynamics (Section 2.2). Therefore, we will consider a distribution of particles in a six-dimensional phase-space (\mathbf{x}, \mathbf{p}) , characterized by a density function $f(\mathbf{x}, \mathbf{p}, t)$. From that, we will obtain the collisionless Boltzmann equation, which is the fundamental equation that we will use to derive the basic equations of hydrodynamics from scratch. These are the continuity equation, Euler's equation, the Navier-Stokes equation involving viscosity effects and the energy equation. We end up with a derivation of other important relations which we will use in this thesis, e.g. the Poisson equation, an equation of state and the scalar virial theorem. Then, we move on to derive the most important equations of magneto-hydrodynamics (Section 2.3). For this, we first have to consider Maxwell's equation in order to obtain the full equation of motion including the contribution of magnetic fields. We then analyze the induction equation, which tells us something about advection and diffusion of the \mathbf{B} -field in the fluid in the limit of very high and very low magnetic Reynolds numbers.

The equations as well as their derivations presented in this chapter are all well-known and can be found in many popular textbooks like Landau & Lifsic (2007), Weinberg (2008), D'Inverno (2009), Nolting (2012), Fliessbach (2012), Bartelmann (2013) or Jackson (2014), to list just a few.

2.1 Introduction to special relativity

Special relativity starts with the assumption that the squared four-vector (the Lorentz-scalar or world scalar) $x^\mu x_\mu$ remains invariant under Lorentz transformations. Moreover, the four-vector $x^\mu = (ct, \mathbf{x})^T$ lives in a four-dimensional Minkowski-space \mathbb{M}^4 , $x^\mu \in \mathbb{M}^4$. The corresponding four-velocity $u^\mu = dx^\mu/d\tau$ can now be written as $u^\mu = \gamma(c, \mathbf{v})^T$, where τ is called the *eigentime* of the observer. If we take two vectors x^μ and \bar{x}^μ from different coordinate systems Σ and $\bar{\Sigma}$, they must fulfill

$$(x^0)^2 - \sum_{\alpha=1}^3 (x^\alpha)^2 \stackrel{!}{=} (\bar{x}^0)^2 - \sum_{\alpha=1}^3 (\bar{x}^\alpha)^2. \quad (2.1)$$

With this, we can define an infinitesimal *line element* $ds^2 = \eta_{\mu\nu} dx^\mu dx^\nu$, where $\eta_{\mu\nu}$ characterizes the geometry of a flat space and is called the *Minkowski metric*¹. It is a second rank tensor and a bilinear map from \mathbb{M} into the real numbers \mathbb{R} ,

$$\eta : \mathbb{M} \times \mathbb{M} \rightarrow \mathbb{R}, (x, y) \mapsto \eta(x, y) = \langle x, y \rangle. \quad (2.2)$$

The Minkowski metric for a flat space now reads

$$\eta_{\mu\nu} = \begin{pmatrix} -1 & 0 & 0 & 0 \\ 0 & +1 & 0 & 0 \\ 0 & 0 & +1 & 0 \\ 0 & 0 & 0 & +1 \end{pmatrix}. \quad (2.3)$$

Here, we adopt the signature $\eta = \text{diag}(-, +, +, +)$. As we see above, the line element is constructed such that it remains invariant under Lorentz transformation. Furthermore, if we assume that the connection between the coordinate transformation is linear, we can write $\bar{x}^\mu = \Lambda_\nu^\mu x^\nu$, where we use Einstein's summation rule². A deeper analysis of the condition of invariance (2.1) together with our assumption of linearity yields the so-called *Lorentz transformation matrix*³:

$$\Lambda_\nu^\mu = \begin{pmatrix} \gamma & 0 & 0 & -\beta\gamma \\ 0 & 1 & 0 & 0 \\ 0 & 0 & 1 & 0 \\ -\beta\gamma & 0 & 0 & \gamma \end{pmatrix}. \quad (2.4)$$

Here, we have $\gamma = 1/\sqrt{1 - \beta^2}$ with $\beta = v/c$. The Lorentz transformations form a non-compact Lie-group, which is called the *Lorentz group*. In particular, the group conserves eigentime distances and expands the Galilei group to relativistic motions. If we now compute the infinitesimal components $d\bar{x}^\mu = \Lambda_\nu^\mu dx^\nu$, we see that

$$\boxed{d\bar{t} = dt/\gamma,} \quad (2.5)$$

$$\boxed{d\bar{l} = dl/\gamma,} \quad (2.6)$$

¹Hermann Minkowski, German mathematician, 22/06/1864 - 12/01/1909

²Albert Einstein, German physicist, 14/03/1879 - 18/04/1955

³Hendrik Antoon Lorentz, Dutch physicist, 18/07/1853 - 04/02/1928

which are the well-known effects of time dilatation and length contraction. The first one says that moving clocks go slow. The second one says that moving observers measure a shorter distance between two points relative to a stationary observer. However, we note that we do not observe any length contraction perpendicular to the direction of motion, which is directly obvious from the structure of the Lorentz tensor given in Eq. (2.4).

Furthermore, we can define the four-momentum $p^\mu = mu^\mu = m\gamma(c, \mathbf{v})^T = (E/c, \mathbf{p})^T$ with the relativistic energy $E = \gamma mc^2$, and evaluate its norm,

$$\boxed{p^\mu p_\mu = \frac{E^2}{c^2} - \mathbf{p}^2 = m^2 u^\mu u_\mu = m^2 c^2}, \quad (2.7)$$

from which we obtain the well-known relation between energy and momentum, that reads $E^2 = p^2 + m^2 c^4$. Furthermore, if we assume that the particle is at rest ($p = 0$), the prominent relation $E = mc^2$ for its rest mass follows.

2.2 Equations of Hydrodynamics

2.2.1 Assumptions and limitations

Hydrodynamics comes with a number of assumptions and limitations. The most important one is the central assumption that the mean free path λ of the individual particles is much smaller than the typical length scale L of the system that we consider, $\lambda \ll L$. With this assumption we always assume that collisions happen very frequently and that the medium is in an equilibrium state. That means that the collisions have no net effect on the equations of motion due to the short mean free path. However, this assumption might change if we analyze other physical processes like phase transitions or situations in which strong gravitational forces act on the medium. Then, the mean free path might become significantly larger and the interactions long-ranged, which would violate our central assumption that $\lambda \ll L$. Because of this we assume that only short-range particle interactions dominate the fluid. However, why can we use the equations of hydrodynamics to describe gas motions in the ISM? The answer is that the ratio between the mean free path of the individual particles and the length scale of the physical system is of the same order of magnitude. Fortunately, this allows us to describe both fluids on earth and the ISM with exactly the same relations.

2.2.2 The Eulerian and the Lagrangian viewpoint

In the following sections we will often switch between the Eulerian⁴ and the Lagrangian⁵ point of view. In case of the Eulerian viewpoint, the evolution of a field

⁴Leonhard Euler, Swiss mathematician and physicist, 15/04/1707 - 18/09/1783

⁵Joseph-Louis Lagrange, Italian-born French mathematician and astronomer, 25/01/1736 - 10/04/1813

$\mathbf{f}(\mathbf{x}, t)$ (e.g. the fluid) is described in the rest-frame of the laboratory. This means that the time derivative is defined as the limit

$$\frac{\partial \mathbf{f}(\mathbf{x}_0, t_0)}{\partial t} = \lim_{\Delta t \rightarrow 0} \frac{\mathbf{f}(\mathbf{x}_0, t_0 + \Delta t) - \mathbf{f}(\mathbf{x}_0, t_0)}{\Delta t}, \quad (2.8)$$

where \mathbf{x}_0 and t_0 are fixed coordinates in space and time.

In the Lagrangian viewpoint, we now switch our perspective and imagine to sit on the fluid element and follow its flow:

$$\begin{aligned} \frac{d\mathbf{f}(\mathbf{x}, t)}{dt} &= \lim_{\Delta t \rightarrow 0} \frac{\mathbf{f}(\mathbf{x} + \mathbf{v}\Delta t, t + \Delta t) - \mathbf{f}(\mathbf{x}, t)}{\Delta t} \\ &\approx \lim_{\Delta t \rightarrow 0} \frac{\mathbf{f}(\mathbf{x}, t) + \Delta t \frac{\partial \mathbf{f}}{\partial t} + \Delta t \mathbf{v} \cdot \nabla \mathbf{f} - \mathbf{f}(\mathbf{x}, t)}{\Delta t} \\ &= \frac{\partial \mathbf{f}}{\partial t} + (\mathbf{v} \cdot \nabla) \mathbf{f}, \end{aligned} \quad (2.9)$$

where we have used a Taylor expansion in the second step. Comparing Eq. (2.8) and (2.9) with each other, we can express one by the other via

$$\boxed{\frac{d}{dt} = \frac{\partial}{\partial t} + (\mathbf{v} \cdot \nabla)}. \quad (2.10)$$

Both terms only differ by the scalar product of \mathbf{v} and ∇ , which describes how the velocity changes along the flow lines.

2.2.3 The collision-less Boltzmann equation

Before we derive the equations of hydrodynamics, we have to consider Boltzmann's equation. To do so, we assume a distribution of particles $f = f(\mathbf{x}, \mathbf{p}, t)$ in phase space, characterized by the canonical conjugate variables (\mathbf{x}, \mathbf{p}) . The collision-less Boltzmann equation reads

$$\frac{df(\mathbf{x}, \mathbf{p}, t)}{dt} = 0. \quad (2.11)$$

It can be interpreted as a conservation law of the phase space density in the Lagrangian (or comoving) frame. We can now write out the time derivative explicitly and find

$$\frac{\partial f}{\partial t} + \dot{\mathbf{x}} \frac{\partial f}{\partial \mathbf{x}} + \dot{\mathbf{p}} \frac{\partial f}{\partial \mathbf{p}} = 0. \quad (2.12)$$

Note, that this equation only holds in the limit of a vanishing collision term $C[f]$, which is a functional of the distribution function f . If we would account for higher order terms in the derivation of our hydrodynamical equations, we would have to replace $0 \rightarrow C[f]$ on the right-hand side of Eq. (2.12).

From now on we assume that no external forces act on the system and therefore $\mathbf{F} = \dot{\mathbf{p}} = 0$. Furthermore, we can define higher moments $\langle \xi^i \rangle$ of our distribution, which then read

$$\langle \xi^i \rangle = \frac{1}{n} \int \xi^i f(\mathbf{x}, \mathbf{p}, t) d^3p, \quad (2.13)$$

where the mean particle number density is defined via

$$n = \int f(\mathbf{x}, \mathbf{p}, t) d^3p. \quad (2.14)$$

In particular, the zeroth moment of $\xi^i = m\mathbf{v}^i$ characterizes the density, the first moment the momentum and the second moment the kinetic energy density of our physical system. We can now express Eq. (2.12) in terms of the statistical moments (2.14) and find the so-called *Maxwell-Boltzmann transport equation*⁶⁷ for the case in which $C[f] = 0$:

$$\boxed{\frac{\partial}{\partial t} n \langle \xi^i \rangle + \nabla_{\mathbf{x}} \cdot (n \langle \xi^i \mathbf{v} \rangle) - n \mathbf{F} \cdot \langle \nabla_{\mathbf{p}} \xi^i \rangle = 0.} \quad (2.15)$$

The first term follows because ξ^i does not depend on time. The second and third terms follow from integration by parts and that we have assumed that \mathbf{F} is independent of the velocity.

2.2.4 Deriving the continuity equation

The derivation of the continuity equation is now fairly easy. If we set $\xi^0 = m$ in Eq. (2.15) and use the definition of the density

$$\rho = \int m f(\mathbf{x}, \mathbf{p}, t) d^3p \quad (2.16)$$

and the momentum density

$$\rho \mathbf{v} = \int m \mathbf{v} f(\mathbf{x}, \mathbf{p}, t) d^3p, \quad (2.17)$$

we immediately obtain our final result

$$\boxed{\frac{\partial \rho}{\partial t} + \nabla \cdot (\rho \mathbf{v}) = 0,} \quad (2.18)$$

where we have again set all external forces to zero ($\mathbf{F} = 0$) in the Maxwell-Boltzmann transport equation. The meaning of this equation is fairly intuitive: It says that changes in density ρ have to be compensated by changes in the current $\mathbf{j} = \rho \mathbf{v}$. The continuity equation is thus an expression for mass conservation.

⁶James Clerk Maxwell, Scottish physicist, 13/06/1831 - 5/11/1879

⁷Ludwig Boltzmann, Austrian physicist, 20/02/1844 - 5/09/1906

2.2.5 The relativistic energy-momentum tensor

We now consider the energy-momentum tensor in the following integral form:

$$T^{\mu\nu} = c^2 \int \frac{d^3p}{E(\mathbf{p})} p^\mu p^\nu f, \quad (2.19)$$

where p^μ and p^ν are relativistic four-momentum vectors in Minkowski-space. We can now evaluate the *time-time component* of Eq. (2.19) and find

$$T^{00} \approx mc^2 \int d^3p \left(1 + \frac{\dot{\mathbf{x}}^2}{2c^2} \right) f = \rho c^2 + n\bar{\epsilon}, \quad (2.20)$$

where we have used the definition of the kinetic energy density from Eq. (2.14),

$$\bar{\epsilon} = \left\langle \frac{m}{2} \dot{\mathbf{x}}^2 \right\rangle = \frac{1}{n} \int d^3p \frac{m}{2} \dot{\mathbf{x}}^2 f, \quad (2.21)$$

as well as an approximation for p^0 in the non-relativistic limit, i.e.

$$p^0 = \frac{E}{c} \approx mc \left(1 + \frac{\dot{\mathbf{x}}^2}{2c^2} \right). \quad (2.22)$$

The component T^{00} can be interpreted as the energy density of the fluid.

The *space-time component* part of the tensor gives

$$T^{0i} = c \int d^3p p^i f = \int d^3p \gamma m c \dot{x}^i f \approx \int d^3p \left(1 + \frac{\dot{\mathbf{x}}^2}{2c^2} \right) m c \dot{x}^i f. \quad (2.23)$$

With the definition of the kinetic energy current,

$$\mathbf{q} = \int d^3p \left(\frac{m \dot{\mathbf{x}}^2}{2} \right) \dot{\mathbf{x}} f, \quad (2.24)$$

we obtain the following expression for T^{0i} :

$$T^{0i} = \left(\rho c \mathbf{v} + \frac{\mathbf{q}}{c} \right)^i. \quad (2.25)$$

A similar derivation yields the *space-space components* of our tensor. If we assume again that $E = \gamma m c^2$ we get:

$$T^{ij} = c^2 \int \frac{d^3p}{E(\mathbf{p})} p^i p^j f = \int d^3p \gamma m \dot{x}^i \dot{x}^j f. \quad (2.26)$$

These are the different (non-)relativistic components of the energy-momentum tensor, which we will use in the following calculations.

2.2.6 Continuity equation for energy and momentum

We now assume energy-momentum conservation, which is

$$\partial_\nu T^{\mu\nu} = 0 \quad (2.27)$$

in the relativistic form and use Einstein's convention for summations. Then, we can compute the time-component of Eq. (2.27), use Eq. (2.20) and (2.23) and find

$$\frac{1}{c} \frac{\partial}{\partial t} (\rho c^2 + n\bar{\epsilon}) + \nabla \cdot \left(\rho \mathbf{v} c + \frac{\mathbf{q}}{c} \right) = 0. \quad (2.28)$$

Using the continuity Eq. (2.18) once again, we finally obtain a similar continuity equation for the energy:

$$\frac{\partial n\bar{\epsilon}}{\partial t} + \nabla \cdot \mathbf{q} = 0. \quad (2.29)$$

We can now compute the space-component of Eq. (2.27). In addition, we neglect the term \mathbf{q}/c^2 , since we assume that the rest mass energy dominates the kinetic energy of the fluid. We then end up with

$$\boxed{\frac{\partial(\rho v^i)}{\partial t} + \frac{\partial T^{ij}}{\partial x^j} = 0.} \quad (2.30)$$

This is the well-known continuity equation for momentum.

2.2.7 Euler's equation of motion

In order to derive the equation of motion for a fluid, we adopt again the relativistic energy-momentum tensor for a perfect fluid in thermodynamic equilibrium:

$$T^{\mu\nu} = \left(\rho + \frac{P}{c^2} \right) u^\mu u^\nu + p \eta^{\mu\nu}. \quad (2.31)$$

Here, P is the fluid pressure and $\eta^{\mu\nu}$ the Minkowski metric. If we take the signature $\eta = \text{diag}(-, +, +, +)$, restrict ourselves to the non-relativistic limit ($P/c^2 \ll \rho$) and focus on the spatial part of the tensor, Eq. (2.31) reduces to

$$T^{\mu\nu} \rightarrow T^{ij} = \rho v^i v^j + P \delta^{ij}, \quad (2.32)$$

where δ^{ij} is the well-known δ -distribution⁸. Plugging Eq. (2.32) into Eq. (2.30), we obtain the following relation:

$$\frac{\partial(\rho v^i)}{\partial t} + \frac{\partial}{\partial x^j} (\rho v^i v^j + P \delta^{ij}) = 0. \quad (2.33)$$

⁸The definition of the δ -distribution can be found in the Appendix.

We can now use the product rule and find the lengthy term

$$\mathbf{v} \frac{\partial \rho}{\partial t} + \rho \frac{\partial \mathbf{v}}{\partial t} + \mathbf{v}(\mathbf{v} \cdot \nabla)\rho + \rho(\mathbf{v} \cdot \nabla)\mathbf{v} + \rho\mathbf{v}(\nabla \cdot \mathbf{v}) + \nabla P = 0. \quad (2.34)$$

By using the continuity equation (2.18) again, we see that the first, third and fifth term cancel each other and we finally end up with *Euler's equation* or the *equation of motion*, which is a partial differential equation of first order:

$$\rho \frac{\partial \mathbf{v}}{\partial t} + (\mathbf{v} \cdot \nabla)\mathbf{v} = -\frac{\nabla P}{\rho}. \quad (2.35)$$

We already know the term on the left side of this equation: it describes the connection between the Eulerian and the Lagrangian viewpoint. Thus, we could also write

$$\rho \frac{d\mathbf{v}}{dt} = -\nabla P, \quad (2.36)$$

which expresses Newton's fundamental second law and describes the equilibrium of force densities.

Moreover, we can assume that additional forces act on individual fluid elements, e.g. the gravitational force $\mathbf{f} = -\nabla\Phi$. Since we have interpreted Euler's equation as a balance of forces, we can easily add additional terms on the right hand side of Eq. (2.35). For example, if the fluid moves in an external gravitational field, we can also write

$$\boxed{\frac{\partial \mathbf{v}}{\partial t} + (\mathbf{v} \cdot \nabla)\mathbf{v} = -\frac{\nabla P}{\rho} - \nabla\Phi.} \quad (2.37)$$

This equation is often used in astrophysical simulations of hydrodynamics including effects of self-gravity.

2.2.8 Viscosity effects in Euler's equation: the Navier-Stokes equation

The Euler equation above does not account for friction or viscosity effects. We now want to include them and derive the so-called *Navier-Stokes equation*^{9,10}. Therefore, we try to expand our energy-momentum tensor (2.32) by adding additional terms that account for these effects.

First, we try to compute shear flows, which can deform the medium. Shear appears if the off-diagonal tensor elements are non-zero. That means we can construct a trace-free part of a shear tensor, which may read

$$v^{ij} - \frac{1}{3}\delta^{ij}\nabla \cdot \mathbf{v}. \quad (2.38)$$

⁹Claude Louis Marie Henri Navier, French physicist, 10/02/1785 - 21/08/1836

¹⁰Sir George Gabriel Stokes, Irish Physicist, 13/08/1819 - 01/02/1903

Thereby, we have subtracted the term $\delta^{ij}\nabla \cdot \mathbf{v}$ from the shear since it describes purely compressional forces. However, we will separate the compression from the shear in the following shear tensor:

$$\sigma^{ij} = 2\eta \left(v^{ij} - \frac{1}{3} \delta^{ij} \nabla \cdot \mathbf{v} \right) - \zeta \delta^{ij} \nabla \cdot \mathbf{v}. \quad (2.39)$$

The two constants η and ζ describe the strength of the shear flow and the compression. We can then expand the energy-momentum tensor and get

$$T^{ij} = \rho v^i v^j + P \delta^{ij} - \sigma^{ij}. \quad (2.40)$$

From this expression, we can compute the equation of motion using Eq. (2.30) again and obtain

$$\frac{\partial \rho v^i}{\partial t} + \frac{\partial \rho v^i v^j}{\partial x^j} + \frac{\partial P}{\partial x^j} = 2\eta \left(\frac{\partial v^{ij}}{\partial x^j} - \frac{1}{3} \frac{\partial (\nabla \cdot \mathbf{v})}{\partial x^i} \right) + \zeta \frac{\partial (\nabla \cdot \mathbf{v})}{\partial x^i}. \quad (2.41)$$

A few more rearrangements on the right-hand side of this equation yields the Navier-Stokes equation,

$$\boxed{\rho \frac{\partial \mathbf{v}}{\partial t} + \rho (\mathbf{v} \cdot \nabla) \mathbf{v} = -\nabla P - \rho \nabla \Phi + \eta \nabla^2 \mathbf{v} + \left(\frac{\eta}{3} + \zeta \right) \nabla (\nabla \cdot \mathbf{v})}, \quad (2.42)$$

where we have again also added a gravitational background with potential Φ . We see, that the Navier-Stokes equation reduces to the Euler equation if $\eta = \zeta = 0$, i.e. in case of a medium without shear and friction.

2.2.9 Characterizing turbulent flows with the Reynolds number

To get an idea of the turbulent properties of a flow, let us compute the ratio of different terms of the Navier-Stokes equation. One is the advection term $(\mathbf{v} \cdot \nabla) \mathbf{v}$ and the other the viscid term $\nu \nabla^2 \mathbf{v}$, where we have introduced the kinematic viscosity ν . With the common scaling analysis, $\nabla \rightarrow 1/L$, we can estimate the relative importance of both effects:

$$\boxed{\mathcal{R} = \frac{v^2}{L} \cdot \frac{L^2}{\nu L} = \frac{Lv}{\nu}}. \quad (2.43)$$

This quantity is called the *Reynolds number*¹¹. Turbulent flows with the same Reynolds number show identical statistical properties, independent of the spatial scale. The flow is then called *scale-free*. In the limit of infinite Reynolds numbers, that means for $\mathcal{R} \rightarrow \infty$, we recover an ideal fluid.

¹¹Osborne Reynolds, British physicist, 23/08/1842 - 21/02/1912

2.2.10 Energy budget equation for a fluid

So far, we have successfully derived the continuity equations and the equation of motion. We want to find an equation that describes the energy budget of our fluid. Therefore, we consider the first law of classical thermodynamics, which reads in its differential form

$$d\epsilon = Tds - Pdv. \quad (2.44)$$

Thereby, ϵ , s and v denote the specific energy, entropy and volume. We now consider the change of energy with time and use the continuity equation in the last step to find the important *energy equation*:

$$\begin{aligned} \frac{d\epsilon}{dt} &= \frac{\partial u}{\partial t} + (\mathbf{v} \cdot \nabla)u \\ &= T \frac{ds}{dt} + \frac{P}{\rho^2} \frac{d\rho}{dt} \\ &= T \frac{ds}{dt} - \frac{P}{\rho} \nabla \cdot \mathbf{v}. \end{aligned} \quad (2.45)$$

This equation describes the change of internal energy in the fluid as a function of entropy change and velocity gradients. It is also commonly used in stellar astrophysics to describe the energy transport in the interior of stars.

2.2.11 Introducing gravity via the Poisson equation

If we want to describe a fluid that moves in an external gravitational field, we somehow have to connect the gravitational potential Φ to the density distribution ρ of the underlying matter field. To do so, we first realize that $\mathbf{g} = -\nabla\Phi$, where

$$\mathbf{g} = -\frac{GM}{r^2} \mathbf{e}_r \quad (2.46)$$

is the gravitational acceleration and \mathbf{e}_r a normal vector in the spherical coordinate system. Furthermore, G is the gravitational constant, $M = \int \rho dV$ the total enclosed mass and r the distance to the center. We now apply Gauss's theorem, which says

$$\int_V \operatorname{div} \mathbf{F} d^{(n)}V = \oint_S \mathbf{F} \cdot \mathbf{n} d^{(n-1)}S. \quad (2.47)$$

Here, the vector \mathbf{n} is the normal vector perpendicular to the surface. If we set $n = 3$ for a three-dimensional space, we can compute the volume integral

$$\int_V \operatorname{div} \mathbf{g} d^{(3)}V = - \int_V \nabla^2 \Phi d^{(3)}V, \quad (2.48)$$

as well as the surface integral over a sphere of constant radius r ,

$$\oint_S \mathbf{g} \cdot \mathbf{n} d^{(2)}S = -4\pi G \int \rho dV. \quad (2.49)$$

Comparing Eq. (2.48) with Eq. (2.49) immediately yields the *Poisson equation*¹²

$$\boxed{\nabla^2 \Phi = 4\pi G \rho}, \quad (2.50)$$

which connects the gravitational potential Φ with the density field ρ . It is a differential equation of second order, where $\nabla^2 = \Delta$ is the Laplace operator. This equation means that once we know the density field, we can also calculate the gravitational potential.

2.2.12 Perturbation theory and sound waves

In this section, we want to analyze how sound waves propagate through a medium. In general, sound waves are induced by perturbations of the thermodynamic quantities ρ and P . Thus, we can perform a perturbation analysis and express

$$\rho = \rho_0 + \delta\rho, \quad P = P_0 + \delta P, \quad \mathbf{v} = \delta\mathbf{v}, \quad (2.51)$$

where the functions ρ_0 , P_0 and \mathbf{v}_0 are considered to be background solutions and $\delta\rho$, δP and $\delta\mathbf{v}$ small perturbations. In our case, we have transformed into the rest frame of the fluid and thus set $\mathbf{v}_0 = 0$.

We now want to perturb the continuity equation as well as Euler's equation by means of our new functions in (2.51). Thereby, we generally neglect terms of higher than first order. We can write

$$\frac{\partial \delta\rho}{\partial t} + \rho_0 \nabla \delta\mathbf{v} = 0 \quad (2.52)$$

for the continuity equation and

$$\frac{\partial \delta\mathbf{v}}{\partial t} + \frac{\nabla \delta P}{\rho_0} = 0 \quad (2.53)$$

for Euler's equation. Combining both of them, yields a wave equation

$$\square \delta\rho = \partial_t^2 \delta\rho - c_s^2 \nabla^2 \delta\rho = 0, \quad (2.54)$$

where $\square = \partial_t^2 - c_s^2 \nabla^2$ is the d'Alembert operator and $c_s^2 = \partial P / \partial \rho$ the sound speed. Eq. (2.54) describes the propagation of sound waves, which are longitudinal waves, while electromagnetic waves are transversal. Furthermore, we can expand this wave equation into plane waves using a Fourier transform, which means that we can easily substitute $\partial_t^2 \rightarrow -\omega^2$ and $\nabla^2 \rightarrow -k^2$ and find the dispersion relation $\omega^2 = k^2 c_s^2$.

For later purposes, we also define the *sonic Mach number* \mathcal{M}_s , which relates the observer's velocity v to the sound speed c_s of the fluid and reads

$$\boxed{\mathcal{M}_s = v/c_s}. \quad (2.55)$$

If $\mathcal{M}_s > 1$, we call a flow supersonic, if $\mathcal{M}_s < 1$ we call it subsonic.

¹²Siméon Denis Poisson, French physicist and mathematician, 21/06/1781 - 25/04/1840

2.2.13 The ideal gas law and the polytropic equation of state

In order to close our hydrodynamical equation system, we need one more equation relating the pressure P to the density ρ of the fluid, $P = P(\rho)$, or to another independent system variable. How can we find such an equation? The answer is given by the canonical ensemble of statistical physics, which reads

$$Z_N(T, V) = \frac{1}{h^{3N} N!} \int \dots \int d^{3N} q d^{3N} p e^{-\beta H(\mathbf{q}, \mathbf{p})}, \quad (2.56)$$

where q and p are canonical conjugate variables, h is the Planck constant, N the number of phase-space dimensions, $\beta = (k_B T)^{-1}$ and k_B the Boltzmann constant. If we want to solve this integral, we first have to specify the Hamiltonian $H(\mathbf{q}, \mathbf{p})$ of our problem. Assuming a gas without any interactions and equal particle masses, our Hamiltonian simply reads

$$H(\mathbf{q}, \mathbf{p}) = \sum_{i=1}^n \frac{\mathbf{p}_i^2}{2m}. \quad (2.57)$$

This is a sum over all kinetic energies of the individual particles. If we plug Eq. (2.57) into Eq. (2.56), we can work out all the momentum integrals and get

$$\left[\int_{-\infty}^{+\infty} dp \exp\left(-\frac{\beta^2}{2m} p^2\right) \right]^{3N} = (2\pi m k_B T)^{3N/2}. \quad (2.58)$$

The space integrals give an additional factor of V^N . We are thus left with the following canonical partition function for our problem:

$$Z_N(T, V) = \frac{(2\pi k_B T m)^{3N/2}}{h^{3N} N!} V^N = c_N V^N, \quad (2.59)$$

with a constant $c_N = (2\pi k_B T m)^{3N/2} / (h^{3N} N!)$. Indeed, the only interesting aspect in this equation is the fact that $Z_N(T, V) \propto V^N$, as we will see below. We are now ready to compute the free energy of our system, which is

$$F(T, N, V) = -k_B T \ln Z_N(T, V) = -k_B T [\ln(c_N) + N \ln(V)]. \quad (2.60)$$

The pressure then easily follows from one of Maxwell's relations. We finally end up with the law of an ideal gas:

$$P = - \left(\frac{\partial F}{\partial V} \right)_{T, N} = \frac{N k_B T}{V} = \frac{\rho k_B T}{m}. \quad (2.61)$$

This is a specific example for a polytropic equation of state, where $P \propto \rho^\gamma$. The constant $\gamma = c_P / c_V$ is the adiabatic index and $c_P - c_V = R$, with the gas constant R . This equation can be generalized to read

$$P = P_0 \left(\frac{\rho}{\rho_0} \right)^\gamma. \quad (2.62)$$

From that, we can compute the sound speed c_s of the gas:

$$\boxed{c_s^2 = \frac{\partial P}{\partial \rho} = \gamma P_0 \frac{\rho^{\gamma-1}}{\rho_0^\gamma} = P_0 \frac{\gamma}{\rho} \left(\frac{\rho}{\rho_0} \right)^\gamma = \frac{\gamma k_B T}{m}}. \quad (2.63)$$

In the last step, we have used the ideal gas law. This equation describes how pressure perturbations in the gas are related to density changes. Since $c_s^2 \propto T$, the speed of sound waves increases with increasing gas temperature.

To get a further idea of the physical meaning of the adiabatic index, we note that γ can also be expressed in terms of the degrees of freedom f of the underlying species. We just give the result without any derivation:

$$\gamma = \frac{c_P}{c_V} = 1 + \frac{2}{f}. \quad (2.64)$$

For a mono atomic gas with $f = 3$ (three translational degrees of freedom) we find $\gamma = 5/3$ and for a two-atomic gas we have $f = 5$ (three translational and two rotational degrees of freedom), thus $\gamma = 7/5$.

2.2.14 Homogeneous functions and the scalar virial theorem

In this thesis, we deal with the characterization of turbulent gas motions. In this context, we use the so-called *virial parameter* α in order to regulate the amount of kinetic turbulent energy in the simulation domain. In this section, we want to get an idea about the physical meaning of this parameter.

Therefore, we start with a general function $f(\mathbf{x})$, which is homogeneous of degree k in \mathbf{x} . We then have

$$\frac{df(a\mathbf{x})}{d(a\mathbf{x})} \cdot \mathbf{x} = \frac{\partial}{\partial a} f(a\mathbf{x}) = \frac{\partial(a^k f(\mathbf{x}))}{\partial a} = k a^{k-1} f(\mathbf{x}). \quad (2.65)$$

For $k = 1$, we find the *Euler theorem* for homogeneous functions:

$$\mathbf{x} \cdot \nabla f(\mathbf{x}) = k f(\mathbf{x}). \quad (2.66)$$

The kinetic energy is homogeneous of degree $k = 2$ in \mathbf{v} and thus we have

$$\mathbf{v} \cdot \frac{\partial T}{\partial \mathbf{v}} = 2T = \mathbf{v} \cdot \mathbf{p} = \frac{d}{dt}(\mathbf{x} \cdot \mathbf{p}) - \mathbf{x} \cdot \dot{\mathbf{p}}. \quad (2.67)$$

Averaging this equation over time, the first term on the right-hand side vanishes, because we assume that the body moves on a bound orbit. Setting $\dot{\mathbf{p}} = -\nabla V(\mathbf{x})$, we end up with the scalar virial theorem,

$$\langle T \rangle_t = \frac{k}{2} \langle V \rangle_t = \alpha \langle V \rangle_t, \quad (2.68)$$

where the virial parameter $\alpha = k/2 = \langle T \rangle_t / \langle V \rangle_t$ can be interpreted as the ratio of kinetic over potential energy. For the specific case of Newtonian gravity, $V \propto r^{-1}$,

we have $k = -1$ and thus find $\langle T \rangle_t = -1/2 \langle V \rangle_t$, which describes a virialized gravitational state. Note, however, that we have neglected effects of thermal pressure sources $U = 3/2 \int d^3x P$ so far. Taking these into account, we find for a static situation

$$\boxed{2(\langle T \rangle_t + \langle U \rangle_t) + \langle V \rangle_t = 0.} \quad (2.69)$$

In analogy, we find the left-hand side of the above equation to be greater than zero for an expanding system and smaller than zero for a collapsing system.

2.2.15 The Rankine-Hugoniot shock jump conditions and shock waves

Formally, a shock is a discontinuity in velocity space. It occurs when a supersonic flow hits an obstacle. To describe this process mathematically, we will approximate the discontinuity as a plane and consider a flow hitting it perpendicularly. Let us call ρ_1 , P_1 and \mathbf{v}_1 density, pressure and velocity of the flow before and ρ_2 , P_2 and \mathbf{v}_2 the corresponding quantities of the fluid after it hits the obstacle. We can then identify the following conservation laws:

$$\rho_1 \mathbf{v}_1 = \rho_2 \mathbf{v}_2, \quad (2.70)$$

$$\left(\frac{\mathbf{v}_1^2}{2} + h_1 \right) \rho_1 \mathbf{v}_1 = \left(\frac{\mathbf{v}_2^2}{2} + h_2 \right) \rho_1 \mathbf{v}_2, \quad (2.71)$$

$$\rho_1 \mathbf{v}_1^2 + P_1 = \rho_2 \mathbf{v}_2^2 + P_2. \quad (2.72)$$

These are conservation of mass current, energy current and momentum current. Furthermore, for a polytropic gas we have the following equations for the enthalpy h and the sound speed c_s :

$$h = \frac{\gamma}{\gamma - 1} \frac{P}{\rho}, \quad c_s^2 = \frac{\gamma P}{\rho}. \quad (2.73)$$

In the next step, we express the velocity in terms of the Mach number \mathcal{M} and write $v_1 = \mathcal{M} c_s$. Putting everything together, we can solve for the following ratio:

$$\frac{\rho_2}{\rho_1} = \frac{(\gamma + 1) \mathcal{M}^2}{(\gamma + 1) + (\gamma - 1)(\mathcal{M}^2 - 1)} = \frac{v_1}{v_2}, \quad (2.74)$$

$$\frac{P_2}{P_1} = \frac{(\gamma + 1) + 2\gamma(\mathcal{M}^2 - 1)}{\gamma + 1} \quad (2.75)$$

The ideal gas law tells us something about the temperature ratio:

$$\frac{T_2}{T_1} = \frac{P_2 \rho_1}{P_1 \rho_2}. \quad (2.76)$$

If we assume an isothermal shock, we can set $\gamma = 1$ and arrive at

$$\boxed{\frac{\rho_2}{\rho_1} = \frac{P_2}{P_1} = \frac{v_2}{v_1} = \mathcal{M}^2.} \quad (2.77)$$

This is an important result and tells us that on the other side of the shock, density, pressure as well as velocity grow quadratically with Mach number. We will use this result later on to estimate the shock densities created by supersonic flows in order to avoid sink particle creation by turbulent compression. The equations above are called the *Rankine-Hugoniot shock jump conditions*.¹³¹⁴

2.2.16 Gravitational stability analysis and the Jeans quantities

In this thesis, we analyze the formation of stars, which gives rise to take a deeper look at a gravitational stability analysis. In the following, we assume that the gravitational collapse is primarily dominated by the thermal and potential energy, U and V , respectively. The scalar virial theorem demands that $2U + V = 0$, if the object is in virial equilibrium. In analogy, the system will expand if $2U + V > 0$, and collapse if $2U + V < 0$.

In order to get an insight into the physics of a cloud that undergoes gravitational collapse, we will again perform a stability analysis and perturb the physical quantities ρ , P , \mathbf{v} and Φ . Doing so, we consider $\rho = \rho_0 + \delta\rho$, $P = P_0 + \delta P$, $\mathbf{v} = \mathbf{v}_0 + \delta\mathbf{v}$ and $\Phi = \Phi_0 + \delta\Phi$, where we again transform into a system where we can set $\mathbf{v}_0 = 0$. In the next step, we plug these relations into the continuity equation, Euler's equation and Poisson's equation and simplify them to read:

$$\frac{\partial\delta\rho}{\partial t} + \rho_0\nabla\delta\mathbf{v} = 0, \quad (2.78)$$

$$\frac{\partial\delta\mathbf{v}}{\partial t} = -c_s^2\nabla\frac{\delta\rho}{\rho_0} - \nabla\delta\Phi, \quad (2.79)$$

$$\nabla^2\delta\Phi = 4\pi G\delta\rho, \quad (2.80)$$

where we have again neglected higher order terms in δ^2 . The last equation contains the so-called *Jeans-swindle*. It says that there cannot be any gravitational force in a homogeneous and infinite extended matter distribution. The problem enters in the boundary conditions of the Poisson equation: Since an infinite distribution has no boundaries, it is therefore inconsistent with Newtonian gravity. We therefore have to set $\Phi_0 = 0$ in our derivation.

In the next step, we combine these three equations by taking $\partial/\partial t$ (2.78), ∇ (2.79) together with (2.80) and find the wave equation

$$\frac{\partial^2\delta\rho}{\partial t^2} - c_s^2\nabla^2\delta\rho - 4\pi G\rho_0\delta\rho = \square\delta\rho - 4\pi G\rho_0\delta\rho = 0. \quad (2.81)$$

We can solve this in Fourier space, which allows us to replace $\partial/\partial t \rightarrow -i\omega$ and $\nabla \rightarrow i\mathbf{k}$. We then end up with a dispersion relation,

$$\omega^2 = c_s^2k^2 - 4\pi G\rho_0, \quad (2.82)$$

¹³William John Macquorn Rankine, Scottish physicist, 05/07/1820 - 24/12/1872

¹⁴Pierre-Henri Hugoniot, French physicist, 05/06/1851 - 1887

which describes the dispersion of the perturbed density waves. We note that we can recover the regular dispersion relation for sound waves, $\omega^2 = c_s^2 k^2$, if the influence of the background density is small.

If $\omega^2 > 0$, we find an oscillating solution of our wave equation. If $\omega^2 < 0$, we find exponentially growing or decaying modes, proportional to $e^{\pm\omega t}$. The state between those two cases, $\omega^2 = 0$, is described via the so-called *Jeans*¹⁵ *wave number* k_J :

$$\boxed{k_J^2 = \frac{4\pi G\rho_0}{c_s^2}}. \quad (2.83)$$

From this, we can also define a Jeans wavelength, since $\lambda = 2\pi/k_J$, which gives us a scale for the gravitational collapse:

$$\lambda_J = \frac{2\pi}{k_J} = \left(\frac{\pi c_s^2}{G\rho_0}\right)^{1/2}, \quad (2.84)$$

From this, we can then estimate a critical mass for gravitational collapse:

$$\boxed{\begin{aligned} M_J &= \frac{4\pi}{3}\rho_0 R_J^3 \\ &= \frac{\pi}{6}\rho_0 \left(\frac{\pi c_s^2}{G\rho_0}\right)^{3/2} \\ &= \frac{1}{6}\pi^{5/2} G^{-3/2} \rho_0^{-1/2} c_s^3. \end{aligned}} \quad (2.85)$$

This mass is called the *Jeans mass*. We have also defined the Jeans radius $R_J = \lambda/2$ and assumed a homogeneous sphere of constant density. The equation says that a cloud becomes gravitationally unstable if its mass $M > M_J$. Since $M_J \propto c_s^3 \propto T^{3/2}$, we find that the Jeans mass increases with increasing gas temperature. This is intuitively clear: A hotter cloud needs much more mass such that gravity can work against the thermal pressure.

However, we note that this analysis is very simplified. In reality, additional effects like pressure or viscosity act in the phase of collapse and will eventually alter this result. Nevertheless, it gives us a rough idea about the scale of the gravitational instable mass and the length scales involved.

2.2.17 Typical timescales in star formation theory

Since we will need to estimate various timescales in the next chapters, we shortly introduce the most important ones.

We begin with the *crossing timescale* t_{cross} , which is simply defined via

$$\boxed{t_{\text{cross}} = \frac{R}{v}}, \quad (2.86)$$

¹⁵Sir James Hopwood Jeans, English physicist and mathematician, 11/09/1877 - 16/09/1946

where R is a typical scale of the system and v the velocity. It is the time that a particle with velocity v needs in order to freely travel through the medium with size R . Writing this scale in terms of the sound speed c_s , we get

$$t_{\text{cross}} \approx 5 \times 10^5 \text{ yr} \left(\frac{R}{0.1 \text{ pc}} \right) \left(\frac{c_s}{0.2 \text{ km s}^{-1}} \right)^{-1}. \quad (2.87)$$

Next, we define the *free-fall time* t_{ff} . This is the time which a homogeneous sphere of pressureless material needs to collapse to a point mass. It can easily be derived by considering a test particle with mass m in a gravitational field of a body with mass M at a position r from the center. According to Newtonian physics, this means that

$$\frac{d^2 R}{dt^2} = -\frac{GM(R)}{R^2} = -\frac{4\pi}{3}G\rho R, \quad (2.88)$$

where $M = 3/4\pi\rho R^3$ is the total mass of the sphere with homogeneous density ρ . We see that this equation describes an harmonic oscillator with the fixed frequency $\omega = 2\pi/T = \sqrt{4\pi/3G\rho}$. From that we can estimate the *dynamical timescale*

$$t_{\text{dyn}} = \frac{T}{4} = \left(\frac{3\pi}{16G\rho} \right)^{1/2}, \quad (2.89)$$

and from that the *free-fall time*,

$$\boxed{t_{\text{ff}} = \frac{t_{\text{dyn}}}{\sqrt{2}} = \left(\frac{3\pi}{32G\rho} \right)^{1/2} \propto \frac{1}{\sqrt{G\rho}}}, \quad (2.90)$$

which can also be written in terms of the hydrogen number density n_{H_2} ,

$$t_{\text{ff}} \approx 0.6 \times 10^6 \text{ yr} \left(\frac{n_{H_2}}{10^4 \text{ H}_2 \text{ cm}^{-3}} \right)^{-1/2}. \quad (2.91)$$

We see that it scales with the square root of the inverse density. Furthermore, we will derive later the *ambipolar diffusion timescale*, which reads

$$\boxed{t_{\text{ad}} \approx \frac{4\pi\gamma\rho_i\rho_n L^2}{B^2}}. \quad (2.92)$$

If we write this equation again in terms of the hydrogen number density as well as the magnetic field strength B and the system scale L , we obtain

$$t_{\text{ad}} \approx 3 \times 10^6 \text{ yr} \left(\frac{n_{H_2}}{10^4 \text{ H}_2 \text{ cm}^{-3}} \right)^{3/2} \left(\frac{B}{30\mu\text{G}} \right)^{-2} \left(\frac{L}{0.1\text{pc}} \right)^2. \quad (2.93)$$

Another timescale is the one for the decay of a magnetic field. It can be estimated to be of the order

$$\boxed{t_{\text{decay}} \approx L^2/\eta}, \quad (2.94)$$

where L is again a typical size scale of the system and η the magnetic diffusivity. This relation will be derived in the next section when we consider the theory of magneto-hydrodynamics.

2.2.18 Summary of the hydrodynamic equations

We have found several differential equations that fully describe our hydrodynamical system: the continuity equation, the equation of motion, the energy equation and the equation of state. If the fluid is also affected by an external gravitational potential Φ , we can further use Poisson's equation. The following coupled differential equations can thus completely describe our hydrodynamical system:

$$\frac{\partial \rho}{\partial t} + \nabla \cdot (\mathbf{v}\rho) = 0, \quad (2.95)$$

$$\frac{\partial \mathbf{v}}{\partial t} + (\mathbf{v} \cdot \nabla) \mathbf{v} = -\frac{1}{\rho} \nabla P - \nabla \Phi, \quad (2.96)$$

$$\frac{d\epsilon}{dt} = T \frac{ds}{dt} - \frac{P}{\rho} \nabla \cdot \mathbf{v}, \quad (2.97)$$

$$P = C\rho^\gamma, \quad (2.98)$$

$$\nabla^2 \Phi = 4\pi G\rho. \quad (2.99)$$

2.3 Equations of Magneto-Hydrodynamics

2.3.1 Assumptions and limitations

Just as in hydrodynamics, magneto-hydrodynamics is also build on several assumptions and limitations. In the following, we will assume non-relativistic velocities, which means that $\beta \ll 1$. Furthermore, plasmas usually consist of ions, positively and negatively charged, which should be described individually. However, in the following we will assume that both are coupled to each other and thus treat the system as a single fluid, which provides a strong simplification. Moreover, our assumptions from hydrodynamics also still hold. In particular, this means that the mean free path of the ions has to be much smaller than the typical length scale of the system under consideration. Keeping these assumptions in mind, we can now derive the equations of magneto-hydrodynamics.

2.3.2 Introducing the relativistic Maxwell equations

With our knowledge about hydrodynamics, we are now ready to extend the equations for the case of non-vanishing magnetic and electric fields. Therefore, we first have to consider Maxwell's equations. In the fully relativistic form, they read

$$\partial_\alpha \bar{F}^{\alpha\beta} = 0, \quad (2.100)$$

$$\partial_\alpha F^{\alpha\beta} = \mu_0 j^\beta, \quad (2.101)$$

where the first equation is the homogeneous and the second the inhomogeneous Maxwell equation. Furthermore,

$$F^{\alpha\beta} = \partial^\alpha A^\beta - \partial^\beta A^\alpha \quad (2.102)$$

denotes the contravariant electromagnetic field tensor, μ_0 the permeability of the vacuum, $j^\mu = \rho_0 u^\mu = (c\rho_0, \mathbf{j})^T$ the four-current and $A^\mu = (\Phi/c, \mathbf{A})$ the vector potential, both given in SI units. The dual field tensor $\bar{F}^{\alpha\beta}$ is related to the tensor $F^{\alpha\beta}$ via

$$\bar{F}^{\mu\nu} = \frac{1}{2}\epsilon^{\mu\nu\rho\sigma}F_{\rho\sigma}, \quad (2.103)$$

where the quantity $\epsilon^{\mu\nu\rho\sigma}$ is the well-known *Levi-Civita tensor*¹⁶, a total anti-symmetric tensor of rank 4. The 2-rank tensor $F^{\alpha\beta}$ is antisymmetric, $F^{\alpha\beta} = -F^{\beta\alpha}$, and contains the information about the electric and magnetic fields \mathbf{E} and \mathbf{B} . The antisymmetry of the tensor reflects the fact that the classical theory of electrodynamics can be described by 6 independent parameters: three for the electric field \mathbf{E} and three for the magnetic field \mathbf{B} . Hence, the only possible realization of a 4-rank tensor to recover the classic Maxwell theory is to require it to be antisymmetric. In particular, it reads

$$F^{\alpha\beta} = \begin{pmatrix} 0 & -\frac{1}{c}E_x & -\frac{1}{c}E_y & -\frac{1}{c}E_z \\ \frac{1}{c}E_x & 0 & -B_z & B_y \\ \frac{1}{c}E_y & B_z & 0 & -B_x \\ \frac{1}{c}E_z & -B_y & B_x & 0 \end{pmatrix}. \quad (2.104)$$

We can now obtain a vectorial notation of Maxwell's equations using the relativistic homogeneous equation from above. If we work out the Einstein summations explicitly, we find two important equations of electrodynamics:

$$\boxed{\operatorname{div} \mathbf{B} = 0,} \quad (2.105)$$

$$\boxed{\operatorname{rot} \left(\frac{1}{c} \mathbf{E} \right) = -\frac{1}{c} \frac{\partial}{\partial t} \mathbf{B}.} \quad (2.106)$$

The first states that the magnetic field is source-free, which means that there exist no magnetic monopoles. The second couples the electric to the magnetic field.

We can do the same for the inhomogeneous Maxwell equation. Working out the Einstein summations again, we find two other important equations:

$$\boxed{\operatorname{div} \mathbf{E} = \frac{\rho}{\epsilon_0},} \quad (2.107)$$

$$\boxed{\operatorname{rot} \mathbf{B} - \frac{1}{c} \frac{\partial}{\partial t} \left(\frac{1}{c} \mathbf{E} \right) = \mu_0 \mathbf{j}.} \quad (2.108)$$

The first tells us that electric charges are the sources of electric fields and the second describes how the fields change in the presence of a current. We have further used the equation $c = 1/\sqrt{\epsilon_0\mu_0}$, relating the permeability of the vacuum μ_0 and the dielectric constant ϵ_0 to the speed of light c . These are all Maxwell equations that we will now use to extend the equations of hydrodynamics and include the contribution from the magnetic field.

¹⁶A precise definition of this pseudo tensor can be found in the Appendix.

2.3.3 The induction equation and the evolution of magnetic fields

First, we consider two different reference frames of a plasma. One frame is a fixed frame that is moving together with the fluid and the other is an external laboratory frame. According to Lorentz transformations, we can write the equation for the electric field, seen by the other reference frame, as

$$\mathbf{E}' = \gamma \left[\mathbf{E} + \frac{\mathbf{v}}{c} \times \mathbf{B} \right]. \quad (2.109)$$

Quantities in the rest frame of the plasma are denoted with a prime and the other quantities without one. In the non-relativistic limit these equations simplify to read

$$\mathbf{E}' = \mathbf{E} + \frac{\mathbf{v}}{c} \times \mathbf{B}. \quad (2.110)$$

Furthermore, we have

$$\mathbf{j}' = \sigma \mathbf{E}' = \sigma \left(\mathbf{E} + \frac{\mathbf{v}}{c} \times \mathbf{B} \right) \approx \mathbf{j}, \quad (2.111)$$

where σ is the *conductivity*. We then obtain for the electric field \mathbf{E} in terms of the current \mathbf{j} and the magnetic field \mathbf{B}

$$\mathbf{E} = \frac{\mathbf{j}}{\sigma} - \frac{1}{c} \mathbf{v} \times \mathbf{B}. \quad (2.112)$$

We now also need *Ampère's law*¹⁷, which we obtain if we neglect the displacement current $c^{-1} \partial \mathbf{E} / \partial t$ in Maxwell's equation. We then get the simple relation

$$\nabla \times \mathbf{B} = \mu_0 \mathbf{j}, \quad (2.113)$$

which describes how magnetic fields \mathbf{B} build under the influence of a current \mathbf{j} . Now we have all ingredients together and can compute the induction equation. Taking Maxwell's equation for a last time and inserting (2.112) we get

$$\frac{1}{c} \frac{\partial \mathbf{B}}{\partial t} = -\nabla \times \mathbf{E} = -\nabla \times \left(\frac{\mathbf{j}}{\sigma} - \frac{1}{c} \mathbf{v} \times \mathbf{B} \right) \quad (2.114)$$

If we now replace the current \mathbf{j} by means of Ampère's law, we finally arrive at the important induction equation:

$$\boxed{\frac{\partial \mathbf{B}}{\partial t} = \nabla \times (\mathbf{v} \times \mathbf{B}) + \eta \nabla^2 \mathbf{B}}, \quad (2.115)$$

In this equation, $\eta = c^2 / (4\pi\sigma)$ is the *magnetic diffusivity*. The induction equation describes the evolution of a magnetic field, which is embedded in a plasma flow with velocity \mathbf{v} . We recognize two terms on the right hand side. The first one will be referred to an advection, the second one to a diffusion process. We will analyze both of them in the next sections.

¹⁷André-Marie Ampère, French physicist, 20/01/1775 - 10/06/1836

2.3.4 Euler's equation of motion with magnetic fields

If a magnetic field influences the dynamics of the medium, our equation of motion needs to be expanded by an additional term. This is the *Lorentz force*:

$$\mathbf{F} = q(\beta \times \mathbf{B}) = \frac{1}{c}(\mathbf{j} \times \mathbf{B}) \quad (2.116)$$

Here, q is the charge of the particle and $\beta = \mathbf{v}/c$ again the ratio of the velocity and the speed of light. By using Ampère's law (2.113), we find the following term¹⁸:

$$\begin{aligned} (\nabla \times \mathbf{B}) \times \mathbf{B} &= \epsilon_{ijk}\epsilon_{klm} \frac{\partial B_m}{\partial x_l} B_k \\ &= (\delta_{il}\delta_{km} - \delta_{im}\delta_{jk}) \frac{\partial B_m}{\partial x_l} B_k \\ &= \left(B_k \frac{\partial B_i}{\partial x_k} - B_k \frac{\partial B_k}{\partial x_i} \right) \\ &= (\mathbf{B} \cdot \nabla)\mathbf{B} - \frac{1}{2}\nabla B^2. \end{aligned} \quad (2.117)$$

The first term describes how \mathbf{B} changes along \mathbf{B} , that means it quantifies a tension. Thus, magnetic fields can be interpreted as strings, which tend to be as straight as possible. The second term characterizes the change of the magnetic energy in the fluid, which is proportional to B^2 .

Taking all these equations together, we can now modify Euler's equation to read:

$$\boxed{\frac{\partial \mathbf{v}}{\partial t} + (\mathbf{v} \cdot \nabla)\mathbf{v} = -\frac{\nabla P}{\rho} - \nabla\Phi + \frac{1}{\mu_0}(\mathbf{B} \cdot \nabla)\mathbf{B} - \frac{1}{2\mu_0}\nabla B^2.} \quad (2.118)$$

Here, we have again made use of the fact that Euler's equation of motion describes a balance of all acting forces and hence we can easily add additional force terms on the right hand side.

2.3.5 Magnetic advection and diffusion processes

We now want to analyze the two terms in the induction equation (2.115) more deeply. Let us start with the first one, that is $\nabla \times (\mathbf{v} \times \mathbf{B})$. Is it called the *advection term* and describes the transport of the \mathbf{B} field with the fluid. Replacing the gradient by a typical length scale of the fluid, $\nabla \rightarrow 1/L$, we see that this term is of the order

$$\nabla \times (\mathbf{v} \times \mathbf{B}) \rightarrow \frac{vB}{L}. \quad (2.119)$$

The second term, $\eta\nabla^2\mathbf{B}$, is a *diffusion term*. We can again estimate its order of magnitude:

$$\eta\nabla^2\mathbf{B} \rightarrow \frac{\eta B}{L^2}. \quad (2.120)$$

¹⁸The following calculation makes us of the relation $\epsilon_{ijk}\epsilon_{klm} = \delta_{jl}\delta_{km} - \delta_{jm}\delta_{kl}$.

The ratio of those two is called the *magnetic Reynolds number* and reads

$$\boxed{\mathcal{R}_M = \frac{\text{advection}}{\text{diffusion}} = \frac{vL}{\eta}}. \quad (2.121)$$

We can now study two limits for the magnetic Reynolds number. First, we consider the limit in which $\mathcal{R}_M \gg 1$. We then see, that the diffusion term can be neglected and we find for the induction equation:

$$\frac{\partial \mathbf{B}}{\partial t} = \nabla \times (\mathbf{v} \times \mathbf{B}), \quad (2.122)$$

In this case, the magnetic field is said to be frozen into the fluid and ideally moves with respect to the flow. In the other limit, $\mathcal{R}_M \ll 1$, we can neglect the advection term and find

$$\frac{\partial \mathbf{B}}{\partial t} = \eta \nabla^2 \mathbf{B}. \quad (2.123)$$

This equation describes a decay of the magnetic field. We can also estimate the decaying timescale by again replacing $\nabla \rightarrow 1/L$ and $\partial/\partial t \rightarrow 1/t$, where L and t are typical length and timescales of the system, and find $t_{\text{decay}} \approx L^2/\eta$.

2.3.6 Generating magnetic fields via the battery mechanism

Up to now, we can describe the evolution of magnetic fields in a plasma, but have not yet discussed how magnetic fields are generated. This process is mainly due to the separation of various charged fluids, that move with different velocities, inducing a current and thus a magnetic field. Hence, we have to consider flows of different charges separately. Therefore, we consider two fluids in a plasma, electrons and ions, negatively and positively charged, respectively. For both, we write Euler's equation including the Lorentz force and an external gravitational potential:

$$nm_e \frac{d\mathbf{v}_e}{dt} = -\nabla P_e - ne \left(\mathbf{E} + \frac{\mathbf{v}_e}{c} \times \mathbf{B} \right) - nm_e \nabla \Phi, \quad (2.124)$$

$$nm_i \frac{d\mathbf{v}_i}{dt} = -\nabla P_i - ne \left(\mathbf{E} + \frac{\mathbf{v}_i}{c} \times \mathbf{B} \right) - nm_i \nabla \Phi. \quad (2.125)$$

Now, we subtract the second from the first and assume that $m_i \gg m_e$. We then find the new equation

$$\frac{d(\mathbf{v}_e - \mathbf{v}_i)}{dt} = -\frac{\nabla P_e}{nm_e} - \frac{e}{m_e} \left(\mathbf{E} + \frac{\mathbf{v}_e}{c} \times \mathbf{B} \right) - \frac{\mathbf{v}_e - \mathbf{v}_i}{\tau}, \quad (2.126)$$

where we have added an additional term on the right-hand side that accounts for the collisions between electrons and ions. We now introduce the current $\mathbf{j} = en(\mathbf{v}_i - \mathbf{v}_e)$. In a stationary state, we have $d\mathbf{j}/dt \approx 0$ and then find for the electric field

$$\mathbf{E} = -\frac{\nabla P_e}{en} - \frac{\mathbf{v}_e}{c} \times \mathbf{B} + \frac{m_e \mathbf{j}}{ne^2 \tau}. \quad (2.127)$$

By means of Maxwell's equations, we can then work out the magnetic field by using Ampère's law (2.113) again. The final result after some algebra is

$$\boxed{\frac{d\mathbf{B}}{dt} = \frac{c^2}{4\pi\sigma} \nabla^2 \mathbf{B} + \nabla \times (\mathbf{v}_e \times \mathbf{B}) - \frac{c}{en^2} (\nabla P_e \times \nabla n)}, \quad (2.128)$$

where we have defined the conductivity $\sigma = ne^2\tau/m_e$. The mechanism for creating magnetic fields is called *battery mechanism*. We realize that this equation has the same structure as the induction equation from above, except a term with a gradient in the number density of the ions. This is exactly the additional term that gives rise to the creation of \mathbf{B} fields, even if $\mathbf{B} = 0$ at the beginning.

2.3.7 Ambipolar diffusion in a magnetized fluid

In this section, we want to discuss what happens, if charged particles move through a magnetic field. If the particles are neutral, they can move freely with respect to the \mathbf{B} field but are still coupled to the plasma via collisions. The charged particles, however, are somewhat frozen into the field. This effect is called *ambipolar diffusion*. We want to try to understand this process mathematically. Therefore, consider a single collision that transfers the momentum between the two species,

$$\Delta \mathbf{p} = \mu(\mathbf{v}_i - \mathbf{v}_n), \quad (2.129)$$

where μ is the reduced mass, $\mu = m_i m_n / (m_i + m_n)$. This causes a friction force,

$$\mathbf{f} = \gamma \rho_i \rho_n (\mathbf{v}_i - \mathbf{v}_n), \quad (2.130)$$

with the friction coefficient γ and the mass densities ρ_i and ρ_n . We can now compute the Lorentz force density, which reads

$$\mathbf{f}_L = \frac{\mathbf{j} \times \mathbf{B}}{c} = \frac{1}{4\pi} (\nabla \times \mathbf{B}) \times \mathbf{B}. \quad (2.131)$$

If we define the relative drift velocity $\mathbf{v}_d = \mathbf{v}_i - \mathbf{v}_n$, we can write

$$\mathbf{v}_d = \frac{(\nabla \times \mathbf{B}) \times \mathbf{B}}{4\pi\gamma\rho_i\rho_n}. \quad (2.132)$$

If we again approximate the gradient by $\nabla \rightarrow 1/L$, we can estimate the relative drift velocity to be of the order

$$v_d \approx \frac{B^2}{4\pi\gamma\rho_i\rho_n L}, \quad (2.133)$$

as well as the typical timescale of the drift:

$$t_d = \frac{L}{v_d} \approx \frac{4\pi\gamma\rho_i\rho_n L^2}{B^2}. \quad (2.134)$$

If the magnetic field is frozen into the plasma, the induction equation in the limit of high Reynolds numbers holds,

$$\frac{\partial \mathbf{B}}{\partial t} = \nabla \times (\mathbf{v}_d \times \mathbf{B}), \quad (2.135)$$

where we now insert the expression for the drift velocity from (2.132) and define the magnetic pressure $P_B = \mathbf{B}^2/(8\pi)$. We then finally arrive at the remarkable equation

$$\boxed{\frac{\partial \mathbf{B}}{\partial t} + \frac{1}{\gamma \rho_i \rho_n} [\nabla(\mathbf{B} \cdot \nabla P_B) - \nabla^2(P_B \mathbf{B})] = 0}, \quad (2.136)$$

which describes the evolution of the magnetic field in the ISM including an ambipolar diffusion process.

2.3.8 Alfvén waves and the Alfvén velocity

Alfvén¹⁹ waves are waves which propagate in a gas plasma. They are induced by ionized particles which oscillate around their rest position in presence of an external magnetic field. There are two possible wave states: Alfvén waves can either be longitudinal or transversal. The latter waves propagate through the medium with a characteristic velocity v_A , which we can easily estimate by considering the following argument. If we assume that kinetic and magnetic energy density are in energy equilibrium, we have

$$\frac{1}{2} \rho v_A^2 = \frac{1}{2} \frac{B^2}{\mu_0}, \quad (2.137)$$

and from that we obtain the Alfvén velocity

$$\boxed{v_A = \frac{B}{\sqrt{\mu_0 \rho}}}. \quad (2.138)$$

The Alfvénic Mach number \mathcal{M}_A is defined as the ratio of the gas velocity v and the Alfvén velocity v_A and reads $\mathcal{M}_A = v/v_A$, in analogy to the sonic Mach number $\mathcal{M}_s = v/c_s$ with sound speed c_s .

However, we also note that a more proper treatment of Alfvén waves requires a strict perturbation analysis of the MHD equations, which can be found in any good textbook about MHD theory.

¹⁹Hannes Olof Gösta Alfvén, Swedish physicist, 30/05/1908 - 02/04/1995

Radiative transfer

In this chapter we introduce some basic concepts of radiative transfer. At the beginning, we will treat electromagnetic radiation as a wave and use a semi-classical approach to derive important equations for the transport of radiation. Later on, we will switch to the quantum mechanical picture of light as energetic particles (or photons γ) that carry the energy $E_\gamma = h\nu$, with h being the Planck constant and ν the frequency of the photon. We start by introducing basic quantities of the radiation field and analyze how radiation interacts with matter (Sections 3.1 and 3.2). We then present other important relations that we will continuously refer to in this thesis, e.g. the Stefan-Boltzmann law, the Planck spectrum or the Einstein coefficients (Sections 3.3, 3.4, 3.5 and 3.6). We also discuss different sources of line broadening and some important line profile functions (Sections 3.7, 3.8, 3.9 and 3.10). We then turn to different heating and cooling processes in the ISM (Section 3.11). We end this chapter with a (naive, but easy) classical treatment of fine structure lines (Section 3.12) and derive the Doppler formula (Section 3.13), which is commonly used to estimate astrophysical velocities.

The equations presented in this chapter can be found in every standard textbook about radiative transfer, e.g. by Tielens (2010), Padmanabhan (2007), Bartelmann (2013) or Rybicki & Lightman (2004).

3.1 Basic quantities of radiative transfer

The conceptual idea of a radiative transfer process is to analyze how a light ray travels through space and time and how it interacts with a given distribution of matter. Before we go into a detailed study, we start with introducing the *specific intensity* I_ν ¹, which describes how much energy dE a light ray carries through an

¹ $[I_\nu] = \text{erg cm}^{-2} \text{s}^{-1} \text{Hz}^{-1} \text{ster}^{-1}$

infinitesimal area element dA per infinitesimal time dt , frequency $d\nu$ and solid angle element $d\Omega$. It can be expressed by

$$I_\nu \equiv \frac{dE}{dA dt d\nu d\Omega}. \quad (3.1)$$

The *mean intensity* J_ν is defined as the integral over the full sphere,

$$J_\nu = \frac{1}{4\pi} \int I_\nu d\Omega. \quad (3.2)$$

Furthermore, we can define the *total intensity* J , which we obtain simply by integrating over the sphere and all frequencies:

$$J = \frac{1}{4\pi} \iint I_\nu d\Omega d\nu. \quad (3.3)$$

We can also define an energy density $u_\nu(\Omega)$ of the radiation field. Therefore, we compute the energy dE , which is

$$dE = u_\nu(\Omega) dV d\nu d\Omega = u_\nu(\Omega) dA c dt d\nu d\Omega, \quad (3.4)$$

where we have introduced the infinitesimal volume element $dV = dA c dt$. Comparing with (3.1) yields the relation

$$u_\nu(\Omega) = \frac{I_\nu}{c} \quad (3.5)$$

and after integrating over all solid angles

$$u_\nu = \int u_\nu(\Omega) d\Omega = \frac{4\pi}{c} J_\nu. \quad (3.6)$$

The relation between the radiation pressure P and the energy density u of an isotropic radiation field is finally given by $P = 1/3u$.

3.2 Interaction of radiation with matter

There are two ways of how radiation can interact with matter, either by emission or by absorption. In the first case, photons are added to a light ray passing through the medium. In the latter case, photons are taken away from the light ray. How can we describe these processes?

Let us start with the process of emission. If a light ray passes a distance $dl = c dt$ through a medium, the intensity that is added to the beam is

$$dI_\nu = j_\nu dl, \quad (3.7)$$

where j_ν is a source function. On the contrary, absorption can be characterized by the Lambert-Beer²³ law (also known from the radioactive decay)

$$dI_\nu = -\alpha_\nu I_\nu dl, \quad (3.8)$$

where $\alpha_\nu = \rho\kappa_\nu$ is the absorption coefficient, ρ the mass density and κ_ν the *opacity* of the medium. Taking everything together, we find the important differential equation for radiative transfer,

$$\boxed{\frac{dI_\nu}{dl} = -\alpha_\nu I_\nu + j_\nu.} \quad (3.9)$$

We can now consider two simple cases. In the first one, we neglect absorption effects, $\alpha_\nu = 0$, and only account for the emission. That drives us to the easy equation

$$\frac{dI_\nu}{dl} = j_\nu, \quad (3.10)$$

which can be integrated to yield the solution

$$I_\nu(l) = I_\nu(0) + \int_0^l dl' j_\nu(l'). \quad (3.11)$$

The interpretation of this term is rather simple: It is just all the emission integrated along the line-of-sight.

For the other case of vanishing source function j_ν , we only have the differential equation

$$\frac{dI_\nu}{dl} = -\alpha_\nu I_\nu, \quad (3.12)$$

which can be solved by rearranging the differentials, that gives

$$I_\nu(l) = I_\nu(0) \exp\left[-\int_0^l dl' \alpha_\nu(l')\right]. \quad (3.13)$$

This is the solution for an exponential decay. However, we can further simplify this equation by introducing an *optical depth* defined by

$$\boxed{d\tau_\nu = \alpha_\nu dl.} \quad (3.14)$$

Thus, the solution of the differential equation with vanishing source function can be shortly written as

$$I_\nu(l) = I_\nu(0)e^{-\tau_\nu}. \quad (3.15)$$

²Johann Heinrich Lambert, Swiss physicist, 26/08/1728 - 25/09/1777

³August Beer, German physicist, 31/07/1825 - 18/11/1863

This brings us to the following terminology: A medium is called *optically thin* (or transparent), if $\tau_\nu < 1$ and optically thick (or opaque) if $\tau_\nu > 1$.

With this definition we can introduce a new source function $S_\nu = j_\nu/\alpha_\nu$. Then, the transfer equation takes the even more simple form

$$\frac{dI_\nu}{d\tau_\nu} = -I_\nu + S_\nu. \quad (3.16)$$

To solve this equation, we now apply a trick and introduce an integration factor e^{τ_ν} together with the properties $\tilde{I}_\nu = I_\nu e^{\tau_\nu}$ and $\tilde{S}_\nu = S_\nu e^{\tau_\nu}$. Then, Eq. (3.16) turns into

$$\frac{d\tilde{I}_\nu}{d\tau_\nu} = \tilde{S}_\nu. \quad (3.17)$$

This has the formal solution

$$\tilde{I}_\nu(\tau_\nu) = \tilde{I}_\nu(0) + \int_0^{\tau_\nu} d\tau'_\nu \tilde{S}_\nu(\tau'_\nu), \quad (3.18)$$

and if we substitute \tilde{S} and \tilde{I} back, we obtain the general solution:

$$I_\nu(\tau_\nu) = I_\nu(0)e^{-\tau_\nu} + \int_0^{\tau_\nu} d\tau'_\nu e^{-(\tau_\nu - \tau'_\nu)} S_\nu(\tau'_\nu). \quad (3.19)$$

From this equation, we can already read off some interesting results, if we assume that the source function is constant, $S_\nu \equiv \text{const.}$. Then, we can solve the integral and find

$$I_\nu(\tau_\nu) = S_\nu + e^{-\tau_\nu}(I_\nu(0) - S_\nu). \quad (3.20)$$

This equation has an easy interpretation. If $S_\nu = 0$, we again encounter the Lambert-Beer law, that we have discussed above. If $\tau \rightarrow \infty$, we find that $I_\nu = S_\nu$, which means that in the case of an infinitely opaque medium, the intensity is dominated by the source function. Vice versa, if $\tau \rightarrow 0$, we have $I_\nu = I_\nu(0)$, i.e. any light ray can pass through the medium without being affected by its opacity.

3.3 Blackbody radiation and the Stefan-Boltzmann law

In the following, we deal with the so-called *blackbody radiation*, which is radiation that is in thermal equilibrium. That means we can treat it with the first law of classical thermodynamics,

$$dU = dQ - PdV. \quad (3.21)$$

In this equation, dQ is the change of heat content, dU the change of internal energy and $dW = -PdV$ the volume work. If we use the change of entropy $dQ = TdS$ as well as $U = uV$ and $P = 1/3u$, we can rewrite the first law of thermodynamics to read

$$dS = \frac{V}{T} \frac{du}{dT} dT + \frac{4}{3} \frac{u}{T} dV. \quad (3.22)$$

From that, we obtain the Maxwell relations

$$\left. \frac{\partial S}{\partial T} \right|_V = \frac{V}{T} \frac{du}{dT}, \quad \left. \frac{\partial S}{\partial V} \right|_T = \frac{4}{3} \frac{u}{T}. \quad (3.23)$$

Next, we make use of the symmetry of second derivatives, also known as the Schwarz integrability condition, saying that

$$\frac{\partial}{\partial V} \left(\frac{\partial S}{\partial T} \right) = \frac{\partial}{\partial T} \left(\frac{\partial S}{\partial V} \right). \quad (3.24)$$

We then find the relation

$$\frac{1}{T} \frac{du}{dT} = -\frac{4}{3} \frac{u}{T^2} + \frac{4}{3} \frac{1}{T} \frac{du}{dT}. \quad (3.25)$$

and from that

$$\frac{du}{u} = 4 \frac{dT}{T} \quad (3.26)$$

This equation can be integrated and we finally obtain the famous *Stefan-Boltzmann law*⁴, relating the energy density of the radiation field to its temperature,

$$\boxed{u(T) = aT^4}, \quad (3.27)$$

where a is an integration constant, also known as the *Stefan-Boltzmann constant*. This law tells us that the energy density of the radiation field grows as the temperature to the fourth. It is a widely used law in astrophysics.

3.4 The Planck spectrum, Wien's law and the Rayleigh-Jeans limit

In this section we derive the so-called *Planck spectrum*⁵ of a *blackbody*. To start with the problem, let us first remember the grand-canonical partition function of quantum statistics that reads

$$Z_{gc}(\mu, V, T) = \sum_n \exp(-\beta(\epsilon_n - \mu N_n)), \quad (3.28)$$

⁴Josef Stefan, Austrian physicist, 24/03/1835 - 7/01/1893

⁵Max Karl Ernst Ludwig Planck, German physicist, 23/04/1858 - 04/10/1947

where μ is the chemical potential, $\beta = 1/(kT)$ a measure for the temperature T , ϵ_n and N_n the energy and the number of particles in the state n . The sum in this formula goes over all possible energy states. In particular, for photons we have a vanishing chemical potential, i.e. $\mu = 0$. Generally, the mean energy U of the system can be computed via

$$\langle U \rangle = -\frac{\partial}{\partial \beta} \ln(Z_{gc}(\mu, V, T)). \quad (3.29)$$

If we assume that the photons carry the energy $\epsilon_n = nh\nu$ with the Planck constant h , we can compute the partition function,

$$Z_{gc}(\mu, V, T) = \sum_n \exp(-nh\nu\beta) = \frac{1}{1 - e^{-h\nu\beta}}. \quad (3.30)$$

In the last step we have used the geometrical series. Thus, we get for the mean energy

$$\langle U \rangle = \frac{h\nu}{e^{\beta h\nu} - 1}, \quad (3.31)$$

where we also find the mean occupation number for the *Bose-Einstein statistics*⁶. We also give the mean occupation number for the so-called *Fermi-Dirac statistics*⁷⁸:

$$\bar{n}_\alpha^{\text{FD}} = \frac{1}{e^{\beta(\epsilon_\alpha - \mu)} + 1}, \quad \bar{n}_\alpha^{\text{BE}} = \frac{1}{e^{\beta(\epsilon_\alpha - \mu)} - 1}. \quad (3.32)$$

These numbers can also be derived by an explicit computation of

$$\bar{n}_\alpha = \frac{1}{\beta} \frac{\partial}{\partial \mu} \ln Z. \quad (3.33)$$

In order to derive the Planck spectrum, we compute the energy density

$$dU = 2 \times \frac{4\pi p^2 dp}{h^3} \times \epsilon \times \bar{n}_\alpha^{\text{BE}}, \quad (3.34)$$

where the factor of two accounts for the two polarization states of the photon and $\epsilon = cp$ is the energy in terms of the momentum. Expressing the momentum in terms of the frequency, $p = h\nu/c$, we find together with $B_\nu = c/(4\pi) dU/d\nu$ the famous Planck formula,

$$B_\nu(T) = \frac{2h}{c^2} \frac{\nu^3}{e^{h\nu/(kT)} - 1}. \quad (3.35)$$

In particular, we can analyze various important cases:

⁶Satyendranath Bose, Indian physicist, 01/01/1894 - 04/02/1974

⁷Enrico Fermi, US American physicist, 29/09/1901 - 28/11/1954

⁸Paul Dirac, British physicist, 08/08/1902 - 20/10/1984

- In the low energy limit, $h\nu \ll kT$, we find

$$\exp\left(\frac{h\nu}{kT}\right) \approx 1 + \frac{h\nu}{kT} + \dots \quad (3.36)$$

Plugging this approximation into Eq. (3.35), we obtain the *Rayleigh-Jeans law*⁹:

$$I_\nu = \frac{2\nu^2}{c^2} kT. \quad (3.37)$$

Here, the temperature T is called the brightness temperature, because it is directly related to an intensity. We will use this approximation in this thesis to convert between brightness temperatures and the intensity.

- In the high energy limit, $h\nu \gg kT$, we can neglect the unity term in the denominator and find *Wien's law*¹⁰:

$$I_\nu = \frac{2h\nu^3}{c^2} \exp\left(-\frac{h\nu}{kT}\right). \quad (3.38)$$

- Furthermore, if we look for the maximum of the Planck spectrum, that is if we compute $\partial B_\nu(T)/\partial\nu = 0$, we find the expression

$$h\nu_{\max} = 2.82kT, \quad (3.39)$$

which is *Wien's displacement law*. Moreover, if we integrate over the whole Planck spectrum, we can now identify Stefan-Boltzmann's constant after a lengthy computation and find

$$\int_0^\infty B_\nu(T) d\nu = \frac{2\pi^4 k^4}{15c^2 h^3} T^4 = aT^4. \quad (3.40)$$

Here, we see that the constant is $a = 2\pi^4 k^4 / (15c^2 h^3)$.

3.5 Absorption and emission processes: the Einstein coefficients

In this section, we will introduce the *Einstein coefficients* and analyze absorption and emission in the ISM on a microscopic scale. Therefore, we define three coefficients: A_{21} , B_{12} , B_{21} . In a simplified two level quantum system, the number A_{21} describes the rates (and in this sense also the probability) for spontaneous emission from

⁹John William Strutt, 3. Baron Rayleigh, British physicist, 12/11/1842 - 30/06/1919

¹⁰Wilhelm Carl Werner Otto Fritz Franz Wien, German physicist, 13/01/1864 - 30/08/1928

the high energy level to the ground state of the particle, the quantity $B_{12}I_\nu$ is the radiation that is absorbed by the medium and $B_{21}I_\nu$ the radiation coming from stimulated emission. If N_1 and N_2 denote the mean number of atoms in the states 2 and 1 in thermal equilibrium, we can write a balance equation that reads

$$N_1 B_{12} I_\nu = N_2 A_{21} + N_2 B_{21} I_\nu, \quad (3.41)$$

from which we find the intensity

$$I_\nu = \frac{A_{21}/B_{21}}{(N_1/N_2)(B_{12}/B_{21}) - 1}. \quad (3.42)$$

Furthermore, in thermodynamic equilibrium we have according to Boltzmann's law

$$\boxed{\frac{N_1}{N_2} = \frac{g_1}{g_2} \exp\left(\frac{h\nu}{kT}\right)}. \quad (3.43)$$

From this we obtain the intensity

$$I_\nu = \frac{A_{21}/B_{21}}{(g_1 B_{12}/g_2 B_{21}) \exp(h\nu/kT) - 1}. \quad (3.44)$$

If we compare Eq. (3.44) with Eq. (3.35), we find the following *Einstein relations*:

$$\boxed{g_1 B_{12} = g_2 B_{21}}, \quad (3.45)$$

$$\boxed{A_{21} = \frac{2h\nu^3}{c^2} B_{21}}. \quad (3.46)$$

We see that once we have determined one coefficient, all other numbers are given.

How are these coefficients related to the absorption and emission functions j_ν and α_ν ? To answer this question, we remember that the energy spontaneously emitted in the volume element dV per solid angle $d\Omega$, per time dt and frequency $d\nu$ is

$$dE = \frac{h\nu\phi(\nu)}{4\pi} n_2 A_{21} dV d\Omega dt d\nu, \quad (3.47)$$

where $\phi(\nu)$ is the line profile function¹¹ and n_2 the number of atoms in level 2. The line profile function is normalized,

$$\int \phi(\nu) d\nu = 1. \quad (3.48)$$

Since dE is the energy that is radiated away from the medium, we find the relation

$$\boxed{j_\nu = \frac{h\nu\phi(\nu)}{4\pi} n_2 A_{21}}. \quad (3.49)$$

¹¹A mathematical treatment of the line profile follows in the next sections.

In the same fashion, we find for the absorption coefficient α_ν

$$\alpha_\nu = \frac{h\nu\phi(\nu)}{4\pi}n_1B_{12}. \quad (3.50)$$

However, α_ν also depends on the number of atoms that radiate due to stimulated emission. Thus, we have to subtract this contribution from our equation and find

$$\alpha_\nu = \frac{h\nu\phi(\nu)}{4\pi}(n_1B_{12} - n_2B_{21}). \quad (3.51)$$

The source function then reads

$$S_\nu = \frac{j_\nu}{\alpha_\nu} = \frac{n_2A_{21}}{n_1B_{12} - n_2B_{21}}. \quad (3.52)$$

If we use Einstein's relations, we can also write α_ν and S_ν in the following form:

$$\alpha_\nu = \frac{h\nu\phi(\nu)}{4\pi}n_1B_{12}\left(1 - \frac{g_1n_2}{g_2n_1}\right), \quad (3.53)$$

$$S_\nu = \frac{2h\nu^3}{c^2}\left(\frac{g_2n_1}{g_1n_2} - 1\right)^{-1}. \quad (3.54)$$

These equations can be further simplified if we assume *local thermal equilibrium* (LTE). LTE means that the thermodynamic parameters (e.g. temperature, pressure, etc.) generally vary in space and time, but vary so slowly that one can safely adopt thermodynamic equilibrium at this point and in its neighbourhood. Conversely, *global thermal equilibrium* (GTE) means that those parameters are completely homogeneous everywhere in space and time. Assuming LTE, we can use Eq. (3.43) to write

$$\alpha_\nu = \frac{h\nu\phi(\nu)}{4\pi}n_1B_{12}\left[1 - \exp\left(-\frac{h\nu}{kT}\right)\right], \quad (3.55)$$

$$S_\nu = B_\nu(T). \quad (3.56)$$

In the case of a non local thermal equilibrium (non-LTE), Eq. (3.43) does not hold and we find a more complicated situation in which the particles do not have a Maxwellian velocity distribution. However, since we do not consider non-LTE physics in this thesis, we will not discuss these effects here.

3.6 Atomic excitation and deexcitation by collisions

How can atoms be excited or deexcited? The answer is: by collisions. Let us assume that the rate for collisional excitation is $n_1n_0C_{12}$, where n_0 is the density of the colliders. Similarly, the rate for deexcitation is $n_2n_0C_{21}$. Both variables C_{12}

and C_{21} are constants and characteristic for the individual species. If we consider a system in thermal equilibrium, then we have the condition that

$$n_1 C_{12} = n_2 C_{21}, \quad (3.57)$$

which leads to the equation

$$\frac{C_{12}}{C_{21}} = \frac{g_2}{g_1} \exp\left(-\frac{h\nu}{kT}\right), \quad (3.58)$$

where we have again used the Boltzmann statistics from Eq. (3.43). The new constants C_{12} and C_{21} can also be related to collisional cross-sections, which, however, we will not compute here.

If we neglect effects of absorption and emission for a while, we can write the following balance equation:

$$n_0 n_1 C_{12} = n_2 A_{21} + n_2 n_0 C_{21}. \quad (3.59)$$

Plugging Eq. (3.59) into Eq. (3.58) we obtain

$$\frac{n_2}{n_1} = \frac{g_2/g_1 \exp(-h\nu/kT)}{1 + n_{\text{cr}}/n_0}, \quad (3.60)$$

where we have defined a critical density $n_{\text{cr}} = A_{21}/C_{21}$ for deexcitation. From this equation we see that if $n_0 \gg n_{\text{cr}}$, the collisional deexcitation is much faster than the spontaneous emission and we find again Eq. (3.43). The line is then said to be *thermalized*. Vice versa, if $n_0 \ll n_{\text{cr}}$, spontaneous emission dominates collisional deexcitation and we find that n_2 is much lower than the corresponding equilibrium value. The line is then said to be *sub-thermally* excited.

Let us now consider a molecular cloud, which has a high density such that $n \gg n_{\text{cr}}$. In this case, most of the atoms that are excited by collisions are deexcited by collisions, too. Thus, the rate of photons emitted by the cloud is $\propto n$ and hence the cooling rate scales linearly with the gas density n . Vice versa, if $n \ll n_{\text{cr}}$ in a low-density cloud, collisional deexcitation is negligible, which means that the rate of collisions is $\propto n^2$ and thus the cooling rate scales quadratically with the gas density. Further details about cooling processes in the ISM can be found in Section 3.11.

3.7 The Lorentz profile of line emission

In this section, we will derive the line profile function arising from a spontaneous decay of an atom from a high to a lower energy state. The decay occurs because the excited energy state has a finite lifetime according to the *Heisenberg uncertainty principle* of quantum mechanics. The profile function is called the *Lorentz profile* or the *natural line width*. To begin with the derivation, let us assume two quantum

mechanical states $|n\rangle$ and $|m\rangle$, that are separated by the well-defined energy difference $E_n - E_m > 0$. We first consider now the state $|k, t\rangle$ in the Schrödinger picture¹² and write

$$|k, t\rangle = e^{-iE_k t/\hbar} |k, 0\rangle, \quad (3.61)$$

where the time-dependent phase information is now encoded in the exponential pre-factor. Next, we perturb the quantum mechanical Hamiltonian H and split it up into a time-independent and a time-dependent part:

$$H = H_0 + H_1(t). \quad (3.62)$$

With this ansatz, Schrödinger's equation reads

$$i\hbar \frac{\partial}{\partial t} \sum_k a_k e^{-iE_k t/\hbar} |k, 0\rangle = \sum_k a_k e^{-iE_k t/\hbar} [H_0 + H_1(t)] |k, 0\rangle, \quad (3.63)$$

where we have expanded the state $|\psi\rangle$ into the eigenstates $|k\rangle$ of the system with new coefficients a_k :

$$|\psi\rangle = \sum_k a_k |k\rangle. \quad (3.64)$$

Carrying out the time-derivative in Eq. (3.63), using the fact that $|k, 0\rangle$ are eigenstates of H_0 ,

$$H_0 |k, 0\rangle = E_k |k, 0\rangle, \quad (3.65)$$

pulling the time-dependence of $H_1(t)$ into a separate phase-factor, $H_1(t) = H_1 e^{-i\omega t}$, and multiplying (3.63) with $\langle j, 0|$ from the left, we end up with

$$\dot{a}_j = -\frac{i}{\hbar} \sum_k a_k e^{-i(\omega - \omega_{kj})t} \langle j, 0|H_1|k, 0\rangle, \quad (3.66)$$

where we have abbreviated $\omega_{kj} = (E_k - E_j)/\hbar$. This is a first-order differential equation in a_k . To solve this, we assume the boundary conditions $a_1 = 1$ and $a_0 = 0$ and find

$$\dot{a}_2 = -\frac{i}{\hbar} e^{-i(\omega - \omega_{12})t} \langle 1, 0|H_1|2, 0\rangle. \quad (3.67)$$

However, we have still ignored the contribution from the spontaneous emission, which can be described via the decay law

$$\dot{a}_2 = -\frac{\Gamma}{2} a_2, \quad (3.68)$$

¹²In the Schrödinger picture all quantum states are explicitly time-dependent.

where Γ is a decay constant. Thus, our new differential equation reads

$$\dot{a}_2 = -\frac{i}{\hbar} e^{-i(\omega-\omega_{12})t} \langle 1, 0 | H_1 | 2, 0 \rangle - \frac{\Gamma}{2} a_2. \quad (3.69)$$

In the next step, we multiply this relation with the factor $e^{\Gamma t/2}$ to see that it can be written as

$$\frac{\partial}{\partial t} (a_2 e^{\Gamma t/2}) = -\frac{i}{\hbar} e^{-i(\omega-\omega_{12}-\Gamma/2)t} \langle 1, 0 | H_1 | 2, 0 \rangle. \quad (3.70)$$

After integrating this relation, we can compute the transition probability $|a_2|^2$ and obtain

$$|a_2|^2 = \frac{\langle 1, 0 | H_1 | 2, 0 \rangle^2}{\hbar^2} \frac{1}{(\omega - \omega_{12})^2 + \Gamma^2/4}. \quad (3.71)$$

This is already the Lorentz profile function, which we call $\phi(\omega)$:

$$\boxed{\phi(\omega) = \frac{1}{2\pi} \frac{\Gamma}{(\omega - \omega_{12})^2 + \Gamma^2/4}.} \quad (3.72)$$

The additional factors enter the equation through our normalization condition (3.48).

3.8 The Doppler profile of thermally moving atoms

Another source of line broadening beyond the natural line width comes from the Doppler effect. If the emitting system moves with a relative velocity v , we can translate the frequency of the emitter ω_0 into a frequency ω being measured by an observer¹³,

$$\omega = \omega_0 \left(1 + \frac{v}{c} \right). \quad (3.73)$$

We expect to find Maxwellian velocities in the gas and thus find the following line profile:

$$\phi(\omega) = \frac{1}{\sqrt{2\pi\sigma_v^2}} \int_{-\infty}^{+\infty} dv \delta_D \left[\omega - \omega_0 \left(1 + \frac{v}{c} \right) \right] \exp \left(-\frac{(v - \bar{v})^2}{2\sigma_v^2} \right) \quad (3.74)$$

Here, we have used the standard deviation σ_v of the velocity field. If we use the relation $\delta_D(ax) = \delta_D(x)/a$ for continuous δ -functions, we can work out the integral to find

$$\boxed{\phi(\omega) = \frac{c}{\omega_0 \sqrt{2\pi\sigma_v^2}} \exp \left[-\frac{c^2}{2\sigma_v^2} \left(\frac{\omega - \bar{\omega}}{\omega_0} \right)^2 \right].} \quad (3.75)$$

This is the profile function for thermally moving atoms.

¹³A derivation of the Doppler formula follows at the end of this chapter.

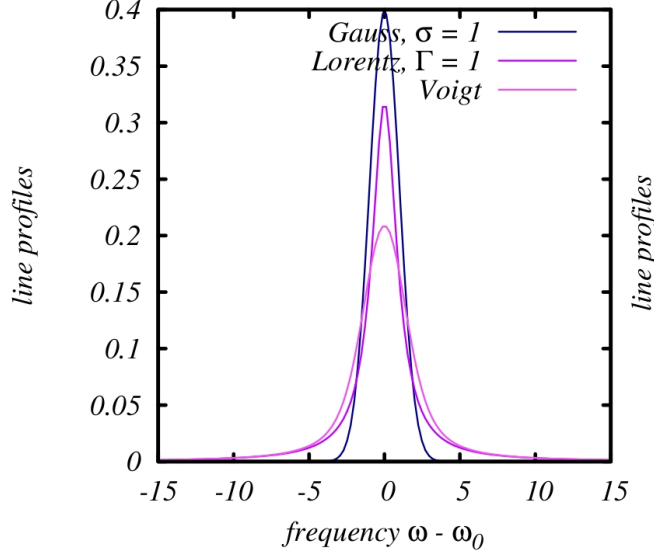
**Figure 3.1:**

Illustration of the different line profiles for $\Gamma = \sigma = 1$ in arbitrary units. This Figure is taken from Bartelmann (2013).

3.9 Convolving the Lorentz and the Doppler profile: the Voigt profile

In a molecular cloud, both profiles, the Lorentz and the Doppler profile, usually act together. Thus, we need to convolve the different profiles. The convolution $\phi_{\text{Doppler}} \circ \phi_{\text{Lorentz}}$ of the Doppler and the Lorentz profiles is called the *Voigt profile*¹⁴. It reads

$$\phi_{\text{Doppler}} \circ \phi_{\text{Lorentz}} = \frac{1}{\sqrt{2\pi\sigma_v^2}} \int_{-\infty}^{+\infty} dv \phi \left[\omega - \omega_{12} \left(1 + \frac{v}{c} \right) \right] \exp \left(-\frac{v^2}{2\sigma_v^2} \right), \quad (3.76)$$

where ϕ is now the Lorentz profile. Before we solve this integral, we introduce the dimensionless variable $q \equiv v/(\sqrt{2}\sigma_v) = v/v_0$ as well as the quantities

$$u \equiv \frac{\omega - \omega_{12}}{\omega_{12}} \frac{c}{v_0}, \quad a \equiv \frac{\Gamma}{2\omega_{12}} \frac{c}{v_0}. \quad (3.77)$$

With this, we can bring the profile

$$\phi \left[\omega - \omega_{12} \left(1 + \frac{v}{c} \right) \right] = \frac{1}{2\pi} \frac{\Gamma}{(\omega - \omega_{12}(1 + v/c))^2 + \Gamma^2/4} \quad (3.78)$$

into the more convenient form

$$\phi(u) = \frac{c}{\pi\omega_{12}v_0} \frac{a}{(u - q)^2 + a^2}. \quad (3.79)$$

¹⁴Woldemar Voigt, German physicist, 02/09/1850 - 13/12/1919

In addition, we can do the same with the Doppler factor and get

$$\frac{dv}{\sqrt{2\pi\sigma_v^2}} \exp\left(-\frac{v^2}{2\sigma_v^2}\right) = \frac{dq}{\sqrt{\pi}} \exp(-q^2). \quad (3.80)$$

Taking everything together, we end up with the Voigt profile, which is the convolution of both the Doppler and the Lorentz line profiles:

$$\phi(u) = \frac{ac}{\pi\sqrt{\pi}\omega_{12}v_0} \int_{-\infty}^{+\infty} dq \frac{\exp(-q^2)}{(u-q)^2 + a^2}. \quad (3.81)$$

In Fig. 3.1 we illustrate the Voigt profile together with the Lorentz and the Doppler profiles. We directly see that the Lorentz profile has much bigger and wider wings than the Doppler profile. Conversely, the Doppler profile function is much sharper than the Lorentz profile. The Voigt profile finally inherits both of these line properties.

3.10 Other processes responsible for line broadening

Beyond the effects of line broadening by thermal motions (Doppler profile) or the quantum mechanic uncertainty principle (natural line broadening, Lorentz profile), there are also other processes which could potentially lead to line broadening. One possibility is *pressure broadening*. If the pressure in a gas is high (e.g. in a star's atmosphere), the mean free path λ of the particles is small, because $\lambda \propto n^{-1} \propto P^{-1}$, and hence collisions dominate the medium. This effect decreases the characteristic time for the (spontaneous) emission of photons and thus changes the line width, because of stimulated photo emission caused by higher collisional rates. Another effect is *rotational broadening*, which leads to an additional Doppler component beside the thermal contribution due to rotation, as well as the broadening by the *Stark* and *Zeemann* effect. Moreover, *opacity broadening* can also affect the line width due to the optical properties of the medium. Each of these mechanisms usually act together, and it is important to distinguish them.

3.11 Heating and cooling processes in the ISM

Heating and cooling are important processes in the ISM, which is why we want to discuss them in more detail. Therefore, we consider again the first law of thermodynamics and differentiate it with respect to the time:

$$\frac{dQ}{dt} = \frac{dE}{dt} + P \frac{dV}{dt}. \quad (3.82)$$

If we assume an ideal gas, we have $E = 3/2Nk_B T$ as well as with $PV = Nk_B T$. Taking everything together, we find

$$\boxed{\frac{dQ}{dt} = \frac{3}{2}Nk_B \frac{dT}{dt} - k_B T \frac{dn}{dt} \equiv \Gamma - \Lambda,} \quad (3.83)$$

where Γ and Λ are the heating and cooling rates, respectively. In a steady state, we have $dQ/dt = 0$ and thus $\Gamma = \Lambda$, which defines an equilibrium temperature T_E . In addition, the cooling rate can also be written as

$$\Lambda = A_{21}n_2E_{21}, \quad (3.84)$$

where A_{21} is again the Einstein coefficient for spontaneous decay, n_2 the number of atoms in the higher level and E_{21} the net energy that is radiated away.

However, what are the dominant heating sources in the ISM? We can identify the following effects together with an order of magnitude estimate (without derivation; further details are given in the books listed at the beginning of this chapter):

- Cosmic ray heating: $\Gamma_{CR} \approx 3.8 \times 10^{-29} n_H \text{ erg s}^{-1} \text{ cm}^{-3}$
- Photoelectric heating: $\Gamma_{PE} \approx 1.8 \times 10^{-25} n_H \text{ erg s}^{-1} \text{ cm}^{-3}$
- Heating by H₂ formation: $\Gamma_{H_2} \approx 2.0 \times 10^{-29} n_H^2 \text{ erg s}^{-1} \text{ cm}^{-3}$
- Photoionization heating: $\Gamma_{PI} \approx 8.0 \times 10^{-25} n_H^2 \text{ erg s}^{-1} \text{ cm}^{-3}$

In these equations, n_H is the particle number density of atomic hydrogen. Comparing these processes, we see that both photoelectric heating and heating by photoionization by far have the biggest influence on the thermodynamics of the cold ISM.

What about possible sources for ISM cooling? We can again identify the following and most important processes:

- Cooling by collisional excitation and subsequent emission of a photon
- Cooling by free-free emission of electrons
- Cooling by collisions between gas and dust grains

3.12 Theoretical background of fine structure lines

In this thesis, we also analyze the fine structure line emission of particles. That is why we want to take a brief view at the physics of fine structure lines in this section, although we caution the reader that the following treatment is far from being complete. Detailed analysis of fine structure line emission processes can be found in any standard textbook about quantum theory (see, e.g. Fliessbach, 2005;

Dirac, 2010; Weinberg, 2015; Nolting, 2015). In this section, we only want to present a rough first order estimate for this process.

In a naive classical approach, the negative electron moves around the positive nucleus and thus sees an electromagnetic field \mathbf{E}' and \mathbf{B}' , for which we have obtained from electrodynamics and a Lorentz transformation the relativistic expression

$$\mathbf{B}' = \gamma \left[\mathbf{B} - \frac{1}{c} (\boldsymbol{\beta} \times \mathbf{E}) \right], \quad (3.85)$$

where the unprimed quantities denote fields in the restframe of the nucleus. If we focus on the non-relativistic case, we have

$$\mathbf{B}' = -\frac{1}{c^2} (\mathbf{v} \times \mathbf{E}). \quad (3.86)$$

We consider now the magnetic moment $\boldsymbol{\mu}_s$ induced by the spin of the electron. According to the Dirac theory, this can be written as

$$\boldsymbol{\mu}_s = g_e \mu_B \frac{\mathbf{S}}{\hbar}, \quad (3.87)$$

where g_e is the Landré factor, μ_B the Bohr magneton and \mathbf{S} the spin vector. If we approximate $g_e \approx 2$, we can expand the Hamiltonian of the system, which then reads

$$H_{\text{cl}} = -\boldsymbol{\mu}_s \cdot \mathbf{B}' = 2 \frac{\mu_B}{\hbar c^2} (\mathbf{E} \times \mathbf{v}) \cdot \mathbf{S}. \quad (3.88)$$

We can then express the electric field according to the Coulomb potential and use

$$\mathbf{E} = -\frac{1}{r} \frac{d\phi}{dr} \mathbf{r} \quad (3.89)$$

with the electric potential ϕ . We then end up with the Hamiltonian

$$H_{\text{cl}} = -\frac{e}{m_e^2 c^2} \left(\frac{1}{r} \frac{d\phi}{dr} \right) (\mathbf{L} \cdot \mathbf{S}), \quad (3.90)$$

where we have defined the angular momentum $\mathbf{L} = m_e \mathbf{r} \times \mathbf{v}$. Although this equation is not entirely exact, it gives us an idea about the underlying physics of fine structure lines. The above equation tells us, that the spin couples to the angular momentum of the electron (also called spin-orbit coupling). Furthermore, quantum mechanics tells us that

$$\mathbf{L} \cdot \mathbf{S} = \frac{1}{2} (\mathbf{J}^2 - \mathbf{L}^2 - \mathbf{S}^2), \quad (3.91)$$

where \mathbf{J} is the total angular momentum. Depending on the corresponding quantum numbers j , l and s , we find that emission lines can be split up and contribute different energy terms in the Hamiltonian, which then lead to different lines in the individual spectra.

3.13 Measuring velocities with the Doppler shift

Since most velocities in the ISM are non-relativistic (of the order of several km/s), we restrict ourselves on a pure classical treatment of the so-called *Doppler shift*¹⁵. A relativistic treatment would require more complicated derivations, which are not necessary for our purposes.

Let us first assume that the emitter moves with velocity v_e away from the observer and radiates waves with wavelength λ_e . That means that the observed wavelength can be written as

$$\lambda_0 = \lambda_e + \Delta s = \lambda_e + v_e \cdot T_e = \lambda_e + \frac{v_e}{c} \lambda_e = \lambda_e \left(1 + \frac{v_e}{c} \right). \quad (3.92)$$

Thereby, we have made use of the well-known relation $c = \lambda\nu$ as well as $T = 1/\nu$, the number of events per unit time. This equation allows us to compute the velocity of the emitter v_e if we know the rest wavelength of the emitter λ_e (which can be measured in any laboratory) and observe the wavelength λ_0 . From this we obtain the corresponding frequencies

$$\nu_0 = \frac{\nu_e}{1 + v_e/c}. \quad (3.93)$$

In the same way we can derive the frequencies if the observer is moving and the emitter is at rest. With the same arguments from above we then find (without a detailed derivation)

$$\nu_0 = \nu_e \left(1 + \frac{v_e}{c} \right). \quad (3.94)$$

We also give the formula that we obtain if we assume that *both* observer and emitter move with their *relative* velocity v , which is the more realistic case in astronomy (since the earth is also moving around the sun):

$$\nu_0 = \frac{\nu_e}{1 + v/c}. \quad (3.95)$$

We will use this formula later to compute the gas velocities v_{gas} for observed frequencies, which can be obtained by solving the above equation:

$$\boxed{v_{\text{gas}} = c \left(\frac{\nu_e}{\nu_0} - 1 \right)}. \quad (3.96)$$

The Doppler shift provides a very simple possibility to measure velocities in the universe. It is a widely used method which allows us to deduce the motion of e.g. interstellar gas by simply observing the wavelength of an emitter. A common tracer

¹⁵Christian Doppler, Austrian physicist, 29/11/1803 - 17/03/1853

that is used by observers is the $J = 1 - 0$ line emission of ^{12}CO , which has a rest frequency of $\nu_{\text{CO}} \approx 110.201354$ GHz. Another tracer commonly used is ^{13}CO with a rest frequency of $\nu_{\text{CO}} \approx 115.271201$ GHz¹⁶. A sensitive detector can measure small variations from this wavelength caused by the own velocity from which v_{gas} can be computed with the help of Eq. (3.96). This provides a very powerful method to gain information about velocities from objects far away from the earth. It is used in many fields in astronomy, e.g. in cosmology as well as in solar astrophysics.

¹⁶Detailed information about the line properties of a large number of common astrophysical tracers such as CO, CS, HCN, and so on is presented in the Leiden Atomic and Molecular Database database (LAMBDA), which can be found under: <http://home.strw.leidenuniv.nl/~moldata/>.

Turbulence theory

In the following sections, we will introduce some basic concepts of turbulence theory. However, the whole field of turbulence itself is by far too large that we could treat all different kinds of interesting phenomena in this thesis. However, the aim is to provide an idea of the basic processes that are relevant to understand most parts of this work. The concepts in this chapter can all be found in standard textbooks of fluid dynamics or turbulence, such as e.g. by Frisch & Kolmogorov (1995), Pope (2000) or Choudhuri (1998).

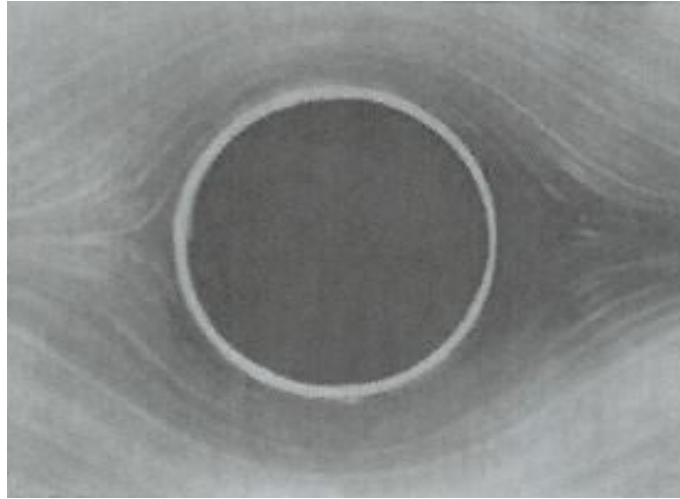
We start and motivate the problem of turbulence (Section 4.1) and then consider some symmetry aspects (Section 4.2). We then motivate the assumption of Kolmogorov of energy cascades in a viscous fluid (Section 4.3) and briefly introduce the ergodic theorem (Section 4.4). Afterwards, we present Kolmogorov's axioms of incompressible turbulence and introduce the concepts of structure functions (Sections 4.5 and 4.6). We then move on and discuss the phenomenology of Kolmogorov and Burgers turbulence (Section 4.7 and 4.8). It follows a detailed discussion of the She & Levèque as well as of the Dubruelle and Boldyrev models (Section 4.9 and 4.10). Finally, we discuss effects of intermittency and the β -model (Section 4.11 and 4.12).

4.1 Motivation of turbulence theory

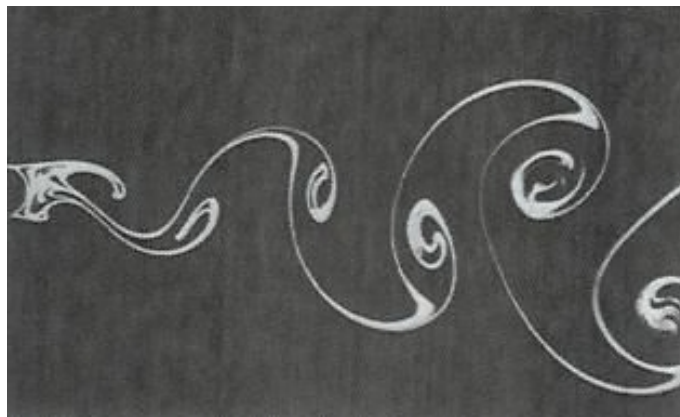
The whole problem and complexity of turbulent phenomena is probably encoded in the Navier-Stokes equation (2.42), which reads

$$\rho \frac{\partial \mathbf{v}}{\partial t} + \rho(\mathbf{v} \cdot \nabla)\mathbf{v} = -\nabla P - \rho \nabla \Phi + \eta \nabla^2 \mathbf{v} + \left(\frac{\eta}{3} + \zeta \right) \nabla(\nabla \mathbf{v}). \quad (4.1)$$

Here, \mathbf{F} describes some external force terms (e.g. gravitational or other external forces). We basically find two terms, which are of particular interest: the advection term $(\mathbf{v} \cdot \nabla)\mathbf{v}$ as well as the viscosity term $\nabla^2 \mathbf{v}$ on the right hand side of Eq. (4.1).

**Figure 4.1:**

Flow past a cylinder with Reynolds number $\mathcal{R} = 0.16$ (taken from Frisch & Kolmogorov, 1995). We observe a left-right and up-down symmetry as well a space- and time-translation symmetry parallel to the axis of the cylinder.

**Figure 4.2:**

Flow past a cylinder with Reynolds number $\mathcal{R} = 140$ (taken from Frisch & Kolmogorov, 1995). The symmetries from Fig. 4.1 are broken now.

**Figure 4.3:**

Flow past two cylinders with Reynolds number $\mathcal{R} = 1800$ (taken from Frisch & Kolmogorov, 1995). At the right side, the symmetries are restored in a statistical sense.

Thereby, we realize that the advection term is the only non-linear term in the Navier-Stokes equation and responsible for all complexity of the turbulence theory. In Section 2.2.9 we have analyzed these terms and introduced a dimensionless quantity, the Reynolds number \mathcal{R} . This number can also be understood as a control parameter to regulate the turbulent flow in an experiment. In particular, we have shown that for given boundaries, \mathcal{R} is *the only* parameter of the viscous fluid that can control the flow.

In order to understand the meaning of this parameter, we want to take a look at different situations where we continuously increase \mathcal{R} . Fig. 4.1 shows a uniform flow with velocity v parallel to the x-axis (from left to right) with $\mathcal{R} = 0.16$. Such a flow with $\mathcal{R} < 1$ is called a *laminar flow*. We directly observe the following symmetries: a left-right and up-down symmetry as well as a space- and time-translation symmetry parallel to the axis of the cylinder. All these symmetries are consistent with the Navier-Stokes equation, as we will see in the next section. However, a closer look at Fig. 4.2 shows that the left-right symmetry is slight broken, which is due to the non-linear advection term. We could get rid of this effect if we would further decrease \mathcal{R} .

If we now increase the Reynolds number to a value of $\mathcal{R} = 140$, we observe the situation given in Fig. 4.2. Clearly, the symmetries shown in Fig. 4.1 are broken now. However, it is still unclear at which exact Reynolds number each symmetry is said to be broken. Going to an even higher value of $\mathcal{R} = 1800$, Fig. 4.3 shows an interesting behavior. Now, we observe some statistical symmetries far at the right-hand side. This suggests that at very high Reynolds numbers, $\mathcal{R} \gg 1$, there is a tendency to restore the symmetries in a *statistical sense*. If this is the case, we will refer the turbulence to be *fully developed*. In the next sections, we will only deal with fully developed turbulence.

4.2 Symmetry groups of turbulence theory

Before we consider different theories of turbulence, we start with a short overview of important symmetries of the theory. In this context, a symmetry describes a (statistical) property of the system that does not change under a specific (coordinate) transformation. Symmetries are important in theoretical physics, because each of them imply the conservation of a physical quantity (e.g. energy, momentum, and others), as shown in a remarkable study by Emmy Noether¹. We can distinguish between continuous (e.g. time and spatial translations) and discrete symmetries (e.g. CPT² symmetries), which can be described by means of a corresponding symmetry group. Thus, we can define an invariance group \mathbf{G} of an equation. A specific element $g_{\text{sym}} \in \mathbf{G}$ is said to be a symmetry, if the equation does not change under g_{sym} . For the Navier-Stokes equation we can identify the following symmetries:

¹Emmy Noether, German mathematician, 23/03/1882 - 14/04/1935

²Charge, Parity and Time symmetries are highly important in particle physics, in particular in studies of the weak interaction.

- *Space translations* $g_\rho : (t, \mathbf{r}, \mathbf{v}) \mapsto (t, \mathbf{r} + \rho, \mathbf{v}), \rho \in \mathbb{R}^3$
- *Time translations* $g_\tau : (t, \mathbf{r}, \mathbf{v}) \mapsto (t + \tau, \mathbf{r}, \mathbf{v}), \tau \in \mathbb{R}$
- *Galilean transformations* $g_U : (t, \mathbf{r}, \mathbf{v}) \mapsto (t, \mathbf{r} + \mathbf{U}t, \mathbf{v} + \mathbf{U}), \mathbf{U} \in \mathbb{R}^3$
- *Parity* $g_P : (t, \mathbf{r}, \mathbf{v}) \mapsto (t, -\mathbf{r}, -\mathbf{v})$
- *Rotations* $g_A : (t, \mathbf{r}, \mathbf{v}) \mapsto (t, A\mathbf{r}, A\mathbf{v}), A \in \text{SO}(\mathbb{R}, 3)$
- *Scalings* $g_\lambda : (t, \mathbf{r}, \mathbf{v}) \mapsto (\lambda^{1-h}t, \lambda\mathbf{r}, \lambda^h\mathbf{v}), \lambda \in \mathbb{R}_+, h \in \mathbb{R}$

The last transformation is of particular interest: If we scale the Navier-Stokes equation according to the transformation rules given, all terms are scaled by a factor of λ^{2h-1} , except the viscosity term, which is scaled with λ^{h-2} . Hence, for a finite viscosity, only $h = -1$ is permitted. This parameter reflects the *similarity principle* and justifies our choice of the Reynolds number in Eq. (2.43).

4.3 Energy cascades in an ideal fluid

We now want to study the energy contribution of the Navier-Stokes equation of a viscous fluid by explicitly evaluating energy flows through various scales. To do that, let us define so-called *high-pass* and *low-pass* filter functions of any arbitrary function f :

$$f_K^<(\mathbf{r}) = \sum_{k \leq K} \hat{f}_{\mathbf{k}} e^{i\mathbf{k}\mathbf{r}}, \quad f_K^>(\mathbf{r}) = \sum_{k > K} \hat{f}_{\mathbf{k}} e^{i\mathbf{k}\mathbf{r}} \quad (4.2)$$

Here, k is the wavenumber and $\hat{f}_{\mathbf{k}}$ is the Fourier transform of an arbitrary function $f_{\mathbf{k}}$. The length $\ell \propto K^{-1}$ is the length scale of the filtering process.

Let us now use the idea of pass-filtering and write the flow velocity $\mathbf{v} = \mathbf{v}_K^< + \mathbf{v}_K^>$ in terms of the filter functions. We now introduce a low-pass filtering operator P_K ,

$$P_K : f(\mathbf{r}) \mapsto f_K^<(\mathbf{r}), \quad (4.3)$$

which simply sets all Fourier modes with wavenumbers greater than K to zero. It can be shown that this operator is also idempotent, that means $P_K^2 = P_K$.

In a next step, we take Eq. (4.1), substitute \mathbf{v} according to the pass-filtering defined above and apply the operator (4.3) to the equation:

$$\frac{\partial \mathbf{v}_K^<}{\partial t} + P_K(\mathbf{v}_K^< + \mathbf{v}_K^>) \cdot \nabla(\mathbf{v}_K^< + \mathbf{v}_K^>) = \mathbf{F}_K^< + \nu \nabla^2 \mathbf{v}_K^<. \quad (4.4)$$

Then, we multiply this equation with $\mathbf{v}_K^<$, take the average and use the incompressibility condition³, which reads $\nabla \cdot \mathbf{v}_K^< = 0$. We then get

$$\frac{\partial}{\partial t} \left\langle \frac{\mathbf{v}_K^<^2}{2} \right\rangle + \langle \mathbf{v}_K^< \cdot [(\mathbf{v}_K^< + \mathbf{v}_K^>) \cdot \nabla(\mathbf{v}_K^< + \mathbf{v}_K^>)] \rangle = \langle \mathbf{v}_K^< \cdot \mathbf{F}_K^< \rangle + \nu \langle \mathbf{v}_K^< \cdot \nabla^2 \mathbf{v}_K^< \rangle. \quad (4.5)$$

³For an incompressible fluid we have $\nabla \mathbf{v} = 0$, while for a compressible fluid it is $\nabla \mathbf{v} \neq 0$.

This equation can be further simplified by realizing that the two terms which come from the second term on the left-hand side vanish identically:

$$\langle \mathbf{v}_K^< \cdot (\mathbf{v}_K^< \cdot \nabla \mathbf{v}_K^<) \rangle = \langle \mathbf{v}_K^< \cdot (\mathbf{v}_K^> \cdot \nabla \mathbf{v}_K^<) \rangle = 0. \quad (4.6)$$

We now define the following quantities:

$$\mathcal{E}_K = \frac{1}{2} \langle \mathbf{v}_K^<{}^2 \rangle, \quad (4.7)$$

$$\mathcal{F}_K = \langle \mathbf{v}_K^< \cdot \mathbf{F}_K^< \rangle, \quad (4.8)$$

$$\Omega_K = \frac{1}{2} \langle \omega_K^<{}^2 \rangle = -\frac{1}{2} \langle \mathbf{v}_K^< \cdot \nabla^2 \mathbf{v}_K^< \rangle, \quad (4.9)$$

$$\Pi_K = \langle \mathbf{v}_K^< \cdot (\mathbf{v}_K^< \cdot \nabla \mathbf{v}_K^>) \rangle + \langle \mathbf{v}_K^< \cdot (\mathbf{v}_K^> \cdot \nabla \mathbf{v}_K^>) \rangle. \quad (4.10)$$

The first is the cumulative energy, the second the cumulative injection due to an external force, the third cumulative enstrophy and the fourth the energy flux through wavenumber K . Taking everything together, we arrive at the final remarkable equation:

$$\boxed{\frac{\partial}{\partial t} \mathcal{E}_K = \mathcal{F}_K - 2\nu\Omega_K - \Pi_K.} \quad (4.11)$$

This equation says that the rate of change of energy \mathcal{E}_K at scales $\ell \propto K^{-1}$ is equal to the injected energy \mathcal{F}_K minus the dissipated energy at those scales, $2\nu\Omega_K$, minus the energy flux Π_K to smaller scales due to advection. This equation confirms the central assumption of Kolmogorov of a hierarchical energy cascade in the turbulent flow from larger to smaller scales, which we will discuss in the next sections.

4.4 A statistical view at the ergodic theorem

In this section we will briefly highlight one important law that we will use in this thesis to derive properties of the turbulent flow. It is the *ergodic theorem* and reads

$$\boxed{\lim_{T \rightarrow \infty} \frac{1}{T} \int_0^{\infty} f(t, \omega) dt = \langle f \rangle,} \quad (4.12)$$

where $f(t, \omega)$ denotes a stationary random function with t and ω being the time and the frequency, respectively. The proof was given by Birkhoff (1927)⁴. It says that we can measure statistical moments in practise either by measuring an infinite amount of time or equivalently, by computing ensemble averages. This allows us to replace *time-averages* by *ensemble-averages*. We will intensively make use of this result in the following chapters.

⁴George David Birkhoff, American mathematician, 21/03/1884 - 12/11/1944

4.5 Kolmogorov axioms of incompressible turbulence

Unfortunately, there is no full theory at the moment, which starts from the Navier-Stokes equation and ends at the same results reported by Kolmogorov (1941)⁵. However, Kolmogorov (1941) found a statistical derivation to describe *incompressible and subsonic turbulence*. However, most of the astrophysical phenomena are of compressible nature and so we expect the Kolmogorov theory to be only a crude approximation for our purposes.

Kolmogorov's axioms are the following (taken from Frisch & Kolmogorov (1995)):

1. **Isotropy:** In the limit of very high Reynolds numbers, all possible symmetries of the Navier-Stokes equation are restored in a statistical sense at small scales far away from any boundaries. The fluid therefore becomes more and more isotropic at small scales.
2. **Self-Similarity:** Under the axiom of 1., the turbulent flow is self-similar at small scales. The flow is scale-invariant with a unique scaling exponent.
3. **Universality assumption:** Under the axiom of 1., the turbulent flow has a finite mean energy rate of dissipation per unit mass ϵ . All the small-scale statistical properties are uniquely and universally determined by the spatial scale ℓ and the velocity scale v .

In order to analyze these axioms, we first define the velocity increment

$$\delta\mathbf{v}(\mathbf{r}, \ell) \equiv \mathbf{v}(\mathbf{r} + \ell) - \mathbf{v}(\mathbf{r}), \quad (4.13)$$

which is simply a measure for the differences in velocity space at two points separated by the vector ℓ . *Homogeneity* now requires

$$\delta\mathbf{v}(\mathbf{r} + \Delta\mathbf{r}, \ell) \stackrel{!}{=} \delta\mathbf{v}(\mathbf{r}, \ell). \quad (4.14)$$

This holds for all displacements $\Delta\mathbf{r}$ and all increments ℓ . *Isotropy* means that the statistical properties do not vary under rotations of ℓ and $\delta\mathbf{v}$.

Self-similarity means that the velocity field is a homogeneous function of degree h in the increment ℓ . This reads

$$\delta\mathbf{v}(\mathbf{r}, \lambda\ell) = \lambda^h \delta\mathbf{v}(\mathbf{r}, \ell) \quad (4.15)$$

As we will find out later, $h = 1/3$ will be determined by the energy dissipation law.

Universality means that the energy cascade will be completely defined by means of the wavenumber k and the mean energy rate of dissipation per unit mass ϵ .

⁵Andrey Nikolaevich Kolmogorov, Soviet mathematician, 25/04/1903 - 20/10/1987

4.6 Introduction to structure functions

How can we define statistical moments of a velocity field? To answer this question, we define a so-called *structure function* of p -th order:

$$S_p(\ell) \equiv \langle |\delta\mathbf{v}(\mathbf{r}, \ell)|^p \rangle = \langle |\delta\mathbf{v}(\mathbf{r} + \ell) - \delta\mathbf{v}(\mathbf{r})|^p \rangle, \quad (4.16)$$

where p is an integer number. This equation defines an arbitrary statistical moment. We can also express it in terms of a PDF $P_\ell(\delta\mathbf{v}(\ell))$, which describes the distribution of velocity increments,

$$S_p(\ell) \equiv \langle |\delta\mathbf{v}(\mathbf{r}, \ell)|^p \rangle = \int |\delta\mathbf{v}(\mathbf{r}, \ell)|^p P_\ell(\delta\mathbf{v}(\ell)) d(\delta\mathbf{v}(\ell)). \quad (4.17)$$

Moreover, we can also split the structure function up into a longitudinal,

$$S_{\parallel}^p(\ell) \equiv \langle |\delta\mathbf{v}_{\parallel}(\mathbf{r})|^p \rangle = \left\langle \left| [\mathbf{v}(\mathbf{r} + \ell) - \mathbf{v}(\mathbf{r})] \frac{\boldsymbol{\ell}}{\ell} \right|^p \right\rangle, \quad (4.18)$$

and a transversal component,

$$S_{\perp}^p(\ell) \equiv \langle |\delta\mathbf{v}_{\perp}(\mathbf{r})|^p \rangle = \langle |\delta\mathbf{v}(\ell) - \delta\mathbf{v}_{\parallel}|^p \rangle, \quad (4.19)$$

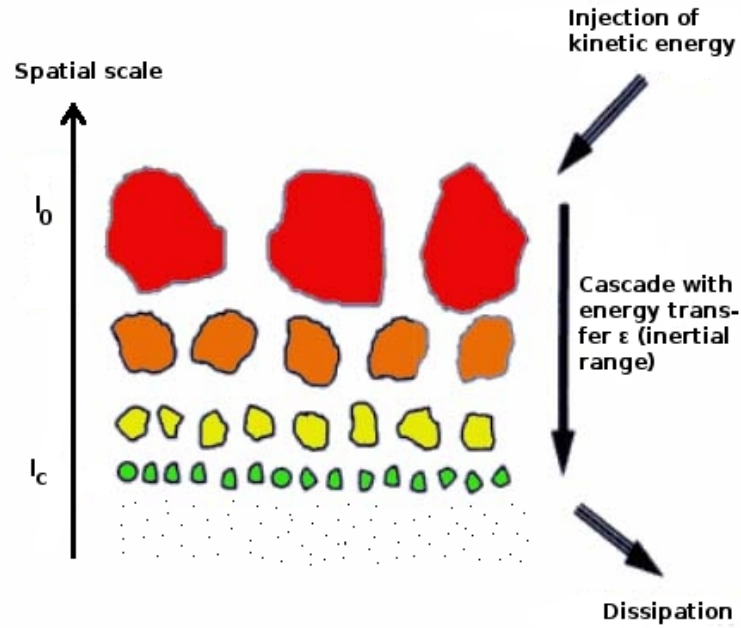
where we subtracted off the longitudinal part.

4.7 Phenomenology of the Kolmogorov theory

As described in the previous sections, Kolmogorov assumes a hierarchical energy cascade. The statistical properties are thereby completely defined through the wavenumber at a specific scale k and the mean energy dissipation rate ϵ . The idea is that eddies in the turbulent fluid dissipate from large to small scales, thereby transferring kinetic energy down the cascade. This is sketched in Fig. 4.4 and is called the *Richardson cascade*⁶. In this picture, kinetic energy is injected into the physical system at a scale ℓ_0 , called the *injection scale*. This is the scale at which we drive our simulations and the largest scale of turbulent eddies. The energy then cascades down with a constant mean energy rate of dissipation ϵ . The range in which this happens is called the *inertial range*. At the end, below a *dissipation scale* ℓ_c , the kinetic energy is dissipated into thermal heat. This is the scale at which the Reynolds number becomes unity, $\mathcal{R} \approx 1$, and where the stream is converted into a laminar flow.

In order to describe this picture quantitatively, we focus again on the central Kolmogorov axioms and try to express the mean energy dissipation rate ϵ as a

⁶Lewis Fry Richardson, British physicist, 11/10/1881 - 30/09/1953

**Figure 4.4:**

Phenomenological picture of Kolmogorov turbulence. The picture shows the *Richardson energy cascade*. Kinetic energy is injected into the system at a scale ℓ_0 , called the *injection scale*. It cascades with a constant mean energy rate of dissipation ϵ in the *inertial range* and is dissipated into thermal heat below a *dissipation scale* ℓ_c . The picture was taken from <http://cictr.ee.psu.edu> (07/12/2015) and was slightly modified.

function of scale and velocity. Thus, the mean energy dissipation rate $\langle \epsilon \rangle$ of kinetic energy in the inertial range, which scales as $e_{\text{kin}} \sim v^2$, must be constant and reads

$$\langle \epsilon \rangle = \frac{de_{\text{kin}}}{dt} \sim v \frac{dv}{dt} \sim \frac{v^2}{t} = \frac{v^3}{\ell} \equiv \text{const.}, \quad (4.20)$$

where we only focus on scaling relations here and leave any constant factors out. We have estimated the characteristic dissipation time to be of the order $t \sim \ell/v$. From that immediately follows

$$v \sim \ell^{1/3} \sim k^{-1/3}. \quad (4.21)$$

We can use this equation to compute a typical time-scale of the energy dissipation,

$$\tau = \frac{\ell}{v} \sim \ell^{2/3}. \quad (4.22)$$

Thus, we can conclude that

$$\boxed{v^p \propto \ell^{\zeta_p}}, \quad (4.23)$$

where ζ_p is an arbitrary function which describes how the velocity fluctuations change with varying spatial scale and p is again an integer number. This means that we can also set for the structure function $S_p(\ell) \propto \ell^{\zeta_p}$. For the Kolmogorov theory we explicitly find that

$$\boxed{\zeta_p = \frac{p}{3}}. \quad (4.24)$$

Moreover, Eq. (4.21) leads us to

$$v(\ell_c) = v_0 \left(\frac{\ell_c}{\ell_0} \right)^{1/3}, \quad (4.25)$$

from which we can directly estimate the Reynolds number at the dissipation scale,

$$\mathcal{R} = \frac{v(\ell_c)\ell_c}{\nu} = \frac{v_0\ell_c^{4/3}}{\ell_0^{1/3}\nu}, \quad (4.26)$$

which we assume to be $\mathcal{R} \approx 1$ (the transition to a laminar flow). We can then obtain the *Kolmogorov dissipation scale*,

$$\boxed{\ell_c = \left(\frac{\nu^3}{\langle \epsilon \rangle} \right)^{1/4}}. \quad (4.27)$$

If we know the viscosity ν as well as the mean energy dissipation rate ϵ of the fluid, we can get an estimate of the scale, where the kinetic energy dissipates into thermal energy. Furthermore, since ℓ_c does not explicitly depend on the spatial scale, the influence of the viscosity on the dissipation scale is large, because $\ell_c \propto \nu^{3/4}$.

In a similar fashion, we can also estimate the kinetic energy spectrum $E(k)$ of the Kolmogorov theory by deriving the energy with respect to the k mode,

$$\boxed{E(k) = \frac{de_{kin}}{dk} \sim k^{-5/3}}, \quad (4.28)$$

where we have used $e_{kin} \sim v^2 \sim k^{-2/3}$ from Eq. (4.21).

The only available physical quantity which we can use to construct an energy equation is the mean energy dissipation rate ϵ . That is why we can simply conclude by pure dimensional analysis that

$$E(k) = C\epsilon^{2/3}k^{-5/3}, \quad (4.29)$$

where C is a dimensionless constant. This is the famous *Kolmogorov energy spectrum*, that we will often use in this thesis. It says that that the energy cascade can be described by a simple power-law.

4.8 Burger's turbulence of a compressible fluid

The central assumption of Kolmogorov turbulence was, that flows are subsonic and incompressible. However, as we will see in the next chapters, this assumption usually does not hold. In many astrophysical problems, flows are supersonic and compressible, such as in the following studies. Is there a better way to describe this problem?

The answer was given in a study by Burgers (1948), shortly after Kolmogorov published his results. In his study, Burgers (1948) assumed a constant momentum cascade, $p \sim v$, instead of a constant energy dissipation rate. We can do the same steps as in the theory of Kolmogorov and write

$$\frac{dp}{dt} \sim \frac{dv}{dt} \sim \frac{v^2}{l} \equiv \text{const.}, \quad (4.30)$$

which directly implies that

$$v \sim \ell^{1/2} \sim k^{-1/2}, \quad (4.31)$$

that is a steeper decline of the velocity in Fourier space. This can be also translated into an energy spectrum, which reads

$$\boxed{E(k) = \frac{de_{kin}}{dk} \sim k^{-6/3}}, \quad (4.32)$$

where we have used $e_{kin} \sim v^2 \sim k^{-1}$. We see that the kinetic energy spectrum also shows a steeper decline in Fourier space with wavenumber k .

4.9 Correction to the Kolmogorov theory: the She-Levèque model

So far, the Kolmogorov theory suffers from a big problem: the relation (4.24) does not seem to agree with experimental studies (see, e.g. Benzi et al., 1993) with $p > 3$. That means that the slopes of the higher order structure functions significantly deviate from the theoretical prediction, as one can clearly see in Fig. 4.5. To account for this, She & Leveque (1994) found a theoretical description, which much better explains the slopes for higher order structure functions. The discrepancy comes from an effect that is called *intermittency* (see also the next sections), which describes a deviation from the log-normal velocity increment distribution, which enters even stronger for large p (see, e.g. Batchelor & Townsend, 1949; Anselmet et al., 1984). The aim is now to find a correction term, which accounts for this effect. Hence, we might expand formula (4.24) by a correction term $\tau_{p/3}$:

$$\zeta_p = \frac{p}{3} + \tau_{p/3}. \quad (4.33)$$

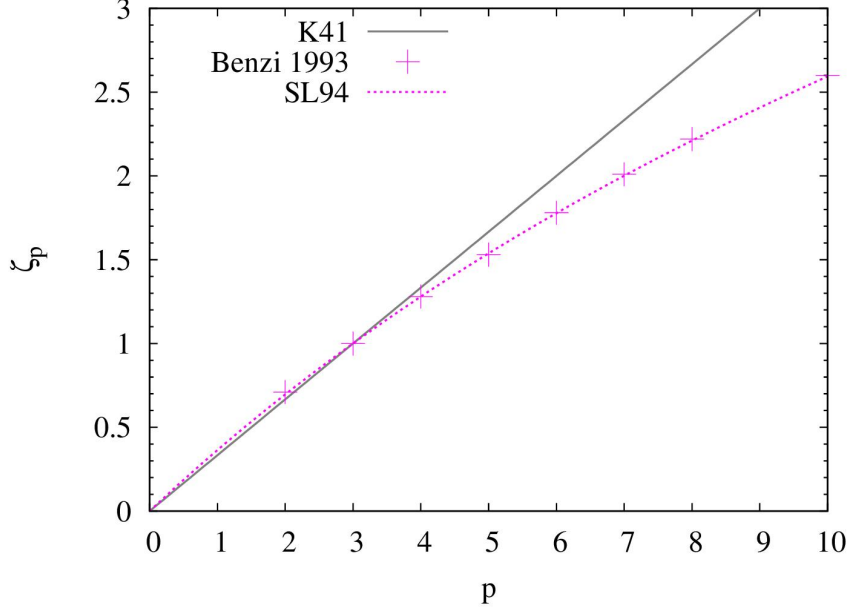


Figure 4.5:

Theoretical prediction of the function ζ_p from the Kolmogorov theory (K41) and the She-Levêque model (SL94). In addition, we show experimental results by Benzi et al. (1993). As one can see, the SL94 model describes the experimental data much better for higher order p as the K41 theory.

We then start with introducing a hierarchy of fluctuation structures, $\epsilon_\ell^{(p)}$, defined by the ratio of successive dissipation moments:

$$\epsilon_\ell^{(p)} \equiv \frac{\langle \epsilon_\ell^{p+1} \rangle}{\langle \epsilon_\ell^p \rangle}. \quad (4.34)$$

What is the exact value of ϵ_ℓ^∞ ? Dimensionally, we can estimate it as the ratio of energy and time, $\epsilon_\ell^\infty \sim \delta E^\infty / t_\ell$. Since we know that the time scales as $t_\ell \sim \ell^{2/3}$, we find that

$$\epsilon_\ell^\infty \sim \ell^{-2/3}. \quad (4.35)$$

In the limit of very high orders, $p \rightarrow \infty$, we see from Eq. (4.34) and (4.35) that

$$\tau_{p+1} - \tau_p \rightarrow -\frac{2}{3} \quad (4.36)$$

holds, or we identify the equal asymptotic law expression

$$\tau_p \rightarrow -\frac{2}{3}p + C, \quad (4.37)$$

where C is a constant that still needs to be determined. Without a proof, we guess that C could be the co-dimension of the high-intensity filaments, which results in

$C = 2$. A more detailed explanation for this choice can be found in She & Leveque (1994). Thus, we end up with

$$\tau_p = -\frac{2}{3}p + 2 + \mathcal{O}(p), \quad (4.38)$$

where $f(p) = \mathcal{O}(p)$ is a higher order contribution coming from p .

Furthermore, She & Leveque (1994) propose that each hierarchical scaling element $\epsilon_\ell^{(p+1)}$ can be described by a universal relation involving $\epsilon_\ell^{(p)}$ and $\epsilon_\ell^{(\infty)}$:

$$\epsilon_\ell^{(p+1)} = A_p (\epsilon_\ell^{(p)})^\beta (\epsilon_\ell^{(\infty)})^{1-\beta}. \quad (4.39)$$

In this equation, β is a constant with $0 < \beta < 1$, as well as A_p . Plugging this equation into Eq. (4.34), we obtain the following relation:

$$\tau_{p+2} - (1 - \beta)\tau_{p+1} + \beta\tau_p + \frac{2}{3}(1 - \beta) = 0. \quad (4.40)$$

Using Eq. (4.38), we obtain a second order differential equation for the higher order contributions $f(p)$:

$$f(p+2) - (1 + \beta)f(p+1) + \beta f(p) = 0. \quad (4.41)$$

The only nontrivial solution to this equation is provided by the ansatz $f(p) = \alpha\beta^p$, where τ_p must satisfy the boundary conditions $\tau_0 = 0$ and $\tau_1 = 0$. This fixes α and β and we find $\alpha = -2$ and $\beta = 2/3$. Hence, the final expression for our correction τ_p is then

$$\tau_p = -\frac{2}{3}p + 2 \left[1 - \left(\frac{2}{3} \right)^p \right] \quad (4.42)$$

and with Eq. (4.33) we arrive at an expression for the scaling exponents

$$\zeta_p = \frac{p}{9} + 2 \left[1 - \left(\frac{2}{3} \right)^{p/3} \right]. \quad (4.43)$$

This function is also shown in Fig. 4.5, together with experimental results from Benzi et al. (1993). As one can see, the modified model describes the experimental data much better for higher order p as the Kolmogorov theory.

Furthermore, we can now derive the correction of the Kolmogorov theory from this equation. Evaluating ζ_2 , we find

$$E(k) \sim k^{-29/9 + 2(2/3)^{2/3}} \approx k^{-5/3 - 0.03}. \quad (4.44)$$

Thus, we see that the correction $\Delta\zeta_2 = 0.03$ to the energy spectrum is rather small, but becomes more and more important for larger values of p .

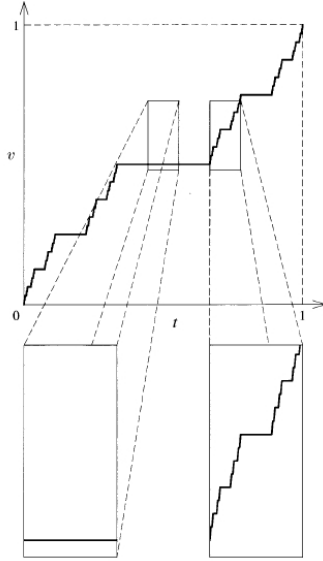


Figure 4.6:

The Cantor function is a prominent example for an intermittent function (taken from Frisch & Kolmogorov, 1995). We see that the self-similarity is clearly broken in some parts of the function. This is a strong indicator of intermittent behavior.

4.10 The Dubrulle and Boldyrev model

In the derivation of the She & Leveque (1994) model, we have made the assumption that the co-dimension of the filaments is $C = 2$. However, depending on the properties of the turbulent structures, this might not always be true. To account for this fact, Dubrulle (1994) and Boldyrev et al. (2002) generalized Eq. (4.43) and found

$$\zeta_p = \Theta(1 - \Delta)p + C(1 - \Sigma^{\Theta p}), \quad (4.45)$$

where $\Sigma = 1 - \Theta/C$. The other parameters Θ and Δ enter the theory through the so-called Kolmogorov refined similarity hypothesis, relating the scaling of fluctuations of the velocity field to the scaling of the fluctuating energy dissipation. This equation has much more free parameters than Eq. (4.43) and may better describe supersonic turbulent motions in different fields of application.

4.11 Deviation from log-normal: effects of intermittency

The central motivation for constructing the She & Leveque (1994) model was the fact that slopes of the higher order structure functions show deviations due to intermittent effects, which are often referred to deviations from a log-normal velocity increment distribution (see, e.g. Batchelor & Townsend, 1949; Anselmet et al.,

1984). In Fig. 4.6, we present a typical example for such an intermittent function, the *Cantor function*⁷. We observe that the function strongly depends on the scale and deviates at different positions. Another way to understand intermittency is the following example. Turbulent structures (e.g. in molecular clouds) are self-similar on a large range of spatial scales, as we have discussed in chapter 1. However, let us imagine that some process breaks this self-similarity in a cloud. If this is the case, we refer this effect to intermittency.

Is there a way how we could characterize these deviations? The answer is yes, if we analyze the wings of the PDF, which should show the strongest deviations. Therefore, we again study the high-pass filter function $\mathbf{v}_k^>(t)$, which we have introduced in Section 4.3. We can say that a velocity function $\mathbf{v}(t)$ is intermittent at small scales, if the fourth statistical moment, which is called the *flatness*,

$$F(k) = \frac{\langle (\mathbf{v}_k^>(t))^4 \rangle}{\langle (\mathbf{v}_k^>(t))^2 \rangle^2}, \quad (4.46)$$

grows with growing wavenumber k . This gives us a direct observable to analyze intermittent effects, because it characterizes deviations from a log-normal velocity distribution. Observationally, however, the problem is that the impact of even tiny variations in the PDF wings induce large variations in $F(k)$. Hence, there have been strong doubts in the past whether such intermittent structures exist, but today there are strong observational evidences for this effect (see, e.g. Frisch & Kolmogorov, 1995 and the references therein).

4.12 Another correction to the Kolmogorov theory: the β -model

Just for completeness, we will also present another model in this section, which accounts for intermittency effects. It is called the β -*model* and the name will shortly become clear. In the β -model we assume that Kolmogorov's theory does not hold for the whole fluid itself, but only for some subregions, depending on the spatial scale we are interested in. According to the Richardson energy cascade, this means that each turbulent eddy only occupies a fraction β of space, with $0 < \beta < 1$. If we assume that an eddy shrinks by a factor of r after each step, we would expect that after n steps the initial eddy of size ℓ_0 has the new size

$$\ell = r^n \ell_0. \quad (4.47)$$

Then, the fraction p_ℓ of space within a daughter-eddy goes as

$$p_\ell = \beta^n = \beta^{\ln(\ell/\ell_0)/\ln(r)} = \left(\frac{\ell}{\ell_0} \right)^{3-D}, \quad (4.48)$$

⁷Georg Cantor, German mathematician, 19/02/1845 - 06/01/1918

where we have defined D such that

$$C = 3 - D = \frac{\ln(\beta)}{\ln(r)}. \quad (4.49)$$

Here, D is the fractal dimension and C the co-dimension. We can then get an estimate for the energy

$$E_\ell \sim v_\ell^2 p_\ell = v_\ell^2 \left(\frac{\ell}{\ell_0} \right)^{3-D}, \quad (4.50)$$

because eddies of size ℓ only fill a fraction p_ℓ of the total volume. According to Kolmogorov's theory, we again assume that the energy flux is constant and reads $\Pi_\ell \sim E_\ell/t_\ell$. We then have

$$\Pi_\ell \sim \frac{v_\ell^3}{\ell} \left(\frac{\ell}{\ell_0} \right)^{3-D} \quad (4.51)$$

and in the inertial range

$$\Pi_{\ell_0} \sim \epsilon \sim \frac{v_0^3}{\ell_0}. \quad (4.52)$$

From Eq. (4.51) and (4.52) we find that

$$v_\ell \sim v_0 \left(\frac{\ell}{\ell_0} \right)^{\frac{1}{3} - \frac{3-D}{3}} \quad (4.53)$$

and the characteristic timescale

$$t_\ell \sim \frac{\ell}{v_\ell} \sim \frac{\ell_0}{v_0} \left(\frac{\ell}{\ell_0} \right)^{\frac{2}{3} - \frac{3-D}{3}}. \quad (4.54)$$

In the final step, we compute again the p -th order structure function and obtain

$$S_p(\ell) = \langle \delta v(\ell)^p \rangle \sim v_0^p \left(\frac{\ell}{\ell_0} \right)^{\zeta_p}, \quad (4.55)$$

assuming again that $S_p(\ell) \sim \ell^{\zeta_p}$ in the inertial range. From that we conclude that

$$\boxed{\zeta_p = \frac{p}{3} + (3 - D) \left(1 - \frac{p}{3} \right)} \quad (4.56)$$

and that the scaling exponent of the velocity field is

$$h = \frac{1}{3} - \frac{3 - D}{3}, \quad (4.57)$$

compared to the Kolmogorov theory, where we find $h = 1/3$. The kinetic energy spectrum then satisfies the relation

$$E(k) \propto k^{-5/3-(3-D)/3}. \quad (4.58)$$

For $p = 3$ we find $\zeta_3 = 1$, as required by the Kolmogorov theory, as well as if we assume $D = 3$.

Note, that the β -model does not reproduce experimental results as accurate as e.g. the She & Leveque (1994) model for larger p . However, it played an important role in the historical context and the development of turbulence theory.

Centroid Velocity Statistics of Molecular Clouds

In this study, we compute structure functions and Fourier spectra of 2D centroid velocity (CV) maps in order to study the turbulent gas dynamics of typical molecular clouds (MCs) in numerical simulations. We account for a simplified treatment of time-dependent chemistry and the non-isothermal nature of the gas and use a 3D radiative transfer tool to model the CO line emission in a post-processing step. We perform simulations using three different initial mean number densities of $n_0 = 30, 100$ and 300cm^{-3} to span a range of typical values for dense gas clouds in the solar neighbourhood. We compute slopes of the centroid velocity increment structure functions (CVISF) and of Fourier spectra for different chemical components: the total density, H_2 number density, ^{12}CO number density as well as the integrated intensity of ^{12}CO ($J = 1 \rightarrow 0$) and ^{13}CO ($J = 1 \rightarrow 0$). We show that optical depth effects can significantly affect the slopes derived for the CVISF, which also leads to different scaling properties for the Fourier spectra. The slopes of CVISF and Fourier spectra for H_2 are significantly steeper than those for the different CO tracers, independent of the density and the numerical resolution. This is due to the larger space-filling factor of H_2 as it is better able to self-shield in diffuse regions, leading to a larger fractal co-dimension compared to CO. The results presented in this chapter are published in Bertram et al. (2015a).

5.1 Introduction

Understanding the dynamics of molecular clouds (MCs) is an important task in astrophysics. It is still a great debate which physical processes regulate star formation. Beyond self-gravity, the radiation field, magnetic fields and a complex thermodynamic and chemical evolution, several studies in the past have shown that turbulent motions play an important role for controlling the star formation process (see, e.g.

Mac Low & Klessen, 2004; Scalo & Elmegreen, 2004; Elmegreen & Scalo, 2004; McKee & Ostriker, 2007; Hennebelle & Falgarone, 2012).

Characterising interstellar turbulence is therefore important for understanding star formation. During the last years large improvements were made in understanding turbulence theory. Kolmogorov (1941) proposed a constant mean energy dissipation rate within an inertial range and assumed that all statistical averaged quantities only depend on this rate, leading to the law of Kolmogorov for incompressible turbulence. This directly leads to the famous 5/3-law of the energy spectrum with a statistically quasi-equilibrium state. Nevertheless, many experimental and theoretical studies in the past decades have shown that the assumption of a constant mean energy dissipation rate is not accurate (Benzi et al., 1993; She & Leveque, 1994; Dubrulle, 1994; Frisch & Kolmogorov, 1995) and seems to deviate significantly from measurements for higher orders of the structure function. This discrepancy has been referred to as intermittency corrections to the Kolmogorov theory. A number of phenomenological models have been proposed since then to explain the differences. She & Leveque (1994) proposed an intermittent scaling for filamentary structures, in excellent agreement with tunnel-flow experimental data (Benzi et al., 1993) for incompressible turbulence. Boldyrev et al. (2002) expanded the work of She & Leveque (1994) for sheet-like shocks or a general fractal dimension of the dissipative structures for compressible turbulence. Later on, other studies developed models for a better understanding of turbulence involving magnetic fields (see, e.g. Goldreich & Sridhar, 1995; Cho et al., 2002).

Studying interstellar turbulence is difficult, since observations are always a complex convolution of the density and the velocity field, affected by many other astrophysical processes. Assessing the influence of projection effects relies on numerical simulations of turbulence that can be compared to observational measurements. In that sense, Lis et al. (1996) have shown that it is possible to use centroid velocity increments (CVI) in order to trace the most intense velocity structures of regions in the interstellar medium (ISM), which do not form stars and to analyse intermittency effects on the basis of the two-point statistics.

Recent studies have revealed in great detail that centroid velocities (CV) and their increments are sensitive to the turbulent driving, density fluctuations and temperatures along the line-of-sight (Lazarian & Esquivel, 2003; Ossenkopf et al., 2006; Esquivel et al., 2007; Hily-Blant et al., 2008; Federrath et al., 2010). Furthermore, the non-uniform chemical makeup of the gas and optical depth effects might also alter the CVI statistics (see, e.g. Burkhart et al. 2013b and Burkhart et al. 2014). Chemical effects may be important for an accurate determination of the velocity fluctuations, since the relation between H_2 as the main constituent of the ISM and CO as a tracer is not linear (see, e.g. Glover et al. 2010; Shetty et al. 2011a). Optical depth effects may as well affect projected structures due to different opacities of the gas tracers (see, e.g. Burkhart et al. 2013a,b, 2014 and Lazarian & Pogosyan 2004). Nevertheless, the question of how different physical processes affect the overall two-point statistics of the CVI remains elusive although much progress has been made during the last years.

In this paper we analyse high-resolution, three-dimensional chemistry models in numerical simulations of turbulent interstellar gas (Glover et al., 2010) to get a better insight into how the choice of chemical species as a tracer of gas affects the two-point statistics of the CV. Therefore we use time-dependent chemistry for modelling the formation and destruction of molecules in the ISM. We then perform radiative transfer calculations and convert our simulations into synthetic 2D CV maps. We focus in this paper on how chemistry and radiative transfer affect the CVI turbulence statistics and the Fourier spectra in different environments, while spanning a range of possible densities representative of MCs.

In Sec. 5.2 we present the simulations, the methods used to compute the CVI, the Fourier spectra and the radiative transfer post-processing. In Sec. 5.3 we present the results of our studies with different mean number densities. We discuss our results in Sec. 5.4 and present our conclusions in Sec. 5.5.

5.2 Methods and simulations

5.2.1 MHD and chemistry simulations

The simulations that we examine in this paper were performed using a modified version of the ZEUS-MP magnetohydrodynamical code (Norman, 2000; Hayes et al., 2006). We make use of a detailed atomic and molecular cooling function, described in detail in Glover et al. (2010) and Glover & Clark (2012), and a simplified treatment of the molecular chemistry of the gas. Our chemical treatment is based on the work of Nelson & Langer (1999) and Glover & Mac Low (2007), and allows us to follow the formation and destruction of H₂ and CO self-consistently within our simulations. Full details of the chemical model can be found in Glover & Clark (2012).

We consider a periodic volume, with side length 20 pc, filled with uniform density gas. We run simulations with three different initial densities, $n_0 = 30, 100$ and 300 cm^{-3} , where n_0 is the initial number density of hydrogen nuclei. The initial temperature of the gas is set to 60 K. We initialise the gas with a turbulent velocity field with uniform power between wavenumbers $k = 1$ and $k = 2$ (Mac Low et al., 1998a; Mac Low, 1999). The initial 3D rms velocity is $v_{\text{rms}} = 5 \text{ km s}^{-1}$, and the turbulence is driven so as to maintain v_{rms} at approximately the same value throughout the run. The gas is magnetised, with an initially uniform magnetic field strength $B_0 = 5.85 \mu\text{G}$, initially oriented parallel to the z -axis of the simulation. We neglect the effects of self-gravity. We assume that the gas has a uniform solar metallicity and adopt the same ratios of helium, carbon and oxygen to hydrogen as in Glover et al. (2010) and Glover & Mac Low (2011). At the start of the simulations, the hydrogen, helium and oxygen are in atomic form, while the carbon is assumed to be in singly ionised form, as C⁺. We also adopt the standard local value for the dust-to-gas ratio of 1:100 (Glover et al., 2010), and assume that the dust properties do not vary with the gas density. The cosmic ray ionisation rate was set to $\zeta = 10^{-17} \text{ s}^{-1}$, but we do not expect our results to be sensitive to this choice (Glover et al., 2010).

For the incident ultraviolet radiation field, we adopt the standard parameterisation of Draine (1978). More detailed information about the simulations that we examine in this paper can be found in Bertram et al. (2014). The runs analysed in this paper were all performed with a numerical resolution of 512^3 zones. We discuss the influence of our limited numerical resolution in more detail in Appendix A.1.

5.2.2 Radiative transfer

To model the CO ($J = 1 \rightarrow 0$) line in the MCs for both ^{12}CO and ^{13}CO we employ the radiative transfer code RADMC-3D¹ (Dullemond, 2012). We use the Large Velocity Gradient (LVG) approximation (Sobolev, 1957) to compute the level populations. The LVG implementation in RADMC-3D is described in Shetty et al. (2011a). For more information about the usage of RADMC-3D on our data we refer the reader to Bertram et al. (2014).

Our simulations do not explicitly track the abundance of ^{13}CO , and so we need a procedure to relate the ^{13}CO number density to that of ^{12}CO . A common assumption is that the ratio of ^{12}CO to ^{13}CO is identical to the elemental abundance ratio of ^{12}C to ^{13}C (see, e.g. Roman-Duval et al., 2010). In the majority of our analysis, we make the same assumption and set the ^{12}CO to ^{13}CO ratio to a constant value, $R_{12/13} = 50$.

However, strictly speaking, we expect the ^{12}CO to ^{13}CO ratio to faithfully reflect the elemental ^{12}C to ^{13}C ratio only in gas where essentially all of the carbon is incorporated into CO. When this is not the case (e.g. at low density and/or low extinction), the effects of chemical fractionation (Watson et al., 1976) and selective photodissociation of ^{13}CO (see, e.g. Visser et al., 2009a) can significantly alter the $^{12}\text{CO}/^{13}\text{CO}$ ratio (Röllig & Ossenkopf, 2013; Szűcs et al., 2014). To explore the effect that this may have on the statistical properties of the ^{13}CO line emission, we have produced a set of ^{13}CO emission maps, where we attempt to account for spatial variations in the $^{12}\text{CO}/^{13}\text{CO}$ ratio. To do this, we made use of the recent numerical results of Szűcs et al. (2014). They find that in turbulent molecular clouds, there is a tight relationship between the mean value of $R_{12/13}$ along a given line-of-sight and the ^{12}CO column density along the same line-of-sight, and give a simple polynomial fitting formula for $R_{12/13}$ as a function of the ^{12}CO column density. To produce our second set of ^{13}CO maps, we therefore first calculate the ^{12}CO column density along one axis of our datacubes, and then use these values to compute the mean value of $R_{12/13}$ for each line-of-sight using the Szűcs et al. (2014) fitting formula. Finally, we derive the number density of ^{13}CO in each cell along each line-of-sight by dividing the ^{12}CO number density by the mean value of $R_{12/13}$. These ^{13}CO number densities are then used to compute the ^{13}CO emission in the same fashion as in our constant ratio models. We note that although this procedure neglects any spatial variations in $R_{12/13}$ along a given line-of-sight, Szűcs et al. (2014) have shown that the resulting emission maps differ by only a few percent from those derived from a self-consistent

¹www.ita.uni-heidelberg.de/~dullemond/software/radmc-3d/

(but costly) chemical treatment. The differences in the CVI statistics of the two sets of ^{13}CO emission maps - those derived using a constant $R_{12/13}$ and those that use a spatially varying value of $R_{12/13}$ - will be discussed in Sec. 5.3.3 below.

Although RADMC-3D accounts for the dust continuum emission as well as the CO line emission, we make sure to subtract off the continuum term before analysing the statistical properties of the synthetic maps. For further information about the usage of RADMC-3D and the calculation of the dust continuum and the line emission we refer the reader to Dullemond (2012).

The radiative transfer calculation yields position-position-velocity (PPV) cubes of brightness temperatures T_B , which are used to compute centroid velocities. We will refer to these as the “intensity” models. In analogy, we construct centroid velocity maps out of the PPP simulation data of the density and velocity field, as described in Sec. 5.2.3. We will refer to these as the “density” models.

5.2.3 Centroid velocity increments

Our study is based on the two-point statistics of line centroid velocities. Following Lis et al. (1996), we analyse the centroid $C(x, y) = C(\mathbf{r})$ of line-of-sight projected velocities, defined as

$$C(\mathbf{r}) = \frac{\int F(\mathbf{r}, z)v_z(\mathbf{r}, z)dz}{\int F(\mathbf{r}, z)dz}, \quad (5.1)$$

where the variable $v_z(\mathbf{r}, z)$ is the line-of-sight velocity in the z -direction. The quantity $F(\mathbf{r}, z)$ is a statistical weight and denotes either the underlying density field or the brightness temperatures from the radiative transfer post-processing.

The centroid velocity increment δC_ℓ is defined as the separation between two points of the CV by spatial distances ℓ , i.e.

$$\delta C_\ell(\mathbf{r}) = C(\mathbf{r}) - C(\mathbf{r} + \boldsymbol{\ell}). \quad (5.2)$$

It thus connects centroid velocities of different regions in the plane.

There are many other techniques to measure velocity fluctuations as a function of spatial scale, e.g. the spectral correlation function (Rosolowsky et al., 1999), the velocity channel analysis (Lazarian & Pogosyan, 2000, 2004), the Δ -variance method (Ossenkopf et al., 2008a,b) or the Principal Component Analysis (Heyer & Schloerb, 1997; Brunt & Heyer, 2002a). The latter has been applied to study the gas dynamics of the same simulation data used in this paper in Bertram et al. (2014).

5.2.4 Structure functions of the CVI

Statistical moments p of the distribution of all possible CVI are called structure functions (CVISF). They are defined as

$$\text{CVISF}_p(\ell) = \langle |\delta C_\ell(\mathbf{r})|^p \rangle \quad (5.3)$$

where the average $\langle \rangle$ is computed over all possible CVI separated by ℓ in the plane. When p increases, the CVISF give a stronger weight to rare events. In our study we have computed the CVISF for each possible line-of-sight direction x , y and z . Although we use a weak magnetic field in the z -direction, the turbulence in our simulations is trans-Alfvénic or mildly super-Alfvénic (see Table 5.1). The field lines are therefore dragged along with the turbulent flow, with the result that the turbulence remains approximately isotropic (see, e.g. Burkhart et al., 2014). Hence, we do not expect significant variations of the CVISF along the different lines-of-sight. We therefore average all CVISF of the different line-of-sight directions and compute all CVISF for $p \leq 6$. Finally, the CVISF were fit to power laws of the form

$$\text{CVISF}_p(\ell) \propto \ell^{\zeta_p}, \quad (5.4)$$

where ζ_p is a function that depends on the statistical moment p of the CVI distribution. To calculate the scaling exponents, we use a fitting range from $1/16$ to $1/5$ of the total box size, as used by Federrath et al. (2010) and Konstandin et al. (2012). For a box with $D = 512$ grid cells for each side this translates to 32 and 102 cells. Figure 5.1 shows an example of a CVISF for orders up to $p = 6$ for one snapshot in time, where the velocity is weighted by the total density field from model n300.

5.2.5 Fourier and power spectra

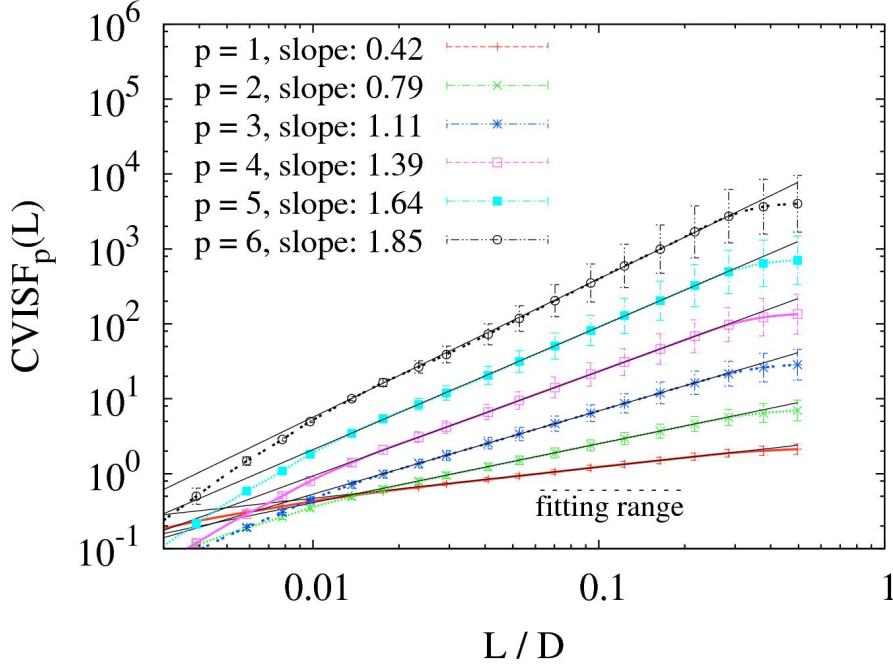
Fourier spectra are used to analyse the scale dependence of the kinetic energy of turbulence simulations. Assessing 3D turbulence power spectra, Kolmogorov (1941) showed through statistical arguments that the kinetic energy should scale as $E(k) \propto k^{-2/3}$ in case of incompressible turbulence, where k is the wavenumber. Later, Burgers (1948) derived $E(k) \propto k^{-1}$ for supersonic, compressive turbulence. We define the power spectrum as the change of the kinetic energy with its wavenumber, i.e. $P(k) = dE/dk$. The kinetic energy spectrum can be computed in Fourier space via

$$E(k)dk = \frac{1}{2} \int \hat{\mathbf{v}} \cdot \hat{\mathbf{v}}^* 4\pi k^2 dk, \quad (5.5)$$

where $\hat{\mathbf{v}}$ denotes the Fourier transform of the velocity field and $\hat{\mathbf{v}}^*$ its complex conjugate. Following Kolmogorov (1941), the kinetic energy down the cascade in the inertial range scales with $\langle \delta v_\ell^2 \rangle \propto \ell^{\zeta_2}$, where ζ_2 is the slope of the second order structure function obtained in the inertial range (or fitting range, as we term it in our case). Thus, the power spectrum can be computed and we obtain

$$P(k) = \frac{dE}{dk} \propto k^{-1-\zeta_2} = k^\alpha, \quad (5.6)$$

where we have used $k \propto \ell^{-1}$ and set $\alpha = -1 - \zeta_2$ as the value of the spectral slope. Hence, the power spectrum can be determined by evaluating ζ_2 of the second order

**Figure 5.1:**

CVI structure function for orders up to $p = 6$ with the inferred slopes ζ_p as a function of spatial scale for one snapshot in time, normalised by the total box size. The velocity here is weighted by the total density field for an initial number density of $n_0 = 300 \text{ cm}^{-3}$. The fitting range is indicated by a horizontal dashed line. Error bars denote $1\text{-}\sigma$ variations for all 3 line-of-sight directions.

structure function. Using Eq. 5.6, we then obtain slopes $P(k) \propto k^{-5/3}$ and $P(k) \propto k^{-2}$ for both Kolmogorov ($\alpha = -5/3$) and Burgers ($\alpha = -2$) turbulence, respectively. In this paper, we compute power spectra for 2D maps of CV in order to obtain information about the underlying physics of the different chemical components.

5.2.6 Theoretical relations for the SF slopes

Following Kolmogorov (1941), we assume that the kinetic energy scales as $E(k) \propto \langle \delta v^2 \rangle$ and $E(k) \propto k^{-2/3}$ in the case of incompressible turbulence, from which it directly follows that $\langle \delta v \rangle \propto \ell^{1/3}$. Furthermore, by taking $\langle \delta v_\ell^p \rangle \propto \ell^{\zeta_p}$, we can infer the theoretical scaling relation for the structure functions (SF) in the sense of Kolmogorov and find

$$\zeta_p = \frac{p}{3}. \quad (5.7)$$

This law will be referred to as K41. Later on, She & Leveque (1994) applied intermittency corrections to K41 and set $\zeta_p = p/3 + \tau_{p/3}$, since Eq. 5.7 seems to deviate significantly from many experimental studies for $p > 3$ (Benzi et al., 1993; She & Leveque, 1994; Dubrulle, 1994; Frisch & Kolmogorov, 1995). The function

$\tau_{p/3}$ thereby includes additional terms that depend on p . She & Leveque (1994) propose

$$\zeta_p = \frac{p}{9} + 2 \left[1 - \left(\frac{2}{3} \right)^{p/3} \right], \quad (5.8)$$

which we refer to as the SL94 model. As shown by Boldyrev et al. (2002), hereafter B02, and Dubrulle (1994), one important parameter in models of supersonic turbulence is the fractal co-dimension, $C = 3 - D$, where D is the dimension of the most intermittent structures. The SL94 model assumes 1D filaments with $D = 1$ as the most intermittent structures, while the B02 model assumes sheet-like structures with $D = 2$. Hence, Boldyrev et al. (2002) and Dubrulle (1994) generalised Eq. 5.8 and found

$$\zeta_p = \Theta(1 - \Delta)p + C(1 - \Sigma^{\Theta p}), \quad (5.9)$$

where $\Sigma = 1 - \Theta/C$. The other parameters Θ and Δ enter the theory through the so-called Kolmogorov refined similarity hypothesis, relating the scaling of fluctuations of the velocity field to the scaling of the fluctuating energy dissipation. We leave those two as free arbitrary parameters for now.

5.3 Results

We analyse different numerical models with and without radiative transfer post-processing and vary the initial number density in the simulation box, in order to study the influence on the structure functions. Table 5.1 gives an overview of the numerical models that we study in this paper. We quote both mass- and volume-weighted quantities, which we define using the expressions $\langle f \rangle_{\text{mass}} = \sum f \rho dV / \sum \rho dV$ and $\langle f \rangle_{\text{vol}} = \sum f dV / \sum dV$, respectively. More detailed analyses of the H_2 and CO distributions produced in this kind of turbulent simulation can be found in previous studies by Glover et al. (2010) and Shetty et al. (2011a). Examples of the integrated intensity and column density PDFs are shown in Shetty et al. (2011a). Figure 5.2 shows the centroid velocity maps computed via Eq. 5.1 for all models and for all chemical components.

5.3.1 Analysis of the CVISF

We compute the CVISF for all models (n30, n100, n300) and all chemical tracers: the total density, H_2 density, CO density, ^{12}CO and ^{13}CO intensity. We average slopes of the CVISF using 3 snapshots in time (with 3 line-of-sight directions each) where we can assume both the chemistry and the turbulence to be in a stationary and converged state. In Figure 5.3 we show slopes ζ_p of the CVISF as a function of the order p for all models and chemical tracers. The error bars denote temporal and spatial $1-\sigma$ fluctuations from the different time snapshots. Moreover, we also show

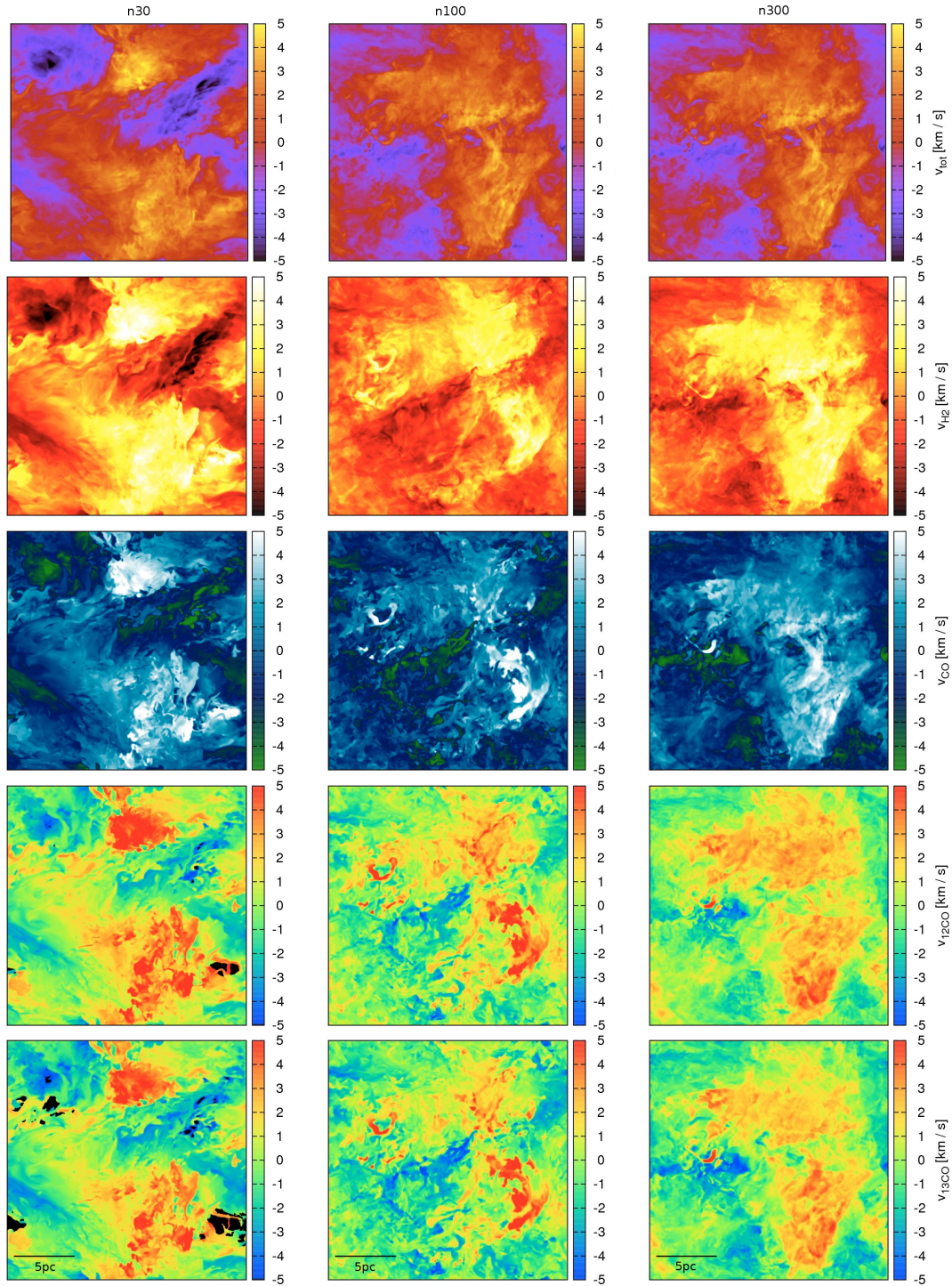


Figure 5.2:

Centroid velocities in z-direction for models n30 (left column), n100 (middle column) and n300 (right column). From top to bottom: CV maps of the total density, H_2 and ^{12}CO density followed by CV maps of the ^{12}CO and ^{13}CO integrated intensities. Each side has a length of 20 pc. Note that the velocity field of the n30 model uses a different turbulent seed than the n100 and the n300 model. Black areas in the ^{12}CO and ^{13}CO map of the n30 model denote regions where the brightness temperatures are zero along the line-of-sight. We mask these regions, because no proper centroid velocities can be computed there.

Model name	n30	n100	n300
Mean density [cm^{-3}]	30	100	300
Resolution	512^3	512^3	512^3
Box size [pc]	20	20	20
t_{end} [Myr]	5.7	5.7	5.7
$\langle \mathcal{M}_s \rangle$	5.1	6.8	10.6
$\langle \mathcal{M}_A \rangle$	1.0	1.1	1.5
$\sigma_\rho / \langle \rho \rangle$	4.6	3.0	3.0
$\langle x_{\text{H}_2} \rangle_{\text{mass}}$	0.61	0.78	0.98
$\langle n_{\text{H}_2} \rangle_{\text{vol}}$ [cm^{-3}]	8.6	36.8	139.3
$\langle n_{\text{H}_2} \rangle_{\text{mass}}$ [cm^{-3}]	263.6	447.1	1455.8
$\langle n_{\text{CO}} \rangle_{\text{vol}}$ [cm^{-3}]	1.4×10^{-4}	1.7×10^{-3}	2.2×10^{-2}
$\langle n_{\text{CO}} \rangle_{\text{mass}}$ [cm^{-3}]	2.3×10^{-2}	4.3×10^{-2}	0.3
$\langle T \rangle_{\text{vol}}$ [K]	223.0	68.4	34.9
$\langle T \rangle_{\text{mass}}$ [K]	56.7	25.8	12.7
$\langle N_{\text{H}_2} \rangle$ [cm^{-2}]	5.3×10^{20}	2.3×10^{21}	8.6×10^{21}
$\langle N_{\text{CO}} \rangle$ [cm^{-2}]	8.7×10^{15}	1.1×10^{17}	1.3×10^{18}

Table 5.1:

Overview of the different models with some characteristic values for the last snapshot. From top to bottom we list: mean number density, resolution, box size, time of the last snapshot, mean sonic Mach number, mean Alfvén Mach number, ratio of density dispersion and mean density, mass-weighted mean abundances of H_2 (i.e. the percentage of atomic hydrogen that has been converted to H_2 , see Glover & Mac Low, 2011), mean volume- and mass-weighted H_2 and CO number density, mean volume- and mass-weighted temperature and mean column density of H_2 and CO.

the K41, SL94 and B02 scaling relations in the plots. We have to keep in mind that a direct comparison of the theoretical models with our CV statistics is nontrivial and sometimes impossible, since we analyse velocity centroids, while the theory predicts scaling relations for the full turbulent velocity field. For a more detailed discussion about the influence of the projection, we refer the reader to Sec. 5.4.3 and 5.4.4.

We find differences between the various models and tracers. In our n300 model we obtain similar slopes of the total density and the H_2 density model as well as for the CO density and the ^{13}CO intensity model within their error bars. The slopes of the total density and the H_2 density model are steeper compared to the different CO tracer models, which flatten to higher order p of the CVISF. The slopes ζ_p of the ^{12}CO intensity model make up an intermediate case. They are slightly steeper than the CO density and ^{13}CO intensity model, but flatter than those of the total density and H_2 density model.

Regarding the n100 model, we find consistent values for ζ_p for all CO tracer cases and for all orders p . Furthermore, we again measure steeper slopes for the total density and H_2 density model, which now slightly deviate from each other at higher order of the CVISF.

In our n30 model we obtain a larger discrepancy between the total density and the H₂ density model. Although the temporal and spatial 1- σ fluctuations are large for both cases, we find a clear separation of the slopes for higher p . Again, all different CO tracers agree with each other within their error bars and are significantly flatter and those of the H₂ and total density cases.

5.3.2 Analysis of the Fourier spectra

Following Eq. 5.5, we compute Fourier spectra and the scaling exponents of the power spectra by fitting a linear function in log-log space to the Fourier spectra in the fitting range of our simulations. The fitting range in k -space translates to wavenumbers from 5 to 16 and has to be chosen carefully due to the artificial accumulation of energy further down the cascade, known as the bottleneck effect (Falkovich, 1994; Dobler et al., 2003; Kaneda et al., 2003; Haugen & Brandenburg, 2004; Kritsuk et al., 2007a; Beresnyak & Lazarian, 2009). In analogy to Figure 5.3, Figure 5.4 shows with k^2 compensated Fourier spectra for the different density models and all chemical components.

In the n300 model we again find a good correlation between the total density and the H₂ density. We measure slopes α of -1.62 ± 0.09 for the former and -1.60 ± 0.09 for the latter, which agree well within their errors. For the CO density, ¹²CO and ¹³CO intensity cases we find slopes of -1.27 ± 0.10 , -1.36 ± 0.08 and -1.30 ± 0.09 , which do not show significant differences within their errors.

The same trends are seen in the other density models. In the n100 model we again do not find a significant difference between the total density and the H₂ density, for which we measure slopes α of -1.57 ± 0.09 and -1.54 ± 0.09 , respectively. For the CO density, ¹²CO and ¹³CO intensity cases we find very flat slopes of -0.98 ± 0.07 , -1.01 ± 0.08 and -0.87 ± 0.09 .

In the low-density n30 model, the slopes α of the total density (-1.49 ± 0.11) and H₂ density (-1.41 ± 0.11) cases agree well within their errors, while the slopes of the CO density, ¹²CO and ¹³CO intensity cases are again much flatter and we measure -1.04 ± 0.09 , -1.01 ± 0.10 and -1.00 ± 0.10 .

Overall, we find a significant difference in the slopes of the H₂ density and all CO tracers for all three density models. Slopes of the total density and H₂ density are found to be significantly steeper than those produced by the different CO tracers, while we do not obtain significant differences in the slopes between the different CO tracers within their errors.

5.3.3 Variation of the abundance of ¹³CO

Our numerical simulations follow the chemistry of ¹²CO, but not of its isotope ¹³CO. Consequently, in order to generate the data on the number density of ¹³CO that we need for our radiative transfer calculation, it is necessary to specify a conversion factor between ¹²CO and ¹³CO. As we explain in Sec. 5.2.2, in most of our analysis, we assume a fixed ¹²CO to ¹³CO ratio, $R_{12/13} = 50$. However, in real molecular

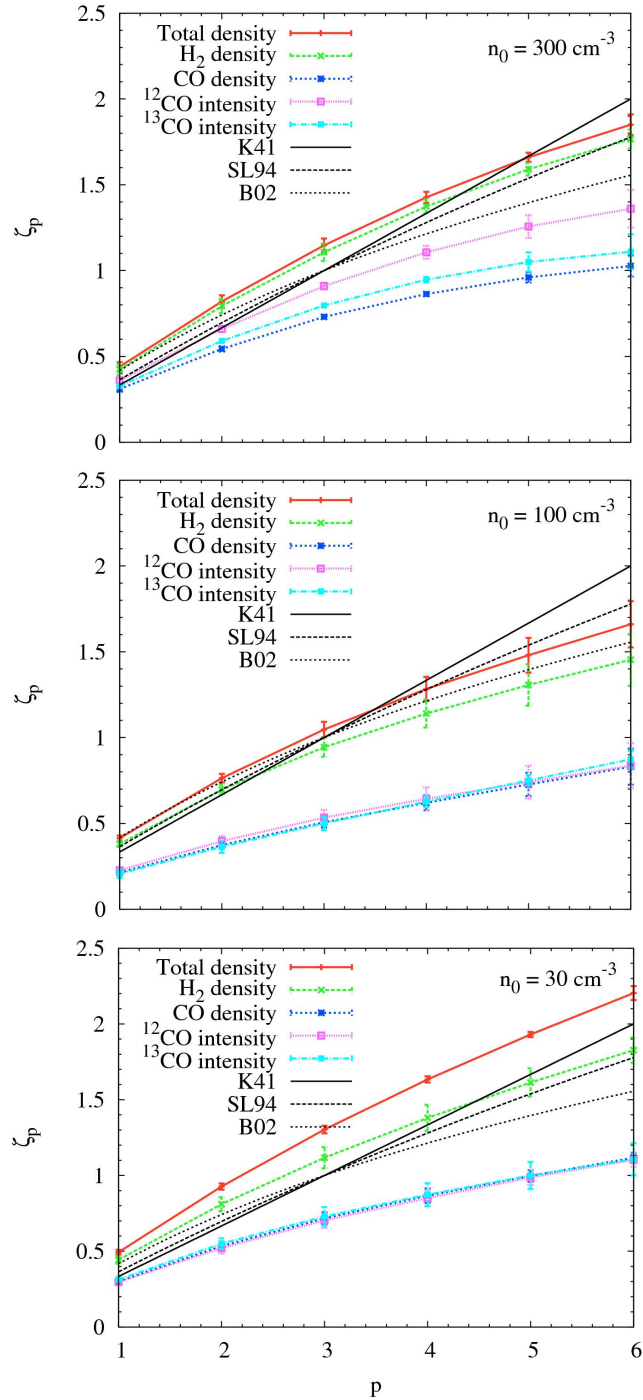


Figure 5.3:

Slopes ζ_p of the structure functions against order p for all chemical models, i.e. the total density, H_2 density and the CO density model as well as the ^{12}CO and ^{13}CO intensity model. For comparison, we also show the theoretical scaling relations (black lines) from Kolmogorov (1941), She & Leveque (1994) and Boldyrev et al. (2002), denoted as K41, SL94 and B02. From top to bottom: runs of the different initial number densities, i.e. $n_0 = 300, 100$ and 30 cm^{-3} . Error bars denote temporal and spatial $1\text{-}\sigma$ fluctuations. Please note that a direct comparison of the theoretical models with our CV statistics is complicated due to the projection along the LoS. For a more detailed discussion about the influence of the projection, we refer the reader to Sec. 5.4.3 and 5.4.4.

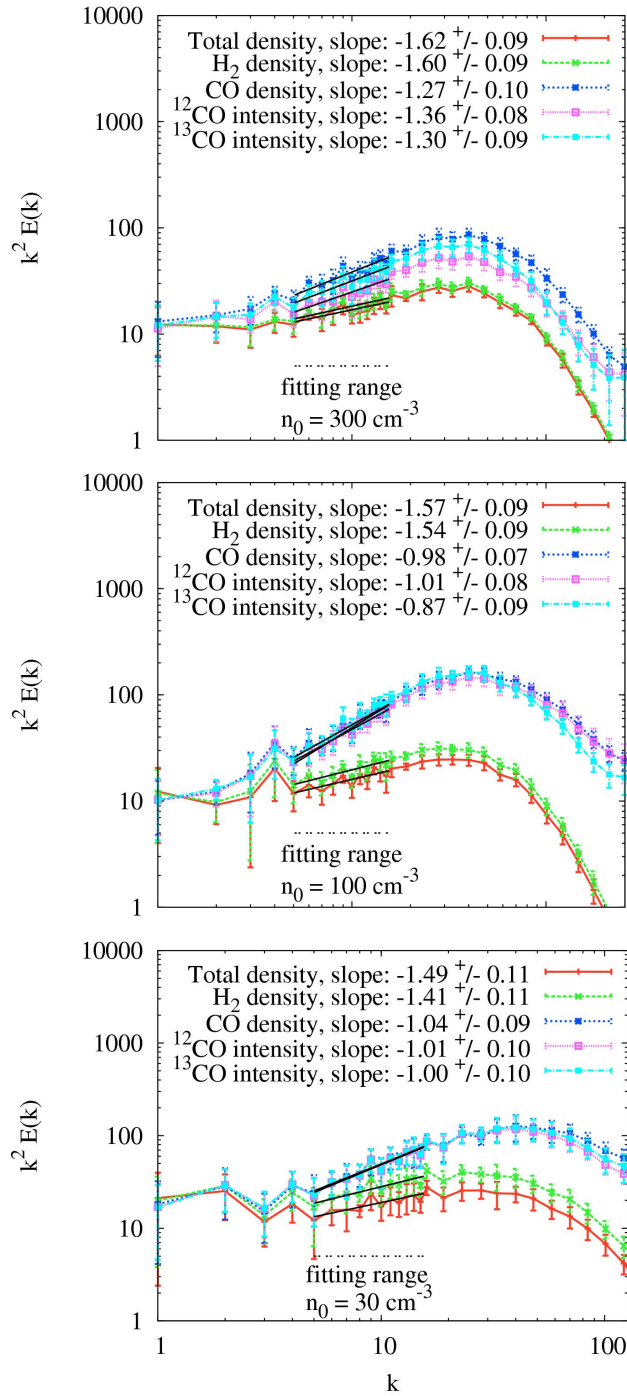


Figure 5.4:

Fourier energy spectra multiplied by k^2 as a function of scale k for all density models and chemical components, i.e. the total density, H_2 density and the CO density model as well as the ^{12}CO and ^{13}CO intensities. From top to bottom: runs of the different initial number densities, i.e. $n_0 = 300, 100$ and 30 cm^{-3} . Error bars denote temporal and spatial $1-\sigma$ fluctuations. In all models, the total density and H_2 density cases show a significantly steeper slope compared to the CO tracer components. The fitting range is indicated by a horizontal dashed line. Slopes with the fitting errors are given in each plot for the different species.

clouds, we expect spatial variations in $R_{12/13}$ in any regions in which the carbon is not all locked up in CO, caused by the two effects of chemical fractionation and selective photodissociation (Röllig & Ossenkopf, 2013; Szűcs et al., 2014). To explore the effect that these variations may have on the CVI statistics of the ^{13}CO emission maps, we produce a set of ^{13}CO emission maps, using a spatially varying $R_{12/13}$ generated following the prescription given in Sec. 5.2.2 and in Szűcs et al. (2014). After applying the radiative transfer post-processing to both models, we compute the two maps of the CV and compare the slopes of the CVISF.

Although we find slight differences in the CV maps on small scales, the slopes ζ_p of the CVISF are essentially the same in both cases. The differences between the results in the two models are smaller than the $1\text{-}\sigma$ temporal and spatial errors in the different snapshots. We thus conclude that the use of a constant $^{12}\text{CO}/^{13}\text{CO}$ ratio is sufficient for obtaining proper slopes of the CVISF for ^{13}CO .

5.4 Discussion

5.4.1 Slopes of the CVISF

As shown in Figure 5.3, we find large differences in the CVISF slopes for the different chemical components and density models. In the n300 model, we find a good correlation between the total density and the H_2 density within their error bars. This is because about 98% of the initial atomic hydrogen gas is in molecular form at this time, meaning that H_2 is an excellent tracer of the total density. Furthermore, ^{13}CO is optically thin and thus we expect the ^{13}CO intensity PPV model to trace the underlying 3D PPP CO density model well, which we can see in Figure 5.3. This argument is also valid for the other density models. On the other hand, ^{12}CO is optically thick and traces H_2 well only in dense regions (see Bertram et al., 2014). This is why it lies between the total density and the CO density models. We discuss the physical implications for this result in Sec. 5.4.4.

Turning to the low-density model n30, we find a larger discrepancy in the slopes of the H_2 density and the total density field, because only 61% of the initial atomic hydrogen gas is now in molecular form. Thus, the H_2 gas does not trace the total gas very well, although it is still the best tracer for the total density field in general. Looking at the different CO tracers, we find a good correlation between the CO density, ^{12}CO and ^{13}CO intensity cases within the error bars.

The n100 model is intermediate between n30 and n300. We find a better correlation of the H_2 and the total density cases than in the n30 model, which comes from the higher fractional abundance of H_2 compared to the n30 model. Furthermore, we again obtain a good correlation between all CO tracer components within their error bars, which means that the turbulence statistics in all three cases are similar.

Nevertheless, regarding the question of whether CO tracer molecules can be used to infer the dynamics of the underlying total density or H_2 density field, we find that in all density models, the slopes of the total density or the H_2 density field might

be underestimated by a factor up to 3 by the use of different CO tracers.

5.4.2 Slopes of the Fourier spectra

Model name	n30	n100	n300
Total density	-3.49 ± 0.11	-3.57 ± 0.09	-3.62 ± 0.09
H ₂ density	-3.41 ± 0.11	-3.54 ± 0.09	-3.60 ± 0.09
CO density	-3.04 ± 0.09	-2.98 ± 0.07	-3.27 ± 0.10
¹² CO intensity	-3.01 ± 0.10	-3.01 ± 0.08	-3.36 ± 0.08
¹³ CO intensity	-3.00 ± 0.10	-2.87 ± 0.09	-3.30 ± 0.09

Table 5.2:

Spectral slopes for all chemical components and density models shown in Figure 5.4. In order to compare our spectral slope values α to those given in Lazarian & Pogosyan (2004), we have to subtract a value of -2, i.e. $\beta = \alpha - 2$. Independent of the individual component, we observe a saturation of the spectral slopes to a value of $\beta \approx -3$.

We can understand the significant differences between the H₂ and the CO tracer cases in the Fourier spectra of the distinct density models by comparing Figure 5.3 with Figure 5.4. In Eq. 5.6 we have shown that the slopes α of the Fourier spectra are related to the structure functions of the turbulence over the second order structure function ζ_2 via $\alpha = -1 - \zeta_2$. The interpretation of slope differences $\Delta\alpha = \zeta_2^{(b)} - \zeta_2^{(a)}$ in Figure 5.4 between different chemical tracers is thus related to the differences in slopes of the second order structure functions. If the differences of values for ζ_2 within one density model are large, we also expect large differences to occur in the slopes of the Fourier spectra, which is indeed the case. The ‘‘average’’ difference for ζ_2 between H₂ and the CO tracers is largest in the n100 model. Hence, we also find the largest slope differences between those two cases in our Fourier spectra for the n100 model. This is why Fourier slopes in Figure 5.4 of all CO tracers are significantly flatter than those of H₂. Since we always find the highest slope values for the total density and H₂ density in Figure 5.3, we also measure steeper exponents of those components in the Fourier spectra.

However, we have to keep in mind that we have used 3D statistical measures to understand the behaviour of the 2D centroid velocity maps. Nevertheless, since we only want to compare relative scaling behaviours in our models, we can safely use 3D statistical tools of turbulence analysis in order to work out trends in 2D data available for observers.

Furthermore, Lazarian & Pogosyan (2004) predicted that the spectral slope should saturate to a value of -3, which was confirmed by several other studies in the past (see, e.g. Stutzki et al. 1998; Stanimirović & Lazarian 2001; Lazarian & Pogosyan 2006; Padoan et al. 2006; Burkhart et al. 2010, Burkhart et al. 2013a). Note that in the context of Lazarian & Pogosyan (2004), the power spectra are defined via $E(k) \propto k^2 P(k) \propto k^\beta$. Thus, if we want to compare our results to those found in

Lazarian & Pogosyan (2004), we have to subtract a value of -2 in order to compensate for the k^2 scaling, i.e. $\beta = \alpha - 2$, where α denotes the Fourier slopes given in Figure 5.4 and β the slopes listed in Lazarian & Pogosyan (2004) or Burkhart et al. 2013a. Table 5.2 gives an overview about the spectral slopes β computed from our slopes values α given in Figure 5.4. Independent of the individual component and the initial density, we also observe a saturation of the spectral slope indices to a value of $\beta \approx -3$ for CO (see also Lazarian & Pogosyan, 2004).

5.4.3 Projection effects

A direct comparison of CVISF to models of 3D turbulence such as proposed by She & Leveque (1994) or Boldyrev et al. (2002) is complicated, since maps of centroid velocities are a complex convolution of the density (or brightness temperature) with the velocity field. Moreover, previous studies have shown that physical effects like opacity or the sonic Mach number also significantly influence the result of the CV analysis (see, e.g. Lazarian & Pogosyan 2004, Burkhart et al. 2013a and Burkhart et al. 2014). Nevertheless, CVI statistics provide a useful tool to study effects of turbulence in observational measurements and to compare those to numerical experiments, since observations rely on spectral PPV information from which the CV maps can directly be inferred.

As shown by Lazarian & Esquivel (2003), Ossenkopf et al. (2006), or Esquivel et al. (2007), CVI statistics are significantly influenced by the underlying density field and thus differ from the pure 3D velocity statistics, unless the ratio of the density dispersion to the mean density is small. This is usually the case in subsonic flows where the Mach number is supposed to be small, which is clearly not the case in our simulations, where we measure supersonic Mach numbers. Table 5.1 gives both the mean Mach number and the ratio of density dispersion and mean density, $\sigma_\rho/\langle\rho\rangle$. We find values $\sigma_\rho/\langle\rho\rangle \gtrsim 3$ and therefore expect the mutual convolution of density and velocity field to play a significant role. Ossenkopf et al. (2006) give an upper limit of $\sigma_\rho/\langle\rho\rangle \lesssim 0.5$ in order to get a proper matching of the CVISF with the 3D structure functions of the turbulence. We thus expect a significant loss in the signatures of intermittency in our CVI statistics compared to the proper 3D data, which limits a direct comparison of the CVISF to the different moments of the structure functions of the underlying 3D velocity field. For further information about the density variance-Mach number relation we refer the reader to Vázquez-Semadeni & García (2001), Lemaster & Stone (2008), Federrath et al. (2008), Federrath et al. (2010), Molina et al. (2012), Burkhart & Lazarian (2012) and Konstandin et al. (2012).

5.4.4 Connection to the fractal dimension

As shown in Figure 5.3, we find increasing differences between the H₂ and the CO tracers with higher order p of the CVISF for all density models. Although we analyse 2D CVI statistics, we can nevertheless gain useful information about the

most dissipative structures in our simulations using theoretical models of 3D velocity statistics. However, as discussed in Kowal et al. (2007), we have to keep in mind that supersonic turbulence contaminates the scaling relations of the CV statistics due to a complex convolution of the supersonic density with the velocity.

In the context of She & Leveque (1994) ($C = 2$), Eq. 5.9 predicts larger slope values ζ_p than in the model given by Boldyrev et al. (2002) ($C = 1$), in which ζ_p becomes flatter for higher order p . Thus, the increasing differences between the H₂ and the CO tracers with higher order p of the CVISF seem to be related to the fractal co-dimension C , which can be interpreted as a space-filling factor, describing the distribution of gas in the MC. As argued in Bertram et al. (2014), H₂ is more extended than CO as it is better able to self-shield in diffuse regions, while CO is a good tracer of H₂ only in compact regions. Hence, we would predict a larger fractal co-dimension for the H₂ gas than for the various CO tracers, leading to the increasing differences in ζ_p as observed in Figure 5.3 between H₂ and CO. However, due to projection and resolution effects it is rather complicated to give general values for the fractal co-dimension of the 3D velocity statistics. The question of how the fractal dimensions of 2D and 3D velocity statistics are related with each other can be addressed in a follow-up study.

5.4.5 Limitations of the models

As described in Bertram et al. (2014), there are some assumptions and limitations inherent to our numerical models that we must keep in mind when interpreting the results. For example, our models do not account for self-gravity, star formation, stellar feedback (e.g. by SN, stellar radiation, etc.) or large-scale dynamics (e.g. spiral arms, SN shells, etc.). Furthermore, we find a minor resolution dependence of the CVISF slopes for CO as discussed in Appendix A.1, which limits the ability to directly compare our theoretical values with observational measurements. However, we can gain useful information about the underlying physics through the relative scaling of the CVISF slopes to get an idea of how the chemistry and a radiative transfer affect the trends seen in tools like CVI statistics or Fourier spectra, which are commonly used by observers.

For future investigations, higher resolution models would be needed in order to measure converged slope values that can be compared to observations. Additionally, simulations that span a wider range of physical parameters, i.e. different metallicities or radiation fields, are important to study in order to analyse the influence on the CVI statistics. Star formation, feedback and stellar winds could also help to improve our understanding of turbulence in MCs.

5.5 Summary and Conclusions

We analysed centroid velocity increment structure functions (CVISF) and Fourier spectra of MCs with time-dependent chemistry and a radiative transfer post-processing

for models of different initial number densities and chemical components: the total number density, H₂ and CO density (each without radiative transfer) as well as ¹²CO and ¹³CO intensity (both with radiative transfer). In each case, we computed CVISF and their Fourier spectra and analysed the slopes of the CVISF within a fitting range used by Federrath et al. (2010) and Konstandin et al. (2012) in order to study the influence of the chemistry and the radiative transfer on the results of the CVI statistics. We report the following findings:

- Optical depth effects can be important for the CVI structure analysis. We find different behaviours of the CVISF slopes for ¹²CO and ¹³CO in different density environments (see Sec. 5.4.1).
- We find the slopes of H₂ in Fourier spectra generally to be steeper than the slopes of different CO tracers (see Sec. 5.4.2). We also find the slopes of the CVISF for the total density and H₂ density to be steeper by a factor of up to 3 than the slopes of different CO tracers.
- We find $\beta \lesssim -3$ for all spectral slope values measured in this study (see Sec. 5.4.2), saturating at a value of -3 in the synthetic CO emission data cubes (see also Lazarian & Pogosyan, 2004).
- We expect the CO gas to have a significantly smaller fractal co-dimension than the H₂ gas, which means that it is less space-filling than H₂ (see Sec. 5.4.4).
- We do not find any variations in the slopes of the CVISF using more realistic abundances of ¹³CO in MCs compared to a constant ¹²CO/¹³CO scaling ratio throughout the whole cloud (see Sec. 5.3.3).
- Following the results of previous studies (see Sec. 5.4.3), we expect a significant loss of information in the turbulence statistics due to projection, since we find values of $\sigma_\rho / \langle \rho \rangle \gtrsim 3$ in our simulations of supersonic turbulence. This limits a direct test of the CVISF to the different moments of the 3D structure functions.

Structure analysis of simulated MCs with the Δ -variance

We employ the Δ -variance analysis and study the turbulent gas dynamics of simulated molecular clouds (MCs). Our models account for a simplified treatment of time-dependent chemistry and the non-isothermal nature of the gas. We investigate simulations using three different initial mean number densities of $n_0 = 30, 100$ and 300 cm^{-3} that span the range of values typical for MCs in the solar neighbourhood. Furthermore, we model the CO line emission in a post-processing step using a radiative transfer code. We evaluate Δ -variance spectra for centroid velocity (CV) maps as well as for integrated intensity and column density maps for various chemical components: the total, H_2 and ^{12}CO number density and the integrated intensity of both the ^{12}CO and ^{13}CO ($J = 1 \rightarrow 0$) lines. The spectral slopes of the Δ -variance computed on the CV maps for the total and H_2 number density are significantly steeper compared to the different CO tracers. We find slopes for the linewidth-size relation ranging from 0.4 to 0.7 for the total and H_2 density models, while the slopes for the various CO tracers range from 0.2 to 0.4 and underestimate the values for the total and H_2 density by a factor of 1.5 – 3.0. We demonstrate that optical depth effects can significantly alter the Δ -variance spectra. Furthermore, we report a critical density threshold of $\sim 100 \text{ cm}^{-3}$ at which the Δ -variance slopes of the various CO tracers change sign. We thus conclude that carbon monoxide traces the total cloud structure well only if the average cloud density lies above this limit. The results presented in this chapter are published in Bertram et al. (2015b).

6.1 Introduction

The interstellar medium (ISM) is dominated by highly turbulent motions, which contribute to regulating stellar birth in interstellar molecular clouds (MCs) (see, e.g. Mac Low & Klessen, 2004; Scalo & Elmegreen, 2004; Elmegreen & Scalo, 2004;

McKee & Ostriker, 2007; Hennebelle & Falgarone, 2012). On large scales, turbulent gas motions support MCs against gravitational collapse. However, the shocks associated with supersonic turbulence will create overdense regions on small scales, which in turn may collapse and form stars and clusters. In addition, ISM turbulence influences other physical processes such as the chemical makeup of the gas and the associated heating and cooling processes, the efficiency with which the external radiation field will be able to penetrate into the interior of dense clouds, as well as the overall magnetic field. Better understanding the role of turbulence in the ISM, therefore, is of pivotal importance for many fields of modern astrophysics (see also the lecture notes by Klessen & Glover, 2014).

Comparing theoretical simulations to observational measurements is very difficult, since observations are always a complex convolution of the density and the velocity field, affected by several other important physical processes (e.g. by magnetic fields, the chemistry, stellar feedback, etc.). Furthermore, it is often difficult to infer reliable physical parameters from observational measurements. For example, observers rely on abundant tracers, e.g. ^{12}CO , in order to measure the amount of H_2 gas in MCs. An obstacle with the line emission of ^{12}CO is that it becomes optically thick in dense cloud regions and thus is not a good tracer for those regions anymore. To avoid this problem, observers also employ other tracers to study the mass distribution within a cloud, e.g. dust or ^{13}CO , which is often optically thin. In addition, molecular tracers like CS, HCN, HCO^+ or NH_3 can be used to study the gas mass in very dense cloud regions. However, comparisons with simulations are needed in order to study the influence of chemical inhomogeneities and optical depth effects on observational measurements.

Lis et al. (1996) introduced maps of centroid velocities (CV) and showed that those are to a certain degree sensitive to the underlying physics. Accordingly, it is possible to use two-point statistics in order to recover important information (e.g. optical depth effects, density and velocity fluctuations, etc.) of an astrophysical system, e.g. by using centroid velocity increment structure functions (see, e.g. Hily-Blant et al., 2008; Federrath et al., 2010), spectral correlation functions (Rosolowsky et al., 1999), the velocity channel analysis (Lazarian & Pogosyan, 2000, 2004), the Principal Component Analysis (Heyer & Schloerb, 1997; Brunt & Heyer, 2002a) or the Δ -variance (see, e.g. Stutzki et al., 1998; Mac Low & Ossenkopf, 2000; Ossenkopf et al., 2001; Bensch et al., 2001; Ossenkopf et al., 2008a,b). The latter provides a wavelet-based measure for characterizing structures in astronomical datasets. For example, Stutzki et al. (1998) used the Δ -variance in order to measure the scaling behavior of structures in observed images by analyzing the line emission of ^{12}CO and ^{13}CO , while Bensch et al. (2001) studied the influence of white noise and beam smoothing on the Δ -variance spectra. Moreover, Ossenkopf et al. (2008b) applied the Δ -variance to interstellar turbulence and observations of MCs and tested the capabilities of the method in a practical use by applying different filter functions with different diameter ratios.

Several studies tried to reveal the influence of projection effects on different statistical quantities, finding that various physical processes might influence the projec-

tion of three-dimensional data on a two-dimensional map on the sky. For example, Lazarian & Pogosyan (2004), Burkhart et al. (2013b), Burkhart et al. (2014) and Bertram et al. (2015a) have shown that optical depth effects might significantly alter the statistics of centroid velocities due to different opacities of the gas tracers. Furthermore, the turbulent driving as well as density and temperature fluctuations along the line-of-sight also have a significant impact on the CV statistics (Lazarian & Esquivel, 2003; Ossenkopf et al., 2006; Esquivel et al., 2007; Hily-Blant et al., 2008). Much progress has been made during the last years in this context, although we are still missing a consistent picture of turbulence theory in the ISM.

In this paper we study high-resolution, 3D and time-dependent chemistry models of hydrodynamical numerical simulations of the turbulent ISM. We use the Δ -variance method (see, e.g. Stutzki et al., 1998; Bensch et al., 2001; Ossenkopf et al., 2008a) in order to study the structure of MCs and analyze how different chemical tracers affect the Δ -variance spectra. We also vary the initial number density in order to explore how different densities affect the statistics. Moreover, we perform a radiative transfer post-processing and produce synthetic maps as well as position-position-velocity (PPV) cubes of the ^{12}CO and ^{13}CO emission. We then compute maps of centroid velocities, column densities and integrated intensities in order to analyze how the chemical inhomogeneity and the variable opacity affect the various Δ -variance spectra.

In Section 6.2 we present our numerical simulations, introduce the radiative transfer post-processing and explain the statistical methods. In Section 6.3 we present our results, which are discussed in Section 6.4. Finally, we summarize our findings and present our conclusions in Section 6.5.

6.2 Methods and simulations

The simulation data presented in the following sections are also used in Bertram et al. (2014) and Bertram et al. (2015a). While Bertram et al. (2014) use the technique of Principal Component Analysis (PCA) in order to statistically analyze the turbulent flows in the spectral data cubes, Bertram et al. (2015a) evaluate the slopes of the structure functions of 2D projected centroid velocities and compute Fourier spectra. Here, we summarize the most important aspects of our hydrodynamical simulations and the radiative transfer post-processing.

6.2.1 Computational method

The simulations in this paper were performed using a modified version of the ZEUS-MP MHD code (Norman, 2000; Hayes et al., 2006). We have embedded a detailed atomic and molecular cooling function, described in Glover et al. (2010) and Glover & Clark (2012), together with a simplified treatment of the molecular gas chemistry. The chemical network is based on the work of Nelson & Langer (1999) and Glover & Mac Low (2007), and allows us to follow the formation and destruction of H_2 and

CO self-consistently within our simulations. The network tracks the abundances of 9 species and follows 30 chemical reactions. We adopt the standard solar abundances of hydrogen and helium. The abundances of carbon and oxygen are taken from Sembach et al. (2000). We use $x_{\text{C}} = 1.4 \times 10^{-4}$ and $x_{\text{O}} = 3.2 \times 10^{-4}$, where x_{C} and x_{O} are the fractional abundances by number of carbon and oxygen relative to hydrogen (for further reading see also Glover et al., 2010; Glover & Mac Low, 2011). When we start our simulations, the carbon is assumed to be singly ionised as C^+ , while the hydrogen, helium as well as the oxygen are in atomic form. For further information about the chemical model we refer the reader to Glover & Clark (2012).

We run simulations with three different initial number densities n_0 of the hydrogen nuclei, $n_0 = 300, 100$ and 30 cm^{-3} . The temperature of the gas at the beginning of our runs is set to a constant value of 60 K. We use an uniform weak magnetic field strength $B_0 = 5.85 \mu\text{G}$, which is initially oriented parallel to the z -axis of the computational domain. We do not include self-gravity. The gas is initially uniform and embedded in a periodic box with a side length of 20 pc. The turbulent simulations are uniformly driven between wavenumbers $k = 1$ and $k = 2$ (Mac Low et al., 1998a; Mac Low, 1999) with a 3D rms velocity of $v_{\text{rms}} = 5 \text{ km s}^{-1}$. This value remains approximately constant throughout the whole simulation period. For the dust-to-gas ratio, we adopt the standard local value of 1:100 (Glover et al., 2010), and assume that the dust properties do not vary with the gas density. The cosmic ray ionization rate was set to $\zeta = 10^{-17} \text{ s}^{-1}$. For the incident ultraviolet radiation field, we adopt the standard parameterization of Draine (1978). This field has a strength $G_0 = 1.7$ in Habing (1968) units, corresponding to an integrated flux of $2.7 \times 10^{-3} \text{ erg cm}^{-2} \text{ s}^{-1}$. We use a numerical resolution of 512³ grid cells and discuss the influence of our limited numerical resolution in more detail in Appendix B.1. Using this value for the resolution as well as the scale of the total box, we can compute the cubic cell size and obtain $\Delta x \approx 0.04 \text{ pc}$ for our numerical simulations.

6.2.2 Radiative transfer post-processing

We use the radiative transfer code RADMC-3D¹ (Dullemond, 2012) in order to model the CO ($J = 1 \rightarrow 0$) line for both ¹²CO and ¹³CO. Furthermore, we apply the Large Velocity Gradient (LVG) approximation (Sobolev, 1957) to compute the level populations, as explained by Shetty et al. (2011a). Beyond the line emission, RADMC-3D also accounts for the dust continuum emission, which we subtract off before we analyze the statistical properties of the synthetic maps. We use a number of 512 channels in velocity space for our radiative transfer post-processing, corresponding to a spectral resolution of $\sim 0.07 \text{ km s}^{-1}$, $\sim 0.06 \text{ km s}^{-1}$ and $\sim 0.05 \text{ km s}^{-1}$ for the n300, n100 and n30 model, respectively.

Our simulations do not explicitly track the abundance of ¹³CO (which would be costly), and so we need a procedure to relate the ¹³CO number density to that of ¹²CO. A common assumption is that the ratio of ¹²CO to ¹³CO is identical to the

¹www.ita.uni-heidelberg.de/~dullemond/software/radmc-3d/

elemental abundance ratio of ^{12}C to ^{13}C (see, e.g. Roman-Duval et al., 2010). In the majority of our analysis, we make the same assumption and set the ^{12}CO to ^{13}CO ratio to a constant value, $R_{12/13} = 50$, which we use to generate a first set of ^{13}CO column density maps. However, the effects of chemical fractionation (Watson et al., 1976) and selective photodissociation of ^{13}CO (see, e.g. Visser et al., 2009a) can significantly alter the value of $R_{12/13}$ within the cloud (Röllig & Ossenkopf, 2013; Szűcs et al., 2014). Therefore, we also explore the effect that this may have on the statistics of the Δ -variance, using numerical results of Szűcs et al. (2014). Szűcs et al. (2014) give a numerical fitting formula, which relates the ratio $R_{12/13}$ to the ^{12}CO column density in the cloud. Thus, we also produce a second set of maps using their routine and compute variable ^{13}CO number densities by dividing the ^{12}CO number densities by the mean value of $R_{12/13}$ from the fitting formula for each line-of-sight. Finally, we can use these ^{13}CO number densities in order to compute the ^{13}CO emission in the same fashion as in our constant ratio models. The differences in the Δ -variance spectra of the two sets of ^{13}CO emission maps - those derived using a constant $R_{12/13}$ and those that use a spatially varying value of $R_{12/13}$ - will be discussed in Section 6.3.3 below.

The radiative transfer calculation yields position-position-velocity (PPV) cubes of brightness temperatures T_B , which are related to the intensity via the Rayleigh-Jeans approximation,

$$T_B(\nu) = \left(\frac{c}{\nu}\right)^2 \frac{I_\nu}{2k_B}, \quad (6.1)$$

where I_ν is the specific intensity at frequency ν and k_B the Boltzmann constant. We will refer to these as the “intensity” models. In analogy, we construct centroid velocity and column density maps out of the PPP simulation data of the density and velocity field, as described in the following Section 6.2.3. We will refer to these as the “density” models, following the notation already used in Bertram et al. (2014) and Bertram et al. (2015a).

6.2.3 Centroid velocity, integrated intensity and column density maps

One part of our study is based on the statistics of centroid velocities. The centroids $C(x, y) = C(\mathbf{r})$ are defined as

$$C(\mathbf{r}) = \frac{\int F(\mathbf{r}, z)v_z(\mathbf{r}, z)dz}{\int F(\mathbf{r}, z)dz}, \quad (6.2)$$

where the variable $v_z(\mathbf{r}, z)$ is the velocity component along the line-of-sight (e.g. the z -direction). Thus, $C(\mathbf{r})$ is a map of line-of-sight projected velocities. The quantity $F(\mathbf{r}, z)$ is a statistical weight. It denotes either the underlying density field or the brightness temperatures from the PPV cubes. As shown by Lis et al. (1996), centroid velocity maps are very sensitive to the underlying physics of a MC, which means that

they can be used in order to infer important information about the astrophysical system. Furthermore, CV maps can be easily computed from observational data that rely on spectral measurements. These can be then translated into maps of centroid velocities via equation (6.2).

Beside the CV maps, we also consider maps of integrated intensity and column density. We calculate the former along a given line-of-sight (e.g. the z -direction) via

$$W(\mathbf{r}) = \int T_B(\mathbf{r}, z) dv, \quad (6.3)$$

where T_B is the brightness temperature, as introduced in Section 6.2.2. The latter is given by

$$N(\mathbf{r}) = \int n(\mathbf{r}, z) dz, \quad (6.4)$$

where n is the number density of an individual chemical component in a given cell in the simulation box.

6.2.4 The Δ -variance method

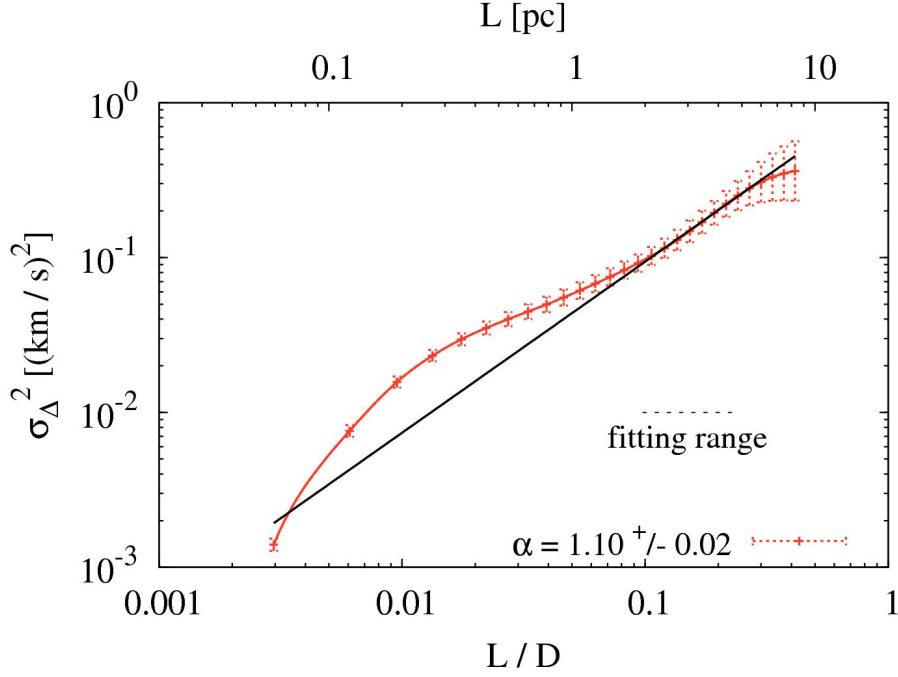
We use the Δ -variance tool developed by Ossenkopf et al. (2008a)². The Δ -variance method measures the variance in a structure $S(\mathbf{r})$ (in our case the maps of centroid velocities, integrated intensities and column densities) on a given spatial scale ℓ , by filtering the dataset with a spherically symmetric up-down-function of size ℓ . It is given by

$$\sigma_{\Delta}^2(\ell) = \left\langle \left(S(\mathbf{r}) * \odot_{\ell}(\mathbf{r}) \right)^2 \right\rangle_{\mathbf{r}}, \quad (6.5)$$

where the average is computed over all positions $\mathbf{r} = (x, y)$ on the sky. The symbol $*$ stands for a convolution and \odot_{ℓ} describes the filter function. In this paper, we use a Mexican hat with a diameter ratio of 1.5. However, we have also analyzed the impact of the filter function and the diameter ratio on the slope values of the spectra, e.g. by using a French hat with a diameter ratio of 3.0. We find that our results do not significantly depend on the specific choice of the filter function and the diameter ratio (see Appendix B.2). The differences between the individual filter functions are described in more detail in Ossenkopf et al. (2008a).

In this study we compute the Δ -variance for each possible line-of-sight direction x , y and z . As shown by Esquivel & Lazarian (2005) and Burkhart et al. (2014), the statistics of velocity centroids are very sensitive to the direction of the magnetic field in the regime of sub-Alfvénic Mach numbers. Although we use a weak magnetic field in the z -direction, the turbulence in our simulations is trans-Alfvénic or mildly

²<http://hera.ph1.uni-koeln.de/~ossk/Myself/deltavariance.html>

**Figure 6.1:**

Example of a Δ -variance spectrum, plotted as a function of spatial scale, normalized by the total box size and averaged over all available time snapshots. The inferred slope α is also indicated (solid line). The Δ -variance is computed on a CV map, where the velocities are weighted by the total density field for an initial number density of $n_0 = 300 \text{ cm}^{-3}$. The fitting range is indicated by a horizontal dashed line. Error bars denote $1\text{-}\sigma$ spatial and temporal variations.

super-Alfvénic (see Table 6.1). The field lines are essentially dragged along with the turbulent flow, with the result that the turbulence remains approximately isotropic. Hence, we do not find significant variations of the Δ -variances along the different directions. We therefore average all Δ -variances of the three line-of-sights. Finally, power-laws of the form

$$\sigma_{\Delta}^2(\ell) \propto \ell^{\alpha} \quad (6.6)$$

were fit to the Δ -variance spectra, where α denotes the slope of the power-law. To calculate the scaling exponents, we use a fitting range from $1/10$ to $1/4$ of the total box size ($0.1 \lesssim \ell/D \lesssim 0.25$), as constrained by Federrath et al. (2010) and Konstandin et al. (2012). For a box with $D = 512$ grid cells for each side this translates to 51 and 128 cells, corresponding to a physical scale of $\sim 2 - 5 \text{ pc}$ in the simulation domain. Extending the fitting range to scales above this limit is complicated since the simulations are driven on large scales, which would significantly bias our results. Additionally, the scales below our limit are influenced by the numerical resolution and the bottleneck effect (Kritsuk et al., 2007b; Konstandin et al., 2015), which is an accumulation of kinetic energy caused by the viscosity of the fluid before it

dissipates into thermal energy. Furthermore, as demonstrated by Konstandin et al. (2015), we also note that a clear and unique identification of the fitting range in numerical simulations with our resolution is complicated. Thus, the specific choice of the fitting range introduces some degree of uncertainty in the Δ -variance slopes, which we conservatively estimate to be of the order of ± 0.1 .

Fig. 6.1 shows an example of a Δ -variance spectrum computed using maps of centroid velocities inferred from our n300 run. The velocities are weighted by the total density field and the spectrum is averaged over all available time snapshots. We also show the fitting slope α for this spectrum. This slope can be translated into a linewidth-size relation, given by $\sigma_{\Delta}(\ell) \propto \ell^{\gamma}$, with a scaling exponent $\gamma = \alpha/2$. The latter equation relates the velocity fluctuations to their spatial scale, which is often referred to as Larson’s law (Larson, 1981). This relation suggests that turbulence plays an important role in the process of star formation and predicts a turbulent energy cascade within the cloud, as proposed by Kolmogorov (1941). Hence, the slopes γ characterize the turbulent velocity hierarchy in our clouds and can be directly compared to values derived from spectral observations of MCs, typically ranging from $\gamma \approx 0.2 - 0.9$ (see, e.g. Larson, 1981; Solomon et al., 1987; Brunt & Heyer, 2002b; Heyer & Brunt, 2004; Heyer et al., 2006; Sun et al., 2006; Hily-Blant et al., 2008; Roman-Duval et al., 2011; Schneider et al., 2011; Russeil et al., 2013; Elia et al., 2014; Alves de Oliveira et al., 2014; Johnston et al., 2014). For further reading about the theory of turbulence in astrophysics and fluids, we refer the reader to Burgers (1948), Benzi et al. (1993), Frisch & Kolmogorov (1995), She & Leveque (1994), Dubrulle (1994), Boldyrev et al. (2002) or Mac Low & Klessen (2004).

Furthermore, the scaling exponents α of the Δ -variance spectra are related to the power-law exponents β of the corresponding Fourier spectra via $\alpha = \beta - 1$ for 3D data (Stutzki et al., 1998), where the power-law spectrum in Fourier space is defined as

$$P(k) \propto k^{-\beta}. \quad (6.7)$$

In this equation, $k = 2\pi/\ell$ denotes the wavevector. In analogy, for a power spectrum of a 2D image, the Δ -variance is related to the power spectrum via $\alpha = \beta - 2$.

We also note that there are many other techniques to measure structural density and velocity fluctuations as a function of spatial scale, e.g. by computing structure functions (see, e.g. Hily-Blant et al., 2008; Federrath et al., 2010) or the spectral correlation function (Rosolowsky et al., 1999), by using the velocity channel analysis (Lazarian & Pogosyan, 2000, 2004) or the Principal Component Analysis (Heyer & Schloerb, 1997; Brunt & Heyer, 2002a; Bertram et al., 2014).

6.3 Results

We perform numerical simulations and apply radiative transfer post-processing to our data in order to analyze the influence of chemical inhomogeneities and optical

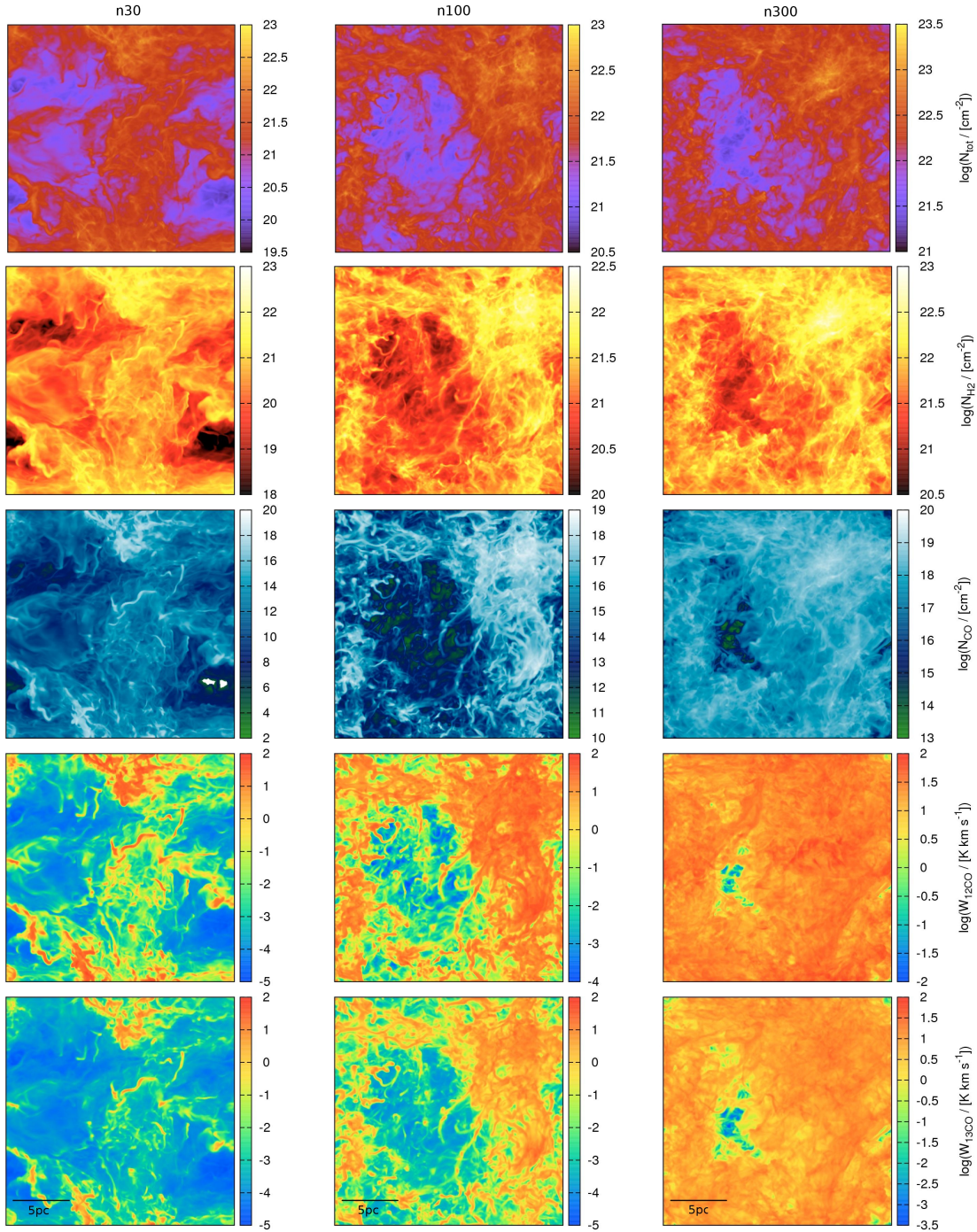


Figure 6.2:

Logarithmic maps of column density as well as velocity-integrated intensity along the z -direction for our n30 (left column), n100 (middle column) and n300 models (right column). From top to bottom we show the different chemical components: total, H_2 and CO column density as well as the integrated intensity of ^{12}CO and ^{13}CO in the $J = 1 \rightarrow 0$ transition. Each side of the simulation domain has a length of 20 pc. Note that the velocity field of the n30 model uses a different turbulent random seed than the n100 and the n300 model. Furthermore, we caution the reader that our color bars use a different scaling in the individual plots.

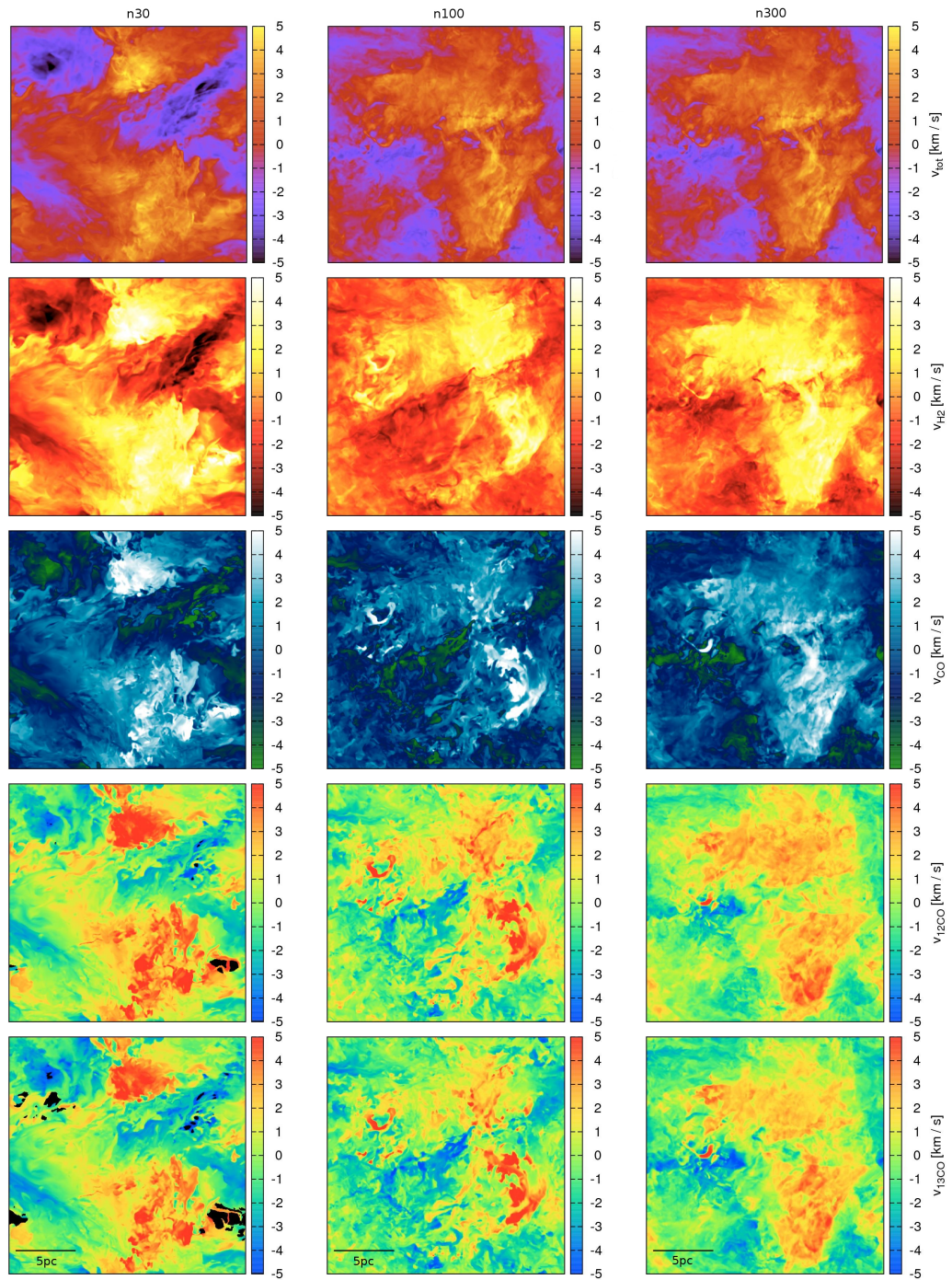


Figure 6.3:

Same as Fig. 6.2, but with maps of centroid velocities (CV). Black areas in the ^{12}CO and ^{13}CO intensity map of the n30 model denote regions where the brightness temperatures are zero along the line-of-sight. We mask these regions, because no proper centroid velocities can be computed there.

Model name	n300	n100	n30
Mean density [cm^{-3}]	300	100	30
Resolution	512 ³	512 ³	512 ³
Box size [pc]	20	20	20
t_{end} [Myr]	5.7	5.7	5.7
$\langle \mathcal{M}_s \rangle$	10.6	6.8	5.1
$\langle \mathcal{M}_A \rangle$	1.5	1.1	1.0
$\sigma_\rho / \langle \rho \rangle$	3.0	3.0	4.6
$\langle x_{\text{H}_2} \rangle_{\text{mass}}$	0.98	0.78	0.61
$\langle n_{\text{H}_2} \rangle_{\text{vol}}$ [cm^{-3}]	140	37	9
$\langle n_{\text{H}_2} \rangle_{\text{mass}}$ [cm^{-3}]	1456	447	264
$\langle n_{\text{CO}} \rangle_{\text{vol}}$ [cm^{-3}]	2.2×10^{-2}	1.7×10^{-3}	1.4×10^{-4}
$\langle n_{\text{CO}} \rangle_{\text{mass}}$ [cm^{-3}]	0.3	4.3×10^{-2}	2.3×10^{-2}
$\langle T \rangle_{\text{vol}}$ [K]	35	68	223
$\langle T \rangle_{\text{mass}}$ [K]	13	26	57
$\langle N_{\text{H}_2} \rangle$ [cm^{-2}]	8.6×10^{21}	2.3×10^{21}	5.3×10^{20}
$\langle N_{\text{CO}} \rangle$ [cm^{-2}]	1.3×10^{18}	1.1×10^{17}	8.7×10^{15}

Table 6.1:

Overview of our different models with some characteristic values measured for the last time snapshot. From top to bottom we list: mean number density, resolution, box size, time of the last snapshot, mean sonic Mach number, mean Alfvén Mach number, ratio of density dispersion and mean density, mass-weighted mean abundances of H₂ (i.e. the percentage of atomic hydrogen that has been converted to H₂, see Glover & Mac Low, 2011), mean volume- and mass-weighted H₂ and CO number densities, mean volume- and mass-weighted temperature and mean column densities of H₂ and CO.

depth effects on the Δ -variance analysis. Table 6.1 gives an overview of our numerical models. Mass- and volume-weighted quantities are defined via $\langle f \rangle_{\text{mass}} = \sum f \rho dV / \sum \rho dV$ and $\langle f \rangle_{\text{vol}} = \sum f dV / \sum dV$, respectively. For more information about the H₂ and CO distributions produced in this kind of turbulent simulation as well as integrated intensity and column density PDFs, we refer the reader to Glover et al. (2010) and Shetty et al. (2011a).

Fig. 6.2 and 6.3 show the column density and integrated intensity maps as well as the centroid velocity maps computed via equations (6.2), (6.3) and (6.4) for all models and chemical components. Regarding Fig. 6.2, we find that the total and H₂ density models show similar structures on all spatial scales, which is because most of the hydrogen is in molecular form at this time (see also Table 6.1). The CO column densities also trace similar structures, but span a much wider range of values, demonstrating that carbon monoxide has very low abundances along the low column density LoS. Furthermore, the ¹²CO and ¹³CO intensity maps also largely reflect the distribution of the carbon monoxide gas. We find that the intensity maps are much smoother and span a smaller range of values (4 – 7 orders of magnitude in integrated intensity compared to 7 – 18 orders of magnitude in column density),

which is due to the fact that the $J = 1 \rightarrow 0$ line of ^{12}CO is easily excited and can be bright even in low-density cloud regions. In the case of the ^{13}CO intensity maps, the abundance is lower by a factor of $R_{12/13} = 50$ compared to the ^{12}CO intensity models. Nevertheless, ^{13}CO is optically thin and so the peaks in the ^{13}CO maps coincide with those of the CO density models.

6.3.1 Δ -variance analysis of the CV maps

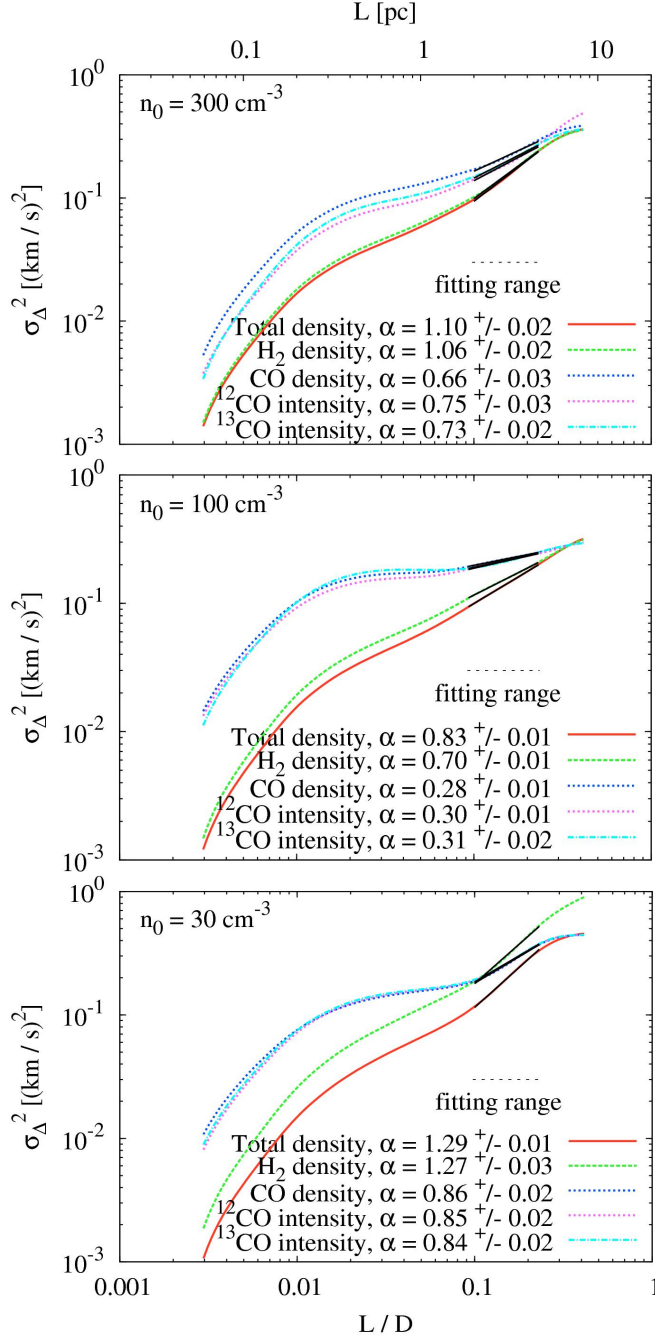
	Total density α	H ₂ density α	CO density α	^{12}CO intensity α	^{13}CO intensity α
n300	1.10 ± 0.02	1.06 ± 0.02	0.66 ± 0.03	0.75 ± 0.03	0.73 ± 0.02
n100	0.83 ± 0.01	0.70 ± 0.01	0.28 ± 0.01	0.30 ± 0.01	0.31 ± 0.02
n30	1.29 ± 0.01	1.27 ± 0.03	0.86 ± 0.02	0.85 ± 0.02	0.84 ± 0.02

Table 6.2:

Spectral slope of the Δ -variance spectrum, computed using centroid velocities weighted by the indicated quantity (see also Fig. 6.4). The errors are computed by the χ^2 fitting method. The slope α is related to the Δ -variance via $\sigma_{\Delta}^2(\ell) \propto \ell^{\alpha}$ in a linear regime. The values α can also be used to compute spectral slopes $\gamma = \alpha/2$ for a linewidth-size relation $\sigma_{\Delta}(\ell) \propto \ell^{\gamma}$, readily comparable to observational measurements.

We compute the Δ -variance for all models (n300, n100 and n30) and all chemical tracers: the total density, H₂ density, CO density, ^{12}CO and ^{13}CO intensity. We average all spectra from 3 snapshots in time (with 3 line-of-sight directions each) where we can assume both the chemistry and the turbulence to be in a stationary and converged state. Fig. 6.4 shows Δ -variance spectra as a function of spatial scale for all density models and chemical tracers, computed for the centroid velocity (CV) maps, as introduced in Section 6.2.3. Table 6.2 summarizes all slope values α obtained from a χ^2 -fit for the Δ -variance of the velocity field, $\sigma_{\Delta}^2(\ell) \propto \ell^{\alpha}$, which are also listed in each plot in Fig. 6.4.

We generally find significant differences between the various models and tracers. In our n300 model, we obtain similar slopes for the total density and the H₂ density (see Table 6.2). Regarding the spectra of those two cases, we find an excellent agreement within the values of σ_{Δ}^2 for both models, as shown in the top plot of Fig. 6.4. For the low-density model n30 (bottom plot of Fig. 6.4), we obtain a large discrepancy between the σ_{Δ}^2 values of total density and the H₂ density model. This is because in this simulation the fraction of molecular gas is much smaller than in the higher density runs and so H₂ no longer follows the total gas density (Glover et al., 2010). The H₂ density is therefore more inhomogeneous than the gas density, and as a result the centroid velocities weighted by H₂ fluctuate more on all scales than those weighted by the total density. The n100 model makes up an intermediate case between the n300 and the n30 density models. In this model, the correlation between the total and the H₂ density is worse than in the n300 case, but still better than in the n30 model.

**Figure 6.4:**

Δ -variance spectra as a function of the spatial scale, averaged over all available time snapshots and the different lines-of-sights x , y and z . The spatial scale is normalized by the total box size. From top to bottom: spectra for our three different density models, i.e. n_{300} , n_{100} and n_{30} , computed for the centroid velocity (CV) maps. In each plot we show the Δ -variance spectra for our various chemical components, i.e. for the total density, H₂ and CO density as well as for the ¹²CO and ¹³CO intensity. We use a fitting range from $1/10$ to $1/4$ of the total box size ($0.1 \lesssim \ell/D \lesssim 0.25$), as constrained by Federrath et al. (2010) and Konstandin et al. (2012), which is indicated by a horizontal dashed line and is the same in each density model. The different power-law functions in the fitting range are indicated with a black solid line on each spectrum. Furthermore, we list the slopes α and their errors from a χ^2 -fit in each plot.

Comparing the total and H₂ density models to the various CO tracers, we find that the slopes of the former are significantly steeper compared to the slopes of the latter, independent of the density (see Table 6.2). However, the Δ -variance spectra of the various CO tracers show a good agreement with each other over nearly all spatial scales. Furthermore, we always find the σ_{Δ}^2 values of the CO tracers to be significantly larger than those of the total and H₂ density. This is because CO is mainly located in denser regions of the cloud (see, e.g. Shetty et al., 2011a,b), leading to higher density contrasts compared to the total and H₂ density and thus to larger variances in velocity space.

6.3.2 Δ -variance analysis of the intensity and column density maps

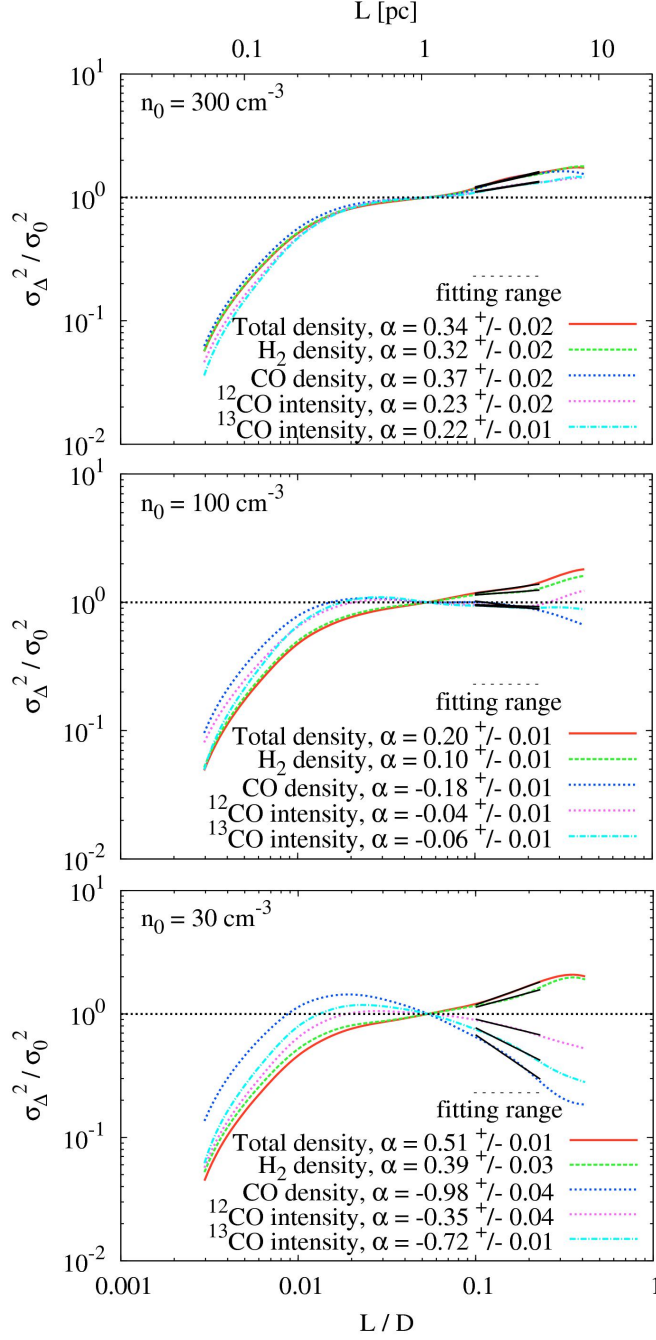
	Total density α	H ₂ density α	CO density α	¹² CO intensity α	¹³ CO intensity α
n300	0.34 ± 0.02	0.32 ± 0.02	0.37 ± 0.02	0.23 ± 0.02	0.22 ± 0.01
n100	0.20 ± 0.01	0.10 ± 0.01	-0.18 ± 0.01	-0.04 ± 0.01	-0.06 ± 0.01
n30	0.51 ± 0.01	0.39 ± 0.03	-0.98 ± 0.04	-0.35 ± 0.04	-0.72 ± 0.01

Table 6.3:

Same as Table 6.2, but for the Δ -variance computed directly from maps of integrated intensity and column density, as defined in equation (6.3) and (6.4). The corresponding Δ -variance spectra are shown in Fig. 6.5.

Beyond the Δ -variance analysis of centroid velocities, we can also apply the same method to any other quantities defined on the x - y plane. In particular, it is possible to carry out a similar analysis for the total, H₂ and CO column densities and the ¹²CO and ¹³CO integrated intensities. The results of this analysis are illustrated in Fig. 6.5. In contrast to Fig. 6.4, we normalize each curve by the corresponding Δ -variance value σ_0^2 measured at an arbitrary spatial scale of 5% of the total box, in order to better compare the spectra computed for the intensity and column density maps with each other. Furthermore, we also show a horizontal dashed line at a value of $\sigma_{\Delta}^2/\sigma_0^2 = 1$ in each plot. Table 6.3 summarizes all slope values α obtained from a χ^2 -fit for the individual Δ -variance spectra.

As for the CV maps, we find significant differences between the spectra of the various models and tracers computed using the maps of integrated intensity and column density directly. In the high-density n300 model, we find a good correlation between the total density and the H₂ density (see also the slopes in Table 6.3), for the same reasons as described in Section 6.3.1. Similarly, the low-density n30 model shows again the largest discrepancy. This is because the fraction of molecular gas is significantly smaller than in the n300 simulation, leading to different values of α . The n100 model again defines an intermediate case between the n300 and the n30 density runs. In this model, the H₂ density better correlates with the total density

**Figure 6.5:**

Same as Fig. 6.4, but computed using maps of integrated intensity and column density. In this plot, we normalize each curve by the corresponding value σ_0^2 measured at an arbitrary spatial scale of 5% of the total box, in order to better compare the spectra computed for the intensity and column density maps with each other. For a better visualization, we also show a horizontal dashed line at a value of $\sigma_{\Delta}^2 / \sigma_0^2 = 1$ in each plot. Furthermore, for clarity, we do not plot the error bars of the individual spectra here. The slopes α and their errors from a χ^2 -fit are listed in each plot for all our chemical components.

than in the low-density n30 run, but still worse than in the high-density n300 run.

Regarding the simulations of the various CO tracers, we obtain very different scaling properties compared to the total and the H₂ density simulations, depending on the mean density. In the high-density n300 model, we find a good correlation between the two CO intensity cases, while the slopes of the total and CO density models are significantly steeper. However, both the total and H₂ density as well as the various CO tracer models show the same trend in σ_{Δ}^2 over all spatial scales, having $\alpha > 0$. This situation changes in the low-density n30 model, and we find strong differences between the CO tracers and the total and H₂ density runs over all spatial scales. While the structure in the computational domain on larger scales for the total and H₂ column density can still be described by a slope $\alpha > 0$, the Δ -variance spectra for the CO tracers have negative slopes in this density run (see Table 6.3). A similar situation as in the low-density n30 simulation can be seen in the intermediate n100 density model. While we again measure $\alpha > 0$ for the total and H₂ density cases, we obtain $\alpha \lesssim 0$ for the CO tracers, meaning that the spatial distribution of observable carbon monoxide is completely different compared to the distribution of the H₂ gas in the n30 and the n100 density simulations.

Looking at Fig. 6.5, we see that the reason that we obtain negative values for α for the CO tracers in the low-density runs is that the corresponding Δ -variance spectra turn over at relatively low spatial scales. This indicates that the CO in these simulations has a characteristic spatial scale of approximately 2% of the total box size, corresponding to around 0.4 pc. This is consistent with what we see in the CO column density projections and integrated intensity maps shown in Fig. 6.2. In the low-density n30 simulation, CO is sufficiently well shielded to resist photodissociation only in the dense filaments formed by turbulent compressions. These structures are thin and contribute strongly to the Δ -variance on scales comparable to their width. Moreover, the fact that this characteristic scale is roughly the same in all CO spectra demonstrates that the radiative transfer post-processing does not significantly change the characteristic spatial cloud signatures in the Δ -variance analysis. Furthermore, ¹²CO is optically thick and thus we always find slightly steeper α slopes for the ¹²CO intensity tracers compared to the optically thin ¹³CO intensity tracers.

6.3.3 Variation of the abundance of ¹³CO

We also analyze the variation of the abundance of ¹³CO, because our simulations only follow the chemistry of ¹²CO, but not of its isotope ¹³CO. Therefore, we produce a set of ¹³CO emission maps, using a spatially varying $R_{12/13}$ generated following the prescription given in Section 6.2.2 and in Szűcs et al. (2014). After applying the radiative transfer post-processing to these maps, we compute the maps of the CV and the integrated intensity and compare the Δ -variance spectra with each other. The results agree with those as described in Bertram et al. (2015a) for the centroid velocity increment structure functions. Although we encounter slight variations on small scales for both the CV and the integrated intensity maps, the spectra of the

Δ -variance do not change significantly as we vary $R_{12/13}$. Thus, the use of a constant $^{12}\text{CO}/^{13}\text{CO}$ ratio is sufficient for obtaining proper Δ -variance spectra for ^{13}CO .

6.4 Discussion

6.4.1 Interpreting the Δ -variance spectra of the CV maps

Regarding the spectra computed on the CV maps in Fig. 6.4, we find a good correlation between the total density and the H_2 density in the n300 model. This is because $\sim 98\%$ of the initial atomic hydrogen is in molecular form at this time. Thus, the spectra of the Δ -variance for the CV maps are primarily dominated by the H_2 mass in this case. Vice versa, if we analyze the CV spectra of the n30 model, we find a larger discrepancy between the total density and the H_2 density, which is because only $\sim 61\%$ of the initial atomic hydrogen is in molecular form at this time. The n100 model is an intermediate case, with this value being $\sim 78\%$. Furthermore, we obtain a good correlation between the various CO tracer components. This indicates, that the turbulence statistics are similar for all three cases and that the impact of the radiative transfer post-processing on the Δ -variance analysis is limited. This is similar to the conclusion presented in Bertram et al. (2015a) based on the analysis of CV increment structure functions.

In general, we find that the slopes α for the total and H_2 density models are significantly steeper than the slopes for the different CO tracer models (see the values in Table 6.2). This indicates that these components have a higher relative amount of structures on larger scales compared to the different CO tracers. Furthermore, as shown by Glover et al. (2010) and Shetty et al. (2011a,b), CO is primarily a good tracer of dense and very compact regions in a cloud. Thus, this leads to less turbulent velocity structures on larger scales and hence to flatter slopes compared to those of the total and H_2 density. However, we find that the different slopes α of the various CO tracers underestimate the slopes of the total and H_2 density by a factor of $\sim 1.5 - 3.0$ (see Table 6.2).

Furthermore, we caution the reader that it is difficult to infer a clear dependence of the slopes on the mean ISM density. It is likely that the statistical measures we derive from our numerical simulations are also sensitive to the specific realization of the turbulent velocity field. Since we are studying flows which are driven on large scales, variance effects can become important, and the statistical properties depend on the random orientation of the turbulent modes as well (see, e.g. Klessen, 2000; Klessen et al., 2000). Hence, in order to obtain slopes that properly converge with the density, we speculate that a large number of simulations with various turbulent realizations would be needed in order to calculate reliable average values (see, e.g. the PCA analysis of the statistics using different realizations of the turbulent velocity field in Bertram et al., 2014). This is prohibited by the high computational costs of the individual simulations, and hence we only focus on one example in this paper, which is enough to illustrate basic trends of the Δ -variance statistics.

We also note that a direct comparison of our 2D Δ -variance statistics to 3D turbulence models is difficult, since all our 2D maps are a complex convolution of the 3D density field (or the brightness temperatures) with the 3D velocity field. Various different physical processes can influence the CV statistics, as shown by previous studies. For example, Lazarian & Pogosyan (2004), Burkhardt et al. (2013a) and Burkhardt et al. (2014) analyzed the impact of the sonic Mach number on the CV statistics, finding that it can significantly alter the results. Moreover, Lazarian & Esquivel (2003), Ossenkopf et al. (2006), Esquivel et al. (2007), Hily-Blant et al. (2008) and Federrath et al. (2010) studied the effects of the turbulent driving as well as temperature and density fluctuations on the CV statistics, also finding significant differences in the statistics and in the inferred CV slopes. Nevertheless, although a direct comparison of the 2D statistical quantities to 3D measures is complicated, we can safely use the 2D Δ -variance analysis in order to work out statistical trends measured in the spectra of the individual models.

6.4.2 Interpreting the spectra of intensity and column density maps

In Section 6.3.1 and 6.3.2 we already justified the correlation between the total and the H_2 density runs in all our density models and compared the different slopes α from Table 6.3 with each other. Furthermore, we established that the observed CO gas distribution in the low-density n30 model does not reflect the spatial distribution of molecular hydrogen very well. This is because CO is mainly located in the dense filaments, while H_2 is more space-filling and distributed over the total cloud, owing to its greater ability to resist photodissociation. Consequently, the Δ -variance spectra of the CO tracers peak at a scale corresponding to the width of these structures. Hence, if we apply the Δ -variance analysis to the maps of integrated intensity or column density, we can obtain important information about the turbulently created high-density peaks within the MC (see also the discussion in Ossenkopf et al., 2001). However, we also note that the physical connection of our slopes α from Table 6.3 to observational measurements is complicated, since observations typically probe smaller spatial scales, which our simulations are not sensitive to due to the limited numerical resolution.

If we compare the CO tracers with the total and H_2 density in the n300 model, we find that the carbon monoxide better reproduces the statistical trends of molecular hydrogen in this high-density run compared to the low-density n30 model. In the n300 run, we generally obtain $\alpha > 0$ for all chemical components, i.e. we find more cloud structures on larger spatial scales. In contrast to the low-density n30 model, this is because carbon monoxide is not only confined to small dense filaments, but instead is distributed over the whole molecular cloud. In particular, a significant amount of CO gas can also be observed between the numerous dense cloud regions. Consequently, we see the Δ -variance spectra peaking at the largest scales, consistent with observational efforts and previous work on this field (see, e.g. Stutzki et al.,

1998; Ossenkopf et al., 2001; Bensch et al., 2001; Sun et al., 2006; Schneider et al., 2011; Russeil et al., 2013; Alves de Oliveira et al., 2014; Elia et al., 2014).

However, regarding the general trend of the slopes α from the n30 to the n300 via the n100 model, we find that the values of α for the CO tracers change sign above a critical density of $\sim 100 \text{ cm}^{-3}$. This is about the number density at which all values α become positive. Thus, we conclude that carbon monoxide traces our total cloud structure well only if the average cloud density lies significantly above a critical threshold of $\sim 100 \text{ cm}^{-3}$. If the mean density in the cloud is significantly smaller than this limit, the observable CO gas does not properly trace the statistical properties of the H_2 gas in the cloud. We speculate that one may also see a similar switch from CO tracing all of the structures to only the dense cores and filaments if one increases the incident field strength or decreases the metallicity, as in both cases, this makes it much easier to photodissociate the diffuse CO (see, e.g. Glover & Clark 2012; Bertram et al. 2015b, submitted). On the contrary, if the mean density in the cloud is too high, CO becomes optically thick and so we suspect that there should also exist an upper density limit above which CO does not properly trace structures of the cloud anymore. We leave such an analysis for further investigations.

6.4.3 Comparison of the Δ -variance to other statistical tools

We have previously applied several other statistical methods to the same set of simulation data in order to study the structural behavior of MCs. For example, Bertram et al. (2014) applied Principal Component Analysis (PCA) to the same data used in this paper, while Bertram et al. (2015a) carried out a similar study using centroid velocity increment structure functions (CVISF) and Fourier spectra.

Comparing the results of the different methods with each other, we generally find consistent results between the different statistical analysis methods. For example, the slopes of the CVISF for the total density and H_2 density models are also significantly steeper compared to the various CO tracers, which is in good agreement to the results of the Δ -variance analysis in this paper. The same holds for the relative scaling of the different CO models, which is the same in the analysis of the CVISF and the Δ -variance. Interestingly, we also find a close relation between the PCA structure analysis and the spectra of the Δ -variance for the CO tracers. The PCA method does not find any structures on larger scales for the CO tracers in the n30 model as well as for some single CO tracers in the n100 model. This result can also be reproduced in the different CO spectra of the Δ -variance analysis, i.e. where the gradient of the individual spectra become negative at a characteristic scale of $\sim 0.4 \text{ pc}$, as described in Sections 6.3.2. This is the situation where small clumpy structures of CO gas dominate the overall composition of carbon monoxide in the MC. In this case, the Δ -variance shows that the most dominant CO structures in the simulation domain can be found at small scales, leading to completely missing principal components on scales larger than $\sim 1 \text{ pc}$, as presented in Fig. 3 in Bertram et al. (2014). Hence, applying the Δ -variance analysis to maps of integrated intensities or column densities gives an idea about characteristic spatial scales in the cloud

of interest. The Δ -variance thus provides a good statistical tool in order to study the relative gas distribution on various cloud scales.

These results indicate that all these various statistical methods are connected to each other and that characteristic structural properties of the MC should be traced by each of them individually. Hence, all various statistical methods have proven to yield reasonable results for the structure analysis of MCs. Nevertheless, the advantage of the Δ -variance method is that it is fast and easy to implement, while the computation of structure functions and principal components is more expensive. Thus, the Δ -variance analysis provides a useful and adequate tool in order to quickly study the internal structure of a cloud. However, the advantage of the structure function analysis is that their results can be easily compared to theoretical models of turbulence.

6.4.4 Previous studies of CV maps

Several studies tried to compute the Δ -variance spectra of CV maps in the past and estimated turbulent slope values α from observational measurements. For example, Ossenkopf et al. (2008b) used optically thick ^{12}CO ($J = 1 \rightarrow 0$) maps of the Polaris Flare to compute centroid velocity maps and to estimate the slope α . The Polaris flare is an archetype of a cloud midway between the diffuse and the molecular phases (Heithausen & Thaddeus, 1990; Meyerdierks & Heithausen, 1996; Falgarone et al., 1998; André et al., 2010; Miville-Deschênes et al., 2010). It is supposed to have a low average density and thus can be compared to our n30 low-density model. Adopting the same ^{12}CO tracer, we find a value of $\alpha = 0.85 \pm 0.02$, in agreement with the estimate of $\alpha \approx 0.9$ found by Ossenkopf et al. (2008b).

Moreover, Ossenkopf & Mac Low (2002) computed the slope α for hydrodynamic supersonic simulations driven at different wavenumbers. They find one power-law range for all models and obtain $\alpha \approx 1.0$, which fits into our range of power-law slopes α from 0.8 – 1.3 for the total density models. Furthermore, Federrath et al. (2009) computed Δ -variance slopes for numerical simulations with both solenoidal and compressive forcing, finding a similar range of α values from 0.8 – 1.4 for the turbulent velocity field. However, these simulations only use supersonic isothermal turbulence, while our runs include more complex physics, e.g. a chemical network, heating and cooling, various initial number densities or the coupling to the radiation field. Thus, if we compare the total variations of slopes α in their and in our models, we find that the influence of the different forcing methods on the slopes α in their simulations is large, while the impact of our additional physical effects (varying density, optical depth effects, etc.) on the slope values remains comparatively small.

6.4.5 Previous studies of intensity and column density maps

As well as computing Δ -variance spectra for maps of centroid velocities, several studies also applied the Δ -variance to maps of integrated intensity or column density.

For example, Bensch et al. (2001) computed Δ -variance spectra on maps of velocity-integrated intensity for ^{12}CO and ^{13}CO ($J = 1 \rightarrow 0$) for various MCs in the Galaxy. Stutzki et al. (1998) analyzed the Δ -variance of an observed ^{12}CO ($J = 1 \rightarrow 0$) image of the Polaris flare as a whole, while Ossenkopf et al. (1998) studied the intensity map of one of its subclouds, MCLD 123.5+24.9.

Comparing all the various Δ -variance spectra in Bensch et al. (2001) or Stutzki et al. (1998) with each other, we find a value $\alpha > 0$ for each of them in the given fitting range, i.e. the spectra increase with increasing spatial lag. At first sight, this is in contradiction to the results that we obtain in this study, where we measure $\alpha < 0$ for the various CO tracers in the n30 and n100 model, given our fitting range. However, this is primarily due to the fact that our Δ -variance spectra peak at roughly the scale of small carbon monoxide clumps in the low-density clouds (see Section 6.4.2). Accordingly, we find more cloud structures on the scales of those localized CO structures, leading to negative α slopes in Figure 6.5. A similar effect can be seen in the Δ -variance analysis of ^{13}CO ($J = 1 \rightarrow 0$) maps of the outer Galaxy shown in Figure 3 of Stutzki et al. (1998). On small scales, a positive power-law slope is recovered, but on large scales α becomes negative as one starts to smooth on scales larger than the typical size of the observed MCs. The same situation is also illustrated in the Δ -variance spectra in Schneider et al. (2011) for the ^{13}CO ($J = 1 \rightarrow 0$) molecular line survey of Cygnus X as well as in a ^{13}CO ($J = 2 \rightarrow 1$) study of the Perseus cloud in Sun et al. (2006), which peak at intermediate cloud scales. However, a Δ -variance analysis of the small sub-regions NGC1333 and L1455 in the Perseus molecular cloud complex shows that α is always positive (see Fig. 6 in Sun et al., 2006), which is in agreement with our finding that a positive slope α might be related to a Δ -variance analysis at lower spatial cloud scales, probing only very localized CO structures. Moreover, Alves de Oliveira et al. (2014) analysed the Chamaeleon molecular cloud complex using data from the Herschel Gould Belt Survey. This complex encompasses three MCs with different star formation histories. One of them is a quiescent cloud, which should be best comparable to our numerical simulations, since we neglect the effects of self-gravity. The Δ -variance analysis of this MC also shows a clear break at mid to large scales (see cloud Cha III in Fig. 5 in Alves de Oliveira et al., 2014), also displaying a characteristic spatial scale in the column density structure.

In our high-density n300 run, the CO gas is distributed over the whole MC and not only confined to small dense fragments. In this case, we also find cloud structures on larger spatial scales, leading to positive α slopes in Figure 6.5.

6.4.6 Model limitations

Since we are running numerical simulations, we have to keep in mind that our runs are subject to various physical simplifications. In the current analysis, we focus on the impact of the chemistry and the opacity of the gas on our results, thus neglecting other physical processes that could bias our analysis. In first instance, we do not account for self-gravity and thus also do not model star formation or stellar

feedback. More specifically we do not account for stellar radiation, SN feedback and other physical processes. We also do not include any large-scale dynamics, e.g. spiral arms or galactic rotation, although these are unlikely to be important on the 20 pc scale studied here. Nevertheless, we can infer useful information about how the chemical composition of the gas and the opacity affect the Δ -variance analysis. We also note that our results depend only weakly on the resolution and that this concerns mostly CO as a tracer molecule, as we show in Appendix B.1. For future investigations, we want to analyze simulations that span a wider range of physical parameters, e.g. with different levels of the external radiation field, varying metallicities or additional physical processes, in order to find out how they affect the statistics.

6.5 Summary and Conclusions

We analyzed Δ -variance spectra of MCs with time-dependent chemistry and radiative transfer post-processing for models of different initial number densities and chemical components: the total number density, H₂ and CO density (each without radiative transfer) as well as ¹²CO ($J = 1 \rightarrow 0$) and ¹³CO ($J = 1 \rightarrow 0$) intensity (both with radiative transfer). In each case, we computed Δ -variance spectra for maps of centroid velocities (CV), integrated intensities and column densities and analyzed the structural behavior of MCs in numerical simulations. We report the following findings:

- We compute Δ -variance spectra of maps of centroid velocities and fit a power-law $\sigma_{\Delta}^2(\ell) \propto \ell^{\alpha}$, in order to characterize the properties of the turbulent hierarchy in the MCs. This power-law can be translated into a linewidth-size relation, i.e. $\sigma_{\Delta}(\ell) \propto \ell^{\gamma}$ with $\gamma = \alpha/2$, readily comparable to slopes that can be derived from spectral observations. We find the slopes α of both the total and H₂ density models to be significantly steeper than the slopes of the different CO tracers, which underestimate the former by a factor of $\sim 1.5 - 3.0$ (see Section 6.3.1).
- The slopes α derived from the CV maps range from 0.8 to 1.3 for the total and H₂ density, while α for the various CO tracers range from 0.3 to 0.8 (see Section 6.3.1). However, we also note that the specific choice of the fitting range might cause further variations of the slopes by ± 0.1 .
- Although we find slight variations between the different slopes α for our various CO models obtained from the CV maps, the impact of the optical depth effects on the spectra computed on maps of centroid velocities remains limited (see Table 6.2).
- This is different in the case of the integrated intensity and column density. The Δ -variance computed from these maps is strongly affected by optical

depth effects. The CO tracers exhibit a very different spatial scaling behavior compared to the total and H₂ density models (see Table 6.3 and Figure 6.5).

- We report a critical number density threshold of $\sim 100 \text{ cm}^{-3}$ at which the spectral slopes α of the CO tracers switch sign for the Δ -variance of integrated intensity and column density maps. We conclude that carbon monoxide traces the total cloud structure well only if the average cloud density lies significantly above this threshold. If the mean density in the cloud is significantly smaller than this limit, the observable CO gas does not properly trace the statistical properties of the H₂ gas in the cloud (see Section 6.3.2).
- The Δ -variance spectra computed on maps of integrated intensity and column density provide a useful statistical measure in order to infer important information about the distribution of gas within a cloud. We also argue that peaks in the Δ -variance spectra correspond to characteristic scales of the morphological structure of the system (see Section 6.3.2).
- Our findings are consistent with previous Δ -variance studies using CO line observations or measurements of the continuum (see Section 6.4.4 and 6.4.5).

Star formation efficiencies of MCs in a galactic center environment

We use the AREPO moving mesh code to simulate the evolution of molecular clouds exposed to a harsh environment similar to that found in the galactic center (GC), in an effort to understand why the star formation efficiency (SFE) of clouds in this environment is so small. Our simulations include a simplified treatment of time-dependent chemistry and account for the highly non-isothermal nature of the gas and the dust. We model clouds with a total mass of $1.3 \times 10^5 M_{\odot}$ and explore the effects of varying the mean cloud density and the virial parameter, $\alpha = E_{\text{kin}}/|E_{\text{pot}}|$. We vary the latter from $\alpha = 0.5$ to $\alpha = 8.0$, and so many of the clouds that we simulate are gravitationally unbound. We expose our model clouds to an interstellar radiation field (ISRF) and cosmic ray flux (CRF) that are both a factor of 1000 higher than the values found in the solar neighbourhood. As a reference, we also run simulations with local solar neighbourhood values of the ISRF and the CRF in order to better constrain the effects of the extreme conditions in the GC on the SFE. Despite the harsh environment and the large turbulent velocity dispersions adopted, we find that all of the simulated clouds form stars within less than a gravitational free-fall time. Increasing the virial parameter from $\alpha = 0.5$ to $\alpha = 8.0$ decreases the SFE by a factor $\sim 4 - 10$, while increasing the ISRF/CRF by a factor of 1000 decreases the SFE again by a factor $\sim 2 - 6$. However, even in our most unbound clouds, the SFE remains higher than that inferred for real GC clouds. We therefore conclude that high levels of turbulence and strong external heating are not enough by themselves to lead to a persistently low SFE at the center of the Galaxy. The results presented in this chapter are published in Bertram et al. (2015c).

7.1 Introduction

Understanding star formation is an important task in theoretical astrophysics (see e.g., Mac Low & Klessen, 2004; Scalo & Elmegreen, 2004; Elmegreen & Scalo, 2004; McKee & Ostriker, 2007; Ballesteros-Paredes et al., 2007). Stars form in molecular clouds (MC) in the interstellar medium (ISM) due to gravitational contraction of overdense gas regions (see also the lecture notes by Klessen & Glover, 2014). Several studies in the past have revealed that the number of stars formed per unit time (referred to as the star formation rate or SFR) is proportional to the amount of gas in the star-forming region (see e.g., Schmidt, 1959; Kennicutt, 1998b) and that the SFR surface density shows a power-law dependence on the gas surface density. This is known as the Schmidt-Kennicutt relation and is an important empirical result in star formation theory. It appears to hold in the disk of our Milky Way and also in distant galaxies (Kennicutt & Evans, 2012). However, there is still some debate about whether a universal relationship holds for all galaxies or not (see, e.g. Shetty et al., 2013, 2014).

As shown by Longmore et al. (2013a), the inner 500 pc region of our Galaxy, known as the Central Molecular Zone (CMZ), contains the largest reservoir of dense gas in the Milky Way, with densities of order of several 10^3 cm^{-3} and a total mass of about $10^7 M_{\odot}$. This would be enough to form several Orion-like clusters, but the measured SFR is significantly smaller (Longmore et al. 2013a). This is a direct contradiction to the Schmidt-Kennicutt relation, which would predict a high SFR in the center of our Galaxy. The key questions are, why on one hand the observed SFR is suppressed by a factor of $\gtrsim 10$ (Longmore et al. 2013a) and on the other hand which physical processes regulate star formation in the central few hundred parsecs of the Milky Way (see, e.g. Longmore et al. 2013a, Kruijssen et al. 2014, Krumholz & Kruijssen 2015).

Several studies have tried to solve this problem of star formation in such an extreme environment, which challenges current star formation theories. For example, Kruijssen et al. (2014) studied the impact of several mechanisms on the SFR on different physical scales, e.g. the very strong radiation field, magnetic fields, turbulent pressure, galactic tides or feedback. They argue that star formation could be episodic due to a gradual build-up of dense gas by spiral instabilities or that variations in the rates of gas flows into the CMZ might significantly alter the star formation process. Longmore et al. (2013a) state, for example, that the order of magnitude higher internal velocity dispersion could disrupt compact regions before they are able to go into gravitational collapse. However, the question of what physical processes are most important for regulating the SFR in the galactic center (GC) remains unresolved.

One important way in which we can distinguish between different models for the regulation of star formation in the GC is by examining whether they produce low star formation efficiencies by reducing the formation of stars in the individual dense clouds present in the CMZ, or whether they instead merely regulate the rate

at which molecular gas is allowed to form these dense clouds. The presence of a number of massive, dense clouds in the CMZ that do not appear to be currently forming stars provides a hint that the star formation efficiencies of individual clouds in the CMZ might be low. An example of such a cloud, which is almost devoid of star formation, is also known as “The Brick” (see e.g. Güsten et al. 1981; Lis et al. 1994; Lis & Menten 1998; Lis et al. 2001; Molinari et al. 2011; Immer et al. 2012; Longmore et al. 2012; Kauffmann et al. 2013; Clark et al. 2013; Johnston et al. 2014; Rathborne et al. 2014; Kruijssen et al. 2015; Pillai et al. 2015, as well as Longmore et al. 2013b for a discussion of several other dense starless clouds close to the Brick that have similar properties). On the other hand, it is also possible that we are just observing the Brick and its neighbouring starless clouds at a very early time in their evolution, before they have started to form stars. This question is difficult to resolve observationally, but numerical simulations can help us to understand which of the possibilities is more likely.

In this paper we investigate the impact of a strong interstellar radiation field (ISRF) and a high cosmic ray flux (CRF) on the SFR in clouds with different initial number densities and varying levels of turbulence. We change the amount of turbulent kinetic energy E_{kin} with respect to the potential energy E_{pot} , as parameterized by $\alpha = E_{\text{kin}}/|E_{\text{pot}}|$ (see Section 7.2.3). We focus on the question of whether such a high ISRF/CRF combined with a high level of turbulence could be the main physical drivers to suppress star formation in the GC. Therefore, we adopt environmental conditions that are similar to those experienced by a typical GC cloud. In particular, we adopted values for the ISRF strength and the CRF comparable to those inferred for the Brick. We model the behaviour of different MCs exposed to this environment using the AREPO moving mesh code (Springel, 2010) and explore the effect of changing their density and turbulent velocity dispersion. For technical reasons, the clouds we model have lower densities than typical GC clouds, and so should be less likely to form stars than real GC clouds. Despite this and despite the harshness of their environment, it proves to be very difficult to suppress star formation within the clouds, as we will see in the following sections.

The structure of our paper is as follows. In Section 7.2 we present the simulations and the methods used in this paper. In Section 7.3 we present the results of our studies with different virial α parameters and various initial number densities. We discuss our results in Section 7.4 and present our conclusions in Section 7.5.

7.2 Methods and simulations

7.2.1 Computational method

Our simulations are performed using the moving mesh code AREPO (Springel, 2010), which uses an unstructured mesh defined by the Voronoi tessellation of a set of discrete points. We make use of a detailed atomic and molecular cooling function, described in detail in Glover et al. (2010) and Glover & Clark (2012b), and a simplified

treatment of the molecular chemistry of the gas. Our chemical treatment is based on the work of Nelson & Langer (1997) and Glover & Mac Low (2007), and allows us to follow the formation and destruction of H_2 and CO self-consistently within our simulations. Full details of the chemical model with a description of how the chemistry interacts with the ISRF via the TREECOL algorithm can be found in Clark et al. (2012). Examples of the use of our chemical model with the AREPO code can be found in Smith et al. (2014a) and Smith et al. (2014b).

We assume that the gas has a uniform solar metallicity and adopt the standard ratio of helium to hydrogen, and abundances of carbon and oxygen taken from Sembach et al. (2000), i.e. $x_{\text{C}} = 1.4 \times 10^{-4}$ and $x_{\text{O}} = 3.2 \times 10^{-4}$, where x_{C} and x_{O} are the fractional abundances by number of carbon and oxygen relative to hydrogen. However, we have to keep in mind that the CMZ has actually a super-solar metallicity. Nevertheless, we use a uniform solar value in order to be conservative regarding the cooling and star formation rates in our runs. At the start of the simulations, hydrogen, helium and oxygen are in atomic form, while carbon is assumed to be in singly ionized form, as C^+ . We also adopt the standard local value for the dust-to-gas ratio of 1:100 (Glover et al., 2010), and assume that the dust properties do not vary with the gas density. The cosmic ray ionization rate of atomic hydrogen is set to $\zeta = 3 \times 10^{-14} \text{ s}^{-1}$ (Clark et al., 2013), which is a factor of ~ 1000 higher than the value in the solar neighbourhood (Yusef-Zadeh et al., 2007). For the incident ultraviolet radiation field, we adopt the same spectral slope as given in Draine (1978). We denote the strength of the Draine ISRF as $G_0 = 1$ and perform simulations with a field strength $G_0 = 1000$ (Clark et al., 2013). The Draine field has a strength $G_0 = 1.7$ in Habing (1968) units, corresponding to an integrated flux of $2.7 \times 10^{-3} \text{ erg cm}^{-2} \text{ s}^{-1}$. Furthermore, as a reference, we also run simulations with local solar neighbourhood values of the ISRF and the CRF in order to explore the effect of a different radiation field on the SFE. In this case, we set the field strength of the ISRF to $G_0 = 1$ and the cosmic ray ionization rate of atomic hydrogen to $\zeta = 3 \times 10^{-17} \text{ s}^{-1}$. Our simulations use a Jeans refinement criterion, which is active over the whole simulation period in order to accurately refine dense and collapsed gas regions in the box. We use a constant number of 8 cells per Jeans length, which is sufficient to avoid artificial fragmentation (Truelove et al., 1998; Greif et al., 2011).

7.2.2 Sink particles

Furthermore, we make use of a sink particle implementation (Greif et al., 2011) based on the prescription in Bate et al. (1995) and Jappsen et al. (2005), to track the star formation process during the simulations. Before a cell is turned into a sink particle, it undergoes a series of tests. First, the particle must reach a critical density threshold of $n_{\text{thresh}} \approx 10^7 \text{ cm}^{-3}$. This value was chosen to be higher than the typical post-shock densities found in the clouds to ensure that we do not attempt to form sinks in regions that are not gravitationally collapsing. For our more extreme run with $n_0 = 10^4 \text{ cm}^{-3}$ we adopt a higher threshold of $n_{\text{thresh}} \approx 10^9 \text{ cm}^{-3}$ in order to account for the two orders of magnitude higher density on average. The second

test is to check whether the new sink particle is sufficiently far away from any other sink particle, measured in terms of one accretion radius r_{acc} . The third is to check whether the size of the cell is less than the accretion radius of the sink particle that it will become.

We set the accretion radius to a constant value of $r_{\text{acc}} \sim 0.01 \text{ pc}$, roughly corresponding to the scale of the thermal Jeans length for a sink particle formation threshold of $n_{\text{thresh}} \approx 10^7 \text{ cm}^{-3}$ at a mean gas temperature of $\sim 20 \text{ K}$. For our model with a threshold of $n_{\text{thresh}} \approx 10^9 \text{ cm}^{-3}$, we adopt the same value for the accretion radius. This is also a reasonable estimate for this higher density model, since more checks will guarantee that the gas is bound and collapsing onto the sink particle. In addition, we explore whether a different value of r_{acc} might have a significant impact on the SFEs by running a simulation in which we increased r_{acc} by a factor of 10. We find that in this case, the SFE increases by around a factor of 1.1 – 1.3. In view of the various error sources for estimating a star formation efficiency per free-fall time (see also the discussion in Section 7.3.1), we find that a different accretion radius does not significantly affect the results of this paper. This is because we are mainly interested in estimating the total mass that goes into gravitational collapse instead of measuring precise SFEs.

Once these preliminary criteria are fulfilled, more checks guarantee that this potential sink particle is in a correct dynamical state. In a first test, we require that the particle is sub-virial, i.e. it needs to fulfill the condition $\alpha \leq 0.5$, where α is the ratio of kinetic and gravitational energy. Second, we ensure that $\alpha + \beta \leq 1$, where β is the ratio of rotational and gravitational energy. Third, we require $\text{div}(\mathbf{a}) < 0$, where \mathbf{a} is the acceleration, which ensures that the particle is not tidally disrupted or bouncing. If all these conditions are achieved, the local gas condensation can become a sink.

7.2.3 Important quantities

In this study, we use the virial α parameter to regulate the amount of turbulent kinetic energy in the simulation domain. We define this as

$$\alpha = \frac{E_{\text{kin}}}{|E_{\text{pot}}|}, \quad (7.1)$$

where E_{kin} and E_{pot} denote the total kinetic and potential energy in the box at the start of the simulation, given via

$$E_{\text{kin}} = \frac{1}{2} M_{\text{tot}} \sigma_v^2 \quad (7.2)$$

and

$$E_{\text{pot}} = -\frac{3GM_{\text{tot}}^2}{5R}. \quad (7.3)$$

In this context, σ_v denotes the turbulent 3D velocity dispersion, M_{tot} and R the total mass and radius of the (initially) uniform sphere and G the gravitational constant. Furthermore, we use

$$M_{\text{tot}} = \frac{4}{3}\pi R^3 \rho, \quad (7.4)$$

where ρ is the initial mass density. However, we note that the virial parameter is also often defined via $\alpha = 2E_{\text{kin}}/|E_{\text{pot}}|$ in the literature, which is different from the notation used above. In our definition, a value of $\alpha = 0.5$ defines virialized clouds, $\alpha = 1.0$ denotes clouds with energy equipartition and $\alpha > 1.0$ describes clouds that are (highly) unbound. In addition, we can estimate the crossing time from these quantities via $t_{\text{cross}} \approx R/\sigma_v$.

Furthermore, we quantify the amount of gas mass being converted to stars (i.e. sink particles) due to gravitational collapse within one free-fall time t_{ff} as

$$\epsilon_{\text{ff}} = t_{\text{ff}} \cdot \frac{\dot{M}_*}{M_{\text{tot}}}, \quad (7.5)$$

where \dot{M}_* is the star formation rate in the computational domain averaged over t_{ff} (Krumholz & McKee, 2005; Krumholz & Tan, 2007; Murray, 2011). The parameter ϵ_{ff} is thus a measure of the star formation efficiency (SFE) of each model. The free-fall timescale itself is defined via

$$t_{\text{ff}} = \sqrt{\frac{3\pi}{32G\rho}}. \quad (7.6)$$

In this paper, we compute ϵ_{ff} for all clouds individually and compare our results to the average SFE inferred for the galactic center region. It is therefore important to emphasize that our study is aimed at testing the idea that the SFE at the galactic center is low because the SFE of the individual dense clouds is low. With our isolated cloud models, we cannot test the competing idea that the SFE of the region is low because it is difficult to form dense clouds there.

7.2.4 Initial conditions and model parameters

For simplicity, we assume that the cloud is initially spherical and embedded in a low-density environment. Furthermore, we apply periodic boundary conditions. We perform two sets of runs in which we vary the virial α parameter, using values $\alpha = 0.5, 1.0, 2.0, 4.0$ and 8.0 . In the first set of runs, we take an initial hydrogen nuclei number density of $n_0 = 100 \text{ cm}^{-3}$ for the cloud. In the second set of runs, we take a number density of 1000 cm^{-3} . In all of our simulations, the density of the gas surrounding the cloud is $\approx 1 \text{ cm}^{-3}$. We use a total mass of $M_{\text{tot}} = 1.3 \times 10^5 M_{\odot}$ and an initial total number of 2×10^6 cells for the whole box, including the low-density regions. The initial cell mass within the uniform cloud corresponds to $\approx 2 M_{\odot}$.

Model name	Virial α	Density n_0 [cm^{-3}]	Radius R [pc]	Velocity σ_v [km/s]	Time t_{ff} [Myr]	ISRF & CRF
GC-0.5-100	0.5	100	19.1	3.7	4.4	1000
GC-1.0-100	1.0	100	19.1	5.2	4.4	1000
GC-2.0-100	2.0	100	19.1	7.4	4.4	1000
GC-4.0-100	4.0	100	19.1	10.5	4.4	1000
GC-8.0-100	8.0	100	19.1	14.7	4.4	1000
GC-0.5-1000	0.5	1000	8.9	5.4	1.4	1000
GC-1.0-1000	1.0	1000	8.9	7.6	1.4	1000
GC-2.0-1000	2.0	1000	8.9	10.8	1.4	1000
GC-4.0-1000	4.0	1000	8.9	15.3	1.4	1000
GC-8.0-1000	8.0	1000	8.9	21.6	1.4	1000
GC-16.0-10000	16.0	10000	4.1	44.9	0.4	1000
SOL-0.5-1000	0.5	1000	8.9	5.4	1.4	1
SOL-8.0-1000	8.0	1000	8.9	21.6	1.4	1
The Brick	1.0	7.3×10^4	2.8	16.0	0.34	$\sim 100 - 1000$

Table 7.1:

Initial conditions for our different cloud models. For each run, we list the virial α parameter, the initial number density, the spherical cloud radius, the velocity dispersion, the free-fall time and the scaling factor of the interstellar radiation field (ISRF) and the cosmic ray flux (CRF) relative to the solar neighbourhood value. For comparison, we also list the parameters for the GC cloud G0.253+0.016, known as “the Brick”, which are given in Table 2 in Longmore et al. (2012).

Given these parameters, we can compute the radii and the initial velocity dispersions of the clouds. The cubic side lengths of the total simulation domain are set to $5 \times$ the individual cloud radii. All clouds are initially at rest and placed in the center of the box. We use an initial random velocity field with a power spectrum of $P(k) \propto k^{-4}$ that consists of a natural mixture of solenoidal and compressive modes, which decays throughout the simulation. The timesteps between the individual snapshots are $\Delta t_{\text{snap}} \approx 22 \text{ kyr}$ and $\Delta t_{\text{snap}} \approx 7 \text{ kyr}$ for models with initial number densities of $n_0 = 100 \text{ cm}^{-3}$ and 1000 cm^{-3} , respectively, corresponding to ~ 200 snapshots per simulation in total.

In addition, we have also modelled an even more extreme cloud with an initial number density of $n_0 = 10^4 \text{ cm}^{-3}$ and a virial α parameter of $\alpha = 16.0$. In this case, we set $\Delta t_{\text{snap}} \approx 2 \text{ kyr}$ for the same total number of time snapshots. However, running further simulations with $n_0 \geq 10^4 \text{ cm}^{-3}$ and $\alpha < 16.0$ is computationally prohibitive, owing to the rapid rate at which stars form in these models. For this reason we only focus on this one more extreme numerical model. Nevertheless, as we discuss in more detail later, such a high α run alone is still enough for our study, since even in this extreme case, the cloud still forms a substantial number of stars. Furthermore, regarding the densities in the CMZ, we have to keep in mind that a significant number of GC clouds have densities higher than those modelled in our

Model name	$\epsilon_{\Delta t}$ [%]	ϵ_{ff} [%]	N_{sink}	t_* [Myr]	t_{end} [Myr]	Δt [Myr]
GC-0.5-100	8.2	25.7	3473	1.30	2.70	1.40
GC-1.0-100	8.5	28.5	4699	1.80	3.12	1.31
GC-2.0-100	8.5	19.1	4166	1.84	3.80	1.96
GC-4.0-100	6.2	14.8	2511	2.56	4.44	1.84
GC-8.0-100	2.3	6.1	644	2.75	4.44	1.65
GC-0.5-1000	4.5	10.9	2966	0.42	1.00	0.58
GC-1.0-1000	4.6	8.0	2531	0.28	1.10	0.82
GC-2.0-1000	6.8	8.0	3218	0.22	1.40	1.18
GC-4.0-1000	2.6	2.9	1035	0.16	1.40	1.24
GC-8.0-1000	0.6	0.7	180	0.12	1.40	1.28
GC-16.0-10000	0.7	0.7	1406	0.02	0.40	0.38
SOL-0.5-1000	5.1	13.2	16248	0.21	0.75	0.54
SOL-8.0-1000	4.3	4.6	8617	0.08	1.40	1.32

Table 7.2:

The star formation efficiencies $\epsilon_{\Delta t}$ give the amount of gas being converted to sink particles within a time $\Delta t = t_{\text{end}} - t_* < t_{\text{ff}}$, where t_{end} denotes the end of our simulation and t_* the time when the first star forms. N_{sink} gives the total number of sink particles formed during the time Δt . To calculate the SFEs per free-fall time, ϵ_{ff} , we extrapolate based on $\epsilon_{\Delta t}$, assuming that the SFR between t_{ff} and t_{end} is the same as between t_* and t_{end} . Some simulations with lower α values are not evolved until one free-fall time, which is due to the high computational costs of the individual runs. Nevertheless, we let all those simulations evolve until a $\epsilon_{\Delta t}$ of at least $\sim 4\%$ is reached.

simulations, which would lead to even larger turbulent velocities in our simulations for the same constant total mass. Table 7.1 gives an overview about the different numerical models and their initial conditions.

7.3 Results

7.3.1 Analysis of the model clouds

Fig. 7.1 shows logarithmic column density maps of the different model clouds presented in Table 7.1. As expected, the shape of all the clouds strongly depends on the specific value of α in each simulation. Table 7.2 gives an overview of the star formation efficiencies and the number of sink particles being formed in each model cloud with varying α , also illustrated in Fig. 7.2. In the Figure, we also show the star formation efficiencies that we derive from simulations performed using the same values of n_0 and α , but with a different random seed for the turbulent velocity field, as explained in more detail in Appendix C.1. Some of the simulations with less turbulent kinetic energy (i.e. those with lower α values) were not evolved until the

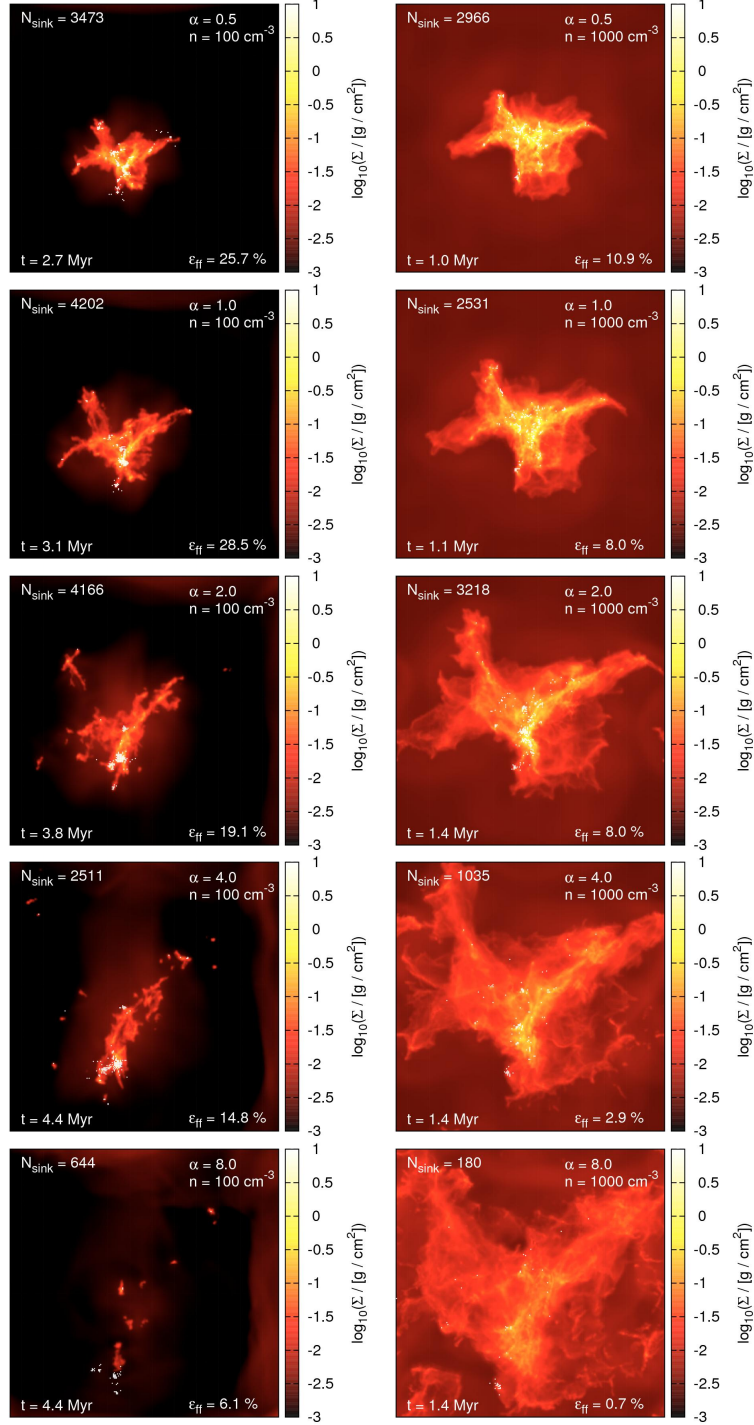


Figure 7.1:

Logarithmic column density maps in z -direction for all cloud models with initial number densities of $n_0 = 100 \text{ cm}^{-3}$ (left column) and 1000 cm^{-3} (right column) for different virial parameters $\alpha = 0.5, 1.0, 2.0, 4.0, 8.0$ (from top to bottom), showing an extract of the central cloud regions. In each plot we give the number of sink particles, the estimated star formation efficiency per free-fall time and the simulation time. Sink particles are formed during the simulations and marked with white dots in each map. The side length of each box shown above corresponds to 74.5 pc and 44.5 pc for the 100 cm^{-3} and 1000 cm^{-3} models, respectively.

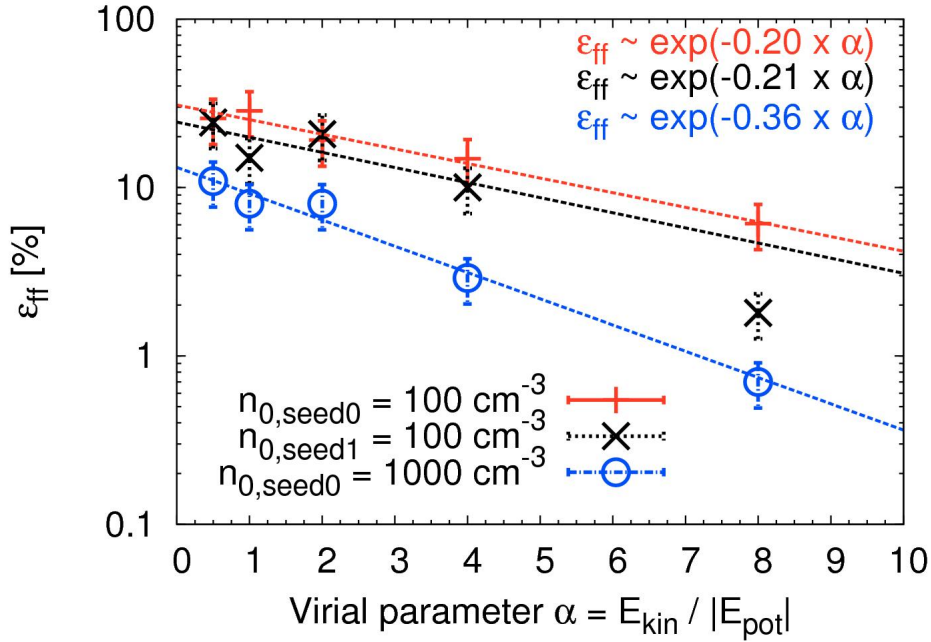
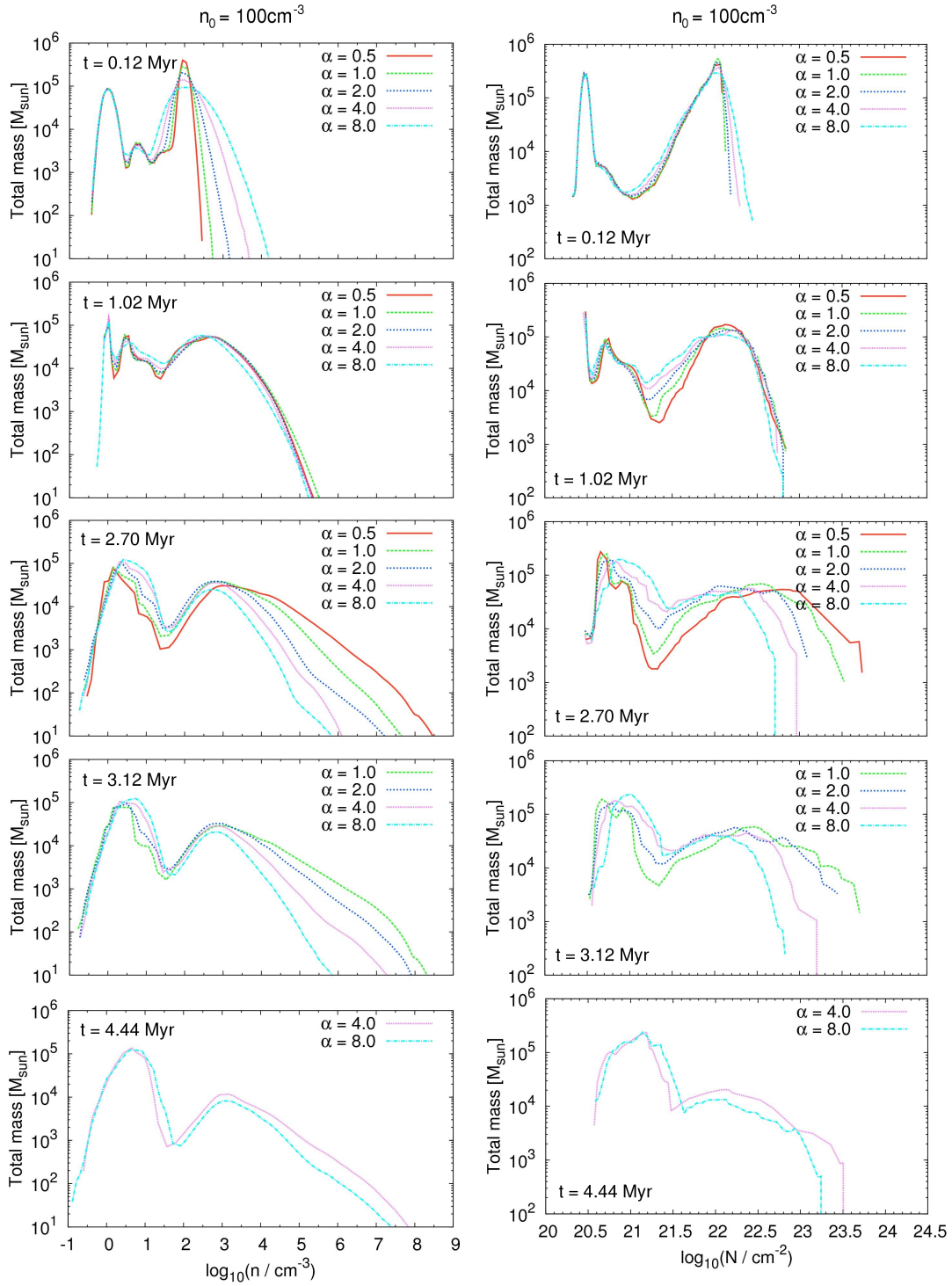


Figure 7.2:

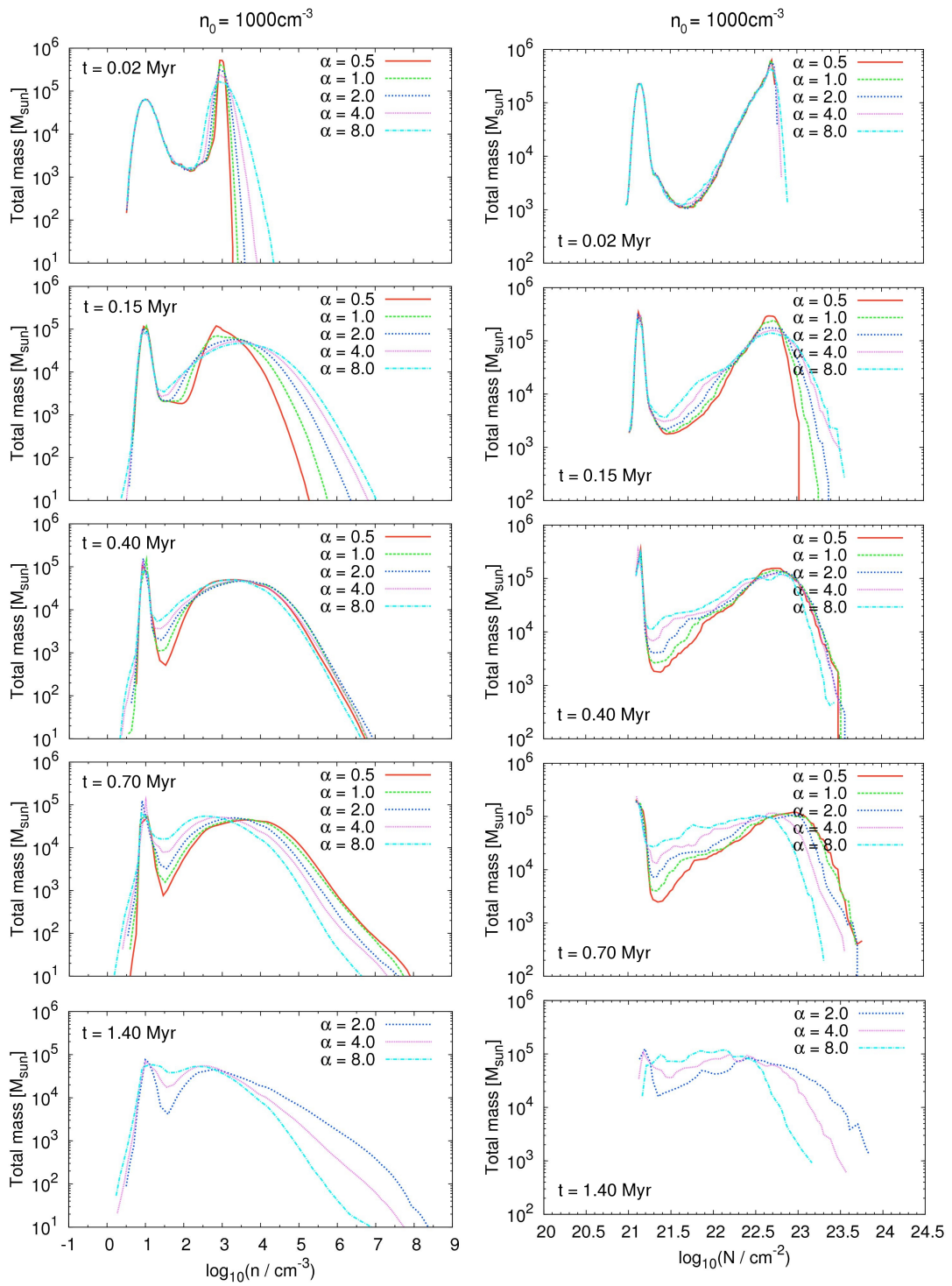
Star formation efficiencies per free-fall time against the corresponding virial α parameter for our fiducial models with $n_{0,\text{seed}0} = 100 \text{ cm}^{-3}$ and $n_{0,\text{seed}0} = 1000 \text{ cm}^{-3}$ (Table 7.2) and for one model using a different seed of the turbulent velocity field with $n_{0,\text{seed}1} = 100 \text{ cm}^{-3}$ (Table C.1). We generally find a decreasing trend of the SFEs with higher α for all density models. Although there are slight differences in the individual SFEs between the two models with $n_{0,\text{seed}0} = 100 \text{ cm}^{-3}$ and $n_{0,\text{seed}1} = 100 \text{ cm}^{-3}$, we nevertheless find the same general trends of decreasing ϵ_{ff} with increasing α . To illustrate the different trends, we also fit exponential functions $\alpha \exp(-\alpha)$ to the models and list the corresponding slopes in the plot. Error bars indicate variations of the SFE of $\sim 30\%$, which we conservatively estimate in Section 7.3.1.

end of one free-fall time. This is because gravitational collapse and star formation become very efficient in these simulations, driving up the computational cost due to the need to refine many high density regions. In these rapidly star-forming runs, we stop our simulations when they either reach one free-fall time or when the computational cost of continuing becomes excessive. In most cases, this occurs once $\sim 8\%$ of the gas has formed stars, but in runs GC-0.5-1000 and GC-1.0-1000 the computational cost climbs so steeply as the gas collapses that we are forced to stop when only $\sim 4\%$ of the gas has formed stars. We note, however, that we do not include the effects of feedback from young stars (see Section 7.4.4), and so the star formation rate is likely to be overestimated at late times in all of our runs.

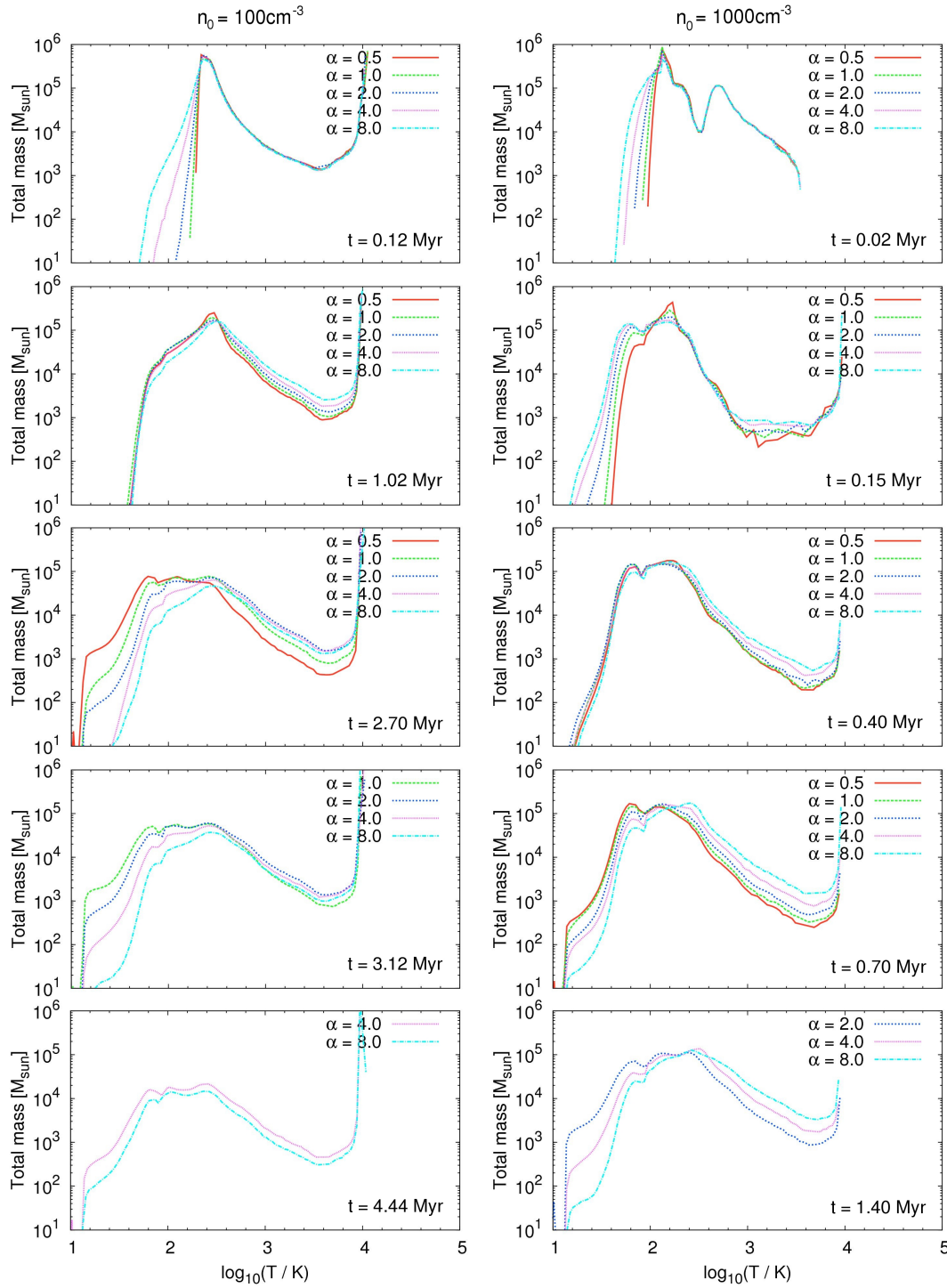
We also have to keep in mind that we start with an idealized, spherical and uniform gas distribution at the beginning, rather than with an MC that is already in an evolved physical state. Measuring the star formation efficiencies from the beginning of the simulation is therefore a questionable procedure, since our results

**Figure 7.3:**

Left column: Mass-weighted volume density PDFs at different times for our five virial α parameters, $\alpha = 0.5, 1.0, 2.0, 4.0$ and 8.0 . Right column: Same as left column, but with column density PDFs. In order to compute the column density PDFs, our simulations were projected onto a regular 1024^2 map. All plots are computed for our models using an initial number density of $n_0 = 100 \text{ cm}^{-3}$.

**Figure 7.4:**

Same as Fig. 7.3, but for our models using an initial number density of $n_0 = 1000 \text{ cm}^{-3}$.

**Figure 7.5:**

Mass-weighted temperature PDFs at different times for our five virial α parameters, $\alpha = 0.5, 1.0, 2.0, 4.0$ and 8.0 , for our models with an initial number density of $n_0 = 100 \text{ cm}^{-3}$ (left column) and $n_0 = 1000 \text{ cm}^{-3}$ (right column).

would be strongly affected by the initial geometry of the MC. Thus, we give two different star formation efficiencies in Table 7.2. The first of these, $\epsilon_{\Delta t}$, denotes the fraction of gas that is converted to stars within a time interval $\Delta t = t_{\text{end}} - t_*$, where t_{end} is the time when we stop the simulation and t_* the time when the first star forms. The other, ϵ_{ff} , is the SFE per free-fall time, which is computed by extrapolating $\epsilon_{\Delta t}$ to one free-fall time. That means we evaluate

$$\epsilon_{\text{ff}} = \epsilon_{\Delta t} \frac{t_{\text{ff}}}{\Delta t}. \quad (7.7)$$

We also note that the number of sink particles N_{sink} that form in each simulation might depend on the specific choice of the sink particle formation threshold n_{thresh} . This number therefore has to be treated with caution, since it is probably not converged, given our resolution, while the SFR is converged (see also Glover & Clark 2012a). However, we are not aiming at resolving the IMF in this study, but instead want to obtain the total mass that goes into gravitational collapse, which is correctly described given our numerical setup.

Furthermore, we note that the largest source of error in estimating ϵ_{ff} is caused by the extrapolation of $\epsilon_{\Delta t}$ to ϵ_{ff} . In general, we assume that the mass accretion rates stay constant through the remaining time of extrapolation. Strictly speaking, this is true only for our $\alpha = 8.0$ and $\alpha = 4.0$ models, as we will see later in Section 7.3.3. Further smaller errors in estimating converged values of ϵ_{ff} are caused by the concrete realization of the turbulent velocity field (see also Appendix C.1), as well as by the specific choice of the sink particle threshold and the accretion radius. Altogether, we think that an error of $\sim 20 - 30\%$ is a conservative estimate. This is acceptable, because we are primarily interested in analyzing how different levels of turbulence, density and the ISRF/CRF affect the formation of stars instead of measuring exact and converged values of the individual star formation efficiencies.

In general, we find active star formation for all three initial densities and for all virial α parameters, even in clouds which are unbound due to a high value of α . The highest efficiencies are found in the models with small virial parameters, which have the lowest turbulent velocity dispersion of all our models (see Table 7.1). The lowest efficiencies are obtained in the GC models with large virial parameters, which are runs with the highest turbulent velocity dispersions. Regarding our extreme GC-16.0-10000 model, we find a SFE of $\epsilon_{\text{ff}} \approx 0.7\%$ even in this case, although the internal velocity dispersion is very high. Moreover, we generally observe a decreasing star formation rate per free-fall time ϵ_{ff} with increasing α (see Fig. 7.2), which we would expect as well due to the increasing amount of turbulent kinetic energy in the simulation domain.

We quantify this and fit an exponential law to the data points shown in Fig. 7.2 using a χ^2 -fit. Our fitting function is defined via

$$\epsilon_{\text{ff}} \propto \exp(-c\alpha), \quad (7.8)$$

where α is the virial parameter and c is a constant, depending on the model. For our model with $n_0 = 100 \text{ cm}^{-3}$, we find $c \approx 0.20 \pm 0.02$, while in the $n = 1000 \text{ cm}^{-3}$

model we obtain a steeper slope $c \approx 0.36 \pm 0.07$ (see Fig. 7.2). Thus, we find strong evidence that ϵ_{ff} depends not only on the virial state of the cloud, but also on its density. Comparing the values for the SFE for our two density models, we find that $\epsilon_{\text{ff}} \sim n_0^{-0.5}$, which means that the SFE per free-fall time is smaller in high density clouds than in clouds with lower density. Interestingly, this is the same scaling with density as the free-fall time itself, which suggests that the change in ϵ_{ff} is driven largely by the change in the free-fall time, rather than by a systematic change in the star formation rate.

In addition, we also run two simulations, SOL-0.5-1000 and SOL-8.0-1000, adopting the lower solar neighbourhood values for the ISRF and the CRF, in order to compare the SFEs we measure in this quiescent environment to those measured for the much harsher GC environment. For the virialized cloud (SOL-0.5-1000), we find an SFE per free-fall time that is around 20% larger than in our corresponding GC model (GC-0.5-1000), demonstrating that for gravitationally bound clouds, the much stronger heating present in the GC has little effect on the star formation rate. It is notable, however, that we form far fewer sink particles in our GC run than in the corresponding solar neighbourhood run, suggesting that the sinks that do form must be systematically larger. Whether this also leads to a systematic change in the initial mass function of the stars forming in this environment remains to be seen; unfortunately, our resolution is too low to allow us to properly address this question. In our runs with $\alpha = 8.0$, we find a much larger difference between the solar neighbourhood and GC runs. In the solar neighbourhood run, increasing α from 0.5 to 8.0 decreases ϵ_{ff} by less than a factor of three, whereas in the corresponding GC runs, the change in ϵ_{ff} is closer to a factor of ~ 16 . Therefore, the combination of high turbulent velocities and strong heating is much more effective at suppressing star formation than either effect individually.

7.3.2 Analysis of the volume, temperature and column density PDF

Fig. 7.3 and 7.4 show the mass-weighted volume density and the column density PDF for both density models with $n_0 = 100 \text{ cm}^{-3}$ and $n_0 = 1000 \text{ cm}^{-3}$ at different times in the cloud evolution for all virial α parameters. In order to compute the column density PDF, our simulations were projected onto a regular 1024^2 map. We have chosen various time snapshots in the evolution, so that all PDFs properly reflect the different physical states of the cloud. At later times, however, we have removed some of the low α runs from the plots, since these runs are not evolved until the one free-fall time limit. Nevertheless, we can still compare the more evolved PDFs to the PDFs of the low α runs from the snapshot shown above at an earlier time. All plots only include the remaining total gas without the mass already converted to sink particles.

The mass-weighted volume density PDF shows two pronounced peaks in each of the plots, suggestive of a two-phase medium. The peaks are found at densities of

$n \approx 1 \text{ cm}^{-3}$ and $n \approx 10^3 \text{ cm}^{-3}$ in the $n_0 = 100 \text{ cm}^{-3}$ model and at $n \approx 10 \text{ cm}^{-3}$ and $n \approx 10^4 \text{ cm}^{-3}$ in the $n_0 = 1000 \text{ cm}^{-3}$ model, respectively. These peaks in the bimodal PDF can be referred to as those of the diffuse ISM and of the denser regions of the MC, which make up most of the mass. We also note that both peaks are well below the density threshold for sink particle formation. Moreover, both the density variance and the mean density generally increase as the simulations evolve with time in our models. In addition, Fig. 7.5 shows the corresponding mass-weighted temperature PDF for both density models. We find that most of the gas has temperatures of several 100 K for all virial parameters, owing to the strong heating by the ISRF and the CRF. This stands in contrast to the situation in local MCs, where a large fraction of the gas mass has $T \sim 10 - 20 \text{ K}$.

Analysing the different temporal evolutions of the PDF for the various α values, we find that the high density regions of runs with larger α values are denser than runs with lower α values during the first $\sim 25\%$ of the free-fall time. This is due to the higher internal velocity dispersion, which can compress the gas more effectively up to higher densities at the beginning of our runs. At later times, the high density regions of simulations with lower α values become denser due to gravitational contraction of the medium. Comparing the PDF of the two density models in Fig. 7.3 and 7.4 in general, we find that both show a similar shape, except a significant shift to larger density values for the 1000 cm^{-3} simulations relative to the 100 cm^{-3} simulations, which is due to the one order of magnitude difference in the initial number density. We also note that we observe a power-law tail at the higher end of the different column density PDF, once star formation has set in, consistent with previous work in this field, e.g. Klessen (2000a), Kritsuk et al. (2011), Federrath & Klessen (2013), Schneider et al. (2013) or Rathborne et al. (2014).

7.3.3 Sink particle formation

Fig. 7.6 shows the mass of gas that is converted to stars (sink particles) as a function of time for the different α parameters and densities. Depending on the amount of kinetic turbulent energy in the box, we find differences in the temporal evolution of star formation. In our models with a lower initial number density of $n_0 = 100 \text{ cm}^{-3}$, we find star formation to be triggered by the global collapse of the MC due to gravitational compression. This is more effective for clouds with lower virial parameter. Hence, in this case, turbulence delays and suppresses star formation. For our other models with higher initial number densities of $n_0 = 1000 \text{ cm}^{-3}$, we find star formation to be triggered by local compression of the gas due to highly turbulent motions, leading to the rapid formation of stars in models with high α values. Overall, star formation is suppressed at high α , but not delayed as observed in our low-density model. Instead we note that turbulence can actually trigger and accelerate star formation in localized patches of the cloud (see also the discussion by Mac Low & Klessen, 2004).

Sink particles can form once all formation criteria presented in Section 7.2.2 are fulfilled. However, highly turbulent motions can locally compress the gas above our

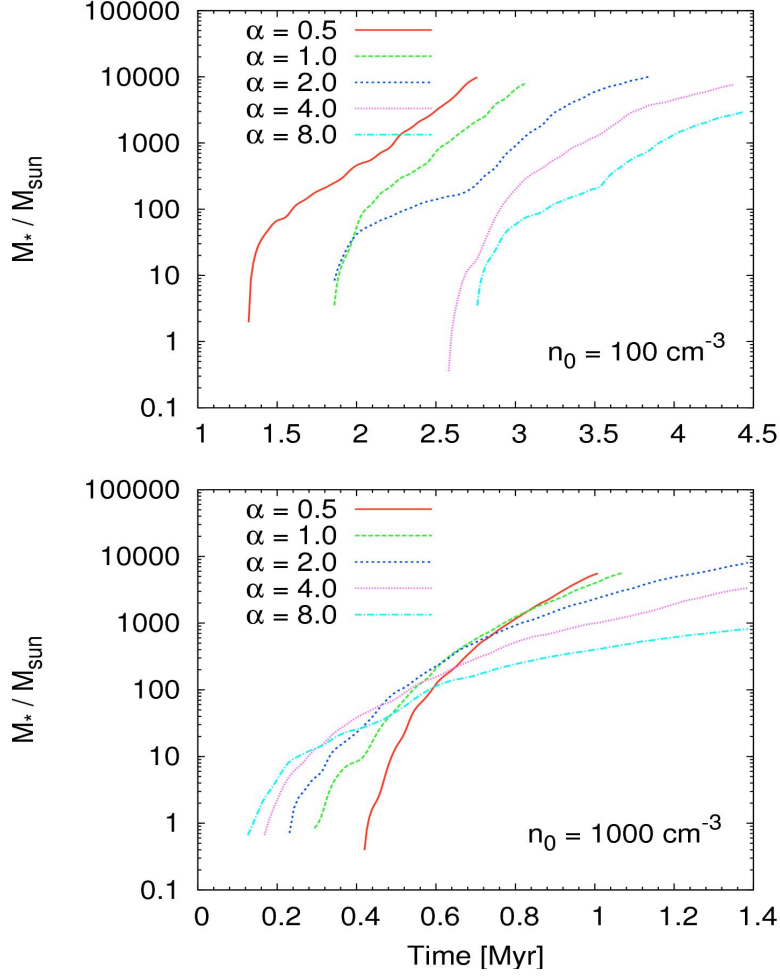
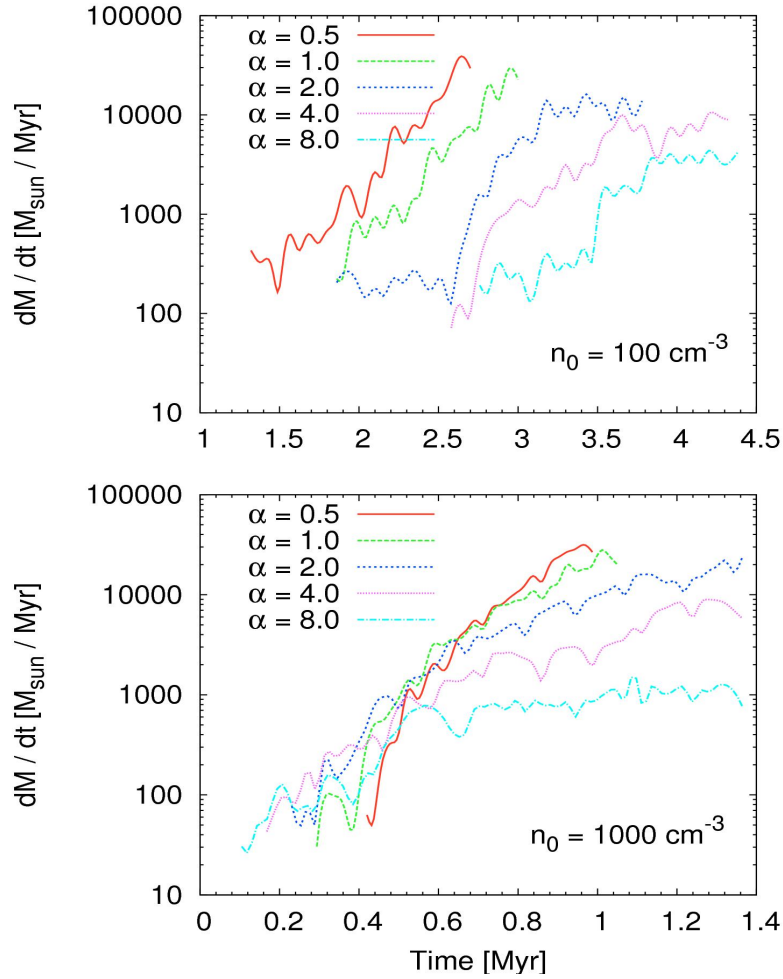


Figure 7.6:

Mass of gas M_* converted to stars (sink particles) as a function of time for the different virial α parameters for our models with initial number densities of $n_0 = 100 \text{ cm}^{-3}$ (top) and $n_0 = 1000 \text{ cm}^{-3}$ (bottom).

sink particle formation threshold more quickly at higher values of the density and the virial parameter. Hence, under our assumptions of sink particle formation, we find that star formation can be triggered by different physical processes, i.e. either by shock compression of the gas leading to overdense regions which fulfill all sink criteria, or by global gravitational collapse. In the latter case, the global collapse dominates the internal velocity dispersions of the cloud, which is e.g. the case in quiescent MCs in the Galaxy. However, we assume that in a CMZ-like environment with highly turbulent motions, star formation is mainly triggered by turbulent shock compression rather than by global gravitational collapse of the cloud as a whole.

Fig. 7.7 shows mass accretion rates for the corresponding density models and different virial parameters of our simulations. Depending on the amount of turbulent kinetic energy, we find a strong dependence of the accretion rates on the α parameter.

**Figure 7.7:**

Mass accretion rates dM/dt for the corresponding density models and different virial α parameters given in Fig. 7.6.

As expected, the gas can be accreted more effectively in case of low α values, i.e. when the kinetic energy is low and the cloud tends to be more gravitationally bound, which holds for all our density models. Furthermore, for those models with a low value of the virial parameter, we find that star formation continues to accelerate during the whole run. If α increases, star formation gets less efficient, the mass accretion rates drop as well and become approximately constant at later times.

7.4 Discussion

7.4.1 Comparison to star formation in the GC

In this study, we have adopted environmental conditions similar to those experienced by a typical GC cloud in order to see whether high levels of turbulence as well as a

much stronger ISRF and CRF will lead to enhanced or reduced star formation rates. As shown by various observations, star formation in the GC is generally thought to be inefficient, i.e. having a factor of $\gtrsim 10$ smaller star formation rate per free-fall time than what is inferred for local star-forming regions (Lis et al. 1994, Murray 2011, Kauffmann et al. 2013, Longmore et al. 2013a). If indeed the high level of turbulence and strong heating by the ISRF and by cosmic rays renders GC clouds very inefficient at forming stars, then this would provide a simple explanation for the low efficiency of star formation in the region as a whole.

Our simulations demonstrate that the rate and efficiency at which star formation occurs depends on the α parameter of the cloud. It is therefore useful to look at the typical α values inferred from observations in the GC. It turns out that most clouds and clumps in the GC tend to be rather unbound, i.e. having values of $\alpha \gtrsim 1$. For example, we find a mean value $\alpha = 3.0 \pm 1.6$ by computing α for different clumps in the GC cloud GCM-0.02-0.07 based on data given by Tsuboi & Miyazaki (2012). Kauffmann et al. (2013) evaluated α for the entire GC cloud G0.253+0.016, finding a value of $\alpha \approx 3.8 \pm 1.0$. However, Longmore et al. (2012) derived a different value. They estimate this cloud to be roughly in virial equilibrium with $\alpha \approx 1$. In this case, the difference between their estimate and the Kauffmann et al. (2013) value comes from their decision to exclude an additional velocity component in the calculation of α . More recently, Rathborne et al. (2015) have computed the virial parameter using data from various observed molecular transitions, finding that the outer regions of G0.253+0.016 may be unbound, while its central region may be bound and collapsing (see Fig. 14 in Rathborne et al., 2015). Furthermore, if we evaluate α for numerous cores from data given in Table 2 in Johnston et al. (2014) for the Brick, we also find that most cores tend to be unbound with $\alpha \gtrsim 2.0$. Overall, therefore, it seems plausible that many of the clouds in the GC that are not currently forming stars have α of a few.

Regarding measurements of the star formation efficiencies per free-fall time, Murray (2011) for example observed a Galaxy-wide average value of $\epsilon_{\text{ff}} \approx 0.6\%$, which is comparable to the lowest ϵ_{ff} in our simulations for highly unbound clouds. Generally, a typical estimate for the star formation efficiency per free-fall time in the Galaxy is $\sim 1\%$, i.e. star formation is quite slow in GMCs (Murray, 2011; Krumholz et al., 2012). We recover larger values than this in almost all of our clouds, rather than finding values strongly suppressed compared to the Galactic average, as would be required to explain the low efficiency of star formation at the galactic center. This holds for runs with both low ($\alpha = 0.5$) and high ($\alpha = 8.0$) values of α , where $\epsilon_{\text{ff}} \gtrsim 1\%$ for the two models with different initial number density. However, we note that these values reflect observed average efficiencies of star formation in the Galaxy as a whole. Thus, a direct comparison with the SFEs derived from numerical simulations of clouds in isolation presented in this study is complicated, since we are only focussing on one specific physical cloud realization, instead of a larger number of individual MCs.

7.4.2 Comparison to previous studies of unbound clouds

Several previous studies tried to reveal the dependence of the SFE on the virial α parameter. For example, Clark et al. (2008) altered the initial level of turbulent support and find that a wide range of SFEs are possible. The SFEs in their study range from up to 60% to as low as around 0.3% after two free-fall times. Furthermore, Clark et al. (2008) also observed a decreasing SFE with increasing α , as confirmed in our study. A similar result was found by Bonnell et al. (2011), who investigated the formation of young stars in a single MC with a total mass that is a factor of 10 smaller than our clouds. Bonnell et al. (2011) concluded that even small changes in the binding energy of the cloud can cause large variations in terms of the SFE, similar to what we find in this paper. They gave an overall SFE of 15% when their calculation was terminated. Moreover, Clark et al. (2005) also showed that unbound clouds result in inefficient star formation, in agreement with Klessen et al. (2000b), Heitsch et al. (2001), Clark & Bonnell (2004), Clark et al. (2008), Bonnell et al. (2011) and the results in this paper.

Furthermore, Padoan et al. (2012) analyzed the SFR in supersonic MHD turbulence, also finding that ϵ_{ff} decreases exponentially with increasing α . In particular, they found that the SFE is insensitive to changes in the sonic Mach number, but sensitive to the Alfvénic Mach number. In their study, a decrease in the Alfvénic Mach number (equivalent to an increase of the magnetic field) additionally reduced the SFE, but only by a factor less than 2. Hence, although we do not account for MHD turbulence, we conclude that an additional external magnetic field might also slightly reduce our values of ϵ_{ff} . These findings are also in agreement with previous studies by Klessen et al. (2000b) and Heitsch et al. (2001), who analyzed the gravitational collapse in turbulent molecular clouds. They find that star formation cannot be prevented by MHD turbulence, but the magnetic fields delay the local collapse due to the magnetic pressure. Furthermore, they also find that strong turbulence can provide some support on global scales, but may trigger collapse and star formation locally at the stagnation points of convergent shocks, in analogy to the findings in this study.

All these studies analyzed the impact of the turbulent kinetic energy on the SFE. However, regarding the generally more extreme physical conditions in the GC, we have to use a significantly higher initial number density and a stronger ISRF/CRF than what was used in these previous studies in order to better match the environmental parameters found in a typical CMZ-like cloud. Surprisingly, our results are similar to those found in previous studies, although we have made use of a more extreme physical setup regarding the internal velocity, the density and the radiation field.

7.4.3 Suppressing star formation

The cloud G0.253+0.016 is supposed to be a typical MC in the GC. However, as shown by Kauffmann et al. (2013) and Johnston et al. (2014), G0.253+0.016 has

almost no evidence of current star formation. In contrast to that, our numerical models show active star formation independent of the initial number density and the virial α parameter of the cloud. Indeed, stars form more rapidly in our model clouds than appears to be the case in the Galaxy as a whole. While our neglect of stellar feedback probably explains some of this discrepancy, stellar feedback can only be effective once star formation is ongoing, but cannot explain an almost complete lack of star formation in G0.253+0.016. We are therefore led to conclude that the harsh GC environment and the high level of turbulence present in the GC clouds cannot by themselves produce low enough star formation efficiencies to explain the globally low efficiency of star formation in the GC. They also do not seem to be able to explain why G0.253+0.016 and its neighbouring clouds are not currently forming stars. What then does suppress star formation in the GC?

One possible explanation could be that the turbulent velocity field in many of the GC clouds is composed of a different mixture of solenoidal and compressive modes than in the model clouds in our study (see, e.g. Federrath et al. 2010a, Federrath 2013, Federrath & Klessen 2013). Fundamentally, the reason that high levels of turbulence do not completely suppress star formation in our model clouds is that the same turbulent motions that support the cloud as a whole against collapse also compress some of its gas up to high densities. This high density gas is formed at stagnation points of the turbulent flow and is not supported against gravitational collapse. It is therefore able to form stars efficiently. However, if compressive modes are absent and the velocity field is dominated by purely solenoidal turbulence (generated e.g. by the strong shear experienced by the clouds as they orbit the center of the Galaxy), then less gas will be compressed to high densities, and it is plausible that star formation could be more strongly suppressed. In addition, the strong magnetic field present in the GC might reduce the level of star formation by slowing down the collapse of dense cores (Pillai et al., 2015). However, as mentioned before, this typically leads to a reduction in the star formation rate and efficiency of only about a factor of ~ 2 , see e.g. Peters et al. (2011), Hennebelle et al. (2011), Commerçon et al. (2011) or Seifried et al. (2013).

Alternatively, it might be that the idea that we can explain the low SFE of the GC region as a whole by requiring the individual clouds to all have low SFEs is simply incorrect. Even in our highly turbulent model clouds, star formation does not begin at $t = 0$ – there is a brief period in the evolution of the cloud during which no stars are yet forming. If, as Longmore et al. (2013b) suggest, G0.253+0.016 and its neighbouring clouds have only formed very recently, then it may simply be that we are catching them too early in their lives to have started forming significant numbers of stars. In this case, we would need to look elsewhere for an explanation of the galactic center’s low star formation rate. In this context, larger-scale effects such as the orbital dynamics of the gas in the deep potential well of the GC, feedback from massive stars in the form of winds and supernovae, or the inflow/outflow of gas into/out of the GC might play important roles by helping to suppress the formation of dense clouds in the GC region. We will explore the possible impact of these various physical processes in a follow-up study.

7.4.4 Limitations of the model

There are a few limitations inherent to our numerical models that one should keep in mind when interpreting our results. Most notably, we do not model feedback from the stars (e.g. jets, stellar winds or radiation) that form during the individual runs. This would help to reduce $\epsilon_{\Delta t}$ and ϵ_{ff} , but cannot entirely suppress star formation. Furthermore, we do not account for spatial variations in the ISRF or the CRF.

We also deliberately do not account for other important physical effects that might modify the star formation rate and efficiency, such as large-scale dynamics (e.g. spiral arms or spiral instabilities), magnetic fields, galactic tides and shear, supernova feedback or the inflow/outflow of gas. This is because we only want to look at the effects of turbulence and a high ISRF/CRF on cloud dynamics in isolation. We leave the analysis of simulations with further physical effects for future studies.

Moreover, the high computational cost of AREPO simulations of clouds with mean densities $n \gg 10^3 \text{ cm}^{-3}$ means that we have to focus on models with number densities $n_0 = 100 \text{ cm}^{-3}$ and $n_0 = 1000 \text{ cm}^{-3}$. However, the density of a typical GC cloud like G0.253+0.016 can be even higher than several $\sim 10^3 \text{ cm}^{-3}$, as shown by various studies in the past (Lis et al., 2001; Immer et al., 2012; Longmore et al., 2012; Kauffmann et al., 2013; Clark et al., 2013; Johnston et al., 2014). Therefore, as shown in Section 7.2.4, we also run one more extreme model with $n_0 = 10^4 \text{ cm}^{-3}$ and $\alpha = 16.0$, finding a SFE of $\epsilon_{\text{ff}} = 0.7\%$. Nevertheless, regarding the trends given in Table 7.2, we expect other high density runs with a virial parameter lower than 16.0 to form stars at an even higher rate due to a lower amount of turbulent kinetic energy.

Fig. 7.2 provides support for this assumption. It clearly shows that ϵ_{ff} depends on the mean density n_0 roughly as $\epsilon_{\text{ff}} \sim n_0^{-0.5}$ (see Section 7.3.1). If this trend continues to higher density, then typical GC clouds with $n \sim 10^4 \text{ cm}^{-3}$ should have about $\sim 1/3$ lower star formation efficiencies per free-fall time than our $n_0 = 1000 \text{ cm}^{-3}$ model. In this case, we still obtain values of $\epsilon_{\text{ff}} \gtrsim 1\%$, which are higher than the average SFE in the Milky Way (see Section 7.4.1). This holds at least for all runs except for the high $\alpha = 8.0$ run, for which we would obtain $\epsilon_{\text{ff}} \sim 0.2\%$, smaller than the value of $\epsilon_{\text{ff}} \approx 0.7\%$ found for the $\alpha = 16.0$ run. However, it is unclear whether this single example can be taken as a systematic evidence for a breaking of our density trends, given the stochasticity with its large uncertainties seen among the results for the 100 cm^{-3} and 1000 cm^{-3} simulations.

7.5 Summary and Conclusions

We have performed numerical simulations of molecular clouds with the moving mesh code AREPO (Springel, 2010) using environmental properties comparable to those experienced by typical galactic center (GC) clouds. We adopted values for the interstellar radiation field (ISRF) and the cosmic ray flux (CRF) that are a factor

of ~ 1000 larger than the values measured in the solar neighbourhood (Clark et al., 2013). We simulated clouds with initial number densities of $n_0 = 100 \text{ cm}^{-3}$ and 1000 cm^{-3} using different virial α parameters of $\alpha = 0.5, 1.0, 2.0, 4.0$ and 8.0 for each density. The total mass was set to a constant value of $M_{\text{tot}} = 1.3 \times 10^5 M_{\odot}$. In addition, we also ran one more extreme simulation with an initial number density of 10^4 cm^{-3} and a virial parameter of $\alpha = 16.0$. Furthermore, we also did two control runs with $n_0 = 1000 \text{ cm}^{-3}$ as well as $\alpha = 0.5$ and $\alpha = 8.0$ and with ISRF and CRF parameters geared towards the solar neighbourhood. An overview of our model parameters is provided in Table 7.1. We report the following findings:

- We find active star formation with $\epsilon_{\text{ff}} \gtrsim 1\%$ in all models regardless of the choice of n_0 and α .
- Our values are more comparable to Galaxy-wide SFEs than to the inferred SFE in the GC, which observations suggest is a factor $\gtrsim 10$ smaller. Star formation is more efficient at lower α values, i.e. when the velocity dispersion in the cloud is small.
- The efficiency of star formation decreases by a factor of $\sim 4-10$ as we increase the virial parameter from $\alpha = 0.5$ to $\alpha = 8.0$.
- We fit exponential functions $\epsilon_{\text{ff}} \propto \exp(-c\alpha)$ to the data, finding $c \approx 0.20 \pm 0.02$ and $c \approx 0.36 \pm 0.07$ for the $n_0 = 100 \text{ cm}^{-3}$ and $n_0 = 1000 \text{ cm}^{-3}$ density models, respectively. Thus, we find strong evidence that ϵ_{ff} depends not only on the virial state of the cloud, but also on its density. To illustrate this quantitatively, we derive a relation $\epsilon_{\text{ff}} \sim n_0^{-0.5}$ for the star formation efficiencies as a function of the density.
- For virialized clouds, we find that even a 1000x higher ISRF strength and CRF has only a small effect on the star formation efficiency, decreasing it by around 20% compared to the value we obtain for a similar cloud in a solar neighbourhood environment. For highly unbound clouds, the stronger ISRF and higher CRF at the galactic center has a much greater effect, decreasing the star formation efficiency by around a factor of 6.
- Even in our most extreme models, we find star formation efficiencies per free-fall time that are close to 1%. None of our models produce values that are consistent with the low SFE per free-fall time that is inferred for the galactic center region as a whole.

We therefore conclude that the idea tested in this paper – that the high levels of turbulence present in the GC region, together with the strong ISRF and high CRF combine to yield a persistently low star formation efficiencies within the dense clouds in this region – does not appear to work in practice. It is possible that including additional physical ingredients (such as magnetic fields, stellar feedback or realistic orbital parameters around the GC) could reduce the star formation efficiencies within

individual dense clouds to levels that are consistent with the mean value inferred for the GC region as a whole. Alternatively, it could be that the idea that we can explain the low SFE of the GC region as a whole by requiring the individual clouds to all have low SFEs is incorrect, and that the bottleneck for star formation in the region is actually the assembly of the dense clouds themselves. This is in agreement with Kruijssen et al. (2014), who speculate that the rate-limiting factor for star formation is the slow evolution of the gas towards collapse. Distinguishing between these two possibilities awaits further work on this topic.

Synthetic observations of MCs in a galactic center environment:

I. Studying maps of column density and integrated intensity

We run numerical simulations of molecular clouds (MCs), adopting properties similar to those found in the Central Molecular Zone (CMZ) of the Milky Way. For this, we employ the moving mesh code AREPO and perform simulations which account for a simplified treatment of time-dependent chemistry and the non-isothermal nature of gas and dust. We perform simulations using an initial density of $n_0 = 10^3 \text{ cm}^{-3}$ and a mass of $1.3 \times 10^5 M_\odot$. Furthermore, we vary the virial parameter, defined as the ratio of kinetic and potential energy, $\alpha = E_{\text{kin}}/|E_{\text{pot}}|$, by adjusting the velocity dispersion. We set it to $\alpha = 0.5, 2.0$ and 8.0 , in order to analyze the impact of the kinetic energy on our results. We account for the extreme conditions in the CMZ and increase both the interstellar radiation field (ISRF) and the cosmic-ray flux (CRF) by a factor of 1000 compared to the values found in the solar neighbourhood. We use the radiative transfer code RADMC-3D to compute synthetic images in various diagnostic lines. These are [CII] at $158 \mu\text{m}$, [OI] ($145 \mu\text{m}$), [OI] ($63 \mu\text{m}$), ^{12}CO ($J = 1 \rightarrow 0$) and ^{13}CO ($J = 1 \rightarrow 0$) at $2600 \mu\text{m}$ and $2720 \mu\text{m}$, respectively. When α is large, the turbulence disperses much of the gas in the cloud, reducing its mean density and allowing the ISRF to penetrate more deeply into the cloud's interior. This significantly alters the chemical composition of the cloud, leading to the dissociation of a significant amount of the molecular gas. On the other hand, when α is small, the cloud remains compact, allowing more of the molecular gas to survive. We show that in each case the atomic tracers accurately reflect most properties of both the H_2 and the total gas and that they provide a useful alternative to molecular lines when studying the CMZ. The results presented in this chapter are published in Bertram et al. (2015d).

8.1 Introduction

The inner few hundred parsecs of our Milky Way, known as the Central Molecular Zone (CMZ), are rich in molecular and dense gas and account for about 5% of the molecular gas content of the Galaxy (Morris & Serabyn, 1996b). As shown by Longmore et al. (2013), the CMZ contains gas with densities of the order of several 10^3 cm^{-3} and a total mass of $\sim 10^7 M_{\odot}$. Furthermore, it is highly turbulent (Shetty et al., 2012) and illuminated by a strong interstellar radiation field (ISRF) combined with a high cosmic-ray flux (CRF) (Yusef-Zadeh et al., 2007; Clark et al., 2013). It thus provides an excellent laboratory for studying the physics of the interstellar medium (ISM) under extreme conditions (such as those that also occur in distant starburst galaxies) with very high resolution.

Previous observations suggested the existence of copious CO gas in the CMZ near the Galactic Center (GC) (Bania, 1977; Burton et al., 1978; Liszt & Burton, 1978; Morris & Serabyn, 1996b; Bitran et al., 1997; Oka et al., 1998; Martin et al., 2004), which might be used to trace the density and velocity structure of the underlying molecular component of the ISM. However, the effect of the extreme physical conditions in the CMZ on the CO distribution within the gas and the degree to which CO is a biased tracer of the underlying cloud properties remain relatively unexplored issues. Previous numerical models of clouds in the CMZ (Clark et al., 2013) or in other harsh environments (Clark & Glover, 2015) have shown that the gas is likely to be highly chemically inhomogeneous. This means that molecular tracers might tell us only little about the kinematics, the temperature and density distributions of the cloud and so on. Hence, in order to learn more about the internal physics (e.g. heating, cooling and the chemistry) of the warm gas, which makes up a large fraction of the total mass, we have to use other probes.

Recently, Clark et al. (2013) have shown that the [OI] $63 \mu\text{m}$ and the [CII] $158 \mu\text{m}$ fine structure lines dominate the cooling in CMZ clouds over a wide range in densities. Moreover, Rodríguez-Fernández et al. (2004) present observations of these fine structure lines in the CMZ, carried out with the ISO satellite. They show that both lines are very strong in this region and can be used to infer important information about the physics of the gas in the CMZ. Hence, using such atomic tracers in order to study the physics of MCs in the CMZ seems to be a promising approach.

In this paper we follow up on this idea and investigate the applicability of atomic tracers to study the properties of the ISM in the CMZ. We aim to provide synthetic observations, readily comparable to observations of fine structure lines. To do so, we compute synthetic observations of MCs in a CMZ-like environment using the radiative transfer code RADMC-3D (Dullemond, 2012) for various diagnostic lines, specifically for [CII] ($158 \mu\text{m}$), [OI] ($145 \mu\text{m}$), [OI] ($63 \mu\text{m}$), ^{12}CO ($2600 \mu\text{m}$) and ^{13}CO ($2720 \mu\text{m}$). We perform simulations of various clouds with the moving mesh code AREPO (Springel, 2010) using environmental properties similar to those experienced by a typical CMZ cloud. In particular, we adopt values for the ISRF strength and the CRF comparable to those inferred for the dense CMZ cloud G0.253+0.016, also

Model name	Virial α	Initial n_0 [cm^{-3}]	3D σ_v [km/s]	Radius R [pc]	Free-fall time t_{ff} [Myr]	End t_{end} [Myr]
GC-0.5-1000	0.5	1000	5.4	8.9	1.40	1.00
GC-2.0-1000	2.0	1000	10.8	8.9	1.40	1.40
GC-8.0-1000	8.0	1000	21.6	8.9	1.40	1.40

Table 8.1: Overview of the initial conditions for our different cloud models.

known as “The Brick” (see e.g. Güsten et al., 1981; Lis et al., 1994; Lis & Menten, 1998; Lis et al., 2001; Molinari et al., 2011; Immer et al., 2012; Longmore et al., 2012; Kauffmann et al., 2013; Clark et al., 2013; Johnston et al., 2014; Rathborne et al., 2014, 2015). We use values for the ISRF and the CRF that mimic the harsh conditions assumed to be found in the CMZ, which are a factor of ~ 1000 larger than the values measured in the solar neighbourhood (Habing, 1968; Draine, 1978; Mathis et al., 1983). We simulated clouds with an initial number density of $n_0 = 10^3 \text{ cm}^{-3}$ and studied the impact of different virial α parameters, $\alpha = 0.5, 2.0$ and 8.0 , on the physical properties. More information about the simulations can be found in Bertram et al. (2015c). Furthermore, we note that this study is the first of two papers which analyze the properties of CMZ-like clouds. In this paper, we focus on maps of column density and integrated intensity, while in Paper II (Bertram et al., in prep.), we study the kinematic properties of our model clouds.

This paper is structured as follows. In section 8.2 we present our numerical simulations and the radiative transfer post-processing tool. In section 8.3 we show and discuss the results of our studies. We present a summary and our conclusions in section 8.4.

8.2 Methods

The numerical simulations studied in this paper are described in more detail in Bertram et al. (2015c). However, we summarize the most important aspects of the simulations here and introduce the radiative transfer post-processing, which we use for computing synthetic observational maps of the clouds in various diagnostic lines.

8.2.1 Hydrodynamical and chemical model

We use the moving mesh code AREPO (Springel, 2010) in order to run numerical simulations of various model clouds. We have added to AREPO a detailed atomic and molecular cooling function, described in detail in Glover et al. (2010) and Glover & Clark (2012), and a simplified treatment of the basic chemistry of the gas. The chemical network is based on the work of Nelson & Langer (1997) and Glover & Mac Low (2007), and allows us to follow the formation and destruction of H_2 and CO self-consistently within our simulations. The network tracks the abundances of 6 species and follows 14 chemical reactions. The simplified Nelson & Langer (1997)

network is known to somewhat overestimate the rate at which CO forms, owing to its neglect of atomic carbon (see the detailed discussion in Glover & Clark, 2012). It also neglects the reaction



which plays an important role in regulating the CO abundance in gas exposed to a high CRF (see, e.g. Clark & Glover, 2015; Bisbas et al., 2015). Our simulations thereby overestimate the CO abundance in the simulated clouds, and hence potentially underestimate the C^+ and O abundance in regions where the CO abundance is large. Therefore, in order to establish the effect that this has on the synthetic maps, we make two versions of each map: one in which we use values for the fractional abundances of C^+ and O taken from the simulations and a second version in which we assume that all of the carbon is in the form of C^+ and all of the oxygen is present as O. This can be achieved by assuming zero CO abundances in our simulations. As discussed in more detail in Appendix D.3, we find only minor differences in the [OI] ($145 \mu\text{m}$) emission PDF and negligible differences in the [OI] ($63 \mu\text{m}$) and [CII] ($158 \mu\text{m}$) PDFs. We therefore conclude that the known weaknesses of our simplified chemical model have little influence on the results we obtain for [CII] and [OI]. Full details of the chemical model with a description of how the chemistry interacts with the ISRF via the TREECOL algorithm can be found in Clark et al. (2012). Further examples of the use of our chemical model with the AREPO code can be found in Smith et al. (2014a) and Smith et al. (2014b).

We assume that the gas has a uniform solar metallicity and adopt the standard ratio of helium to hydrogen. The abundances of carbon and oxygen are taken from Sembach et al. (2000). We use $x_{\text{C}} = 1.4 \times 10^{-4}$ and $x_{\text{O}} = 3.2 \times 10^{-4}$, where x_{C} and x_{O} are the fractional abundances by number of carbon and oxygen relative to hydrogen. We note that the CMZ has super-solar metallicity. Nevertheless, we use a uniform solar value in order to be conservative regarding the cooling rates in our runs. When we start the simulations, hydrogen, helium and oxygen are in atomic form, while carbon is assumed to be in singly ionized form, as C^+ . We adopt the standard local value for the dust-to-gas ratio of 1:100 (for further discussion see, e.g. Glover et al., 2010). We set the cosmic ray ionization rate (CRIR) of atomic hydrogen to $\zeta = 3 \times 10^{-14} \text{ s}^{-1}$ (Clark et al., 2013). This value is a factor ~ 1000 higher than the value measured in dense clouds in the solar neighbourhood (van der Tak & van Dishoeck, 2000) and is comparable to the high value that has previously been inferred in the CMZ (Yusef-Zadeh et al., 2007; Clark et al., 2013). Note, however, that it is only around a factor of 100 higher than the value derived in more diffuse gas in the solar neighbourhood (Indriolo et al., 2015). For the interstellar radiation field, we adopt the same spectral shape as given in Draine (1978). We denote the strength of the Draine ISRF as $G_0 = 1$ and perform simulations with a field strength $G_0 = 1000$ (Clark et al., 2013). This corresponds to an integral flux in the energy range $6 - 13.6 \text{ eV}$ of $2.7 \times 10^{-3} \text{ erg cm}^{-2}\text{s}^{-1}$.

8.2.2 Model parameters

The clouds that we model are initially spherical and located at the center of a large box of low-density gas. For the box, we use periodic boundary conditions. However, this is simply a convenient choice, since the boundaries do not influence the dense cloud evolution, because the size of the box is taken to be much larger than the size of the cloud. The cloud has a uniform initial hydrogen nuclei number density, which we set to 10^3 cm^{-3} , and a total mass of $M_{\text{tot}} = 1.3 \times 10^5 M_{\odot}$. The initial cloud radius is $R \approx 8.9 \text{ pc}$. In all of our simulations, the density of the gas surrounding the cloud is $\approx 1 \text{ cm}^{-3}$, but we note that our results are insensitive to this value provided that it is much smaller than the mean cloud density. The cubic side length of the total simulation domain is set to $5 \times$ the individual cloud radius of 8.9 pc , i.e. 44.5 pc in total. All clouds have zero bulk velocity and are placed in the center of the box. The Voronoi cells initially have approximately constant volumes. We initially start with 2×10^6 cells in total. The initial cell mass within the cloud corresponds to $\approx 2 M_{\odot}$.

We make use of a Jeans refinement criterion in order to accurately refine dense and collapsed gas regions in the box over the whole simulation time. We use a constant number of 8 cells per Jeans length, which is sufficient to avoid artificial fragmentation (see, e.g. Truelove et al. 1998, Greif et al. 2011 as well as Federrath et al. 2010b). Our code also includes a sink particle formation algorithm (Bate et al., 1995; Jappsen et al., 2005; Greif et al., 2011) to properly track the formation of stars during each run. Although our numerical models show active star formation by the end of the simulations, we ignore the sink particles in this study, since we only want to focus on the physical properties of the different gas phases. A more detailed analysis of the star formation history of our runs and the sink particle algorithm that we use can be found in Bertram et al. (2015c).

We assume that the gas has a turbulent velocity field with an initial power spectrum $P(k) \propto k^{-4}$ and consists of a natural mixture of solenoidal and compressive modes (see, e.g. Federrath et al. 2010a). The strength of the turbulence is set by our choice of the initial virial α parameter. This is defined as $\alpha = E_{\text{kin}}/|E_{\text{pot}}|$, i.e. the kinetic energy $E_{\text{kin}} = 1/2 M_{\text{tot}} \sigma_v^2$ divided by the potential energy $E_{\text{pot}} = -3GM_{\text{tot}}^2/(5R)$ measured at the beginning of each run. The quantity σ_v denotes the 3D rms velocity dispersion in the cloud. We note that the virial parameter is also often calculated as $\alpha = 2E_{\text{kin}}/|E_{\text{pot}}|$ in the literature, which is different from the notation used in this paper (see, e.g. Federrath & Klessen, 2012). With our definition, a value of $\alpha = 0.5$ corresponds to a cloud in virial equilibrium and $\alpha > 1.0$ describes clouds that are gravitationally unbound. In order to span a large range in the virial parameter space, we analyze models with $\alpha = 0.5, 2.0$ and 8.0 . Note that although it is convenient to parameterize the models in terms of α , the underlying physical quantity that changes as we change α is the turbulent velocity dispersion of the gas, since we keep M_{tot} and the initial radius R fixed in all three models. It is therefore the changes to the velocity field, and the consequent changes to the density distribution of the gas, that dictate the observed trends seen

in our simulations. However, for simplicity and clarity, we will simply refer to the different α models in our discussions in the following sections.

The turbulence is not driven and hence decays throughout the simulation (Mac Low et al., 1998b). The timesteps between the individual snapshots are $\Delta t_{\text{snap}} \approx 7 \text{ kyr}$, corresponding to ~ 200 snapshots per simulation in total. Table 8.1 summarizes the initial conditions of our clouds. We note that due to the high computational cost of our $\alpha = 0.5$ model, we had to stop our run already at $t \approx 0.7 t_{\text{ff}}$, while the other runs end at one free-fall time. This is due to an intense refinement of dense gas regions within the cloud. Furthermore, regarding the densities in the CMZ, we have to keep in mind that a significant number of CMZ clouds have densities higher than those modelled in our simulations, which would lead to even larger turbulent velocities in our simulations for the same constant total mass.

8.2.3 Radiative transfer

We post-process our data in order to generate synthetic line emission maps for the atomic and molecular tracers listed in Table 8.2, using the radiative transfer code RADMC-3D¹ (Dullemond, 2012). We use the Large Velocity Gradient (LVG) approximation (Sobolev, 1957) to compute the C⁺, O and CO level populations. The LVG implementation in RADMC-3D is described in Shetty et al. (2011a). We use the rate coefficients for collisional excitation and de-excitation by atomic and molecular hydrogen tabulated in the Leiden database (Schöier et al., 2005).

At the moment, RADMC-3D cannot deal with AREPO data directly. Thus, we have to map the simulation output onto a cubic grid. For that, we adopt a resolution of 512 cells in all three spatial dimensions, corresponding to a cell size of $\Delta x = \Delta y = \Delta z = 0.087 \text{ pc}$. Moreover, we also use 512 channels in velocity space for our radiative transfer post-processing, corresponding to a spectral resolution of 0.057 km s^{-1} , 0.066 km s^{-1} and 0.102 km s^{-1} for our models with $\alpha = 0.5, 2.0$ and 8.0 . Our choice of spatial resolution is determined by technical limitations within RADMC-3D: as it is a serial code, our grid size is limited by the requirement that the data should all fit within the memory of the computer that we use to carry out the post-processing. However, for most of our tracers, we find only minor differences in the emission as we increase the grid resolution. In particular, we find that a resolution of 512^3 grid cells is enough in order to properly recover the emission of the cloud for all of the tracers apart from the [OI] $63 \mu\text{m}$ line (see Appendix D.1). Hence, our main conclusions are not strongly affected by our choice of spatial resolution.

Our simulations do not explicitly track the abundance of ^{13}CO and so we need a procedure to relate the ^{13}CO number density to that of ^{12}CO . A common assumption is that the ratio of ^{12}CO to ^{13}CO is identical to the elemental abundance ratio of ^{12}C to ^{13}C (see, e.g. Roman-Duval et al., 2010). We make the same assumption and set the ^{12}CO to ^{13}CO ratio to a constant value, $R_{12/13} = 60$. In reality, physical effects like chemical fractionation (Watson et al., 1976) and photodissociation (Visser et al.,

¹www.ita.uni-heidelberg.de/~dullemond/software/radmc-3d/

Tracer	Type	Transition	λ [μm]	ν [GHz]
^{12}CO	Molecular	$J = 1 \rightarrow 0$	2600	115
^{13}CO	Molecular	$J = 1 \rightarrow 0$	2720	110
[CII]	Atomic	$^2P_{3/2} \rightarrow ^2P_{1/2}$	158	1900
[OI]	Atomic	$^3P_1 \rightarrow ^3P_2$	63	4744
[OI]	Atomic	$^3P_0 \rightarrow ^3P_1$	145	2060

Table 8.2:

Tracer name and type, quantum mechanical transition, wavelength λ and frequency ν of various fine structure lines, which we model with the radiative transfer code RADMC-3D.

2009b) will alter the abundances of ^{13}CO relative to ^{12}CO , leading to a variable value of $R_{12/13}$ within the cloud. However, Szűcs et al. (2014) have shown that the resulting ^{13}CO maps do not differ greatly from those that we would obtain by assuming a constant ratio of ^{12}CO to ^{13}CO , and so we expect this approximation to be adequate.

The radiative transfer calculation yields position-position-velocity (PPV) cubes of brightness temperatures T_B , which are related to the intensity via the Rayleigh-Jeans approximation,

$$T_B(\nu) = \left(\frac{c}{\nu}\right)^2 \frac{I_\nu}{2k_B}, \quad (8.2)$$

where I_ν is the specific intensity at frequency ν and k_B the Boltzmann constant. For each run, we carry out the post-processing for each of the tracers listed in Table 8.2 along an arbitrary line of sight (LoS), using the last snapshot of each model. Since we use isotropic turbulence without magnetic fields, we do not expect our results to significantly depend on the specific choice of the LoS and hence we only focus on emission observed along the z -direction (see also Appendix D.2).

8.3 Results

In this section, we analyze various physical cloud parameters using the latest time snapshot (see Table 8.1). We start with the thermal state of the MCs (Section 8.3.1) and investigate which chemical components best trace the total shape of the cloud (Section 8.3.2). Afterwards, we estimate the effective cloud radii by using synthetic observations in various diagnostic lines (Section 8.3.3). We then explore the ability of the lines listed in Table 8.2 to trace dense MC regions (Section 8.3.4) and continue with a quantitative estimate of the mass fraction of the cloud that is traced by the line emission (Section 8.3.5). At the end, we discuss the X_{CO} -factor of the MCs.

8.3.1 Thermal state of the clouds

In Fig. 8.1 we show the two-dimensional PDFs of gas temperatures and densities within the clouds for the different virial parameters and for all chemical components:

total mass, molecular hydrogen, atomic oxygen, ionized carbon and carbon monoxide. These PDFs are mass-weighted, with the colour-coding indicating the fraction of the total mass of the cloud (in the upper row of panels) or of the species of interest (in the remaining panels) located at each point in density-temperature space. The number densities shown in the upper row of panels are the total number density of particles; in the remaining panels, we show instead the number density of the species of interest (n_{H_2} , n_{O} , etc.). Figure 8.1 demonstrates that the thermal state of the clouds for all of the components only weakly depends on the virial parameter. However, we find strong differences in the PDFs between the various tracers.

We find a significant amount of warm gas at densities $n \lesssim 1000 \text{ cm}^{-3}$ and temperatures between $T \approx 300 - 10^4 \text{ K}$. We also note that there is a substantial scatter in the temperature at every value of the density in this regime. This gas corresponds to the warm and tenuous envelope in the outer regions of the clouds with low extinction. It is heated by the strong external ISRF via the photoelectric effect. For densities higher than $n \gtrsim 1000 \text{ cm}^{-3}$, we find an inverse relationship between the temperature and the density. The temperature decreases with increasing density, owing to the efficient self-shielding of the dense gas from the external radiation field. Such high densities only occur in the inner regions of the clouds with temperatures of $T < 100 \text{ K}$, which are cold enough to result in active star formation (for further information about the star formation history of our numerical simulations, we refer the reader to Bertram et al. 2015c). These are also the parts of the cloud in which we find molecular H_2 and CO gas in our simulations.

If we compare the thermal state of the total mass to the thermal state of the other tracers, we find that only the atomic oxygen and ionized carbon show a similar behavior over the whole range of temperatures. This is because these components exist in the diffuse cloud regions as well as in the denser, more shielded gas. We also see that molecular hydrogen is strongly dissociated in the diffuse, warm envelope of the cloud. It only reaches maximal temperatures of $\sim 4000 \text{ K}$, which is lower than the warmest regions observed for the total gas. In the case of CO , the range of temperatures ($30 - 300 \text{ K}$) is even smaller. This suggests that CO traces a denser, colder part of the cloud than $[\text{CII}]$ or $[\text{OI}]$. We will examine the consequences of this in more detail in the following sections.

8.3.2 Tracing the shape of the MC

Fig. 8.2 shows logarithmic column density maps for the total density and the H_2 density computed along the LoS in the z -direction for virial parameters $\alpha = 0.5, 2.0$ and 8.0 for the last time snapshots (see Table 8.1). We see that as we increase α , and hence the velocity dispersion of the gas, the structure of the cloud changes significantly. When $\alpha = 0.5$ and the cloud is gravitationally bound, it remains relatively compact. It is therefore able to shield itself relatively well from the effects of the high external ISRF, with the result that the H_2 column density traces the total column density fairly well. In the runs with $\alpha = 2$ and $\alpha = 8$, however, the cloud is not gravitationally bound and hence starts to expand. In addition, the strong

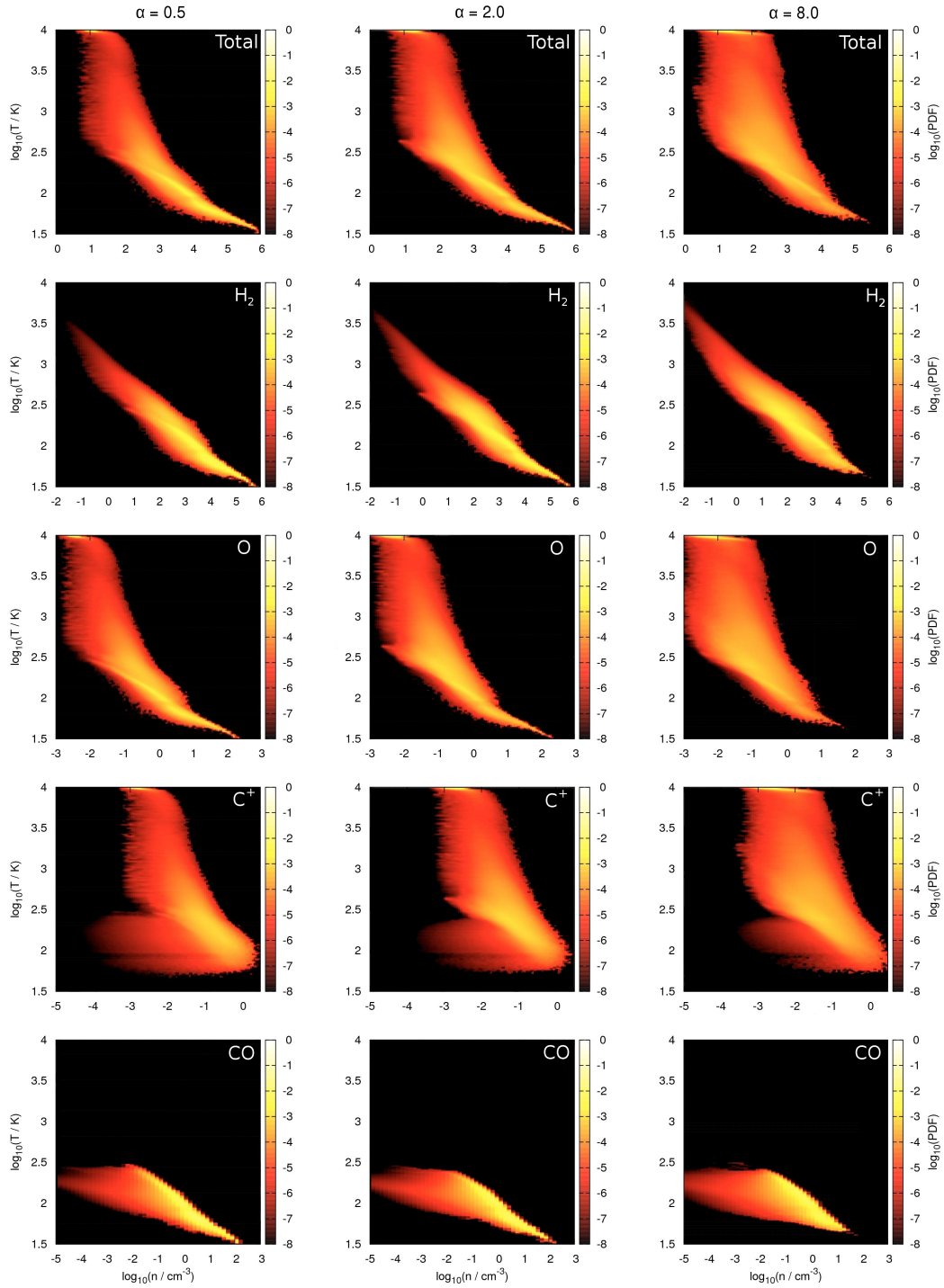
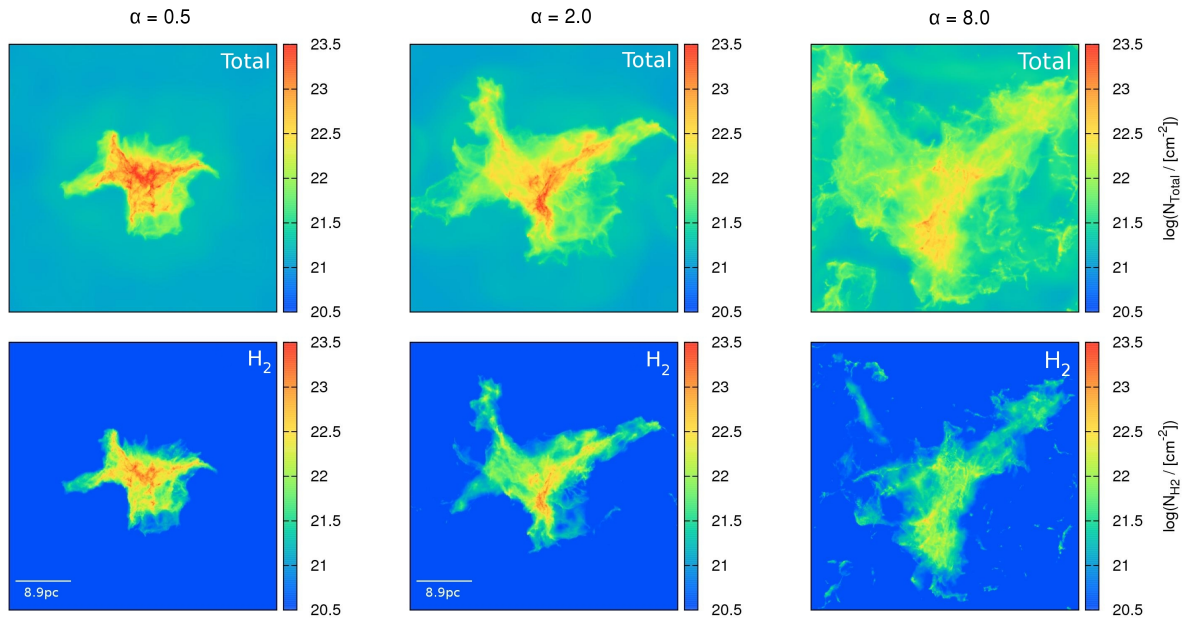


Figure 8.1:

Physical state of the clouds at the end of our simulations. We show two-dimensional PDFs of gas temperature and number density for various chemical components for runs with $\alpha = 0.5$ (left column), 2.0 (middle column), and 8.0 (right column). In the upper row, the number densities shown are the total particle number density. In the remaining rows, on the other hand, they are the number density of the chemical species indicated in the panel (e.g. n_{H_2} , n_{O} , etc.). Note that the scaling of the density axis therefore differs from panel to panel. The color coding shows the fraction of the total gas mass in each logarithmic density and temperature bin.

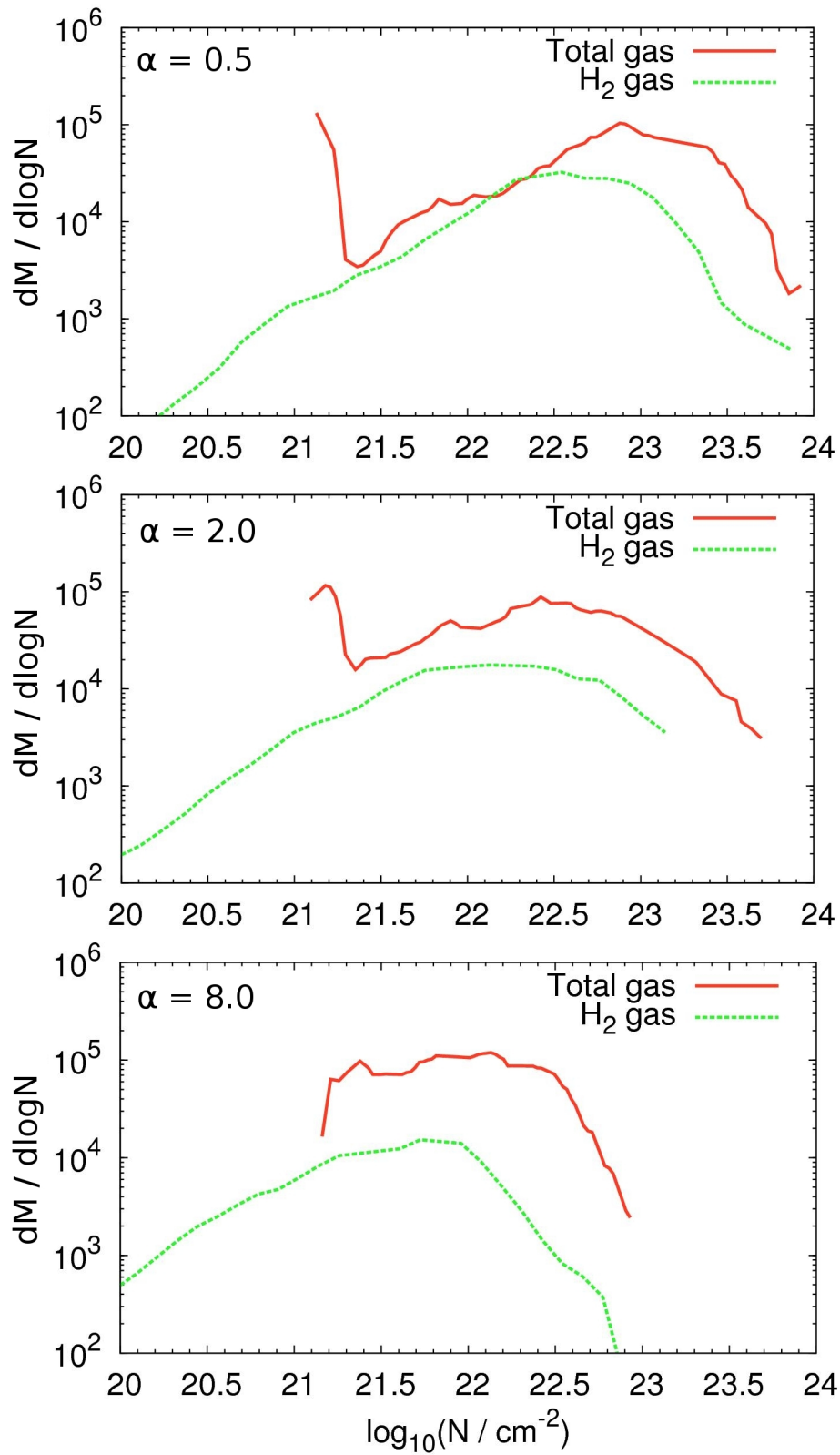
**Figure 8.2:**

Logarithmic column density maps computed along the LoS in the z -direction for the total density (top row) and the H_2 density (bottom row) for different virial parameters: $\alpha = 0.5$ (left column), 2.0 (middle column) and 8.0 (right column). Each side has a length of 44.5 pc. The initial cloud radius of 8.9 pc is indicated in the bottom panels.

Model	[CII] (158 μm) [K km s $^{-1}$]	[OI] (145 μm) [K km s $^{-1}$]	[OI] (63 μm) [K km s $^{-1}$]	^{12}CO (2600 μm) [K km s $^{-1}$]	^{13}CO (2720 μm) [K km s $^{-1}$]
GC-0.5-1000	3.0	1.0	0.6	1.0	1.0
GC-2.0-1000	3.0	1.0	0.6	0.3	0.3
GC-8.0-1000	3.0	0.8	0.5	0.1	0.1

Table 8.3:

Threshold values W_{thresh} used for the integrated intensity maps in Fig. 8.4 in order to estimate the effective cloud radius R_{eff} . The values are chosen such that the denser cloud regions can be clearly separated from the diffuse gas phase around it, leading to a reasonable estimate for the effective cloud radii presented in Table 8.4.

**Figure 8.3:**

Total mass per unit logarithmic column density for the total and the H_2 gas as shown in Fig. 8.2 for our different virial parameters: $\alpha = 0.5$ (top), 2.0 (middle) and 8.0 (bottom).

Model	total mass – [pc]	[CII] (158 μm) [pc]	[OI] (145 μm) [pc]	[OI] (63 μm) [pc]	^{12}CO (2600 μm) [pc]	^{13}CO (2720 μm) [pc]
GC-0.5-1000	11.0	9.0	8.7	8.1	6.6	6.2
GC-2.0-1000	13.1	13.8	13.0	12.2	7.6	6.8
GC-8.0-1000	17.5	20.1	19.9	19.7	8.4	6.9

Table 8.4:

Effective radii of the clouds shown in Fig. 8.4, as inferred from equation 8.3, based on the threshold intensities given in Table 8.3. For comparison, we also give the effective radii of the clouds that incorporate $\sim 80\%$ of the total gas mass in the second column.

turbulence opens up large channels into the cloud by lowering the column density locally, allowing radiation to penetrate deeper into the MC, leading to enhanced photodissociation of the molecular hydrogen. Hence, we do not find a good correlation between the total and the H_2 column density in the $\alpha = 2.0$ and $\alpha = 8.0$ runs. Molecular hydrogen can only exist in the most dense regions of the cloud, where it is best able to self-shield from the strong external radiation field.

This is also illustrated in Fig. 8.3, which shows the corresponding column density PDFs for three virial parameter models. If we compare the H_2 column density PDFs with each other, we find that the peak column density in the $\alpha = 0.5$ model is shifted to larger values compared to the $\alpha = 8.0$ model by about one order of magnitude. This is because the turbulent kinetic energy in the virialized $\alpha = 0.5$ run is much smaller than in the $\alpha = 8.0$ run, leading to denser cloud regions and thus to larger average column densities. Moreover, the fraction of H_2 gas in the total box decreases with increasing virial parameter, owing to the high external ISRF, which photodissociates those molecular components more effectively as the radiation can penetrate deeper into the cloud’s interior. Furthermore, we see that the H_2 gas generally extends to much lower column densities than the total gas. This is because the total gas consists of both atomic and molecular hydrogen and thus does not fall below lower values than $N_{\text{tot}} \approx 10^{21} \text{ cm}^{-2}$ due to the HI background, while the fraction of H_2 gas can continuously decrease in the outer regions due to photodissociation.

In analogy to Fig. 8.2, Fig. 8.4 shows velocity-integrated intensity maps computed along the LoS in the z -direction for the same virial parameters and the different tracers presented in Table 8.2. We again find that the molecular tracers ^{12}CO and ^{13}CO are photodissociated at the edges of the MC by the strong external ISRF. This effect is even stronger if the amount of turbulent kinetic energy in the box is high. Comparing the different tracers to the total gas column in Fig. 8.2, we find that the cloud’s shape is well reproduced by all atomic tracers, although the integrated brightness temperatures of these lines are significantly smaller than those of the ^{12}CO and ^{13}CO lines. This holds for all three virial parameter models. Conversely, in the case of CO, we find that neither of its isotopologues describes the total gas distribution of the cloud. However, we observe that they do remain reasonably good

tracers of the dense H_2 , owing to the effect of self-shielding. We will quantify this finding in Section 8.3.5.

8.3.3 Estimating the effective cloud radii

In the previous section we established that carbon monoxide is not a good tracer for the total column density, while the atomic species better reflect the distribution of the total gas mass. In this context, CO tends to significantly underestimate the radius of the total cloud in such an extreme environment. This can compromise any observational estimates of the virial parameter α , which requires an accurate estimate for the cloud's radius (see also our follow-up study in Paper II). However, we note that it is generally complicated to define a proper cloud radius. Molecular clouds are complex hierarchical systems and estimates of cloud radii always come with some assumptions of how to define outer cloud boundaries. Hence, if we refer to the effective cloud radius in the following, we always mean the radius of a spherical cloud with the same surface area.

Below, we try to estimate the effective cloud radius R_{eff} in a similar fashion to what would be applied to observational data sets. At first sight, this seems to be complicated, since all clouds shown in Fig. 8.4 are far away from a spherical geometry. Nevertheless, we can estimate an effective radius by adopting an integrated intensity threshold W_{thresh} for each map and counting the number of cells N , which fulfill $W_{\text{cloud}} > W_{\text{thresh}}$. The values for W_{thresh} are listed in Table 8.3 and are chosen so that there is a clear separation between emission from the cloud and from the diffuse gas in which it is embedded. Our results are not particularly sensitive to the exact value chosen for W_{thresh} , as long as it is large enough to not be contaminated by the diffuse emission, but not so large that we miss significant emission from the cloud itself. For example, in the case of model GC-0.5-1000, values of W_{thresh} anywhere in the range $2 < W_{\text{thresh}} < 10 \text{ K km s}^{-1}$ give essentially the same results for R_{eff} . For comparison, we also give the effective radii of the clouds that incorporate $\sim 80\%$ of the total gas mass.

We have also verified that our adapted thresholds are comparable or greater than the practical thresholds that we would obtain using modern instruments to measure the line emission. For example, in a single pointing, the GREAT instrument (German REceiver for Astronomy at Terahertz Frequencies, Heyminck et al., 2012) on-board the Stratospheric Observatory for Infrared Astronomy (SOFIA) can measure integrated intensities of the [CII] line down to around $\sim 0.06 \text{ K km s}^{-1}$ in around one hour of integration time², although multipixel array detectors are available today that become more and more efficient. Mapping an entire cloud using multiple pointings obviously allows one to spend much less time per pointing, yielding a higher threshold, but it remains plausible to map extended regions with a sensitivity comparable to or better than the adopted threshold.

We compute the effective cloud radius R_{eff} by assuming an effective cloud area

²<https://great.sofia.usra.edu/cgi-bin/great/great.cgi>

$A_{\text{eff}} = \pi R_{\text{eff}}^2$, where $A_{\text{eff}} = N\Delta x^2$ and Δx is the cell size introduced in Section 8.2.3. Thus, we get

$$R_{\text{eff}} = \sqrt{\frac{A_{\text{eff}}}{\pi}} = \Delta x \sqrt{\frac{N}{\pi}}. \quad (8.3)$$

Table 8.4 shows the different effective radii of the various clouds presented in Fig. 8.4, computed via equation (8.3). If we compare the different values listed in Table 8.4, we find that the cloud radii measured with the integrated intensities of ^{12}CO and ^{13}CO are significantly smaller by a factor of 1.5 – 2.5 compared to the values measured with the integrated intensities of the atomic tracers. This is because the strong ISRF and high CRF destroy the molecular tracers in the more diffuse regions, leading to smaller effective radii. Conversely, the radii measured with the atomic components roughly agree with each other for one specific virial parameter model and give the best radius estimate for the total cloud that incorporates $\sim 80\%$ of all gas. These values confirm our assumption that the atomic species accurately reflect the spatial distribution of the total gas column and that they yield a robust estimate of the effective radius of the cloud.

8.3.4 Tracing the total and H_2 column density

Now we turn to the densest parts of the cloud, because this is where stars are formed, and we study how well atomic fine-structure lines can be used to trace this regime. Fig. 8.5 and 8.6 show velocity-integrated intensities plotted against the total column density and H_2 column density for the different virial parameters and all tracers presented in Table 8.2. In these plots, we also show the the mean value at each column density, which is indicated by a black solid line. The small fluctuations at high column densities in each plot are caused by the small number of cells available to compute an average value of W .

We find clear differences for the various chemical components. For the total density in Fig. 8.5, we observe that the ^{12}CO and ^{13}CO tracers fall off sharply with decreasing column density below $\sim 10^{22} \text{ cm}^{-2}$, which is due to photodissociation of the gas in the diffuse cloud regions, owing to the strong external radiation field. On the other hand, at high column densities, we find a saturation of the ^{12}CO emission due to the effect of the line opacity, while the ^{13}CO emission is a significantly better tracer of the column density than ^{12}CO . This is because ^{13}CO is optically thin and consequently can better trace compact regions within the cloud. However, even in a small regime where N_{tot} and W_{CO} show some degree of correlation, we find a substantial amount of scatter around the mean value for both ^{12}CO and ^{13}CO . Furthermore, we also show the scatter plots for the different atomic species in Fig. 8.5. As expected, we see that all atomic components extend to significantly lower column densities of $\sim 10^{21} \text{ cm}^{-2}$ compared to carbon monoxide. Hence, both atomic carbon and oxygen are much better tracers of the low column density material of the total gas in the cloud. However, both the [CII] $158 \mu\text{m}$ and the [OI] $63 \mu\text{m}$ line saturate at higher column densities, owing to the effect of the line opacity and thus

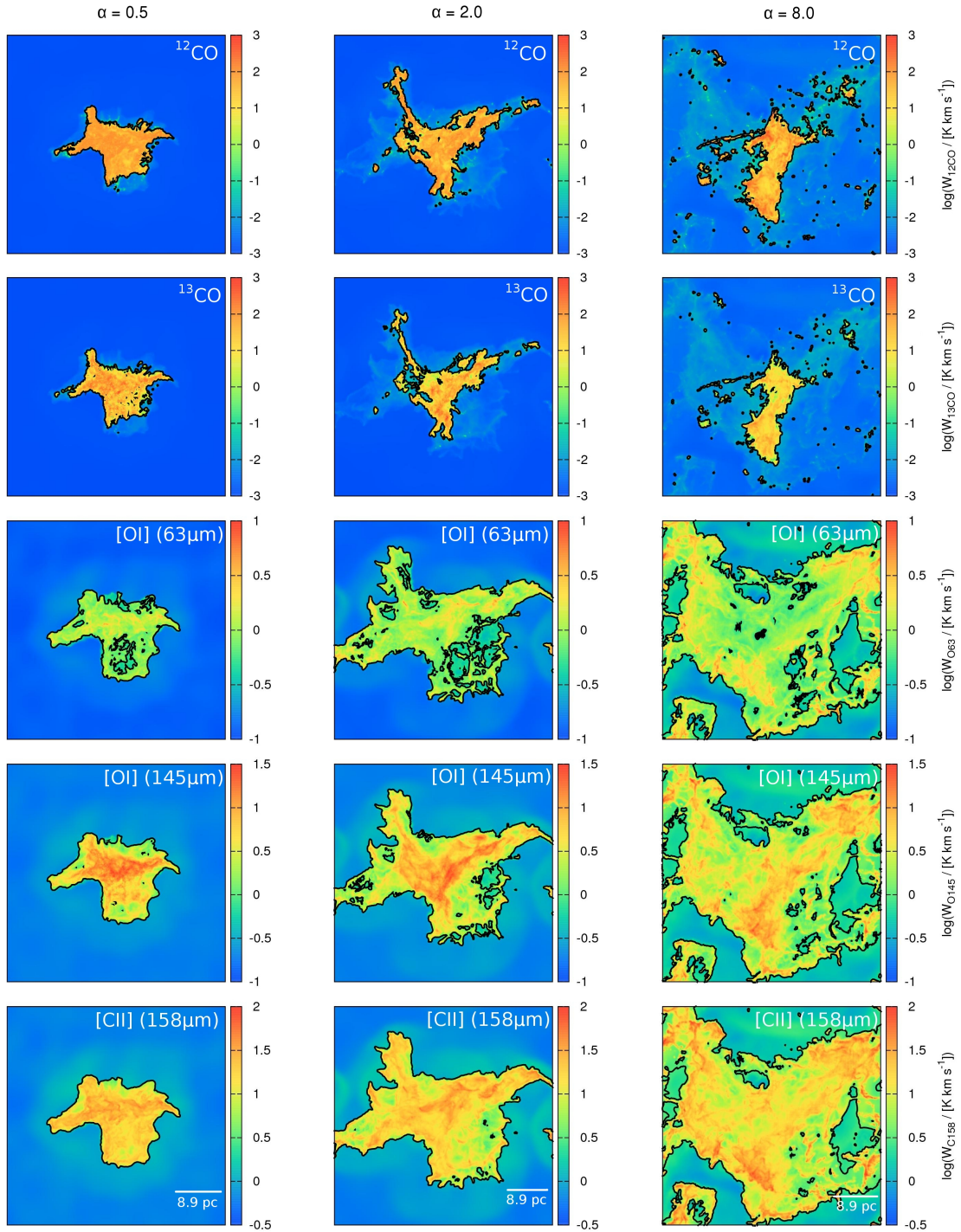


Figure 8.4:

Velocity-integrated intensity maps computed along the LoS in the z -direction for different virial parameters: $\alpha = 0.5$ (left column), 2.0 (middle column) and 8.0 (right column). From top to bottom: integrated intensity maps for ^{12}CO ($J = 1 \rightarrow 0$), ^{13}CO ($J = 1 \rightarrow 0$), [OI] ($63 \mu\text{m}$), [OI] ($145 \mu\text{m}$) and [CII] ($158 \mu\text{m}$). Note the different scaling in the colorbars at the right hand side. Each side has a length of 44.5 pc. The initial cloud radius of 8.9 pc is indicated in the bottom panels. The contour lines show the threshold values given in Table 8.3.

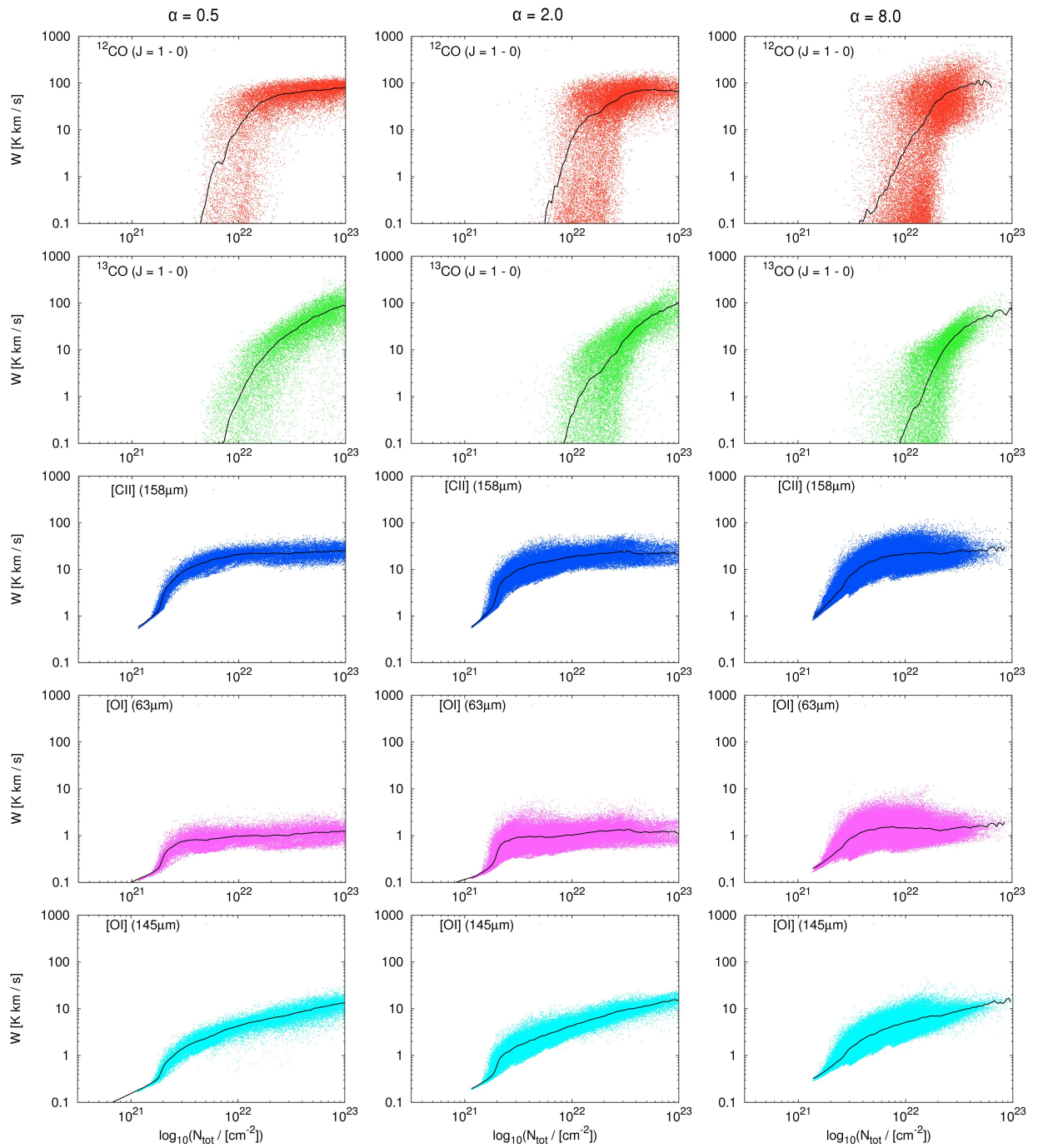


Figure 8.5:

Log-log plot showing velocity-integrated intensities against total column density for different virial parameters: $\alpha = 0.5$ (left column), 2.0 (middle column) and 8.0 (right column). Shown are all our tracers presented in Table 8.2. In each plot, the mean value is indicated by a black solid line.

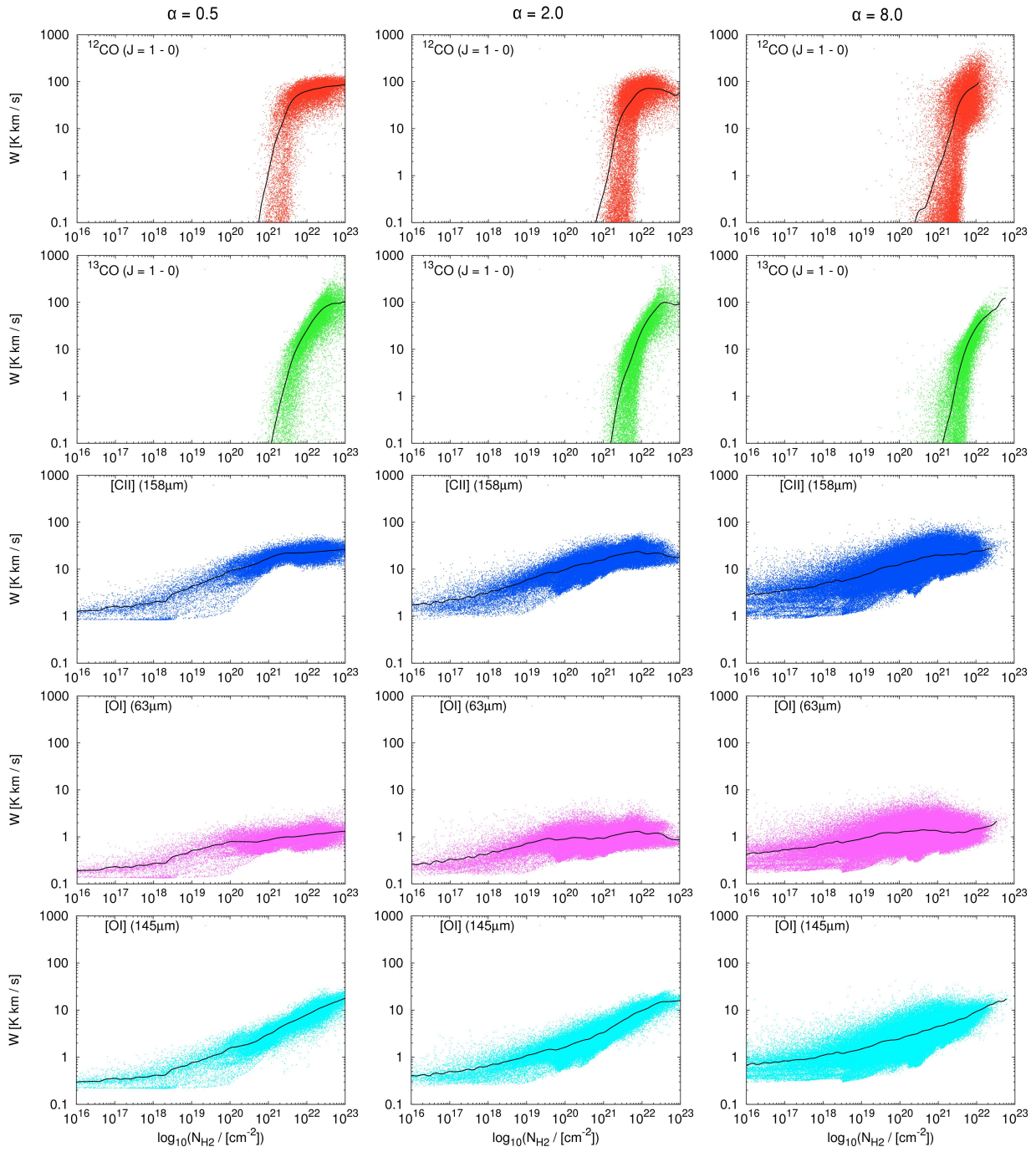


Figure 8.6: Same as Fig. 8.5, but with the column density of H_2 .

either ^{13}CO or the [OI] $145\ \mu\text{m}$ line is to be preferred as tracers for the dense cloud material.

For the H_2 column density in Fig. 8.6, we find a different result. Firstly, we see that both ^{12}CO and ^{13}CO extend to significantly lower H_2 column densities of $\sim 5 \times 10^{20} - 10^{21}\ \text{cm}^{-2}$, reflecting the fact that CO is a better tracer of molecular mass than of total mass. At higher column densities, we find a qualitatively similar behavior as for the total gas in Fig. 8.5, again owing to the effect of the line opacities. Moreover, we also show the scatter plots for the different atomic species. We note that both the atomic oxygen and carbon extend over a much larger range in H_2 column density than in total gas column density, showing that those components can also be used in order to accurately trace a large fraction of the molecular hydrogen mass. However, the correlation between the emission of [CII] $158\ \mu\text{m}$, [OI] $63\ \mu\text{m}$ and N_{H_2} breaks down at H_2 column densities above $\sim 10^{20} - 10^{21}\ \text{cm}^{-2}$, owing to the optical depth of these lines in this density regime. This means that one has to rely on other probes in order to infer information about the compact gas regions. On the contrary, the correlation between the [OI] $145\ \mu\text{m}$ emission and N_{H_2} seems to be provide a better way to study the dense H_2 clumps in the cloud.

We also analyze the impact that our over-estimation of the CO abundance may have on the relationship between the integrated intensity of the atomic tracers and the column density (see Appendix D.3). However, the influence of this turns out to be small.

8.3.5 Mass fraction traced by the emission

In Section 8.3.2 we speculated that a significant fraction of the total gas mass may not be traced by ^{12}CO or ^{13}CO . To quantify this finding, Fig. 8.7 shows the fraction of total and H_2 gas mass observed along the LoS having velocity-integrated intensities greater than a minimum value W_{min} for our various tracers. Furthermore, we analyze how this mass fraction changes as we vary W_{min} . In this context, Fig. 8.7 defines a theoretical limit for detecting gas above a given sensitivity threshold, e.g. determined by the telescope or the detector.

We see that all lines are a strong function of the minimum velocity-integrated intensity and of the virial parameter. In case of the mass fraction of the total gas, we find that our different atomic tracers recover almost all of the total mass if the minimum integrated intensity is $W_{\text{min}} \approx 0.1\ \text{K km s}^{-1}$ in the $\alpha = 0.5$ model and $W_{\text{min}} \approx 1.0\ \text{K km s}^{-1}$ in the $\alpha = 2.0$ and $\alpha = 8.0$ models. Furthermore, as already indicated in Section 8.3.2, we see that in the case of very small threshold values W_{min} in the $\alpha = 0.5$ model, both ^{12}CO and ^{13}CO only trace about 75% of the total mass or less. This fraction decreases even further for higher α values. For example, if we adopt $W_{\text{min}} \approx 0.1\ \text{K km s}^{-1}$ in the cloud with $\alpha = 8.0$, we find that only $\sim 40\%$ of the total mass is traced by CO, while all atomic tracers recover almost 100% of the total gas mass. Furthermore, we observe narrow emission ranges for some of the atomic components, which trace almost 100% of the total mass. For example, regarding our intermediate $\alpha = 2.0$ model and the [OI] $63\ \mu\text{m}$ tracer, almost 100%

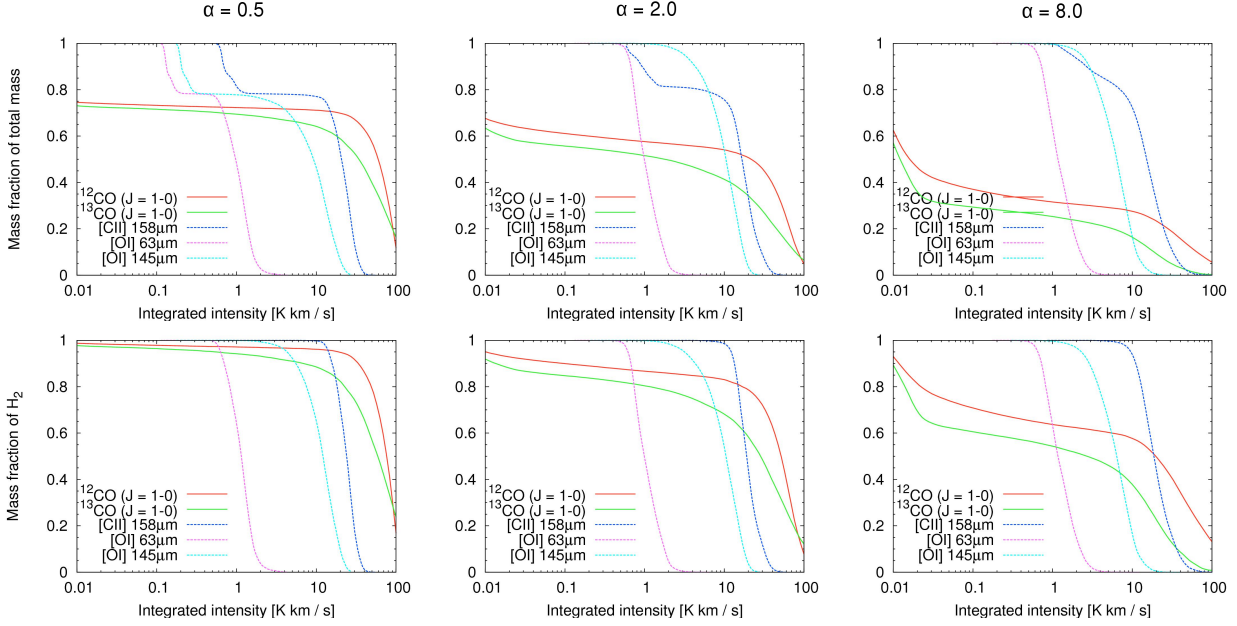


Figure 8.7:

Cumulative fraction of the total (top row) and H_2 (bottom row) mass in the cloud for different virial parameters $\alpha = 0.5$ (left column), 2.0 (middle column) and 8.0 (right column), traced by our various chemical components presented in Table 8.2, as a function of the minimum velocity-integrated intensity in the line.

of the total mass lies in the narrow emission range between $0.5 < W_{\min} < 3.0$. In the case of the other α models, we find a similar behavior. This is because there are almost no lines-of-sight having higher values of integrated intensity (see also Fig. 8.5 and 8.6), which may be different in even denser clouds.

Regarding the H_2 mass, we see that both ^{12}CO and ^{13}CO trace a higher H_2 mass fraction compared to the total mass of the cloud. This is because the molecular hydrogen can only exist in dense regions of the cloud, owing to the ability to self-shield from the external radiation field. This is similar to our finding for the carbon monoxide. Furthermore, we observe that the atomic components recover almost 100% of the H_2 mass if we set $W_{\min} \approx 0.5 \text{ K km s}^{-1}$. Hence, we find that those components again trace a significantly higher mass fraction of the gas compared to the carbon monoxide. Regarding both ^{12}CO and ^{13}CO , we see that the amount of mass recovered by those molecular tracers decreases with higher virial parameter for a fixed minimum value of the integrated intensity. For example, if we adopt a value of $W_{\min} \approx 0.1 \text{ K km s}^{-1}$, almost 98% of the H_2 mass is traced by ^{12}CO for our $\alpha = 0.5$ model, while $\sim 90\%$ is traced in our $\alpha = 2.0$ and only $\sim 70\%$ can be recovered in the $\alpha = 8.0$ model. Moreover, similar to the mass fraction of the total gas mass, we also find a narrow emission range for the various atomic lines in all α models, which trace about 100% of the H_2 mass. In contrast, the emission of the ^{12}CO and ^{13}CO molecules is extended over a much wider range in integrated intensities. Hence, a much larger emission range is needed in order to trace the whole mass of molecular

hydrogen in the cloud.

In summary, we conclude that CO is only a good tracer for the molecular content of the cloud, but can miss a significant fraction of the total gas mass, particularly for unbound clouds.

8.3.6 Estimating the CO-to-H₂ conversion factor

Based on our maps of column densities for H₂ (Fig. 8.2) and velocity-integrated intensities for ¹²CO (Fig. 8.4), we also estimate the value of the CO-to-H₂ conversion factor, X_{CO} , in our various models. X_{CO} is a widely used quantity in particular in extragalactic astronomy to derive H₂ column densities from CO observations (Bolatto et al., 2013). It is defined via

$$X_{\text{CO}} = \frac{N_{\text{H}_2}}{W_{\text{CO},1-0}}, \quad (8.4)$$

where N_{H_2} denotes the H₂ column density and $W_{\text{CO},1-0}$ the velocity-integrated brightness-temperature. Previous studies tried to estimate the X_{CO} -factor in both observations and numerical simulations (see, e.g. Solomon et al., 1987; Polk et al., 1988; Young & Scoville, 1991; Dame et al., 2001; Liszt et al., 2010; Leroy et al., 2011; Glover & Mac Low, 2011; Glover & Clark, 2012; Bolatto et al., 2013; Narayanan & Hopkins, 2013; Clark & Glover, 2015). For example, Shetty et al. (2011a,b) investigated the X_{CO} -factor in numerical simulations of turbulent clouds, varying environmental properties such as the initial number density, the metallicity and the external UV field, finding cloud average values $X_{\text{CO}} \approx 2 - 4 \times 10^{20} \text{ cm}^{-2} \text{ K}^{-1} \text{ km}^{-1} \text{ s}$ for solar-metallicity models. Moreover, Bolatto et al. (2013) review the efforts to measure the CO-to-H₂ conversion factor for molecular clouds in the Milky Way disk, recommending a similar factor $X_{\text{CO}} \sim 2 \times 10^{20} \text{ cm}^{-2} \text{ K}^{-1} \text{ km}^{-1} \text{ s}$ with $\pm 30\%$ uncertainty. However, all these studies arrived at the conclusion that the X_{CO} -factor in the Galaxy is remarkably constant, having a value of $X_{\text{CO}} \approx 2 - 4 \times 10^{20} \text{ cm}^{-2} \text{ K}^{-1} \text{ km}^{-1} \text{ s}$.

Nevertheless, in the last few years concerns have been raised that the X_{CO} -factor may be significantly different from the canonical value in MCs located in the galactic center. For example, Narayanan et al. (2012) have shown that large gas temperatures and velocity dispersions can increase the CO intensity, thus decreasing X_{CO} . On the other hand, the strong ISRF and CRF can also destroy the carbon monoxide, increasing X_{CO} (Clark & Glover, 2015). In addition, observational measurements of X_{CO} at the center of other nearby spiral galaxies typically find values that are lower than the canonical Galactic value (Sandstrom et al., 2013). Moreover, conditions in the Galactic Center are somewhat similar to those found in ULIRGs, and there is considerable observational evidence that X_{CO} is smaller in ULIRGs than in normal spiral galaxies (see e.g. the detailed discussion in Bolatto et al., 2013). So far, we are still missing a reliable picture of the X_{CO} -factor in different (and extreme) physical environments.

In the following, we evaluate the X_{CO} -factor for our three α models and list our results in Table 8.5. In general, the X_{CO} -factors given in Table 8.5 are computed

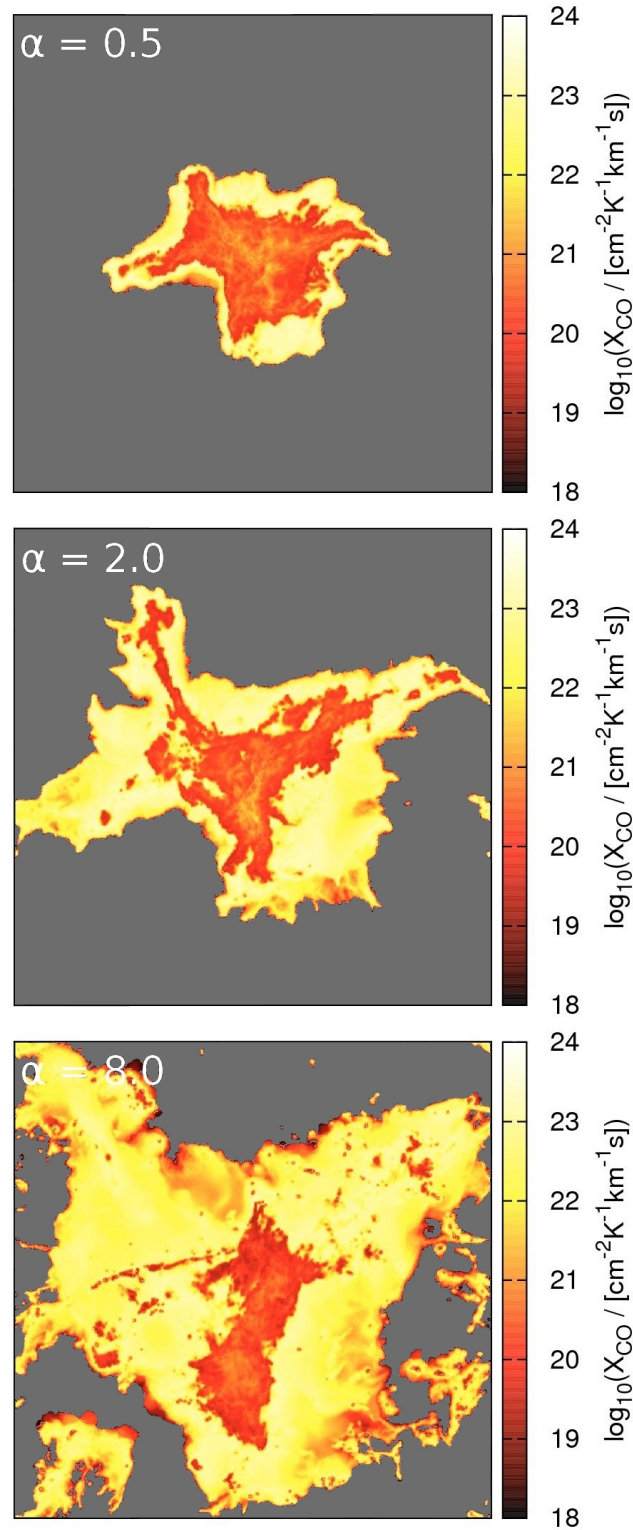


Figure 8.8:

Logarithmic maps of the CO-to-H₂ conversion factor, $X_{\text{CO}} = N_{\text{H}_2}/W_{\text{CO}}$, for the three models: $\alpha = 0.5$ (top), 2.0 (middle) and 8.0 (bottom). The average X_{CO} -factor values are given in Table 8.5. We see that only the inner parts of the cloud yield the canonical X_{CO} -factor value on average, while the outer cloud regions exhibit significantly larger X_{CO} values. The gray background denotes regions where the CO emission is zero. Hence, it is impossible to compute a value for X_{CO} there.

Model	X_{CO}
	$[\text{cm}^{-2} \text{K}^{-1} \text{km}^{-1} \text{s}]$
GC-0.5-1000	3.9×10^{20}
GC-2.0-1000	2.6×10^{20}
GC-8.0-1000	1.3×10^{20}

Table 8.5:

Values of the CO-to-H₂ conversion factor, relating the amount of ¹²CO ($J = 1 \rightarrow 0$) emission W_{CO} to the H₂ column density N_{H_2} for all our α runs. For the computation of the X_{CO} -factor, we only include pixels where the velocity-integrated intensity for carbon monoxide is larger than the corresponding threshold given in Table 8.3. Thus, X_{CO} only accounts for regions with a significant amount of CO emission in the cloud.

by taking the ratio of the mean values of the H₂ column density and the velocity-integrated intensity of CO. We only include pixels where the velocity-integrated intensity for carbon monoxide is larger than the corresponding threshold given in Table 8.3. These are 1.0, 0.3 and 0.1 K km s⁻¹ for the models with $\alpha = 0.5, 2.0$ and 8.0. Thus, X_{CO} only accounts for regions with a significant available amount of CO emission in the cloud, as illustrated in Fig. 8.4.

We find a range of values for the CO-to-H₂ conversion factor in Table 8.5, reaching from $\sim 1 - 4 \times 10^{20} \text{ cm}^{-2} \text{K}^{-1} \text{km}^{-1} \text{s}$. Our estimates are in good agreement to estimates of the canonical X_{CO} -factor in the Milky Way. However, we again emphasize that our Nelson & Langer (1997) network overestimates the rate at which CO forms (see also Section 8.2.1) and hence we expect that our X_{CO} -factors listed in Table 8.5 are lower limits.

Furthermore, we show logarithmic maps of the X_{CO} -factor for all our α models in Fig. 8.8. Here, the X_{CO} -values are evaluated by computing the ratio of the H₂ column density and the velocity-integrated intensity of CO for each individual pixel. The gray background denotes regions where the CO emission is zero. Hence, it is impossible to compute a value for X_{CO} there. We find significantly different values for the inner and the outer parts of the clouds. While the inner cloud regions reproduce the canonical X_{CO} -factor value on average, we find that the outer cloud regions exhibit significantly larger X_{CO} values compared to the canonical one. This is because the carbon monoxide is photodissociated at the edges of our clouds by the strong ISRF, leading to an increase in X_{CO} . In contrast, the molecular CO is better able to self-shield in the dense parts of the cloud and hence we observe that those regions fairly reproduce the canonical value.

8.4 Summary and Conclusions

In this paper we have analyzed synthetic images of MCs in a CMZ-like environment. For this purpose, we have performed numerical simulations of model clouds with the moving mesh code AREPO (Springel, 2010) using environmental properties

comparable to those experienced by typical CMZ clouds. We adopted values for the interstellar radiation field (ISRF) and the cosmic-ray flux (CRF) that are a factor of ~ 1000 larger than the values measured in the solar neighbourhood (Clark et al., 2013). We simulated clouds with an initial number density of $n_0 = 10^3 \text{ cm}^{-3}$ and studied the impact of different virial α parameters of $\alpha = 0.5, 2.0$ and 8.0 . The total cloud mass was set to a constant value of $M_{\text{tot}} = 1.3 \times 10^5 M_{\odot}$. Furthermore, we used the radiative transfer code RADMC-3D (Dullemond, 2012) to compute synthetic maps of our clouds in important diagnostic lines, i.e. we model the emission of the cloud in [CII] ($158 \mu\text{m}$), [OI] ($145 \mu\text{m}$), [OI] ($63 \mu\text{m}$), ^{12}CO ($2600 \mu\text{m}$) and ^{13}CO ($2720 \mu\text{m}$). We report the following findings:

- Atomic carbon and oxygen is found in both cold and warm regions in the clouds, but CO only traces cold regions (see Section 8.3.1).
- If the cloud is virialized ($\alpha = 0.5$), the H_2 gas is much better able to self-shield from the high external ISRF compared to other runs with a larger α value. This is because the gravitational pressure compresses the gas to much higher densities because the amount of turbulent kinetic energy in the box is smaller in the low α models than in the high virial parameter models. In the latter case, radiation can penetrate deeper into the MC, leading to photodissociation of the molecular hydrogen (see Section 8.3.2).
- We show that the atomic components trace the shape of the total cloud very well even in diffuse cloud regions (see Section 8.3.2).
- On the other hand, the molecular gas (H_2 as well as CO) is photodissociated at the edges of the MC by the strong external ISRF.
- As a consequence, the photodissociation has a strong impact on measurements of the effective MC radius using a molecular tracer, which tend to significantly underestimate the radius of the total cloud in environments where the external radiation field and the turbulent kinetic energy is high. However, we find that the atomic tracers recover a significantly larger fraction of the total cloud mass (see Section 8.3.3).
- We find a large dynamical range for the [OI] $145 \mu\text{m}$ line in column density space, which traces both the H_2 and the total gas up to the most dense regions in the cloud. In contrast, the [OI] $63 \mu\text{m}$ and [CII] $158 \mu\text{m}$ lines already saturate at significantly lower column densities. Hence, we would not expect that those components trace the compact MC regions very well (see Section 8.3.4).
- We find that all atomic components trace almost 100% of the H_2 and the total gas mass above a sensitivity threshold of $W_{\text{min}} \approx 0.1 \text{ K km s}^{-1}$ for the velocity-integrated intensities. However, we also find that CO only traces a significantly lower mass fraction of H_2 and the total density compared to the atomic components (see Section 8.3.5).

- We compute values of the CO-to-H₂ conversion factor $X_{\text{CO}} = N_{\text{H}_2}/W_{\text{CO}}$, which relates the H₂ column density N_{H_2} to the amount of ¹²CO ($J = 1 \rightarrow 0$) emission W_{CO} . We find values in the range $X_{\text{CO}} \approx 1 - 4 \times 10^{20} \text{ cm}^{-2} \text{ K}^{-1} \text{ km}^{-1} \text{ s}$, in good agreement to the canonical X_{CO} -factor values obtained in observations of MCs in the Milky Way (see Section 8.3.6). However, we caution that simplifications in our chemical model mean that these values are lower limits.

Synthetic observations of MCs in a galactic center environment:

II. Analyzing the internal cloud kinematics

We use the AREPO moving mesh code to simulate molecular clouds exposed to an extreme environment found in the Central Molecular Zone (CMZ). Our simulations include a simplified treatment of time-dependent chemistry and account for the highly non-isothermal nature of the gas and the dust. Our clouds have a total and constant mass of $1.3 \times 10^5 M_{\odot}$. We explore the effect of varying the virial α parameter, $\alpha = E_{\text{kin}}/|E_{\text{pot}}|$, that is the ratio of kinetic and potential energy, and adjust the internal velocity dispersion. We use values $\alpha = 0.5, 2.0$ and 8.0 to span a large range in virial space and hence, most of our clouds are gravitationally unbound. We use an interstellar radiation field and a cosmic ray flux which are both a factor of 1000 higher than the values found in the solar neighbourhood. Furthermore, we use the radiative transfer code RADMC-3D to compute synthetic images of our clouds measured in various diagnostic lines. We model the line emission for [CII] ($158 \mu\text{m}$), [OI] ($145 \mu\text{m}$), [OI] ($63 \mu\text{m}$), ^{12}CO ($2600 \mu\text{m}$) and ^{13}CO ($2720 \mu\text{m}$). We show that the thermal energy in such extreme environments can be high enough to dominate the turbulent kinetic energy, which means that spectral observations most likely trace the thermal velocities of the gas. Furthermore, we analyze the internal cloud kinematics and estimate the virial parameter as it can be inferred from observational measurements. We demonstrate that the atomic components yield a good estimate of the underlying virial state of the clouds and that they can be used to accurately trace the internal velocity dispersions of the total gas in clouds located in the CMZ. The results presented in this chapter will soon be submitted to MNRAS.

9.1 Introduction

Understanding the physical processes behind the formation of stars is an important task in astrophysics. It is known that the turbulent dynamics of a molecular cloud (MC) significantly affect the process of star formation (see, e.g. Mac Low & Klessen, 2004; Scalo & Elmegreen, 2004; Elmegreen & Scalo, 2004; McKee & Ostriker, 2007; Hennebelle & Falgarone, 2012). Stars form in MCs due to gravitational collapse of dense gas regions. Therefore, the cloud has to cool in order to lose thermal energy. Furthermore, if the cloud is highly turbulent, the turbulent pressure can also act against gravitational collapse. Conversely, supersonic flows can also create overdense regions in the cloud induced by shock compression of the gas, which lead to seeds of protostars. Hence, understanding the internal cloud kinematics is crucial for understanding star formation.

Stars form in nearly all regions in our Milky Way. However, the physics put forward for their formation seems to be controlled by different processes, which strongly depend on the physical environment. In this context, the Galactic Center (GC) is a very extreme region in our Galaxy. The inner few hundred parsecs are known as the Central Molecular Zone (CMZ), a region which is rich in molecular and very dense gas. It is supposed to be highly turbulent (Oka et al., 1998, 2001; Shetty et al., 2012; Tsuboi & Miyazaki, 2012) and to have significantly higher gas densities than MCs found in the solar neighbourhood (Longmore et al., 2013). Furthermore, the interstellar radiation field (ISRF) and the cosmic-ray flux (CRF) in the CMZ seem to be enhanced by a factor of $\sim 100 - 1000$ (Yusef-Zadeh et al., 2007; Clark et al., 2013; Indriolo et al., 2015; Ginsburg et al., 2015) compared to their canonical values (Habing, 1968; Draine, 1978; Mathis et al., 1983).

Several studies in the past tried to measure the internal kinematics of various CMZ clouds, in an effort to understand the role of turbulence in the star formation process in such an extreme environment. One important parameter to characterize the internal dynamics of a cloud is the virial α parameter, defined as the ratio of kinetic to potential energy of the system. If $\alpha = 0.5$, the cloud is virialized (i.e. in virial equilibrium). If the virial parameter is larger than unity, $\alpha > 1$, the turbulent kinetic energy dominates the evolution of the MC and the cloud is unbound. Clouds in the CMZ generally appear to be unbound, with $\alpha \gtrsim 1$. For example, Kauffmann et al. (2013) evaluated α for the entire GC cloud G0.253+0.016, which is known as “The Brick” (see e.g. Güsten et al., 1981; Lis et al., 1994; Lis & Menten, 1998; Lis et al., 2001; Molinari et al., 2011; Immer et al., 2012; Longmore et al., 2012; Kauffmann et al., 2013; Clark et al., 2013; Johnston et al., 2014; Rathborne et al., 2014). They find a value of $\alpha \approx 3.8 \pm 1.0$. This estimate is in good agreement with a value of $\alpha \gtrsim 2$ for various clumps within the Brick, which can be computed based on data given in Table 2 in Johnston et al. (2014). Moreover, Tsuboi & Miyazaki (2012) have measured α values for different clumps in the GC cloud GCM-0.02-0.07, for which we find a mean value of $\alpha = 3.0 \pm 1.6$ based on their data.

To gain information about the internal cloud dynamics, observers rely on spec-

Tracer	Type	Transition	λ [μm]	ν [GHz]
^{12}CO	Molecular	$J = 1 \rightarrow 0$	2600	115
^{13}CO	Molecular	$J = 1 \rightarrow 0$	2720	110
[CII]	Atomic	$^2P_{3/2} \rightarrow ^2P_{1/2}$	158	1900
[OI]	Atomic	$^3P_1 \rightarrow ^3P_2$	63	4744
[OI]	Atomic	$^3P_0 \rightarrow ^3P_1$	145	2060

Table 9.1:

Tracer name and type, quantum mechanical transition, wavelength λ and frequency ν of various fine structure lines, which we model with the radiative transfer code RADMC-3D.

tral measurements of different tracers, e.g. CO, CS or NH_3 , which are abundant molecules in MCs in the CMZ (see, e.g. Bania, 1977; Burton et al., 1978; Liszt & Burton, 1978; Morris & Serabyn, 1996b; Bitran et al., 1997; Oka et al., 1998; Martin et al., 2004; Mills & Morris, 2013; Rathborne et al., 2014). Beside those molecular tracers, Clark et al. (2013) have investigated the effect of line cooling in MCs in a typical CMZ-like environment for atomic tracers like [OI] (63 μm) and [CII] (158 μm), finding that they dominate the cooling over a wide range in densities. Furthermore, Rodríguez-Fernández et al. (2004) present observations of these fine structure lines in the CMZ, carried out with the ISO satellite. They show that both lines are bright enough to be observed and that they can be used to infer important information about the physics of the ISM in the CMZ.

In this paper, we investigate how well the kinematic properties of clouds in a CMZ-like environment can be probed using the [OI] and [CII] fine structure lines. We do this with the help of numerical simulations carried out with the AREPO moving mesh code (Springel, 2010). Our simulations include a simplified treatment of time-dependent chemistry and account for the highly non-isothermal nature of the gas and the dust. They were previously described in a companion paper (Bertram et al., 2015d; hereafter, Paper I) in which we investigated the usefulness of the same lines as tracers of the cloud column density.

The present paper is structured as follows. In section 9.2 we briefly describe our numerical simulations, the radiative transfer post-processing tool and list our model parameters. In section 9.3 we show and discuss the results of our studies. In section 9.4 we present a summary and our conclusions.

9.2 Methods

9.2.1 Hydrodynamical and chemical model

We perform simulations using the moving mesh code AREPO (Springel, 2010). We make use of a detailed atomic and molecular cooling function, described in detail in Glover et al. (2010) and Glover & Clark (2012), and a simplified treatment of the

Model name	Virial α	Initial n_0 [cm ⁻³]	3D σ_v [km/s]	Radius R [pc]	Free-fall time t_{ff} [Myr]	End t_{end} [Myr]
GC-0.5-1000	0.5	1000	5.4	8.9	1.40	1.00
GC-2.0-1000	2.0	1000	10.8	8.9	1.40	1.40
GC-8.0-1000	8.0	1000	21.6	8.9	1.40	1.40

Table 9.2: Overview of the initial conditions for our different cloud models.

molecular chemistry of the gas. Our chemical treatment is based on the work of Nelson & Langer (1997) and Glover & Mac Low (2007), and allows us to follow the formation and destruction of H₂ and CO self-consistently within our simulations. The network tracks the abundances of 6 species and follows 14 chemical reactions. Full details of the chemical model with a description of how the chemistry interacts with the ISRF via the TREECOL algorithm can be found in Clark et al. (2012). Examples of the use of our chemical model with the AREPO code can be found in Smith et al. (2014a,b). To obtain the abundances of ¹³CO, we set the ¹²CO to ¹³CO ratio to a constant value, $R_{12/13} = 60$, since our simulations do not explicitly track the abundances of the isotopologues of ¹²CO (see also the discussion in Szűcs et al., 2014). Furthermore, we note that our chemical network is known to somewhat overestimate the rate at which CO forms, owing to its neglect of atomic carbon. However, we find that this has only a small impact on our results. For a detailed discussion of this effect, we refer the reader to Paper I.

The CMZ has super-solar metallicity. However, we use a uniform solar value in order to be conservative regarding the cooling rates in our runs. We adopt the standard ratio of helium to hydrogen, and abundances of carbon and oxygen taken from Sembach et al. (2000). These are $x_{\text{C}} = 1.4 \times 10^{-4}$ and $x_{\text{O}} = 3.2 \times 10^{-4}$, where x_{C} and x_{O} are the fractional abundances by number of carbon and oxygen relative to hydrogen. At the beginning of the simulations, the hydrogen, helium and oxygen are in atomic form, while the carbon is assumed to be in singly ionized form, as C⁺. We also adopt the standard local value for the dust-to-gas ratio of 1:100 (Lilley, 1955), and assume that the dust properties do not vary with the gas density. For the initial gas and dust temperature we choose a value of 20 K. The cosmic ray ionization rate (CRIR) of atomic hydrogen is set to $\zeta = 3 \times 10^{-14} \text{ s}^{-1}$ (Clark et al., 2013). This value is a factor ~ 1000 higher than the value measured in dense clouds in the solar neighbourhood (van der Tak & van Dishoeck, 2000) and is comparable to the high value that has previously been inferred in the CMZ (Yusef-Zadeh et al., 2007; Clark et al., 2013; Ginsburg et al., 2015). For the incident ultraviolet radiation field, we adopt the same spectral shape as given in Draine (1978). We denote the strength of the Draine ISRF as $G_0 = 1$ and perform simulations with a field strength $G_0 = 1000$ (Clark et al., 2013), corresponding to an integral flux in the energy range 6 – 13.6 eV of $2.7 \times 10^{-3} \text{ erg cm}^{-2} \text{ s}^{-1}$.

The simulations analyzed in this paper were originally carried out as part of the study of star formation in extreme environments presented in Bertram et al. (2015c),

and a more extensive discussion of the simulation setup and the dynamical evolution of the clouds can be found in that paper.

9.2.2 Radiative transfer calculation

We use the radiative transfer code RADMC-3D¹ (Dullemond, 2012) to generate synthetic maps for various chemical components, as previously described in Paper I. The atomic and molecular transitions for which we produce synthetic maps are listed in Table 9.1. At the moment, RADMC-3D cannot deal with AREPO data directly, and so we have to map the simulation output onto a cubic grid. We adopt a grid size of 44.5 pc and a grid resolution of 512^3 cells, resulting in a cell size of 0.087 pc. For each cloud, we consider a range of velocities wide enough to encompass all of the line emission from the cloud, and break this velocity range up into 512 distinct velocity channels. The width of these channels is then 0.057 km s^{-1} , 0.066 km s^{-1} and 0.102 km s^{-1} for our models with $\alpha = 0.5, 2.0$ and 8.0 , respectively.

The radiative transfer calculations provide the intensities of the different tracers at each LoS position (x, y) at a given frequency ν , which can be translated into brightness temperatures T_B via the Rayleigh-Jeans approximation. We perform the radiative transfer post-processing for all tracers and virial parameters for an arbitrary Line-of-Sight (LoS), using the last snapshot of each model. Since we use isotropic turbulence without magnetic fields, we do not expect our results to significantly depend on the specific choice of the LoS and hence we only focus on emission observed along the z -direction.

9.2.3 Model parameters

We model clouds which are initially spherical and embedded in a low-density environment with a number density of $\approx 1 \text{ cm}^{-3}$. We use periodic boundary conditions. The cloud has a uniform initial hydrogen nuclei number density, which we set to 10^3 cm^{-3} with a total mass of $M_{\text{tot}} = 1.3 \times 10^5 M_{\odot}$. We initially start with 2×10^6 cells in total. At the beginning of the simulations, the cloud radius is $R \approx 8.9 \text{ pc}$. The cubic side length of the total box is set to 5x the cloud radius, corresponding to 44.5 pc in total. All clouds have zero bulk velocity and are placed in the center of the box.

The initial random velocity field is described by a power spectrum of $P(k) \propto k^{-4}$ that consists of a natural mixture of solenoidal and compressive modes, which decays throughout the simulation. The strength of the turbulent kinetic energy is regulated via the virial α parameter, hereafter defined as $\alpha = E_{\text{kin}}/|E_{\text{pot}}|$, that is the kinetic energy $E_{\text{kin}} = 1/2 M_{\text{tot}} \sigma_v^2$ divided by the potential energy $E_{\text{pot}} = -3GM_{\text{tot}}^2/(5R)$ measured at the beginning of each run. We analyze models with $\alpha = 0.5, 2.0$ and 8.0 in order to span a large range of values in the virial parameter space.

¹www.ita.uni-heidelberg.de/~dullemond/software/radmc-3d/

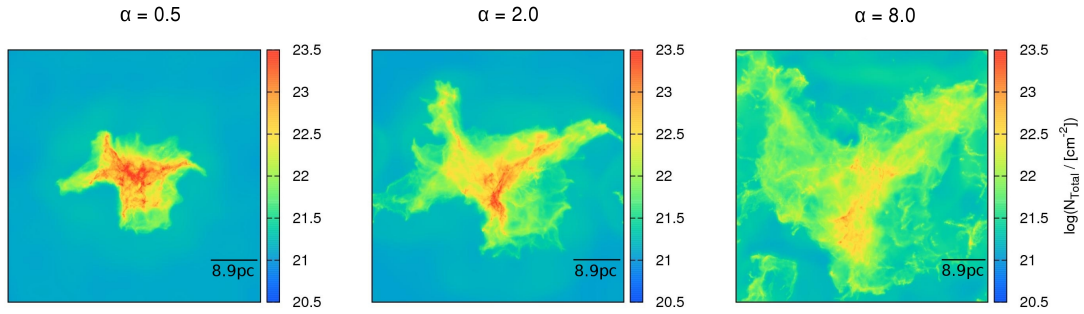


Figure 9.1:

Logarithmic column density maps computed along the LoS in the z -direction for the total density for different virial parameters: $\alpha = 0.5$ (left), 2.0 (middle) and 8.0 (right). Each side has a length of 44.5 pc. The initial cloud radius of 8.9 pc is indicated in each panel.

The free-fall time of our spherical cloud corresponds to $t_{\text{ff}} \approx 1.4$ Myr. Since we produce ~ 200 snapshots for each simulation, the timestep between the individual snapshots is $\Delta t_{\text{snap}} \approx 7$ kyr. Table 9.2 summarizes the initial conditions of our clouds.

9.3 Results

In this section, we analyze the cloud kinematics using the latest time snapshot from our simulations (see Table 9.2). We begin with a short discussion on maps of total column density and velocity-integrated intensity (Section 9.3.1). Afterwards, we estimate the internal velocity dispersion of the total cloud mass (Section 9.3.2). Then, we ask how well the different atomic and molecular components listed in Table 9.1 trace the internal velocity dispersion of the total gas. Therefore, we evaluate both the intensity-weighted rms velocities (Section 9.3.3) as well as the full width at half maximum (FWHM) which we derive from the different line spectra (Section 9.3.4). Afterwards, we study the temporal evolution of the virial parameter in our simulations (Section 9.3.5). At the end, we estimate the value of α as it can be inferred from observational measurements by using synthetic observations (Section 9.3.6).

9.3.1 Column density and velocity-integrated intensity maps

In Fig. 9.1, we show logarithmic maps of column density of the total gas mass computed along the z -direction for our different virial parameter models $\alpha = 0.5, 2.0$ and 8.0. We see that the shape of the cloud strongly depends on its virial state. If the cloud is virialized ($\alpha = 0.5$), it remains relatively compact since the cloud is gravitationally bound. However, if we increase the virial parameter ($\alpha = 2.0$ and 8.0), the turbulence can disperse the gas more efficiently. In those cases, the cloud is not gravitationally bound and hence the external radiation field can penetrate

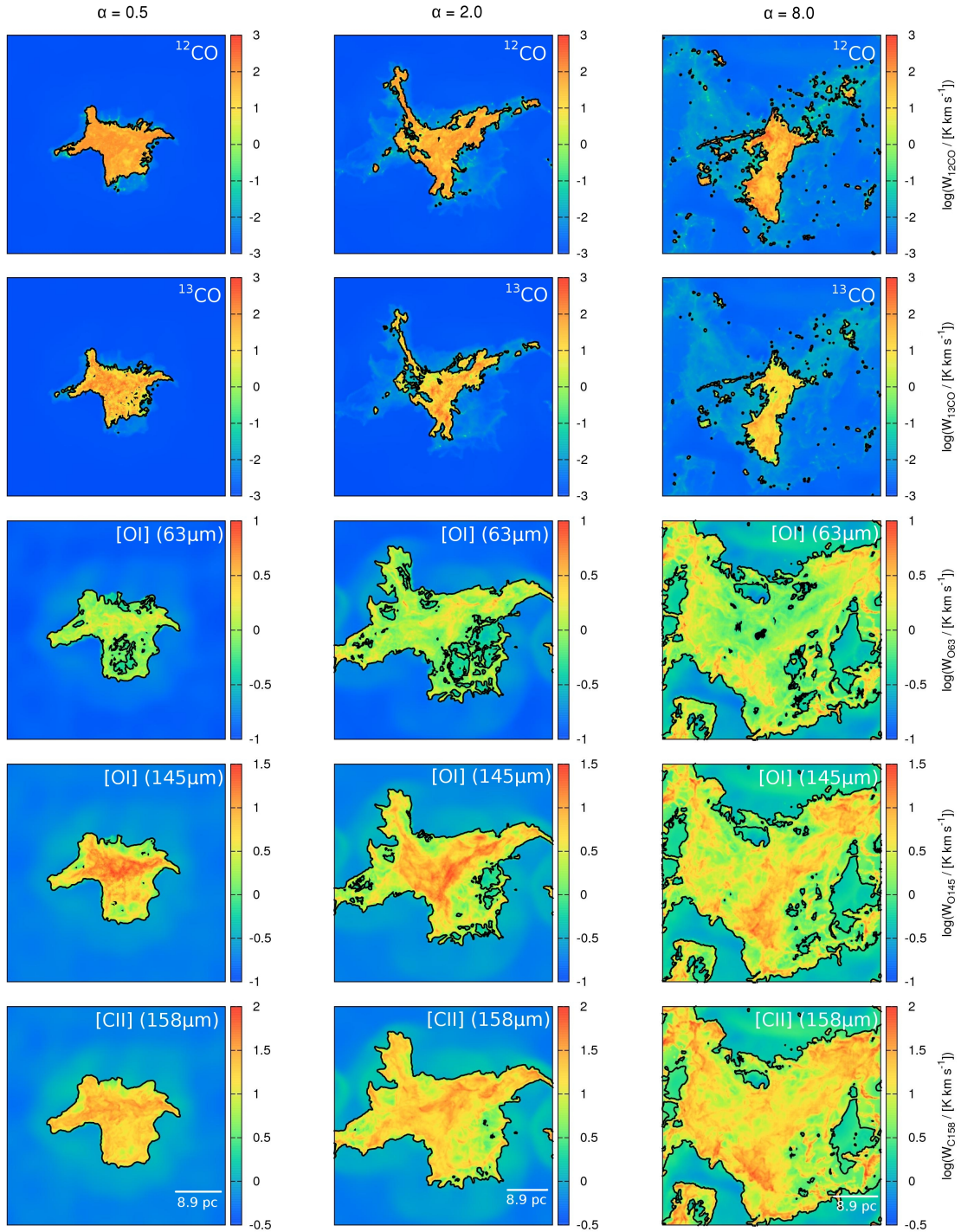


Figure 9.2:

Velocity-integrated intensity maps computed along the LoS in the z -direction for different virial parameters: $\alpha = 0.5$ (left column), 2.0 (middle column) and 8.0 (right column). From top to bottom: integrated intensity maps for ^{12}CO ($J = 1 \rightarrow 0$), ^{13}CO ($J = 1 \rightarrow 0$), $[\text{OI}] (63 \mu\text{m})$, $[\text{OI}] (145 \mu\text{m})$ and $[\text{CII}] (158 \mu\text{m})$. Note the different scaling in the colorbars at the right hand side. Each side has a length of 44.5 pc. The initial cloud radius of 8.9 pc is indicated in the bottom panels. The contour lines show the threshold values given in Table 3 in Paper I.

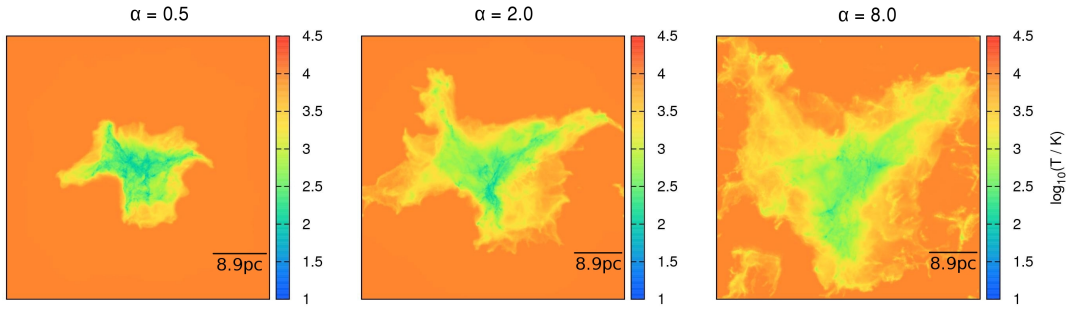


Figure 9.3:

Logarithmic maps of density-weighted mean temperatures computed via Eq. 9.4 along the z -direction for the different virial parameters: $\alpha = 0.5$ (left), 2.0 (middle) and 8.0 (right). Each box has a size of 44.5 pc. The initial cloud radius of 8.9 pc is indicated in each panel. The temperatures extend from $\sim 50 - 100$ K in the coldest regions to $\sim 10,000$ K in the hottest regions around each cloud.

much deeper into the cloud's interior. The corresponding column density PDFs are shown in Paper I.

In analogy to Fig. 9.1, Fig 9.2 shows logarithmic maps of velocity-integrated intensity along the LoS in the z -direction for our different virial parameter models and tracers listed in Tab. 9.1. The contour lines indicate the threshold values which are given in Table 3 in Paper I. They characterize the boundaries of the clouds. If we compare the MCs from Fig. 9.2 with the total gas column shown in Fig. 9.1, we see that a significant fraction of CO gas is photodissociated at the edges of the MCs by the strong external radiation field. This effect is even stronger the larger the virial parameter is, since the turbulence can open up larger channels for the external radiation to penetrate deeper into the cloud. Furthermore, we find that the atomic tracers well reproduce the total cloud's shape, although their emission lines are significantly fainter than the lines of the different carbon monoxide tracers. This holds for all our α models. Conversely, we see that the CO tracers do not describe the total gas distribution very well.

9.3.2 Estimating the velocity dispersion of the total cloud mass

In the following, we examine how well the emission of our various tracers from Table 9.1 reflect the internal velocity dispersion of the cloud. Therefore, we first compute the velocity dispersion of the total gas mass. However, spectral observations in different lines are usually affected by two main contributions. The first contribution σ_{turb} comes from the underlying turbulent velocity field, and the second one σ_{therm} comes from thermal motions of the gas. To compute the former, we first construct cubes of position-position-velocity (PPV) for the total mass by using the full 3D information of the total density and the velocity field from our simulations. The turbulent contribution to the internal velocity dispersions is then computed

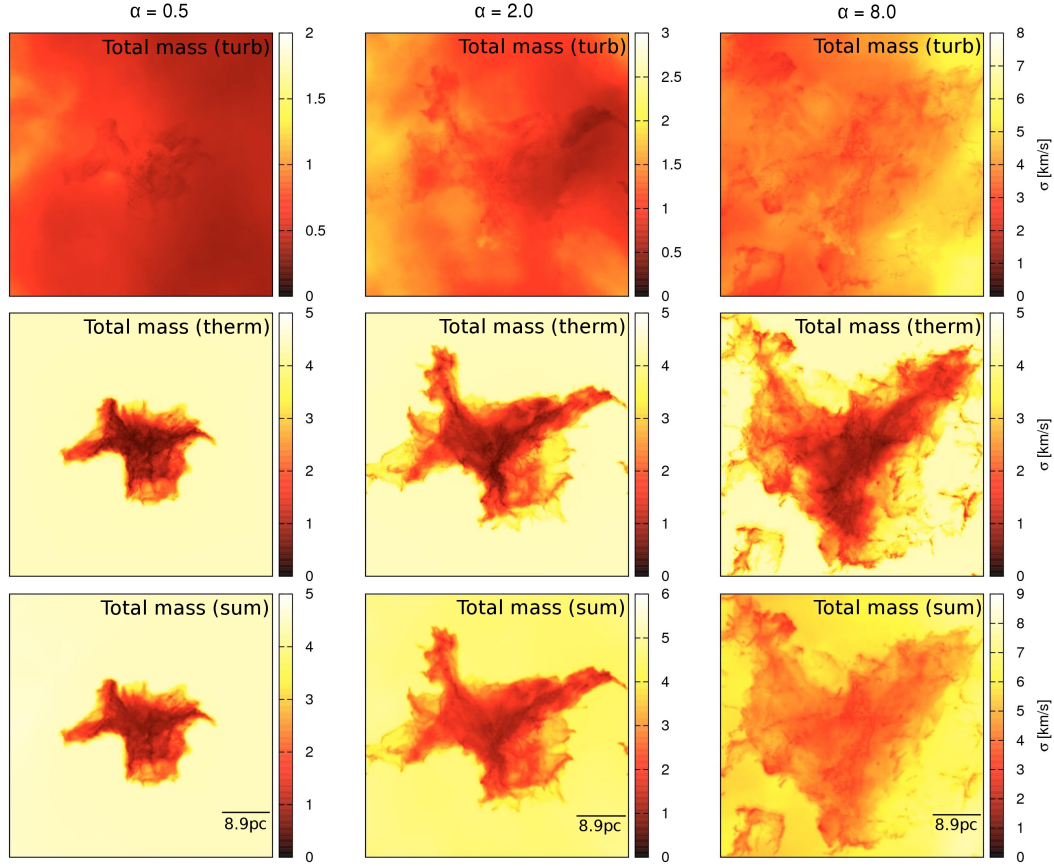


Figure 9.4:

Maps of 1D rms velocity dispersions σ for the total gas mass computed along the z -direction for the different virial parameters: $\alpha = 0.5$ (left column), 2.0 (middle column) and 8.0 (right column). In the first row, we show the velocity dispersions coming from the turbulent velocity field. In the second row, we show the velocity dispersions coming from the thermal contribution of the gas, computed via Eq. 9.3 with temperatures shown in Fig. 9.3. The third row shows the square root of the geometrical sum, $\sigma_{\text{tot}}^2 = \sigma_{\text{turb}}^2 + \sigma_{\text{therm}}^2$, of both turbulent and thermal contributions. Note the different scaling in the colorbars at the right hand side. Each box has a length of 44.5 pc. The initial cloud radius of 8.9 pc is indicated in the bottom panels.

by evaluating the second moment of the velocity distribution for each individual line-of-sight in the PPV cube:

$$\sigma_{\text{turb}}^2 = \frac{\int M(v - \bar{v})^2 dv}{\int M dv}. \quad (9.1)$$

In this equation, σ_{turb} is the 1D rms value, v is the velocity along the LoS, M the total mass at the given velocity v and \bar{v} the centroid velocity along each LoS, defined as

$$\bar{v} = \frac{\int M \cdot v dv}{\int M dv}. \quad (9.2)$$

Furthermore, we estimate the thermal contribution to the velocity dispersions by evaluating

$$\sigma_{\text{therm}}^2 = \frac{kT}{3m}, \quad (9.3)$$

where we have converted 3D into 1D rms dispersion measures. For the temperatures T , we adopt density-weighted mean temperatures, which are computed for each LoS via

$$\langle T \rangle = \frac{\int \rho T dz}{\int \rho dz}, \quad (9.4)$$

with the total mass density ρ .

In Fig. 9.3, we present logarithmic maps of density-weighted mean temperatures along the LoS in the z -direction for our different virial parameter models. We find a large range of gas temperatures. In the interior and dense parts of the clouds, we measure the coldest gas temperatures of 50 – 100 K. These are the regions where the gas is best able to self-shield from the strong external radiation field. In the outer regions of the clouds, the gas temperatures strongly increase to values of $\sim 300 - 3.000$ K, while the hot and diffuse regions around each cloud have high temperatures of ~ 10.000 K. Temperature PDFs for all models can be found in Paper I.

In Fig. 9.4, we show maps of 1D rms velocity dispersions of the total gas computed along the z -direction for our different virial parameter models. In the first row, we show the velocity dispersions σ_{turb} coming from the turbulent velocity field (Eq. 9.1). In the second row, we show the velocity dispersions σ_{therm} coming from the thermal contribution of the gas (Eq. 9.3). The third row shows the geometrical sum σ_{tot} of both contributions, i.e.

$$\sigma_{\text{tot}}^2 = \sigma_{\text{turb}}^2 + \sigma_{\text{therm}}^2. \quad (9.5)$$

In Tab. 9.3 we list the mean values for the corresponding velocity components shown in Fig. 9.4. Depending on the virial state of the cloud, we find different

Model	$\langle\sigma_{\text{turb}}\rangle$ [km s ⁻¹]	$\langle\sigma_{\text{therm}}\rangle$ [km s ⁻¹]	$\langle\sigma_{\text{tot}}\rangle$ [km s ⁻¹]
GC-0.5-1000	0.56	1.54	1.65
GC-2.0-1000	1.18	1.79	2.30
GC-8.0-1000	3.95	1.95	4.23

Table 9.3:

Mean values of the different components of the velocity dispersions shown in Fig. 9.4. The mean of σ_{turb} is computed by averaging over all pixels in the maps, while the mean of σ_{therm} and σ_{tot} only includes those pixels where the internal cloud velocities can be clearly separated from the velocities of the hot and diffuse gas around each cloud.

results for the individual contributions. If the cloud is virialized ($\alpha = 0.5$), we see that the mean velocity dispersion from the thermal contribution is significantly larger than the mean velocity dispersion from the turbulence. Thus, in this bound cloud, we expect the total velocity dispersion to be dominated primarily by the high temperatures of the gas. In the other extreme case, if the cloud is highly unbound ($\alpha = 8.0$), we now see that the turbulent kinetic energy dominates the thermal energy and hence we expect that the total velocity dispersion is mainly dominated by turbulent motions. Our model with $\alpha = 2.0$ is a transient case in which the thermal contribution to the total velocity dispersion is still slightly larger than the turbulent one, but where both $\langle\sigma_{\text{turb}}\rangle$ and $\langle\sigma_{\text{therm}}\rangle$ slowly approach a similar value as we go to even higher values of the virial parameter. In all α models, the mean value of σ_{therm} only changes slightly because the mean temperatures in those runs all have a similar value.

This is also illustrated in Fig. 9.5, which shows the evolution of both kinetic and thermal energy in the total box. We see that in the virialized $\alpha = 0.5$ model, the thermal energy always dominates the kinetic energy by a factor of ~ 3 . Conversely, in the extreme $\alpha = 8.0$ model, we find that the kinetic energy is always at least a factor of ~ 2 larger than the thermal energy. In the $\alpha = 2.0$ model, we find that the thermal energy is slightly larger than kinetic energy at the end after one free-fall time. Moreover, we see that the kinetic energy continuously decreases with time in the $\alpha = 2.0$ and $\alpha = 8.0$ run, which is because we are using decaying turbulence. The same effect can be seen at the beginning of the $\alpha = 0.5$ model, but after ~ 0.7 Myr the kinetic energy increases again, owing to the gravitational infall of the gas. Furthermore, we see that the thermal energy in all α models is similar.

This has important consequences for measurements of the line width in clouds in the CMZ. It means that it is likely for observations of such clouds with $\alpha \lesssim 2$ to pick out only the thermal contribution, owing to the effect that the thermal energy might dominate the turbulent kinetic energy of the gas. Only in those clouds in which the virial parameter is sufficiently large, spectral observations of the line width are likely to reproduce the turbulent contribution of the underlying velocity field much better than spectral observations of clouds with low values of α .

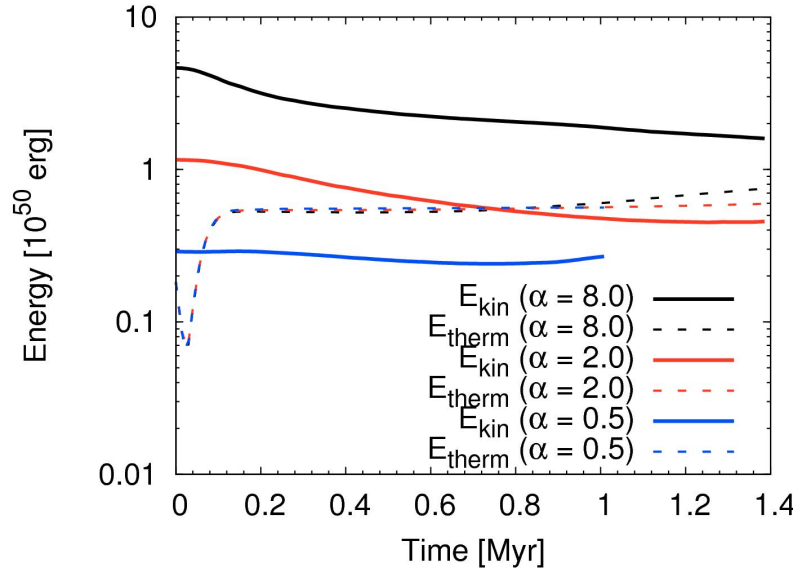


Figure 9.5:

Temporal evolution of both kinetic and thermal energy for our three models with $\alpha = 0.5, 2.0$ and 8.0 in our simulations. The energy scale is normalized to a constant value of 10^{50} erg.

9.3.3 Estimating the velocity dispersions of the different tracers

Observational measurements usually rely on spectral information of different tracers. In the following, we want to estimate how well or not different atomic and molecular tracers reproduce the internal velocity dispersion of the total cloud mass studied in the previous section. Therefore, we again compute maps of velocity dispersions for each individual LoS along the z -direction using Eq. 9.1 for the various α models and tracers listed in Tab. 9.1. However, this time we weight the velocities with the brightness temperatures T_B given in the PPV cubes after the radiative transfer post-processing. The maps are shown in Fig. 9.6. The gray background in the ^{12}CO and ^{13}CO maps denotes regions where the abundances of CO are zero. Hence, it is impossible to compute a value for the velocity dispersions there. Furthermore, we again compute mean values of the 1D rms velocity dispersions for all components shown in Fig. 9.6 and list them in Tab. 9.4. We do this by adopting the same threshold values for the velocity-integrated intensity maps presented in Paper I. The values in Tab. 9.4 are then computed by evaluating the mean of σ for all LoS for which the corresponding velocity-integrated intensity is smaller than the threshold values given in Tab. 3 in Paper I. We also list the corresponding values for the total mass in Tab. 9.4, where we chose the mean number of σ_{tot} from Tab. 9.3.

In general, we find different mean velocity dispersions for our various tracers. In case of the ^{12}CO and ^{13}CO tracers, we find that they significantly underestimate the

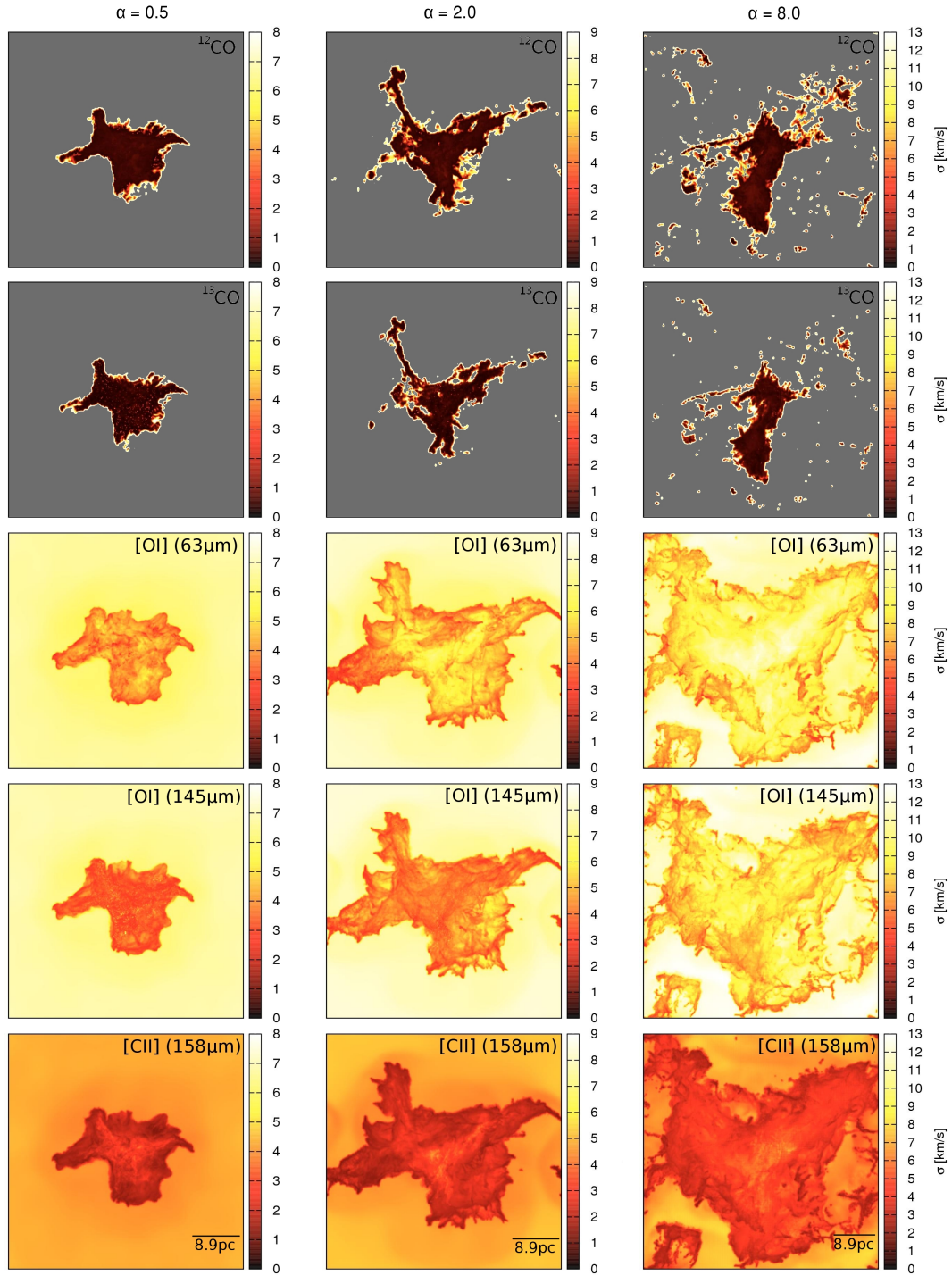


Figure 9.6:

Maps of velocity dispersions σ computed along the z -direction via Eq. 9.1 for different virial parameters: $\alpha = 0.5$ (left column), 2.0 (middle column) and 8.0 (right column). From top to bottom: velocity dispersions for models of ^{12}CO ($J = 1 \rightarrow 0$), ^{13}CO ($J = 1 \rightarrow 0$), $[\text{OI}]$ (63 μm), $[\text{OI}]$ (145 μm) and $[\text{CII}]$ (158 μm). Note the different scaling in the colorbars at the right hand side. Each side has a length of 44.5 pc. The initial cloud radius of 8.9 pc is indicated in the bottom panels. The gray background in the ^{12}CO and ^{13}CO maps denotes regions where the abundances of CO are zero. Hence, it is impossible to compute a value for the velocity dispersions there.

Model	total mass – [pc]	[CII] (158 μm) [pc]	[OI] (145 μm) [pc]	[OI] (63 μm) [pc]	^{12}CO (2600 μm) [pc]	^{13}CO (2720 μm) [pc]
0.5	1.65	1.94	3.23	3.96	0.47	0.40
2.0	2.30	2.40	4.29	4.77	0.52	0.52
8.0	4.23	4.23	8.17	7.91	0.71	0.78

Table 9.4:

Mean values of the 1D rms velocity dispersions shown in Fig. 9.6 for our various tracers and virial parameters. We compute the velocity dispersions by adopting the threshold values for the velocity-integrated intensity maps presented in Paper I. The values above are then computed by evaluating the mean of all sight lines for which the corresponding integrated intensity is smaller than the threshold values given in Tab. 3 in Paper I. The values for the total mass are taken from Tab. 9.3.

Model	total mass – [km s $^{-1}$]	[CII] (158 μm) [km s $^{-1}$]	[OI] (145 μm) [km s $^{-1}$]	[OI] (63 μm) [km s $^{-1}$]	^{12}CO (2600 μm) [km s $^{-1}$]	^{13}CO (2720 μm) [km s $^{-1}$]
0.5	1.65	1.90	0.88	2.35	1.38	0.66
2.0	2.30	2.12	1.12	2.47	1.41	0.87
8.0	4.23	3.90	3.00	4.58	2.45	2.17

Table 9.5:

Same as Table 9.4, but with values of the full width at half maximum (FWHM).

mean velocity dispersions of the total mass by a factor of $\sim 3-6$. This is because CO only traces the very dense parts of each cloud and is photo-dissociated in the outer cloud regions. However, both CO tracers yield similar values for the internal velocity dispersions. Furthermore, we find the remarkable result that the [CII] (158 μm) line yields the best estimate for σ_{tot} of the total gas with an accuracy better than $\sim 20\%$. The estimates of the oxygen lines, [OI] (145 μm) and [OI] (63 μm), are worse than the [CII] (158 μm) line and tend to overestimate the value of σ_{tot} by a factor of ~ 2 . However, they still give better estimates than the different CO tracers. Thus, we conclude that the atomic tracers, most notably [CII] (158 μm), yield robust estimates of the internal velocity dispersions of the total gas mass.

9.3.4 Computing spectra and the FWHM of the different tracers

In practice, a common approach is to adopt the spectral information and take the full width at half maximum (FWHM) as a measure for the internal velocities in a cloud. To do this, we compute spectra for each individual tracer and α models. They are presented in Fig. 9.7 and show 1D rms velocities. We plot the mean brightness temperatures as well as the mean brightness temperatures normalized by

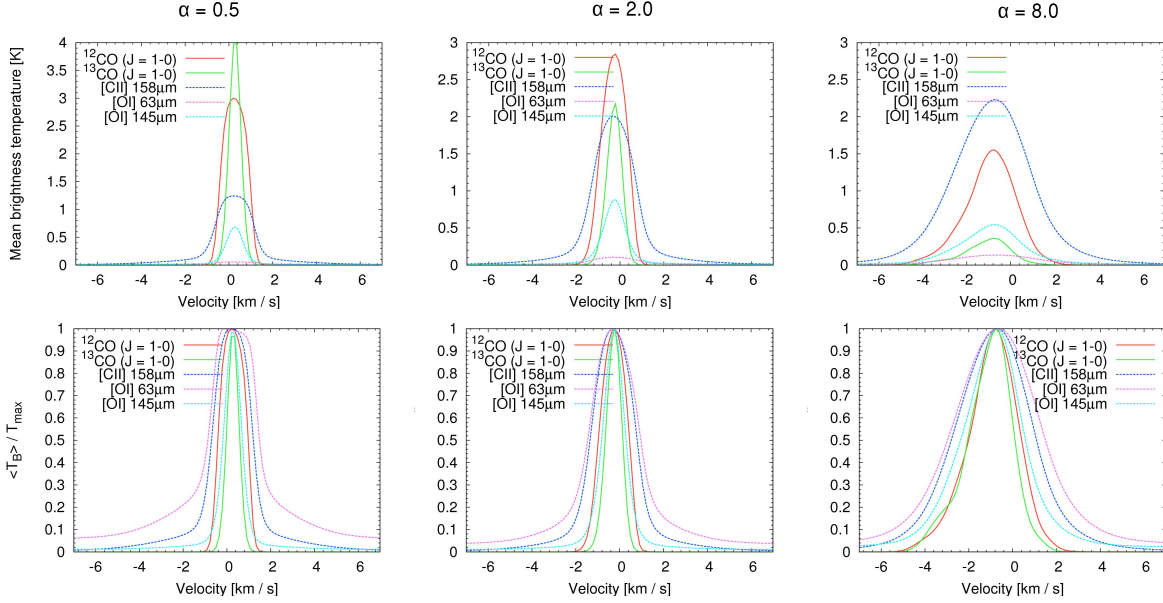


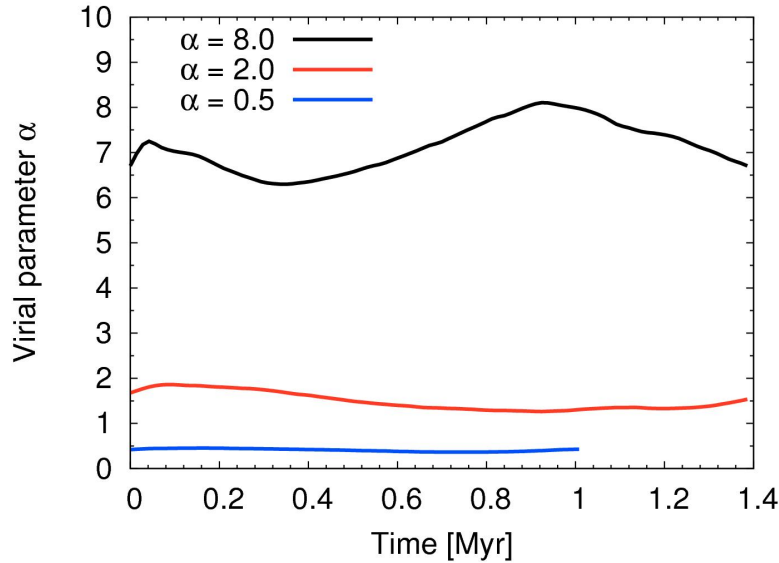
Figure 9.7:

Mean brightness temperatures (first row) as well as mean brightness temperatures normalized by the maximum value (second row) against the internal cloud velocity for our various tracers given in Table 9.1 for different virial parameters $\alpha = 0.5$ (left column), 2.0 (middle column) and 8.0 (right column). The spectra are computed by using Eq. 9.1, but this time we take the mean value of all brightness temperatures at a given velocity.

the maximum value against the internal cloud velocity. The spectra are computed by using Eq. 9.1, but this time we take the mean value of all brightness temperatures at a given velocity. The values of the FWHM are listed in Tab. 9.5.

In general, we find that all lines with larger α values are significantly broader than lines with lower values of α . This is unsurprising, since the internal velocity dispersions in clouds with greater α values are larger and thus lead to larger line widths. Furthermore, we see that the [OI] (63 μm) line is very faint in all models (see also the corresponding emission maps in Paper I). The mean brightness temperature of this line is always below $\sim 0.2\text{K}$. Moreover, we observe that both ^{12}CO and ^{13}CO lines attenuate with increasing α . This is due to the high external radiation field, which can penetrate deeper into the interior of the cloud and photodissociate a large fraction of the CO gas. Conversely, the atomic lines are getting brighter with increasing α , which is because they can now be excited more easily by the external radiation within the cloud. Furthermore, we see that the lines of ^{12}CO and ^{13}CO are significantly narrower than the lines of all other atomic tracers.

The values in Tab. 9.5 show a similar trend, although they slightly differ from those presented in Tab. 9.4. Most notably, we find that the values for the atomic tracers given in Table 9.4 are significantly smaller than the values of the FWHM for the same tracers in Table 9.5. This is because there is a significant mass fraction primarily at high velocities (see the normalized spectra in the second row of Fig.

**Figure 9.8:**

Temporal evolution of the virial α parameter for our three models with $\alpha = 0.5, 2.0$ and 8.0 in our simulations.

9.7). If we compute the 1D rms values given in Tab. 9.4, the high velocity regions in the cloud significantly contribute to the velocity dispersions, resulting in slightly larger values compared to the FWHM.

Furthermore, we again find that both ^{12}CO and ^{13}CO significantly underestimate the value of σ_{tot} for the total gas, but this time only by a factor of $\sim 2-3$, depending on the virial state of the cloud. Moreover, the $[\text{CII}]$ ($158\ \mu\text{m}$) line yields the best estimate for σ_{tot} of the total gas, again with an accuracy better than $\sim 10-20\%$. Furthermore, the estimate of the $[\text{OI}]$ ($145\ \mu\text{m}$) line is worse than the one of the $[\text{CII}]$ ($158\ \mu\text{m}$) line, but now tend to underestimate the value of σ_{tot} by a factor of up to ~ 2 . However, the $[\text{OI}]$ ($63\ \mu\text{m}$) line also gives fairly robust estimates of the total velocity dispersions.

9.3.5 Evolution of the virial parameter in the simulations

In the following, we examine the evolution of the virial α parameter in our simulations. Therefore, we estimate both kinetic and potential energy of the cloud and evaluate the ratio $\alpha = E_{\text{kin}}/|E_{\text{pot}}|$ for each time snapshot. Since the cloud radius changes significantly during the simulations, we have to find a way to estimate the effective radius R_{eff} as a function of time. Therefore, we define the effective radius as the radius of a sphere in the box which incorporates $\sim 80\%$ of the total gas mass. For the velocity dispersion σ , we adopt the 3D rms value of the total gas in the box, which is a reasonable approach as seen in Fig. 9.4. We then estimate the potential energy via $E_{\text{pot}} \approx -GM_{R_{\text{eff}}}^2/R_{\text{eff}}$. Accordingly, the kinetic energy is given by $E_{\text{kin}} \approx 1/2M_{R_{\text{eff}}}\sigma^2$. In Fig. 9.8, we show the evolution of α as a function of the

Model	total mass – [pc]	[CII] (158 μm) [pc]	[OI] (145 μm) [pc]	[OI] (63 μm) [pc]	^{12}CO (2600 μm) [pc]	^{13}CO (2720 μm) [pc]
GC-0.5-1000	11.0	9.0	8.7	8.1	6.6	6.2
GC-2.0-1000	13.1	13.8	13.0	12.2	7.6	6.8
GC-8.0-1000	17.5	20.1	19.9	19.7	8.4	6.9

Table 9.6:

Effective radii of the clouds, based on the threshold intensities given in Table 3 in Paper I. For comparison, we also give the effective radii of the clouds that incorporate $\sim 80\%$ of the total gas mass in the second column.

simulation time.

Although we find variations of the order of $\sim 10 - 20\%$ for the individual values of α , the virial parameter does not change strongly during the first free-fall time in our runs. At the time when we stop our simulations, we measure values of $\alpha \sim 0.4$, 1.5 and 6.7 for our three numerical models, which are slightly smaller than the initial setup values of $\alpha = 0.5$, 2.0 and 8.0. However, we also note that the value of α shown in Fig. 9.8 only gives a first estimate of the virial parameter. This is primarily because we have to define an approximation for both kinetic and potential energy in the simulation domain, which are not computed simultaneously during our runs.

9.3.6 Estimating the virial state of the cloud

In this section, we want to estimate the virial α parameter as it could be inferred from observational measurements. Therefore, we first compute the virial cloud mass, which is defined as

$$M_{\text{virial}} \approx \frac{R_{\text{eff}}\sigma^2}{G}, \quad (9.6)$$

where R_{eff} is the effective cloud radius, G the gravitational constant and σ the 3D rms velocity dispersion. The 1D rms velocity dispersions are given in Table 9.4 and 9.5, which we translate into 3D rms values by using the relation $\sigma_{3\text{D},\text{rms}} = \sigma_{1\text{D},\text{rms}}\sqrt{3}$. The effective cloud radii R_{eff} for the synthetic clouds are listed in Table 9.6 and adopted from Paper I. The virial parameter can now be computed via

$$\alpha \approx \frac{M_{\text{virial}}}{M_{\text{tot}}}. \quad (9.7)$$

In this equation, M_{tot} is the cloud mass within the effective cloud radius R_{eff} .

In Table 9.7, we present the virial α parameters for all cloud models and tracers as they can be inferred from observational measurements. To compute the α values, we first use the internal velocity dispersions given in Table 9.4. We find that no tracer really yields a perfect estimate of the underlying kinematics for all models.

Initial α	Final α	[CII] (158 μm)	[OI] (145 μm)	[OI] (63 μm)	^{12}CO (2600 μm)	^{13}CO (2720 μm)
0.5	0.4	0.3	0.7	1.0	0.01	0.01
2.0	1.5	0.6	1.9	2.2	0.02	0.02
8.0	6.7	2.9	10.5	9.8	0.03	0.03

Table 9.7:

Virial parameters for all cloud models and tracers. Given are the initial and final α parameter measured for the total gas (see Sec. 9.3.5) as well as estimates for the different tracers computed via Eq. 9.7 using the velocity dispersions from Table 9.4. We note that the values might differ by $\sim 10 - 20\%$ due to the uncertainties in the estimate of the effective cloud radius.

Initial α	Final α	[CII] (158 μm)	[OI] (145 μm)	[OI] (63 μm)	^{12}CO (2600 μm)	^{13}CO (2720 μm)
0.5	0.4	0.3	0.05	0.4	0.1	0.02
2.0	1.5	0.5	0.13	0.6	0.2	0.04
8.0	6.7	2.4	1.42	3.3	0.4	0.26

Table 9.8: Same as Table 9.7, but using the velocity dispersions given in Table 9.5.

While the [CII] (158 μm) line gives a good estimate for the $\alpha = 0.5$ model, both [OI] (145 μm) and [OI] (63 μm) lines better reproduce the kinematics of the unbound clouds with $\alpha = 2.0$ and 8.0. The accuracy of these atomic tracers lies within a range of $\sim 20 - 30\%$, depending on the individual model. Furthermore, we find that the CO tracers underestimate the value of α by a large factor of $\sim 10 - 100$. Thus, a molecular tracer like carbon monoxide is certainly not an appropriate tracer for the kinematics of clouds in such an extreme environment. However, we also note that the virial parameters might differ by $\sim 10 - 20\%$ due to the uncertainties in the estimates of the effective cloud radii and the velocity dispersions.

In analogy, Table 9.8 shows the virial parameters computed with the internal velocity dispersions from Table 9.5. In this case, we find that all tracers significantly underestimate the value of α . This is primarily because the values of the FWHM in Tab. 9.5 are much smaller than the values from Tab. 9.4 for the various tracers (see also the discussion in Sec. 9.3.4). Furthermore, the α values of the CO tracers are again much smaller than the values of the atomic components.

However, what can we learn about the virial state of a cloud with spectral observations of different fine structure lines? In general, we find that the values of the atomic tracers listed in Tab. 9.7 give a reasonable estimate of the dynamical state of each cloud. Although none of the atomic tracers give an exact estimate of the α parameter of the total gas, the trends reproduced by the individual atomic components correctly reflect the virial state of the clouds and whether they are bound or unbound. Furthermore, we also see that we can obtain a good estimate for the number of α if we compute the mean value of all atomic tracers. These are 0.7 ± 0.4 ,

1.6 ± 0.8 and 7.7 ± 4.2 , in good agreement with the values 0.4, 1.5 and 6.7 measured at the end of the simulations. Thus, we conclude that measurements of the different atomic tracers can be used to estimate the virial parameter of clouds in a CMZ-like environment.

9.4 Summary and Conclusions

In this paper we have analyzed synthetic images of MCs using environmental properties comparable to those experienced by typical CMZ-like clouds. We have performed numerical simulations of MCs with the moving mesh code AREPO (Springel, 2010). For this purpose, we adopted values for the interstellar radiation field (ISRF) and the cosmic-ray flux (CRF) that are a factor of ~ 1000 larger than the canonical values measured in the solar neighbourhood (Clark et al., 2013; Indriolo et al., 2015; Ginsburg et al., 2015). Our clouds all have an initial number density of $n_0 = 10^3 \text{ cm}^{-3}$ and a total mass of $M_{\text{tot}} = 1.3 \times 10^5 M_{\odot}$. Furthermore, we studied the impact of different virial α parameters on the physical properties. In particular, we use $\alpha = 0.5, 2.0$ and 8.0 in order to span a large range in the virial parameter space. Our simulations include a simplified treatment of time-dependent chemistry and account for the highly non-isothermal nature of the gas and the dust. We used the radiative transfer code RADMC-3D (Dullemond, 2012) to compute synthetic maps of our clouds in important diagnostic lines. In particular, we model the emission of the clouds in [CII] ($158 \mu\text{m}$), [OI] ($145 \mu\text{m}$), [OI] ($63 \mu\text{m}$), ^{12}CO ($2600 \mu\text{m}$) and ^{13}CO ($2720 \mu\text{m}$). We find the following:

- We first estimate the internal velocity dispersion of the total cloud mass. We find that the thermal energy significantly dominates the kinetic energy in the $\alpha = 0.5$ and $\alpha = 2.0$ models. Thus, it is likely that spectral observations primarily reproduce the signatures of thermal motions. Conversely, in the $\alpha = 8.0$ model, the kinetic energy dominates the thermal energy in the cloud and hence it is likely for this case that spectral measurements mainly trace the turbulent velocity field (see Section 9.3.2).
- In a next step, we ask how well the different atomic and molecular components trace the internal velocity dispersions of the total mass within our clouds. Therefore, we estimate the internal velocity dispersions of our model clouds by computing both the intensity-weighted 1D rms velocities as well as the full width at half maximum (FWHM) of the individual line spectra. In both cases, we find that the atomic tracers yield a much better estimate of the mean internal velocity dispersion of the cloud than the molecular tracers, although the velocities derived with the FWHM significantly underestimate the total cloud velocities (see Section 9.3.3 and 9.3.4).
- We compute the virial α parameter of the total gas as a function of time and show that it does not vary strongly within the first free-fall time in our runs (see Section 9.3.5).

- We then estimate the virial α parameter as it can be inferred from observational measurements. We find different results depending on how we derive the velocity dispersions.
- If we compute α by using the FWHM, we find that all tracers significantly underestimate the value of the virial parameter, owing to the small values of the FWHM (see Section 9.3.6).
- If we compute α by using the intensity-weighted 1D rms velocities, we find a much better agreement of the real and the estimated virial parameter. However, this depends again on the individual model. While the [CII] ($158\ \mu\text{m}$) line gives a good estimate for the $\alpha = 0.5$ model, both [OI] ($145\ \mu\text{m}$) and [OI] ($63\ \mu\text{m}$) lines better reproduce the kinematics of the unbound clouds with $\alpha = 2.0$ and 8.0 . The accuracy of these atomic tracers lies within a range of $\sim 20 - 30\%$, depending on the individual model. Furthermore, we find that the CO tracers underestimate the value of α by a large factor of $\sim 10 - 100$. Thus, a molecular tracer like carbon monoxide is certainly not an appropriate tracer for the kinematics of clouds in such an extreme environment, because it is photodissociated by the strong external radiation field (see Section 9.3.6).
- Finally, we conclude that the atomic tracers give a reliable idea of the dynamical state of the cloud. Furthermore, they can be used to accurately estimate the virial parameter of the system.

Discussion and outlook

10.1 Summary of this thesis

In this thesis, we investigated the role of turbulence in molecular clouds (MCs) and analyzed its effect on the star formation process. We considered typical MCs in a) the Milky Way disk as well as b) clouds located in a more extreme environment in the Central Molecular Zone (CMZ) near the Galactic Center (GC). We showed that supersonic turbulent motions are a key ingredient to regulate star formation and that they affect important observables, e.g. the star formation rate as well as the turbulence statistics. Our approach was primarily numerical. We modelled a number of different MCs and analyzed the turbulent gas dynamics. All our simulations accounted for a simplified treatment of time-dependent chemistry and the non-isothermal nature of the gas and dust. Furthermore, we performed radiative transfer post-processing for several fine structure lines, such as ^{12}CO ($J = 1 - 0$) or ^{13}CO ($J = 1 - 0$), and compared our numerical results to observations. The main results of our studies are summarized below.

a) Molecular clouds in the Milky Way disk (see chapters 5 and 6):

- *Optical depth effects can significantly influence the statistical analysis.* For example, in case of the CVISF analysis, we find different behavior of the CVISF slopes for ^{12}CO and ^{13}CO in varying density environments. We obtain the same results in case of the Fourier spectra and the Δ -variance. In these cases, the CO tracers exhibit a very different spatial scaling behavior compared to the total and the H_2 density models.
- *The slopes for the total and H_2 density models are generally steeper than the slopes of ^{12}CO and ^{13}CO .* For the CVISF and the Δ -variance, we find the slopes for the total density and H_2 density to be steeper by a factor of up to

$\sim 1.5 - 3$ than the slopes of the different CO tracers. We argue that this is due to the higher space-filling factor (the fractal co-dimension) for the H₂ gas than for the CO tracers. That means that H₂ is more extended than CO as it is better able to self-shield in diffuse regions, while CO is a good tracer of H₂ only in compact regions. This behavior gives a clear imprint into the statistics of turbulence.

- *Carbon monoxide traces the total cloud structure well only if the average cloud number density is $n > 100 \text{ cm}^{-3}$.* Around this threshold the spectral slopes α of the CO tracers switch sign for the Δ -variance of integrated intensity and column density maps. If the mean density in the cloud is significantly smaller than this limit, the observable CO gas does not accurately trace the statistical properties of the H₂ gas in the cloud. Thus, we would expect that CO is not a good tracer of the molecular hydrogen content in low-density MCs.
- *The Δ -variance provides a powerful measure to infer important information about the distribution of gas within a cloud.* We argue that peaks in the Δ -variance spectra correspond to characteristic scales of the morphological structure of the system.
- *Our findings are consistent with previous studies using CO line observations or measurements of the continuum.* However, we remind that our models are subject to various physical simplifications. For example, we do not account for self-gravity and thus also do not model star formation or stellar feedback in these models. More specifically we also do not account for stellar radiation, SN feedback and other physical processes.

b) Molecular clouds in the CMZ (see chapters 7, 8 and 9):

- *We find active star formation with efficiencies $\epsilon_{\text{ff}} \gtrsim 1\%$ in all models.* This is regardless of the choice of the initial number density and the amount of turbulent kinetic energy. Thus, our values are more comparable to Galaxy-wide SFEs than to the inferred SFE in the GC, which observations suggest is a factor $\gtrsim 10$ smaller.
- *Star formation is more efficient at lower virial parameters.* This is the case when the velocity dispersion in the cloud is small. We demonstrate that the SFE decreases by a factor of $\sim 4 - 10$ as we increase the virial parameter from $\alpha = 0.5$ to $\alpha = 8.0$.
- *For clouds with low virial α , a by a factor of ~ 1000 enhanced IRSF and CRF has only little effect on the SFE.* This can decrease by around 20% compared to the value we obtain for a similar cloud in a solar neighbourhood environment. For highly unbound clouds, the stronger IRSF and higher CRF at the GC has

a much greater effect, decreasing the star formation efficiency by a factor of ~ 6 .

- *Even in our most extreme models with high α , we find SFEs per free-fall time that are close to 1%.* None of our models produce values that are consistent with the low SFE per free-fall time that is inferred for the GC region as a whole.
- *We conclude that high levels of turbulence together with the strong ISRF and high CRF cannot explain the low SFEs found in the GC.* Therefore, it is possible that including additional physical ingredients (such as magnetic fields, stellar feedback or realistic orbital parameters around the GC) could reduce the star formation efficiencies within individual dense clouds to levels that are consistent with the mean value inferred for the GC region as a whole.
- *Atomic carbon and oxygen is found in both cold and warm regions in the clouds, but CO only traces cold regions.* This is primarily because carbon monoxide is photodissociated in the outer cloud regions, while the atomic components can be excited and radiate by photo emission. We show that the atomic components trace the shape of the total cloud very well even in diffuse cloud regions.
- *We find that atomic carbon and oxygen are good tracers of various cloud properties, e.g. the cloud radius, the internal velocity dispersion and others.* The molecular gas (H_2 as well as CO) is photodissociated at the edges of the MC by the strong external ISRF. As a consequence, the photodissociation has a strong impact on measurements of the effective MC radius using a molecular tracer, which tend to significantly underestimate the radius of the total cloud in environments where the external radiation field and the turbulent kinetic energy is high. Conversely, the atomic components properly trace the shape of the total cloud and thus yield good estimates of the cloud radius. Furthermore, we find that all atomic components trace almost 100% of the H_2 and the total gas mass above a sensitivity threshold of $W_{\min} \approx 0.1 \text{ K km s}^{-1}$ for the velocity-integrated intensities.
- *We find a large dynamical range for the [OI] $145\mu\text{m}$ line in column density space.* This indicates that this particular fine structure line traces both the H_2 and the total gas up to the most dense cloud regions.
- *Our values of the CO-to- H_2 conversion factor $X_{CO} = N_{H_2}/W_{CO}$ agree with the canonical value.* We find values in the range $X_{CO} \approx 1-4 \times 10^{20} \text{ cm}^{-2} \text{ K}^{-1} \text{ km}^{-1} \text{ s}$, in good agreement to the canonical X_{CO} -factor values obtained in observations of MCs in the Milky Way.
- *The atomic tracers best reproduce the dynamics of the total cloud.* This can be characterized by means of the virial α parameter, defined as the ratio of

kinetic and potential energy of the system. We find that the atomic tracers give a reliable idea of the dynamical state of the cloud and that they can be used to accurately estimate the virial parameter of the system.

10.2 Idea for further investigations and some open questions

During the last years a lot of progress has been made in terms of both theoretical and observational studies. However, present numerical studies are mainly limited by the high computational costs, produced by expensive multiscale and multiphysical processes. In the following, we present some idea for further projects and how these are related to open questions on the field. We note that this list is far from complete and that the projects listed below are only related to the specific questions studied in this thesis. More open aspects and how to approach them can be found in the science literature.

1. **Modelling more realistic turbulent clouds in simulations**

Due to high computational costs, every model of turbulence is subject to a number of simplifications. In our case, feedback processes do not play any role in the numerics. These are e.g. stellar radiation, stellar winds or supernova feedback, which could be the most important driver of ISM turbulence. A set of simulations, which account at least for some of these individual processes, would be highly interesting and helpful to better understand the dynamics of the ISM.

2. **Increasing the accuracy of numerical simulations to better resolve the spatial scales**

Again, the high computational costs limit the numerical resolution at which we study the turbulent dynamics. Furthermore, the radiative transfer post-processing takes additional time to connect the numerical results to the observable world (Dullemond, 2012). It would be helpful to better resolve the different spatial scales and also to run larger scale simulations to investigate how turbulence on large scales affect the dynamics on smaller scales. Most of our homogeneous 3D data cubes use a resolution of 512^3 cells. Extending this to at least 1024^3 grid cells and more could help to better resolve very dense regions and to learn about the turbulence properties (Konstandin et al., 2015).

3. **Extending the chemical model and including more complex species**

At the moment, our chemical network tracks the abundances of 9 species and follows 30 chemical reactions (Nelson & Langer, 1999; Glover & Mac Low, 2007). Thus, it is only possible to model very basic chemical processes in the ISM. However, extending the chemical model requires again additional computational costs and so the question is whether it will be possible to include

more reactions in the network. The problem thereby is that the complexity of the network grows exponentially. Will it be possible to track a significantly larger number of species including more complex molecules (e.g. NH_3 , CS , CH_4 , HCN , and others) and PAHs (e.g. C_{10}H_8 , $\text{C}_{32}\text{H}_{14}$, etc.)?

4. **Modelling more realistic extreme CMZ-like clouds with higher number densities**

Right now, the cloud number densities that we use ($\sim 10^3 \text{ cm}^{-3}$) to model extreme CMZ-like clouds are still about one order of magnitude lower than typical volume densities found in the CMZ (Lis et al., 2001; Immer et al., 2012; Longmore et al., 2012; Kauffmann et al., 2013; Clark et al., 2013; Johnston et al., 2014). Further increasing the number density leads to a very heavy refinement of the cells in the simulation domain primarily in collapsing regions due to the adaptive code routine. Certainly, this is a challenging numerical task, which requires much more memory and computational power. Nevertheless, it is necessary to run simulations with such a high density to study the ISM physics in the CMZ.

5. **Embedding additional physical processes in the numerical codes**

Our simulations of CMZ-like clouds do not account for a number of important physical processes. For example, our runs do not account for the strong magnetic field, which was shown to be enhanced by a factor of ~ 1000 compared to the mean value measured in solar neighbourhood clouds (Pillai et al., 2015). Furthermore, a numerical problem with the fields is how they interact with the sink particles. What happens with the magnetic flux in the medium if the gas fulfills the conditions for sink particle formation? What about supernova and stellar feedback? Thus, additional code development is required to study even more realistic star formation in those extreme environments.

6. **Studying the impact of large-scale motions and structures on the star formation process**

In the studies presented in this thesis, we only analyze molecular clouds in isolation. Of course, this is a simple picture, but a first step towards better understanding multiscale processes. However, including those processes might give us an important insight into the process of star formation. Another project idea would be to study MCs on an orbit around the galactic center and analyze how large-scale motions and structures of the Galaxy including shear effects affect parameters like the star formation efficiencies, the gas properties, the turbulence and so on (Kruijssen et al., 2015). This requires multiscale runs, which are computationally expensive, if one wants to refine several orders of spatial scales.

7. **Analyzing the IMF in numerical simulations**

In this thesis, we have studied star formation efficiencies in clouds located

in an extreme environment. However, the sink particle masses are not accurate enough to properly resolve the initial mass function (IMF) in our runs (Greif et al., 2011). Nevertheless, it would be highly interesting to study the dependence of various environmental parameters, such as e.g. the interstellar radiation field, the magnetic field, the turbulent kinetic energy or the metallicity, on the mass distribution of stars. How do cosmic-rays, for example, affect the IMF (Papadopoulos et al., 2011; Papadopoulos & Thi, 2013)?

8. Studying the impact of purely solenoidal driven turbulence on the SFE

Another project would deal with the impact of purely solenoidal driven turbulence on the SFE. It is known that solenoidal velocity modes can strongly influence the SFEs and suppress the formation of stars (Federrath et al., 2010; Federrath, 2015b). However, it is not yet clear which effect such a velocity field has on the SFEs in such an extreme environment. How do the SFEs change in absence of compressive modes?

9. Could an interplay of various physical effects explain the low SFEs measured in the CMZ?

So far, we could show that high levels of turbulence together with a strong external radiation field cannot explain by themselves the low SFEs measured in the CMZ. However, the question is whether an interplay of various effects, such as e.g. the strong magnetic field, feedback of supernova and hot OB stars, shear as well as the high turbulence level and the strong external radiation field, could significantly reduce the SFEs (see, e.g. Federrath, 2015b). This is surely a challenging study, because a simulation has to account for multiple physical processes. However, it would help further our insights into the formation of stars in the central few hundred parsecs of our Galaxy.

10. The Millennium Prize Problem: Does a solution of the Navier-Stokes equation exist?

We have seen that the Navier-Stokes equation is all about turbulence: the non-linear term generates local anisotropies which lead to the whole complexity of turbulent motions. So far, there is no analytic solution which describes turbulence. Does such a solution exist at all? Although a few phenomenological models exist (see, e.g. those by Kolmogorov, 1941; Burgers, 1948; She & Leveque, 1994), our knowledge about the nature of turbulence is very limited. Under which conditions do solutions of the Navier-Stokes equation exist? This problem is also listed in the Millennium Prize Problems in mathematics and is clearly the most challenging problem in turbulence theory in those days. An analytic explanation would certainly support further studies about the dynamics in the ISM.

10.3 Closing remarks

During the last 10 – 15 years, the developments in theoretical astrophysics have dramatically increased due to the availability of new computational methods. In principle, we are able today to model a large number of different astrophysical phenomena, e.g. star, galaxy and planet formation, jets, black holes, star clusters, supernovae, neutron stars, brown and white dwarfs and even the evolution of the whole Universe. We can adopt different initial conditions to see how each of them influence the physics. We can track the evolution of gas and matter on many scales and see how they interact with magnetic fields, radiation and so on. Doubtless, these theoretical possibilities have strongly increased our knowledge about the Universe. However, there is still a lot of work left and perhaps we can say that mankind is soon entering a new epoch of astrophysical research. This can be seen by considering the two following aspects:

1. New options for theoretical astrophysics

The greatest challenge in computational astrophysics for the next years will be to embed various physical processes in existing codes (e.g. AREPO, GADGET, FLASH, ZEUS-MP, ENZO, etc.) *altogether* (Springel, 2005; Norman, 2000; Fryxell et al., 2000; O’Shea et al., 2004; Springel, 2010). This is important because astrophysics always relies on multiphysical and multiscale processes. These processes complicate any proper numerical treatment, since a code has to account for non-linear physics that affect each other on various spatial scales. This calls for new computational techniques as well as for advanced super-computer systems, which would be able to run this advanced software. At the moment, we usually separate different phenomena: We analyze the dynamics of the ISM *or* study the evolution of a galaxy, each one without really connecting them to the other. Of course, this is because it provides a simple situation. Moreover, we are also somehow limited in computational power and memory. However, at some point, we have to go deeper into the individual processes. That immediately leads to the question: Will it be possible to model the entire evolution of the Universe with all ingredients in *one* single simulation? The trend has started to go into this direction, if we consider the Illustris simulation, for example (Vogelsberger et al., 2014). However, what we really need is to run simulations using physics beyond the usual hydrodynamics and self-gravity models and to combine galactic scale with small scale codes.

2. Development of advanced observational techniques

Theoretical models are useless unless we are able to connect our predictions to the real world. In accordance with the development of theoretical models, observational measurements need to be improved as well. Fortunately, the international community has realized that astrophysical research strictly depends on the development of new observational techniques and new telescopes.



Figure 10.1:

Two of the most promising telescopes for upcoming astronomical research: the Atacama Large Millimeter/submillimeter Array (ALMA, left) and the Global Astrometric Interferometer for Astrophysics (GAIA, right).

In this context, we are also entering a new era of observing our Universe. For example, with ALMA we will be able to gain important information about the formation of stars and planets, with a quality never achieved by any telescope before. With JWST we will be able to look for the first stars in our Universe as well as to study the structure and evolution of distant galaxies. GAIA will be able to measure positions, distances and motions of stars and even exoplanets with high accuracy. Hopefully, LISA will be launched to detect gravitational waves, founding a completely new science of gravitational wave astronomy, which will provide us fascinating insights into the physics shortly after the Big Bang. These are some of the major milestones in the field of astronomy for the next decades. In Fig. 10.1, we show two images of the promising ALMA and the GAIA telescope¹². And finally, big surveys of GMCs in the Milky Way taken with different tracers are needed to obtain deeper insights into the processes of star and galaxy formation.

However, we will only be successful if both theoretical and practical scientists work together and stimulate their discussions. Then, we will enter a golden age for astronomical research and hopefully lift the last mysteries of our fascinating Universe.

¹Image credit (ALMA, 07/12/2015): <https://de.wikipedia.org/wiki/ALMA>

²Image credit (GAIA, 07/12/2015): <http://blogs.esa.int>

Appendix

Centroid Velocity Statistics of Molecular Clouds

A.1 Resolution study

To study the influence of resolution on the CVISF slopes and the Fourier spectra, we have performed runs of 512^3 and 256^3 grid cells and evaluated the CVISF and Fourier slopes for all available chemical components and initial number densities. As an example, Figure A.1 shows slopes of the CVISF for an initial number density of $n_0 = 100 \text{ cm}^{-3}$ for both a resolution of 512^3 and 256^3 grid cells. Table A.1 gives the corresponding slope values and errors for both resolution models for $p = 6$, since we would expect variations of the CVISF slopes due to intermittency particularly at higher orders. For the total density and the H_2 density, we measure similar slopes within the errors, while the slopes of the different CO tracers differ by $1-2\sigma$. This sensitivity to numerical resolution is a consequence of the high degree of chemical inhomogeneity in the numerical simulations. As shown in Bertram et al. (2014), CO is mainly located in dense gas regions which can be resolved more accurate in the 512^3 than in the 256^3 runs. It is thus rather complicated to compare non-converged

Res	Total density	H_2 density	^{12}CO density	^{12}CO intensity	^{13}CO intensity
512^3	1.66 ± 0.13	1.45 ± 0.15	0.83 ± 0.10	0.84 ± 0.13	0.88 ± 0.05
256^3	1.68 ± 0.10	1.45 ± 0.08	0.72 ± 0.06	0.75 ± 0.09	0.74 ± 0.07

Table A.1:

Slopes of the CVISF for our highest order $p = 6$ for the different chemical components and for different runs with 512^3 and 256^3 grid cells. As an example, we show values for a fixed initial number density of $n_0 = 100 \text{ cm}^{-3}$. The slopes of the total density and H_2 density cases are similar within their errors, while the slope values of the different CO tracers significantly deviate with resolution.

CVISF slopes with observational measurements. Nevertheless, we find that although the individual slope values might be different for the distinct resolutions, the relative scaling behaviour of ζ_p is conserved throughout the different resolution runs and hence our fundamental physical conclusions derived in this paper should be unaffected. The same arguments hold for the Fourier spectra given in Figure A.2. Although the slope values of the individual chemical components are significantly different between the two resolution models, the relative scaling behaviour of the energy spectra is conserved.

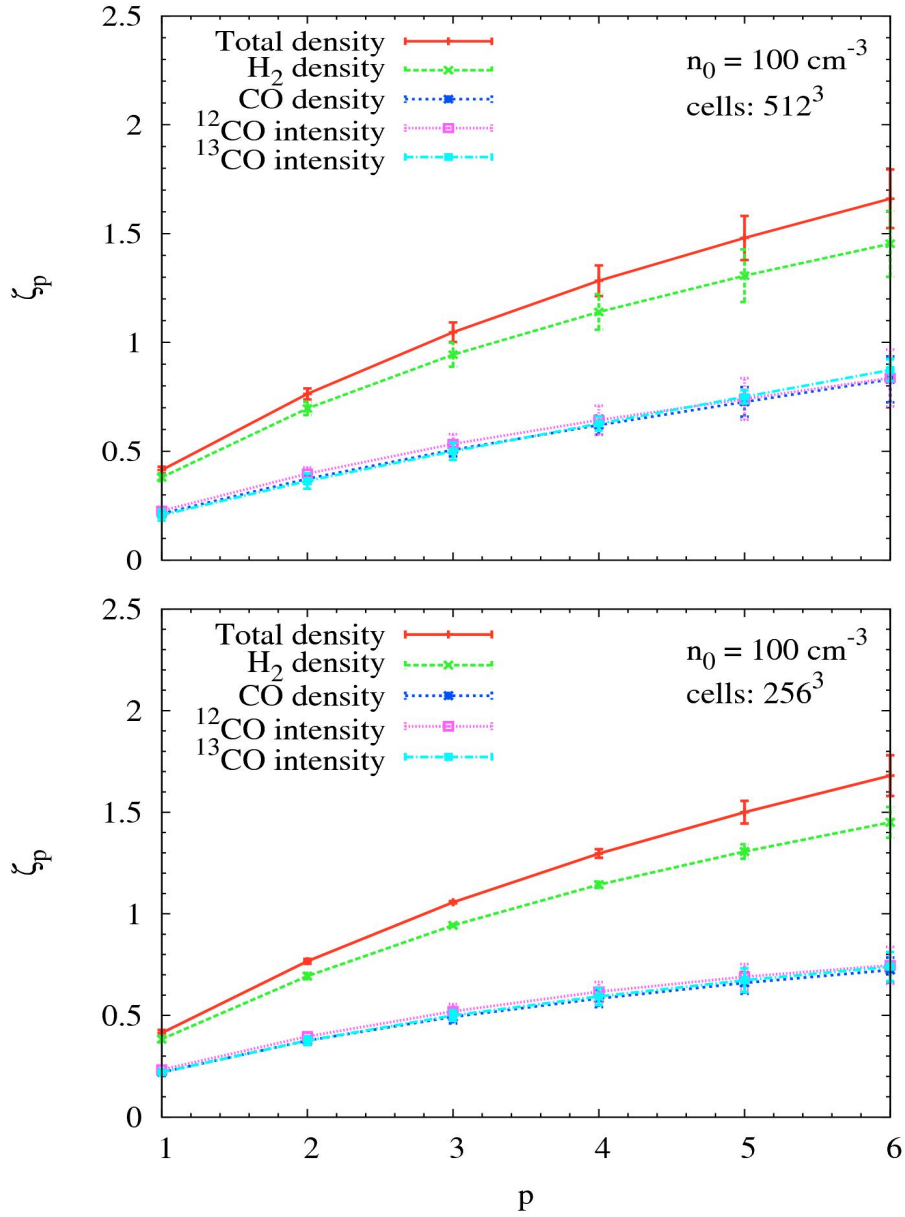
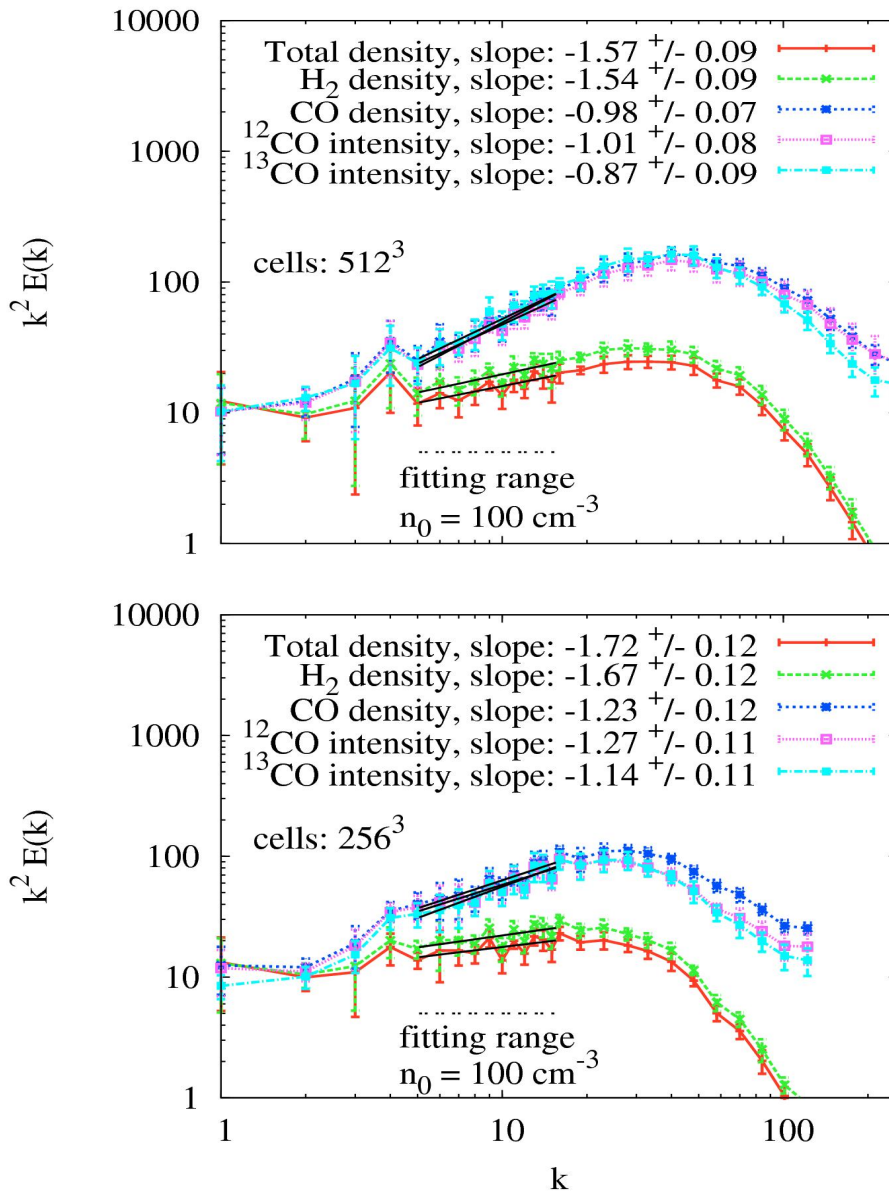


Figure A.1:

Slopes ζ_p of the structure functions against order p for all chemical models, i.e. the total density, H_2 density and the CO density model as well as the ^{12}CO and ^{13}CO intensity model. From top to bottom: runs of different simulations of 512^3 and 256^3 grid cells with a fixed initial number density of $n_0 = 100 \text{ cm}^{-3}$. Error bars denote temporal and spatial $1-\sigma$ fluctuations. Although the individual slope values might be different for the distinct resolutions, the relative scaling behaviour of ζ_p is conserved.

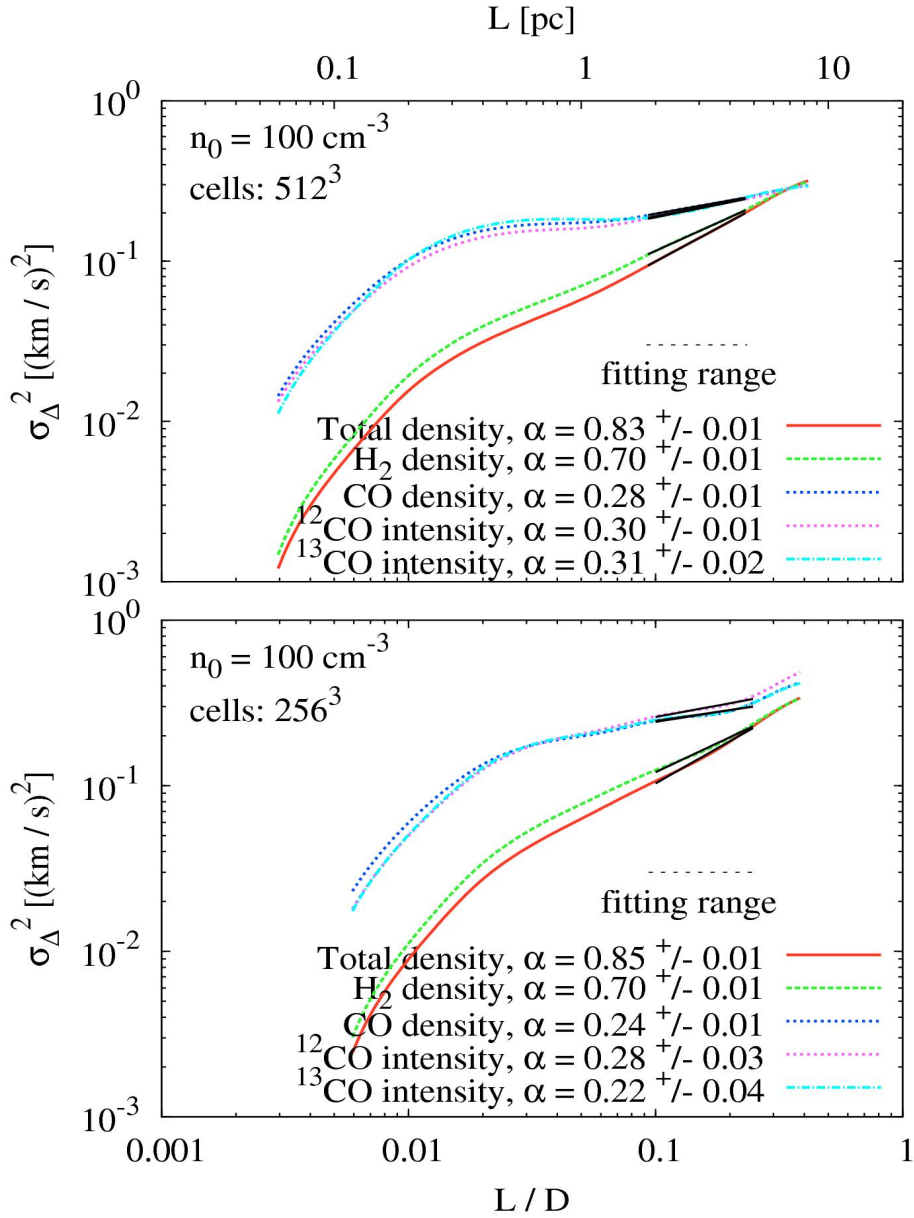
**Figure A.2:**

Fourier energy spectra multiplied by k^2 as a function of scale k for all chemical components, i.e. the total density, H_2 density and the CO density model as well as the ^{12}CO and ^{13}CO intensities. From top to bottom: runs of different simulations of 512^3 and 256^3 grid cells with a fixed initial number density of $n_0 = 100 \text{ cm}^{-3}$. Error bars denote temporal and spatial $1\text{-}\sigma$ fluctuations. In all models, the total density and H_2 density cases show a significantly steeper slope compared to the CO tracer components. The fitting range is indicated by a horizontal dashed line. Slopes with the fitting errors are given in each plot for the different species. Although the individual slope values might be different for the distinct resolutions, the relative scaling behaviour of the energy spectra is conserved.

Structure analysis of simulated MCs with the Δ -variance

B.1 Resolution study

We study the influence of the numerical resolution on the results of the Δ -variance. Therefore, we have performed runs with resolutions of 512^3 and 256^3 grid cells and evaluate the spectra and slopes for the CV maps for all chemical components for a fixed initial number density of $n_0 = 100 \text{ cm}^{-3}$. The results and their interpretation is the same for all other density models. Fig. B.1 shows spectra of the Δ -variance with the corresponding slopes α , in analogy to Fig. 6.4. The fitting range for the 256^3 model is downscaled by a factor of 2 compared to the 512^3 model, i.e. we fit from 25 to 64 cells in the spatial domain. We find similar α values for the total density and the H_2 density models. However, the slope values α differ by up to $\sim 20 - 30\%$ between the different resolution models for the various CO tracers. This is because CO is mainly located in dense regions of the cloud (Bertram et al., 2014), which can be resolved more accurately at a higher resolution, leading to significant differences between the two resolution models. These results agree with the results in the resolution study of the structure function analysis presented in Bertram et al. (2015a). However, the variations caused by the effect of resolution are rather small, since α also strongly depends on the specific choice of the fitting range, which might also cause slope variations by about ± 0.1 . Nevertheless, we find a similar relative scaling behavior in the two resolution models between the spectra of the different chemical components.

**Figure B.1:**

Same as Fig. 6.4, but with runs of different resolutions with 512³ and 256³ grid cells with a fixed initial number density of $n_0 = 100 \text{ cm}^{-3}$, computed for the centroid velocity (CV) maps. We find similar α values for the total density and the H₂ density models, while the values α differ by up to $\sim 20 - 30\%$ between the different resolution models for the various CO tracers.

B.2 Comparison of spectra with different filter functions

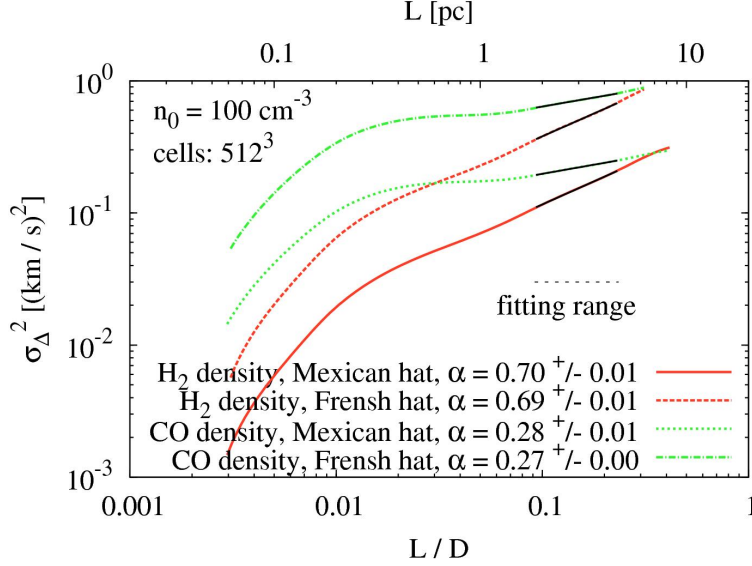


Figure B.2:

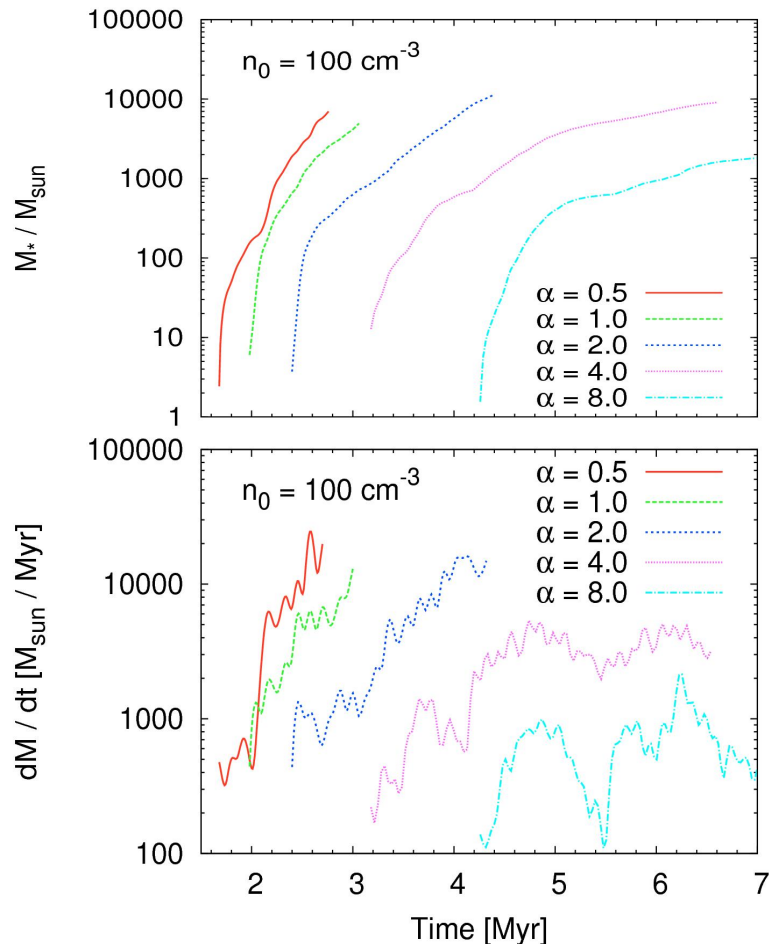
Same as Fig. 6.4, but with the Δ -variance spectra for the H_2 and CO density models for a fixed initial number density of $n_0 = 100 \text{ cm}^{-3}$ and a resolution of 512^3 grid cells, computed for the centroid velocity (CV) maps. In order to analyze the impact of the filter function and its diameter ratio on our results, we compute the H_2 and CO density spectra using both a Mexican hat with a diameter ratio of 1.5 and a French hat with a diameter ratio of 3.0. We do not find any significant differences in the slopes α within the fitting errors if we use another filter function for the Δ -variance analysis.

We also study the influence of the filter function and the choice of the specific diameter ratio on our Δ -variance spectra. Therefore, as an example, Fig. B.2 shows the Δ -variance spectra for the H_2 and CO density models for a fixed initial number density of $n_0 = 100 \text{ cm}^{-3}$ and a resolution of 512^3 grid cells, computed on maps of centroid velocities. For each model, we evaluate the spectra using different filter functions and diameter ratios. In particular, we compute the Δ -variance spectra using a Mexican hat with a diameter ratio of 1.5 as well as a French hat with a diameter ratio of 3.0. In analogy to Section 6.3.1, we fit a power-law within a given fitting range to the spectra and compare the slopes with each other, which are shown in Fig. B.2. Thereby, we do not find any significant differences between the slopes derived from spectra with various filter functions and diameter ratios within the fitting errors for our models. The individual normalizations of the spectra are caused by the variable choice of the diameter ratio, affecting the computation of the Δ -variance analysis (see, e.g. Ossenkopf et al., 2008a). However, the shape of the individual spectra for one chemical model is also approximately conserved.

Star formation efficiencies of MCs in a galactic center environment

C.1 Simulations with a different random seed

We ran numerical simulations with the same setup described in Section 7.2.4 for an initial number density of $n_0 = 100 \text{ cm}^{-3}$ using a different random seed for the turbulent velocity field. Fig. C.1 shows the mass of gas that is converted to stars (sink particles) for the different α parameters as a function of time and their accretion rates. Table C.1 gives an overview of the star formation efficiencies and the number of sink particles that are formed in each cloud. Since star formation sets in later in this turbulent environment compared to our fiducial models presented in Section 7.3.1, we let the two runs GC-4.0-100-SEED and GC-8.0-100-SEED evolve beyond one free-fall time in order to get a significant number of sink particles. Although star formation starts at later times, caused by the different statistical flows of the turbulent velocity field, we again measure large efficiencies ϵ_{ff} for all numerical models even in highly turbulent environments. We also find the same statistical trends as already observed in Table 7.2, i.e. that the SFEs per free-fall time strongly depend on the virial parameter. However, a direct comparison of the ϵ_{ff} values in models with various random seeds is complicated due to the statistics of the turbulent velocity fields, leading to a completely different star formation history and thus to variable SFE.

**Figure C.1:**

Same as Fig. 7.6 and 7.7, but using a different random seed for the turbulent velocity field. The number of sink particles formed by the end of each run, as well as the SFEs, are given in Table C.1.

Model name	$\epsilon_{\Delta t}$ [%]	ϵ_{ff} [%]	N_{sink}	t_* [Myr]	t_{end} [Myr]	Δt [Myr]
GC-0.5-100-SEED	5.7	24.3	2483	1.70	2.73	1.03
GC-1.0-100-SEED	4.1	15.0	1420	1.98	3.10	1.12
GC-2.0-100-SEED	9.4	20.7	2717	2.40	4.40	2.00
GC-4.0-100-SEED	7.6	10.0	2067	3.20	6.56	3.36
GC-8.0-100-SEED	1.1	1.8	405	4.25	7.00	2.75

Table C.1:

Same as Table 7.2, but using a different random seed for the turbulent velocity field.

Synthetic observations of MCs in a galactic center environment:

I. Studying maps of column density and integrated intensity

D.1 Radiative transfer post-processing: influence of grid resolution

Since RADMC-3D cannot deal with AREPO data directly, we have to map the simulation output onto a cubic grid. The results presented in this paper are all based on a grid resolution of 512^3 cells. However, we examine the sensitivity of our results to the choice of the number of grid cells in each dimension. Therefore, we run a similar radiative transfer post-processing with RADMC-3D, using resolutions of 256^3 and 128^3 grid zones. In Fig. D.1 we compare the probability density functions (PDF) of the velocity-integrated intensities for our various tracers for the different grid resolutions, while using the intermediate $\alpha = 2.0$ cloud models as an example. We find that a resolution of 512^3 grid cells is enough in order to properly recover the emission of the cloud for all of the tracers apart from the [OI] $63\mu\text{m}$ line. In the case of [OI] $63\mu\text{m}$, the maps are well-converged for integrated intensities of below 1.5 K km s^{-1} , but at higher integrated intensities, increasing the resolution depresses the PDF. However, as we have already seen in Section 8.3.4, integrated intensities of this magnitude are only recovered for [OI] $63\mu\text{m}$ along lines of sight where the line is already optically thick. The precise values of the integrated intensity that we recover in this regime therefore do not significantly affect our conclusions.

For all of the tracers, we find that the differences between the PDFs we recover from the 256^3 and 512^3 runs are always significantly smaller than the differences

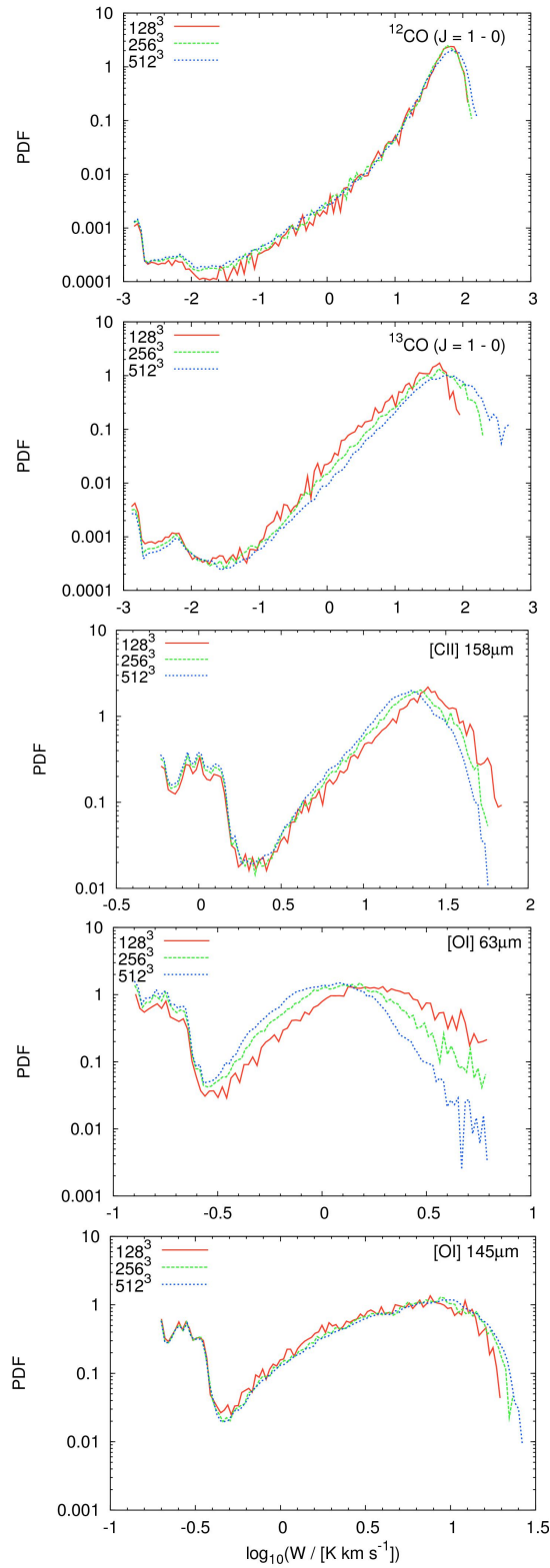


Figure D.1:

Emission PDFs for our various tracers for different resolution models with 128^3 , 256^3 and 512^3 grid cells for clouds with $\alpha = 2.0$.

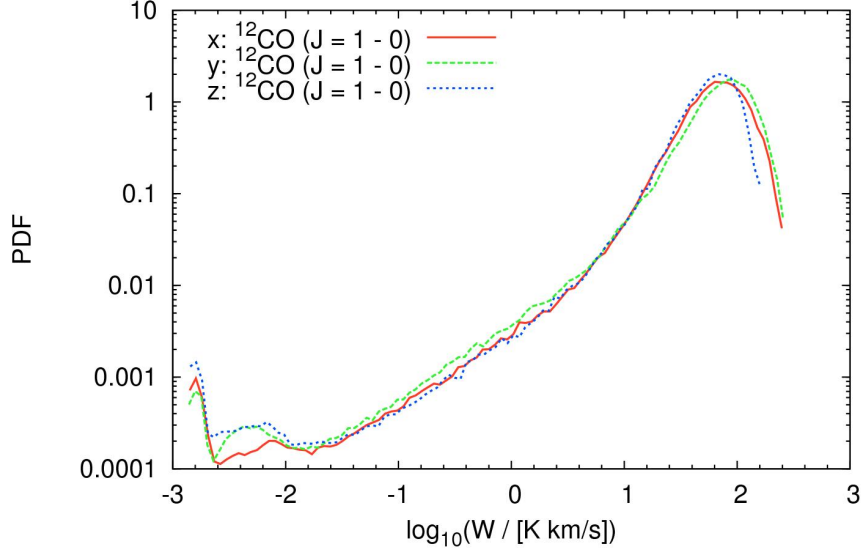


Figure D.2:

Example of emission PDFs for the ^{12}CO tracer for the resolution model with 512^3 grid cells. We choose the intermediate cloud model with $\alpha = 2.0$. The above figure shows the emission PDF for the x -, y - and z -direction. Although there are slight variations in the different PDFs, the bulk emission is the same for all directions.

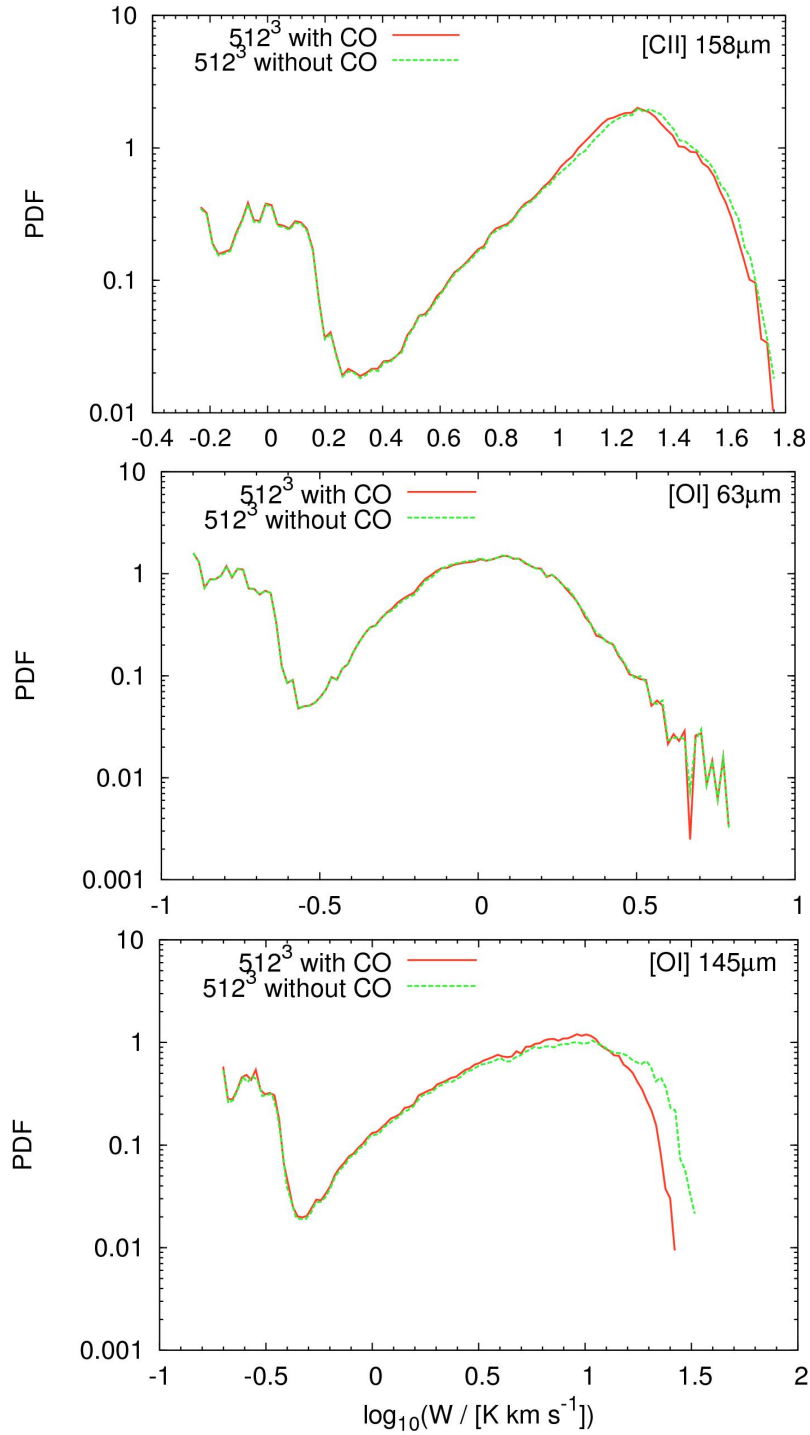
between the 128^3 and 256^3 models. Thus, we do not expect to find larger differences in the PDFs for models with even higher resolution, e.g. between 512^3 and 1024^3 . Hence, due to the significant increase of the computational costs for the radiative transfer post-processing for even higher resolution runs, we focus on models with a resolution of 512^3 grid cells in this paper, which is enough to demonstrate our basic conclusions.

D.2 Dependence on viewing angle

When constructing our synthetic emission maps, we choose to focus on a line of sight (LoS) parallel to the z -axis of the simulation volume. However, as the turbulence in our simulations is isotropic, we expect our results to be insensitive to this choice. To test this, we have also made maps of ^{12}CO for LoS parallel to the x and y axes, using our standard grid resolution of 512^3 zones, for the run with $\alpha = 2.0$. The resulting integrated intensity PDFs are shown in Figure D.2. Although there are slight variations in the different PDFs for x , y and z , the bulk emission is the same for all directions. We find a similar behavior also for the other atomic tracers. Hence, we conclude that it is enough to focus on one specific LoS, for example the z -direction, in order to get an idea about the underlying physical parameters of the cloud. We note, however, that for magnetized clouds this is not necessarily true, as in this case the turbulence will no longer be isotropic, unless the field is very weak.

D.3 Influence of the CO abundance on the line emission of [CII] and [OI]

In Section 8.2.1 we emphasize that the simplified Nelson & Langer (1997) network that we use in our study is known to somewhat overestimate the rate at which CO forms in our simulations. Thus, we may expect that this has a consequence on the distribution of the line emission of [CII] and [OI]. In order to quantify this, we perform additional runs of radiative transfer post-processing with updated abundances of carbon and oxygen for comparison by assuming zero CO abundances in our simulations. As an example, we plot the different line emission PDFs for our various atomic tracers for a fixed resolution of 512^3 grid cells for clouds with $\alpha = 2.0$. The result is shown in Fig. D.3. We find that the [CII] $158 \mu\text{m}$ and [OI] $63 \mu\text{m}$ line emission are unaffected by the changed abundances. This suggests that in the region where the CO abundance is uncertain, these two lines are already optically thick and hence are insensitive to this uncertainty. Support for this interpretation comes from the behavior of the [OI] $145 \mu\text{m}$ line. As we have already seen, this has a much smaller optical depth, and hence is more strongly altered by the changed abundances. However, even in this case, the effect is relatively small: the brightest regions become around 0.1 dex brighter, but the majority of the PDF remains unaffected. We can therefore conclude that the inaccuracy introduced into our predicted [CII] and [OI] maps by our simplified chemical model is unimportant.

**Figure D.3:**

Emission PDFs for our various atomic tracers for a fixed resolution of 512^3 grid cells for clouds with $\alpha = 2.0$. Shown are the PDFs given in Fig. D.1 (with CO) together with PDFs computed from additional runs of radiative transfer post-processing with updated abundances of carbon and oxygen assuming zero CO abundances in our simulations (without CO). We do not find significant changes in the different emission PDFs of the atomic tracers.

Tables of constants and unit systems

Symbol	Value	Name
c	$2.998 \times 10^{10} \text{ cm s}^{-1}$	speed of light
e	$4.803 \times 10^{-10} \text{ cm}^{3/2} \text{ g}^{1/2} \text{ s}^{-1}$	electron charge
G	$6.673 \times 10^{-8} \text{ cm}^3 \text{ g}^{-1} \text{ s}^{-2}$	gravitational constant
k_B	$1.381 \times 10^{-16} \text{ cm}^2 \text{ g s}^{-2} \text{ K}^{-1}$	Boltzmann constant
R	$8.314 \times 10^7 \text{ erg K}^{-1} \text{ mol}^{-1}$	universal gas constant
N_A	$6.022 \times 10^{23} \text{ mol}^{-1}$	Avogadro constant
h	$6.626 \times 10^{-27} \text{ erg s}$	Planck constant
\hbar	$6.582 \times 10^{-16} \text{ erg s}$	reduced Planck constant
m_e	$9.109 \times 10^{-28} \text{ g}$	electron mass
m_p	$1.673 \times 10^{-24} \text{ g}$	proton mass
m_n	$1.675 \times 10^{-24} \text{ g}$	neutron mass
μ_0	$1.398 \times 10^{-20} \text{ cm}^{-2} \text{ s}^2$	vacuum permeability
ϵ_0	7.958×10^{-2}	vacuum permittivity

pc	3.086×10^{18} cm	parsec
AU	14.959.787.070.000 cm	astronomical unit
ly	9.461×10^{17} cm	light year
M_{\odot}	1.989×10^{33} g	mass of the sun
R_{\odot}	6.963×10^{10} cm	radius of the sun
L_{\odot}	1.367×10^6 g s ⁻³	solar constant
a	5.6704×10^{-5} erg cm ⁻² K ⁻⁴ s ⁻¹	Stefan-Boltzmann constant
μ_B	9.274×10^{-21} erg G ⁻¹	Bohr magneton

Table E.1: Physical constants used in this PhD thesis given in cgs units.

SI units	cgs units	Definition
1 m	100 cm	length
1 s	1 s	time
1 kg	1000 g	mass
10^{-7} J	1 erg = 1 cm ² g s ⁻²	energy
10^{-5} N	1 dyn = 1 cm g s ⁻²	force
1 T	10^4 G = 1 cm ^{-1/2} g ^{1/2} s ⁻¹	magnetic field strength
1 Pa	10 cm ⁻¹ g s ⁻²	pressure

Table E.2: Different unit systems used in this thesis.

Tables of symbols, physical definitions and nomenclature

Symbol	Definition	Name
n		particle number density
N		particle number
m		particle mass
V		volume
M	$M = \int \rho dV$	total mass
ℓ		spatial scale
ρ	$\rho = nm$	density
ρ_{el}		charge density
L		length scale
T		temperature
P		pressure
F		force

\mathbf{g}	$\mathbf{g} = -\nabla\Phi$	gravitational acceleration
E	$E^2 = c^2p^2 + m^2c^4$	relativistic energy
λ		mean free path
\mathbf{v}		velocity
c_s	$c_s^2 = \frac{dP}{d\rho}$	sound speed
Φ		gravitational potential
λ_J	$\lambda_J = \left(\frac{\pi c_s^2}{G\rho}\right)^{1/2}$	Jeans wavelength
$\eta^{\mu\nu}$	$\eta^{\mu\nu} = \text{diag}(-1, +1, +1, +1)$	Minkowski metric
Λ_ν^μ		Lorentz transformation matrix
$F^{\mu\nu}$	$F^{\mu\nu} = \partial^\mu A^\nu - \partial^\nu A^\mu$	covariant electromagnetic field tensor
A^μ	$A^\mu = (\Phi/c, \mathbf{A})$	vector potential
Φ		electromagnetic potential
γ	$\gamma = \frac{1}{\sqrt{1-v^2/c^2}}$	Lorentz factor
ds^2	$ds^2 = \eta_{\mu\nu}dx^\mu dx^\nu$	relativistic line element
x^μ	$x^\mu = (ct, \mathbf{x})^T$	four-vector
u^μ	$u^\mu = dx^\mu/d\tau = \gamma(c, \mathbf{v})^T$	four-velocity
p^μ	$p^\mu = mu^\mu = (E/c, \mathbf{p})^T$	four-momentum
j^μ	$j^\mu = \rho_0 u^\mu$	four-current
$T^{\mu\nu}$	$T^{\mu\nu} = \left(\rho + \frac{P}{c^2}\right)u^\mu u^\nu + p\eta^{\mu\nu}$	energy-momentum tensor
M_J	$M_J = \frac{4\pi}{3}\rho\left(\frac{\lambda_J}{2}\right)^3$	Jeans mass

t_{dyn}	$t_{\text{dyn}} = \left(\frac{3\pi}{16G\rho}\right)^{1/2}$	dynamical timescale
t_{ff}	$t_{\text{ff}} = \left(\frac{3\pi}{32G\rho}\right)^{1/2}$	free-fall timescale
t_{cross}	$t_{\text{cross}} = \frac{L}{v}$	crossing timescale
t_{ad}		ambipolar diffusion timescale
t_{decay}	$t_{\text{decay}} = L^2/\eta$	decay timescale of the magnetic field
E		electric field
B		magnetic field
j		current density
Φ	$\Phi = \int \mathbf{B} \, d\mathbf{A}$	magnetic flux
σ		conductivity
η	$\eta = \frac{c^2}{4\pi\sigma}$	magnetic diffusivity
μ		shear coefficient
ν	$\nu = \frac{\mu}{\rho}$	viscosity
\mathcal{R}	$\mathcal{R} = \frac{Lv}{\nu}$	Reynolds number
\mathcal{R}_M	$\mathcal{R}_M = \frac{Lv}{\eta}$	magnetic Reynolds number
ϵ		energy dissipation rate per unit mass
ℓ_c	$\ell_c = \left(\frac{\nu^3}{\langle\epsilon\rangle}\right)^{1/4}$	Kolmogorov dissipation scale
ζ_p		slope of the p-th order structure function
k	$k = \frac{2\pi}{L}$	wave number
$E(k)$		energy at wavenumber k
$P(k)$	$P(k) = dE/dk$	power spectrum

β	$\beta = \frac{v}{c}$	ratio of velocity and speed of light
v_A	$v_A = \frac{B}{\sqrt{\mu_0 \rho}}$	Alfvén velocity
\mathcal{M}_s	$\mathcal{M}_s = \frac{v}{c_s}$	sonic Mach number
\mathcal{M}_A	$\mathcal{M}_A = \frac{v}{v_A}$	Alfvénic Mach number
Σ	$\Sigma = \int \rho \, ds$	mass column density
$N(\mathbf{r})$	$N(\mathbf{r}) = \int n(\mathbf{r}, z) \, dz$	number column density
I_ν	$I_\nu = \frac{dE}{dA \, dt \, d\nu \, d\Omega}$	specific intensity
J	$J = \frac{1}{4\pi} \iint I_\nu \, d\Omega \, d\nu$	total intensity
J_ν	$J_\nu = \frac{1}{4\pi} \int I_\nu \, d\Omega$	mean intensity
u_ν	$u_\nu = \frac{4\pi}{c} J_\nu$	energy density
S_ν	$S_\nu = j_\nu / \alpha_\nu$	source function
B_ν	$B_\nu(T) = \frac{2h}{c^2} \frac{\nu^3}{e^{\beta h\nu} - 1}$	Planck spectrum
T_B	$T_B = \left(\frac{c}{\nu}\right)^2 \frac{I_\nu}{2k_B}$	brightness temperature
Ω		solid angle
ν		frequency
ω	$\omega = 2\pi\nu$	cyclic frequency
κ_ν		opacity
α_ν	$\alpha_\nu = \rho\kappa_\nu$	absorption coefficient
τ_ν	$\tau_\nu = \alpha_\nu L$	optical depth
A_{21}		Einstein coefficient for spontaneous emission
B_{12}		Einstein coefficient for absorption

B_{21}		Einstein coefficient for stimulated emission
γ	$\gamma = c_P/c_V$	adiabatic index
$\phi(\omega)$		line profiles
Γ		heating rate
Λ		cooling rate
\mathbf{S}		spin vector
\mathbf{L}		angular momentum vector
\mathbf{J}	$\mathbf{J} = \mathbf{L} + \mathbf{S}$	total angular momentum vector
$W(\mathbf{r})$	$W(\mathbf{r}) = \int T_B(\mathbf{r}, z) dv$	integrated intensity
σ_Δ^2	$\sigma_\Delta^2(\ell) = \left\langle \left(S(\mathbf{r}) * \odot_\ell(\mathbf{r}) \right)^2 \right\rangle_{\mathbf{r}}$	Δ -variance
$S_p(\ell)$	$S_p(\ell) \equiv \langle \delta\mathbf{v}(\mathbf{r} + \boldsymbol{\ell}) - \delta\mathbf{v}(\mathbf{r}) ^p \rangle$	structure function
α	$\alpha = E_{\text{kin}}/ E_{\text{pot}} $	virial parameter
G_0		Draine field
ζ		cosmic-ray ionization rate
ϵ_{ff}	$\epsilon_{\text{ff}} = t_{\text{ff}} \cdot \frac{\dot{M}_*}{M_{\text{tot}}}$	star formation efficiency per free-fall time
X_{CO}	$X_{\text{CO}} = N_{\text{H}_2}/W_{\text{CO}}$	X_{CO} -factor

Table F.1: Physical symbols and definitions used in this thesis.

Symbol	Definition	Name
$\mathbf{a} \cdot \mathbf{b}$	$\sum_i a_i b_i$	classical scalar product
$a^\mu b_\mu$	$\sum_\mu a^\mu b_\mu$	relativistic scalar product
$\mathbf{a} \times \mathbf{b}$	$\sum_i \epsilon_{ijk} a_i b_j \mathbf{e}_k$	cross product
∇	$\sum_i \frac{\partial}{\partial x_i}$	nabla operator
\square	$\square = \partial_t^2 - c_s^2 \nabla^2$	d'Alembert operator
$\frac{\partial}{\partial x} = \partial_x$		partial derivative in x -direction
$\frac{d}{dt}$		total time derivative
$\langle \dots \rangle$		ensemble average
\dot{f}		time derivative
δ_{ij}	$\delta_{ij} = \begin{cases} 1, & \text{if } i = j, \\ 0, & \text{if } i \neq j. \end{cases}$	Kronecker delta
ϵ_{ijk}	$\epsilon_{ijk} = \begin{cases} +1, & \text{even permutation,} \\ -1, & \text{odd permutation,} \\ 0, & \text{else.} \end{cases}$	Levi-Civita symbol

Table F.2: Mathematical nomenclature used in this thesis.

Lists

G.1 List of Figures

- 1.1 The Pleiades are an example of an open star cluster in the Milky Way, containing middle-aged hot B-type stars. The cluster is made up of ~ 3.000 stars at a distance of ~ 120 pc from Earth in the constellation of Taurus. In the picture we can also still see the diffuse gas out of which the stars formed. Image credit (07/12/2015): NASA, ESA and AURA/Caltech, D. Soderblom and E. Nelan (STScI), F. Benedict and B. Arthur (University of Texas), and B. Jones (Lick Observatory). 18
- 1.2 Cosmic star formation history as a function of look-back time and redshift. Shown are both far-UV and infrared measurements of the cosmic star formation rate (SFR) density ψ . We observe a maximum SFR density at $z \approx 2$. Today, the SFR density decreases continuously (taken from Madau & Dickinson, 2014). 19
- 1.3 Velocity integrated spectral line maps of the rotational transition $^{12}\text{CO } J = 1 \rightarrow 0$, $^{12}\text{CO } J = 2 \rightarrow 1$ and $^{13}\text{CO } J = 1 \rightarrow 0$, observed towards the Polaris Flare, and one of its cores, MCLD 123.5+24.9. The transition and the telescope are indicated at the top of each panel. The line intensity is given in main beam brightness temperature, T_{mb} . Iso-intensity levels are shown from 2 to 8 in steps of 2 (CfA map), 1 to 11 by 2 (KOSMA), 1 to 4 by 1 (FCRAO), 5 to 17 by 2 (IRAM, $^{12}\text{CO } J = 1 \rightarrow 0$), 3 to 11 by 2 (IRAM, $^{12}\text{CO } J = 2 \rightarrow 1$), in units of K km s^{-1} . This Figure is taken from Bensch et al. (2001). 25

1.4	The Galactic Center with its surrounding Central Molecular Zone (CMZ). This image was taken with the NRAO Very Large Array at 20 cm (purple) and with the Caltech Submillimeter Observatory at 1.1 mm (orange). The purple regions are HII regions which are illuminated by supernovae remnants and hot massive stars. The orange regions are cold dust regions of molecular gas with temperatures of 20 – 30 K. The scale of the CMZ is about ~ 200 pc in radius. The investigators are Adam Ginsburg and John Bally (University of Colorado, Boulder) and Farhad Yusef-Zadeh (Northwestern University).	33
1.5	Prominent examples of applications using the moving mesh code AREPO. The left plot shows a Kelvin-Helmholtz instability, while the right plot illustrates a Sedov-Taylor expansion in a low resolution calculation, most notably used to study the dynamics of supernova explosions. Each plot shows the density field overlaid with the Voronoi tessellation in black. We directly see the big advantage of the unstructured and moving mesh, which allows us to accurately track the flows in the simulations with high precision.	36
3.1	Illustration of the different line profiles for $\Gamma = \sigma = 1$ in arbitrary units. This Figure is taken from Bartelmann (2013).	77
4.1	Flow past a cylinder with Reynolds number $\mathcal{R} = 0.16$ (taken from Frisch & Kolmogorov, 1995). We observe a left-right and up-down symmetry as well a space- and time-translation symmetry parallel to the axis of the cylinder.	84
4.2	Flow past a cylinder with Reynolds number $\mathcal{R} = 140$ (taken from Frisch & Kolmogorov, 1995). The symmetries from Fig. 4.1 are broken now.	84
4.3	Flow past two cylinders with Reynolds number $\mathcal{R} = 1800$ (taken from Frisch & Kolmogorov, 1995). At the right side, the symmetries are restored in a statistical sense.	84
4.4	Phenomenological picture of Kolmogorov turbulence. The picture shows the <i>Richardson energy cascade</i> . Kinetic energy is injected into the system at a scale ℓ_0 , called the <i>injection scale</i> . It cascades with a constant mean energy rate of dissipation ϵ in the <i>inertial range</i> and is dissipated into thermal heat below a <i>dissipation scale</i> ℓ_c . The picture was taken from http://cictr.ee.psu.edu (07/12/2015) and was slightly modified.	90
4.5	Theoretical prediction of the function ζ_p from the Kolmogorov theory (K41) and the She-Levèque model (SL94). In addition, we show experimental results by Benzi et al. (1993). As one can see, the SL94 model describes the experimental data much better for higher order p as the K41 theory.	93

4.6	The Cantor function is a prominent example for an intermittent function (taken from Frisch & Kolmogorov, 1995). We see that the self-similarity is clearly broken in some parts of the function. This is a strong indicator of intermittent behavior.	95
5.1	CVI structure function for orders up to $p = 6$ with the inferred slopes ζ_p as a function of spatial scale for one snapshot in time, normalised by the total box size. The velocity here is weighted by the total density field for an initial number density of $n_0 = 300 \text{ cm}^{-3}$. The fitting range is indicated by a horizontal dashed line. Error bars denote $1\text{-}\sigma$ variations for all 3 line-of-sight directions.	105
5.2	Centroid velocities in z-direction for models n30 (left column), n100 (middle column) and n300 (right column). From top to bottom: CV maps of the total density, H_2 and ^{12}CO density followed by CV maps of the ^{12}CO and ^{13}CO integrated intensities. Each side has a length of 20 pc. Note that the velocity field of the n30 model uses a different turbulent seed than the n100 and the n300 model. Black areas in the ^{12}CO and ^{13}CO map of the n30 model denote regions where the brightness temperatures are zero along the line-of-sight. We mask these regions, because no proper centroid velocities can be computed there.	107
5.3	Slopes ζ_p of the structure functions against order p for all chemical models, i.e. the total density, H_2 density and the CO density model as well as the ^{12}CO and ^{13}CO intensity model. For comparison, we also show the theoretical scaling relations (black lines) from Kolmogorov (1941), She & Leveque (1994) and Boldyrev et al. (2002), denoted as K41, SL94 and B02. From top to bottom: runs of the different initial number densities, i.e. $n_0 = 300, 100$ and 30 cm^{-3} . Error bars denote temporal and spatial $1\text{-}\sigma$ fluctuations. Please note that a direct comparison of the theoretical models with our CV statistics is complicated due to the projection along the LoS. For a more detailed discussion about the influence of the projection, we refer the reader to Sec. 5.4.3 and 5.4.4.	110
5.4	Fourier energy spectra multiplied by k^2 as a function of scale k for all density models and chemical components, i.e. the total density, H_2 density and the CO density model as well as the ^{12}CO and ^{13}CO intensities. From top to bottom: runs of the different initial number densities, i.e. $n_0 = 300, 100$ and 30 cm^{-3} . Error bars denote temporal and spatial $1\text{-}\sigma$ fluctuations. In all models, the total density and H_2 density cases show a significantly steeper slope compared to the CO tracer components. The fitting range is indicated by a horizontal dashed line. Slopes with the fitting errors are given in each plot for the different species.	111

- 6.1 Example of a Δ -variance spectrum, plotted as a function of spatial scale, normalized by the total box size and averaged over all available time snapshots. The inferred slope α is also indicated (solid line). The Δ -variance is computed on a CV map, where the velocities are weighted by the total density field for an initial number density of $n_0 = 300 \text{ cm}^{-3}$. The fitting range is indicated by a horizontal dashed line. Error bars denote $1\text{-}\sigma$ spatial and temporal variations. 123
- 6.2 Logarithmic maps of column density as well as velocity-integrated intensity along the z -direction for our n30 (left column), n100 (middle column) and n300 models (right column). From top to bottom we show the different chemical components: total, H_2 and CO column density as well as the integrated intensity of ^{12}CO and ^{13}CO in the $J = 1 \rightarrow 0$ transition. Each side of the simulation domain has a length of 20 pc. Note that the velocity field of the n30 model uses a different turbulent random seed than the n100 and the n300 model. Furthermore, we caution the reader that our color bars use a different scaling in the individual plots. 125
- 6.3 Same as Fig. 6.2, but with maps of centroid velocities (CV). Black areas in the ^{12}CO and ^{13}CO intensity map of the n30 model denote regions where the brightness temperatures are zero along the line-of-sight. We mask these regions, because no proper centroid velocities can be computed there. 126
- 6.4 Δ -variance spectra as a function of the spatial scale, averaged over all available time snapshots and the different lines-of-sights x , y and z . The spatial scale is normalized by the total box size. From top to bottom: spectra for our three different density models, i.e. n300, n100 and n30, computed for the centroid velocity (CV) maps. In each plot we show the Δ -variance spectra for our various chemical components, i.e. for the total density, H_2 and CO density as well as for the ^{12}CO and ^{13}CO intensity. We use a fitting range from $1/10$ to $1/4$ of the total box size ($0.1 \lesssim \ell/D \lesssim 0.25$), as constrained by Federrath et al. (2010) and Konstandin et al. (2012), which is indicated by a horizontal dashed line and is the same in each density model. The different power-law functions in the fitting range are indicated with a black solid line on each spectrum. Furthermore, we list the slopes α and their errors from a χ^2 -fit in each plot. 129

- 6.5 Same as Fig. 6.4, but computed using maps of integrated intensity and column density. In this plot, we normalize each curve by the corresponding value σ_0^2 measured at an arbitrary spatial scale of 5% of the total box, in order to better compare the spectra computed for the intensity and column density maps with each other. For a better visualization, we also show a horizontal dashed line at a value of $\sigma_\Delta^2/\sigma_0^2 = 1$ in each plot. Furthermore, for clarity, we do not plot the error bars of the individual spectra here. The slopes α and their errors from a χ^2 -fit are listed in each plot for all our chemical components. 131
- 7.1 Logarithmic column density maps in z-direction for all cloud models with initial number densities of $n_0 = 100 \text{ cm}^{-3}$ (left column) and 1000 cm^{-3} (right column) for different virial parameters $\alpha = 0.5, 1.0, 2.0, 4.0, 8.0$ (from top to bottom), showing an extract of the central cloud regions. In each plot we give the number of sink particles, the estimated star formation efficiency per free-fall time and the simulation time. Sink particles are formed during the simulations and marked with white dots in each map. The side length of each box shown above corresponds to 74.5 pc and 44.5 pc for the 100 cm^{-3} and 1000 cm^{-3} models, respectively. 149
- 7.2 Star formation efficiencies per free-fall time against the corresponding virial α parameter for our fiducial models with $n_{0,\text{seed0}} = 100 \text{ cm}^{-3}$ and $n_{0,\text{seed0}} = 1000 \text{ cm}^{-3}$ (Table 7.2) and for one model using a different seed of the turbulent velocity field with $n_{0,\text{seed1}} = 100 \text{ cm}^{-3}$ (Table C.1). We generally find a decreasing trend of the SFEs with higher α for all density models. Although there are slight differences in the individual SFEs between the two models with $n_{0,\text{seed0}} = 100 \text{ cm}^{-3}$ and $n_{0,\text{seed1}} = 100 \text{ cm}^{-3}$, we nevertheless find the same general trends of decreasing ϵ_{ff} with increasing α . To illustrate the different trends, we also fit exponential functions $\propto \exp(-c\alpha)$ to the models and list the corresponding slopes in the plot. Error bars indicate variations of the SFE of $\sim 30\%$, which we conservatively estimate in Section 7.3.1. 150
- 7.3 Left column: Mass-weighted volume density PDFs at different times for our five virial α parameters, $\alpha = 0.5, 1.0, 2.0, 4.0$ and 8.0 . Right column: Same as left column, but with column density PDFs. In order to compute the column density PDFs, our simulations were projected onto a regular 1024^2 map. All plots are computed for our models using an initial number density of $n_0 = 100 \text{ cm}^{-3}$ 151
- 7.4 Same as Fig. 7.3, but for our models using an initial number density of $n_0 = 1000 \text{ cm}^{-3}$ 152
- 7.5 Mass-weighted temperature PDFs at different times for our five virial α parameters, $\alpha = 0.5, 1.0, 2.0, 4.0$ and 8.0 , for our models with an initial number density of $n_0 = 100 \text{ cm}^{-3}$ (left column) and $n_0 = 1000 \text{ cm}^{-3}$ (right column). 153

7.6	Mass of gas M_* converted to stars (sink particles) as a function of time for the different virial α parameters for our models with initial number densities of $n_0 = 100 \text{ cm}^{-3}$ (top) and $n_0 = 1000 \text{ cm}^{-3}$ (bottom).	157
7.7	Mass accretion rates dM/dt for the corresponding density models and different virial α parameters given in Fig. 7.6.	158
8.1	Physical state of the clouds at the end of our simulations. We show two-dimensional PDFs of gas temperature and number density for various chemical components for runs with $\alpha = 0.5$ (left column), 2.0 (middle column), and 8.0 (right column). In the upper row, the number densities shown are the total particle number density. In the remaining rows, on the other hand, they are the number density of the chemical species indicated in the panel (e.g. n_{H_2} , n_{O} , etc.). Note that the scaling of the density axis therefore differs from panel to panel. The color coding shows the fraction of the total gas mass in each logarithmic density and temperature bin.	173
8.2	Logarithmic column density maps computed along the LoS in the z -direction for the total density (top row) and the H_2 density (bottom row) for different virial parameters: $\alpha = 0.5$ (left column), 2.0 (middle column) and 8.0 (right column). Each side has a length of 44.5 pc. The initial cloud radius of 8.9 pc is indicated in the bottom panels.	174
8.3	Total mass per unit logarithmic column density for the total and the H_2 gas as shown in Fig. 8.2 for our different virial parameters: $\alpha = 0.5$ (top), 2.0 (middle) and 8.0 (bottom).	175
8.4	Velocity-integrated intensity maps computed along the LoS in the z -direction for different virial parameters: $\alpha = 0.5$ (left column), 2.0 (middle column) and 8.0 (right column). From top to bottom: integrated intensity maps for ^{12}CO ($J = 1 \rightarrow 0$), ^{13}CO ($J = 1 \rightarrow 0$), $[\text{OI}]$ ($63 \mu\text{m}$), $[\text{OI}]$ ($145 \mu\text{m}$) and $[\text{CII}]$ ($158 \mu\text{m}$). Note the different scaling in the colorbars at the right hand side. Each side has a length of 44.5 pc. The initial cloud radius of 8.9 pc is indicated in the bottom panels. The contour lines show the threshold values given in Table 8.3.	179
8.5	Log-log plot showing velocity-integrated intensities against total column density for different virial parameters: $\alpha = 0.5$ (left column), 2.0 (middle column) and 8.0 (right column). Shown are all our tracers presented in Table 8.2. In each plot, the mean value is indicated by a black solid line.	180
8.6	Same as Fig. 8.5, but with the column density of H_2	181
8.7	Cumulative fraction of the total (top row) and H_2 (bottom row) mass in the cloud for different virial parameters $\alpha = 0.5$ (left column), 2.0 (middle column) and 8.0 (right column), traced by our various chemical components presented in Table 8.2, as a function of the minimum velocity-integrated intensity in the line.	183

- 8.8 Logarithmic maps of the CO-to-H₂ conversion factor, $X_{\text{CO}} = N_{\text{H}_2}/W_{\text{CO}}$, for the three models: $\alpha = 0.5$ (top), 2.0 (middle) and 8.0 (bottom). The average X_{CO} -factor values are given in Table 8.5. We see that only the inner parts of the cloud yield the canonical X_{CO} -factor value on average, while the outer cloud regions exhibit significantly larger X_{CO} values. The gray background denotes regions where the CO emission is zero. Hence, it is impossible to compute a value for X_{CO} there. 185
- 9.1 Logarithmic column density maps computed along the LoS in the z -direction for the total density for different virial parameters: $\alpha = 0.5$ (left), 2.0 (middle) and 8.0 (right). Each side has a length of 44.5 pc. The initial cloud radius of 8.9 pc is indicated in each panel. 194
- 9.2 Velocity-integrated intensity maps computed along the LoS in the z -direction for different virial parameters: $\alpha = 0.5$ (left column), 2.0 (middle column) and 8.0 (right column). From top to bottom: integrated intensity maps for ^{12}CO ($J = 1 \rightarrow 0$), ^{13}CO ($J = 1 \rightarrow 0$), [OI] ($63 \mu\text{m}$), [OI] ($145 \mu\text{m}$) and [CII] ($158 \mu\text{m}$). Note the different scaling in the colorbars at the right hand side. Each side has a length of 44.5 pc. The initial cloud radius of 8.9 pc is indicated in the bottom panels. The contour lines show the threshold values given in Table 3 in Paper I. 195
- 9.3 Logarithmic maps of density-weighted mean temperatures computed via Eq. 9.4 along the z -direction for the different virial parameters: $\alpha = 0.5$ (left), 2.0 (middle) and 8.0 (right). Each box has a size of 44.5 pc. The initial cloud radius of 8.9 pc is indicated in each panel. The temperatures extend from $\sim 50 - 100$ K in the coldest regions to ~ 10.000 K in the hottest regions around each cloud. 196
- 9.4 Maps of 1D rms velocity dispersions σ for the total gas mass computed along the z -direction for the different virial parameters: $\alpha = 0.5$ (left column), 2.0 (middle column) and 8.0 (right column). In the first row, we show the velocity dispersions coming from the turbulent velocity field. In the second row, we show the velocity dispersions coming from the thermal contribution of the gas, computed via Eq. 9.3 with temperatures shown in Fig. 9.3. The third row shows the square root of the geometrical sum, $\sigma_{\text{tot}}^2 = \sigma_{\text{turb}}^2 + \sigma_{\text{therm}}^2$, of both turbulent and thermal contributions. Note the different scaling in the colorbars at the right hand side. Each box has a length of 44.5 pc. The initial cloud radius of 8.9 pc is indicated in the bottom panels. 197
- 9.5 Temporal evolution of both kinetic and thermal energy for our three models with $\alpha = 0.5, 2.0$ and 8.0 in our simulations. The energy scale is normalized to a constant value of 10^{50} erg. 200

- 9.6 Maps of velocity dispersions σ computed along the z -direction via Eq. 9.1 for different virial parameters: $\alpha = 0.5$ (left column), 2.0 (middle column) and 8.0 (right column). From top to bottom: velocity dispersions for models of ^{12}CO ($J = 1 \rightarrow 0$), ^{13}CO ($J = 1 \rightarrow 0$), [OI] ($63 \mu\text{m}$), [OI] ($145 \mu\text{m}$) and [CII] ($158 \mu\text{m}$). Note the different scaling in the colorbars at the right hand side. Each side has a length of 44.5 pc. The initial cloud radius of 8.9 pc is indicated in the bottom panels. The gray background in the ^{12}CO and ^{13}CO maps denotes regions where the abundances of CO are zero. Hence, it is impossible to compute a value for the velocity dispersions there. 201
- 9.7 Mean brightness temperatures (first row) as well as mean brightness temperatures normalized by the maximum value (second row) against the internal cloud velocity for our various tracers given in Table 9.1 for different virial parameters $\alpha = 0.5$ (left column), 2.0 (middle column) and 8.0 (right column). The spectra are computed by using Eq. 9.1, but this time we take the mean value of all brightness temperatures at a given velocity. 203
- 9.8 Temporal evolution of the virial α parameter for our three models with $\alpha = 0.5, 2.0$ and 8.0 in our simulations. 204
- 10.1 Two of the most promising telescopes for upcoming astronomical research: the Atacama Large Millimeter/submillimeter Array (ALMA, left) and the Global Astrometric Interferometer for Astrophysics (GAIA, right). 216
- A.1 Slopes ζ_p of the structure functions against order p for all chemical models, i.e. the total density, H_2 density and the CO density model as well as the ^{12}CO and ^{13}CO intensity model. From top to bottom: runs of different simulations of 512^3 and 256^3 grid cells with a fixed initial number density of $n_0 = 100 \text{ cm}^{-3}$. Error bars denote temporal and spatial $1\text{-}\sigma$ fluctuations. Although the individual slope values might be different for the distinct resolutions, the relative scaling behaviour of ζ_p is conserved. 221

- A.2 Fourier energy spectra multiplied by k^2 as a function of scale k for all chemical components, i.e. the total density, H_2 density and the CO density model as well as the ^{12}CO and ^{13}CO intensities. From top to bottom: runs of different simulations of 512^3 and 256^3 grid cells with a fixed initial number density of $n_0 = 100 \text{ cm}^{-3}$. Error bars denote temporal and spatial $1\text{-}\sigma$ fluctuations. In all models, the total density and H_2 density cases show a significantly steeper slope compared to the CO tracer components. The fitting range is indicated by a horizontal dashed line. Slopes with the fitting errors are given in each plot for the different species. Although the individual slope values might be different for the distinct resolutions, the relative scaling behaviour of the energy spectra is conserved. 222
- B.1 Same as Fig. 6.4, but with runs of different resolutions with 512^3 and 256^3 grid cells with a fixed initial number density of $n_0 = 100 \text{ cm}^{-3}$, computed for the centroid velocity (CV) maps. We find similar α values for the total density and the H_2 density models, while the values α differ by up to $\sim 20 - 30\%$ between the different resolution models for the various CO tracers. 224
- B.2 Same as Fig. 6.4, but with the Δ -variance spectra for the H_2 and CO density models for a fixed initial number density of $n_0 = 100 \text{ cm}^{-3}$ and a resolution of 512^3 grid cells, computed for the centroid velocity (CV) maps. In order to analyze the impact of the filter function and its diameter ratio on our results, we compute the H_2 and CO density spectra using both a Mexican hat with a diameter ratio of 1.5 and a French hat with a diameter ratio of 3.0. We do not find any significant differences in the slopes α within the fitting errors if we use another filter function for the Δ -variance analysis. 225
- C.1 Same as Fig. 7.6 and 7.7, but using a different random seed for the turbulent velocity field. The number of sink particles formed by the end of each run, as well as the SFEs, are given in Table C.1. 228
- D.1 Emission PDFs for our various tracers for different resolution models with 128^3 , 256^3 and 512^3 grid cells for clouds with $\alpha = 2.0$ 230
- D.2 Example of emission PDFs for the ^{12}CO tracer for the resolution model with 512^3 grid cells. We choose the intermediate cloud model with $\alpha = 2.0$. The above figure shows the emission PDF for the x -, y - and z -direction. Although there are slight variations in the different PDFs, the bulk emission is the same for all directions. 231

- D.3 Emission PDFs for our various atomic tracers for a fixed resolution of 512^3 grid cells for clouds with $\alpha = 2.0$. Shown are the PDFs given in Fig. D.1 (with CO) together with PDFs computed from additional runs of radiative transfer post-processing with updated abundances of carbon and oxygen assuming zero CO abundances in our simulations (without CO). We do not find significant changes in the different emission PDFs of the atomic tracers. 233

G.2 List of Tables

- 1.1 Different observable properties of various molecular cloud types and some famous examples, taken from Stahler & Palla (2006). 24
- 1.2 Examples of possible driving mechanisms in MCs together with a magnitude estimate of the injected energy \dot{e} . For further discussions, see the review by Mac Low & Klessen (2004). 27
- 1.3 Comparison of some important physical properties measured in solar neighbourhood clouds and in clouds located in the Central Molecular Zone (CMZ). 35
- 5.1 Overview of the different models with some characteristic values for the last snapshot. From top to bottom we list: mean number density, resolution, box size, time of the last snapshot, mean sonic Mach number, mean Alfvén Mach number, ratio of density dispersion and mean density, mass-weighted mean abundances of H_2 (i.e. the percentage of atomic hydrogen that has been converted to H_2 , see Glover & Mac Low, 2011), mean volume- and mass-weighted H_2 and CO number density, mean volume- and mass-weighted temperature and mean column density of H_2 and CO. 108
- 5.2 Spectral slopes for all chemical components and density models shown in Figure 5.4. In order to compare our spectral slope values α to those given in Lazarian & Pogosyan (2004), we have to subtract a value of -2, i.e. $\beta = \alpha - 2$. Independent of the individual component, we observe a saturation of the spectral slopes to a value of $\beta \approx -3$ 113
- 6.1 Overview of our different models with some characteristic values measured for the last time snapshot. From top to bottom we list: mean number density, resolution, box size, time of the last snapshot, mean sonic Mach number, mean Alfvén Mach number, ratio of density dispersion and mean density, mass-weighted mean abundances of H_2 (i.e. the percentage of atomic hydrogen that has been converted to H_2 , see Glover & Mac Low, 2011), mean volume- and mass-weighted H_2 and CO number densities, mean volume- and mass-weighted temperature and mean column densities of H_2 and CO. 127

6.2	Spectral slope of the Δ -variance spectrum, computed using centroid velocities weighted by the indicated quantity (see also Fig. 6.4). The errors are computed by the χ^2 fitting method. The slope α is related to the Δ -variance via $\sigma_{\Delta}^2(\ell) \propto \ell^{\alpha}$ in a linear regime. The values α can also be used to compute spectral slopes $\gamma = \alpha/2$ for a linewidth-size relation $\sigma_{\Delta}(\ell) \propto \ell^{\gamma}$, readily comparable to observational measurements.	128
6.3	Same as Table 6.2, but for the Δ -variance computed directly from maps of integrated intensity and column density, as defined in equation (6.3) and (6.4). The corresponding Δ -variance spectra are shown in Fig. 6.5.	130
7.1	Initial conditions for our different cloud models. For each run, we list the virial α parameter, the initial number density, the spherical cloud radius, the velocity dispersion, the free-fall time and the scaling factor of the interstellar radiation field (ISRF) and the cosmic ray flux (CRF) relative to the solar neighbourhood value. For comparison, we also list the parameters for the GC cloud G0.253+0.016, known as “the Brick”, which are given in Table 2 in Longmore et al. (2012).	147
7.2	The star formation efficiencies $\epsilon_{\Delta t}$ give the amount of gas being converted to sink particles within a time $\Delta t = t_{\text{end}} - t_{*} < t_{\text{ff}}$, where t_{end} denotes the end of our simulation and t_{*} the time when the first star forms. N_{sink} gives the total number of sink particles formed during the time Δt . To calculate the SFEs per free-fall time, ϵ_{ff} , we extrapolate based on $\epsilon_{\Delta t}$, assuming that the SFR between t_{ff} and t_{end} is the same as between t_{*} and t_{end} . Some simulations with lower α values are not evolved until one free-fall time, which is due to the high computational costs of the individual runs. Nevertheless, we let all those simulations evolve until a $\epsilon_{\Delta t}$ of at least $\sim 4\%$ is reached.	148
8.1	Overview of the initial conditions for our different cloud models.	167
8.2	Tracer name and type, quantum mechanical transition, wavelength λ and frequency ν of various fine structure lines, which we model with the radiative transfer code RADMC-3D.	171
8.3	Threshold values W_{thresh} used for the integrated intensity maps in Fig. 8.4 in order to estimate the effective cloud radius R_{eff} . The values are chosen such that the denser cloud regions can be clearly separated from the diffuse gas phase around it, leading to a reasonable estimate for the effective cloud radii presented in Table 8.4.	174
8.4	Effective radii of the clouds shown in Fig. 8.4, as inferred from equation 8.3, based on the threshold intensities given in Table 8.3. For comparison, we also give the effective radii of the clouds that incorporate $\sim 80\%$ of the total gas mass in the second column.	176

8.5	Values of the CO-to-H ₂ conversion factor, relating the amount of ¹² CO ($J = 1 \rightarrow 0$) emission W_{CO} to the H ₂ column density N_{H_2} for all our α runs. For the computation of the X_{CO} -factor, we only include pixels where the velocity-integrated intensity for carbon monoxide is larger than the corresponding threshold given in Table 8.3. Thus, X_{CO} only accounts for regions with a significant amount of CO emission in the cloud.	186
9.1	Tracer name and type, quantum mechanical transition, wavelength λ and frequency ν of various fine structure lines, which we model with the radiative transfer code RADMC-3D.	191
9.2	Overview of the initial conditions for our different cloud models.	192
9.3	Mean values of the different components of the velocity dispersions shown in Fig. 9.4. The mean of σ_{turb} is computed by averaging over all pixels in the maps, while the mean of σ_{therm} and σ_{tot} only includes those pixels where the internal cloud velocities can be clearly separated from the velocities of the hot and diffuse gas around each cloud.	199
9.4	Mean values of the 1D rms velocity dispersions shown in Fig. 9.6 for our various tracers and virial parameters. We compute the velocity dispersions by adopting the threshold values for the velocity-integrated intensity maps presented in Paper I. The values above are then computed by evaluating the mean of all sight lines for which the corresponding integrated intensity is smaller than the threshold values given in Tab. 3 in Paper I. The values for the total mass are taken from Tab. 9.3.	202
9.5	Same as Table 9.4, but with values of the full width at half maximum (FWHM).	202
9.6	Effective radii of the clouds, based on the threshold intensities given in Table 3 in Paper I. For comparison, we also give the effective radii of the clouds that incorporate $\sim 80\%$ of the total gas mass in the second column.	205
9.7	Virial parameters for all cloud models and tracers. Given are the initial and final α parameter measured for the total gas (see Sec. 9.3.5) as well as estimates for the different tracers computed via Eq. 9.7 using the velocity dispersions from Table 9.4. We note that the values might differ by $\sim 10 - 20\%$ due to the uncertainties in the estimate of the effective cloud radius.	206
9.8	Same as Table 9.7, but using the velocity dispersions given in Table 9.5.	206

A.1	Slopes of the CVISF for our highest order $p = 6$ for the different chemical components and for different runs with 512^3 and 256^3 grid cells. As an example, we show values for a fixed initial number density of $n_0 = 100 \text{ cm}^{-3}$. The slopes of the total density and H_2 density cases are similar within their errors, while the slope values of the different CO tracers significantly deviate with resolution.	219
C.1	Same as Table 7.2, but using a different random seed for the turbulent velocity field.	228
E.1	Physical constants used in this PhD thesis given in cgs units.	236
E.2	Different unit systems used in this thesis.	236
F.1	Physical symbols and definitions used in this thesis.	241
F.2	Mathematical nomenclature used in this thesis.	242

Acknowledgements

This work would not have been possible without many people who supported me during the last years. This is the right time and place to say thank you.

First, I thank my supervisors Prof. Dr. Ralf S. Klessen and Dr. Simon C. O. Glover that they offered me the possibility to work at the Institute for Theoretical Astrophysics (ITA) in Heidelberg and in the field of astronomy. Every day I felt that this was absolutely the right choice. I am deeply thankful to them because I had all freedom and support a PhD student could have. Furthermore, both of them have put a lot of help and work into our joint publications. They helped a lot to improve the quality of each individual paper.

I also thank the Konrad-Adenauer foundation for the financial support via their “Promotionsförderung” and the Deutsche Forschungsgemeinschaft (DFG) for their financial support via the SFB 881 “The Milky Way System”. I also like to mention the International Max Planck Research School (IMPRS) in Heidelberg for the ideal support during my PhD.

The last years at ITA were extremely intense. I learned a lot not only about astronomy, but also about theoretical physics. Furthermore, I like to thank all the great people that I met during my PhD time here at ITA. In particular, I want to mention Dr. Christian Baczynski, Carla June Bernhard, Dr. Frank Bigiel, Dr. Paul C. Clark, Dr. Diane Cormier, Prof. Dr. Cornelis Dullemond, Dr. Volker Gaibler, Dr. Dimitrios Gouliermis, Dr. Daniel Harsono, Tilman Hartwig, Dr. Sacha Hony, Maria Jesus Jimenez, Basma Klinger-Araifa, Dr. Lukas Konstandin, Sylvia Matyssek, Juan Ibanez Mejia, Dr. Jan-Pieter Paardekooper, Dr. Eric Pellegrini, Dr. Mei Sasaki, Anna T. P. Schauer, Dr. Jennifer Schober, Dr. Rahul Shetty, Dr. Rowan J. Smith, Dr. Laszlo Szucs, Robin Gopala Treb, Dr. Daniel Whalen and Katharina M. J. Wollenberg for our joint time at the institute and the familiar atmosphere. I hope that I did not forget anybody. If yes, please don't be cross with me too long.

I also acknowledge the support of Prof. Dr. Henrik Beuther for reviewing my PhD thesis and that he was part of my thesis committee. I also thank Prof. Dr.

Eva K. Grebel and Prof. Dr. Markus K. Oberthaler for being part of my defence committee. Further gratitudes go to Prof. Dr. Alyssa A. Goodman for hosting me during my research stay at Harvard university. I also like to thank Prof. Dr. Stella S. R. Offner, Prof. Dr. Mordecai-Mark Mac Low and Prof. Dr. Mark Krumholz that they invited me to their institutes to talk about my scientific research.

Finally, I want to thank my girlfriend Sylvia Gaiser for her great patience, the lovingly support and the encouragement over the years. She never was annoyed when I was talking too enthusiastically about theoretical physics and astronomy during our free time. I'm also very grateful to my parents, Martin and Monika Bertram, and my whole family for the whole financial, logistical and mental support and that they made my physics studies possible at all.

Erik Bertram
Heidelberg, December 2015

Bibliography

- Abraham J., Abreu P., Aglietta M., Aguirre C., Allard D., Allekotte I., Allen J., Allison P., Alvarez-Muñiz J., Ambrosio M., et al. 2008, *Physical Review Letters*, 101, 061101
- Alexander T., 2005, *Phys. Rep.*, 419, 65
- Alves J., Lada C. J., Lada E. A., 1999, *Astrophys. J.*, 515, 265
- Alves J., Lada C. J., Lada E. A., Kenyon S. J., Phelps R., 1998, *Astrophys. J.*, 506, 292
- Alves J., Lombardi M., Lada C. J., 2007, *Astron. & Astrophys.*, 462, L17
- Alves de Oliveira C., Schneider N., Merín B., Prusti T., Ribas Á., Cox N. L. J., Vavrek R., Könyves V., Arzoumanian D., Puga E., Pilbratt G. L., Kóspál Á., André P., et al 2014, *Astron. & Astrophys.*, 568, A98
- André P., Men'shchikov A., Bontemps S., Könyves V., Motte F., Schneider N., Didelon P., Minier V., Saraceno P., Ward-Thompson D., di Francesco J., White G., Molinari S., Testi L., Abergel 2010, *Astron. & Astrophys.*, 518, L102
- Anselmet F., Gagne Y., Hopfinger E., Antonia R., 1984, *Journal of Fluid Mechanics*, 140, 63
- Arzoumanian D., André P., Didelon P., Könyves V., Schneider N., Men'shchikov A., Soubie T., Zavagno A., Bontemps S., di Francesco J., Griffin M., Hennemann M., et al 2011, *Astron. & Astrophys.*, 529, L6
- Balbus S. A., Hawley J. F., 1991, *Astrophys. J.*, 376, 214
- Balbus S. A., Hawley J. F., 1998, *Reviews of Modern Physics*, 70, 1

- Ballesteros-Paredes J., Hartmann L. W., Vázquez-Semadeni E., Heitsch F., Zamora-Avilés M. A., 2011, *Mon. Not. R. Astron. Soc.*, 411, 65
- Ballesteros-Paredes J., Klessen R. S., Mac Low M.-M., Vazquez-Semadeni E., 2007, *Protostars and Planets V*, pp 63–80
- Ballesteros-Paredes J., Vázquez-Semadeni E., Scalo J., 1999, *Astrophys. J.*, 515, 286
- Bally J., Langer W. D., Stark A. A., Wilson R. W., 1987, *The Astrophysical Journal*, 312, L45
- Banerjee R., Pudritz R. E., 2006, *Astrophys. J.*, 641, 949
- Bania T. M., 1977, *Astrophys. J.*, 216, 381
- Bartelmann M., 2013, *Theoretical astrophysics. Physics textbook*, Wiley-VCH, Weinheim
- Basri G., 2000, *Annual Review of Astronomy and Astrophysics*, 38, 485
- Batchelor G. K., Townsend A. A., 1949, *Proceedings of the Royal Society of London A: Mathematical, Physical and Engineering Sciences*, 199, 238
- Bate M. R., Bonnell I. A., Bromm V., 2003, *Monthly Notices of the Royal Astronomical Society*, 339, 577
- Bate M. R., Bonnell I. A., Price N. M., 1995, *Mon. Not. R. Astron. Soc.*, 277, 362
- Bensch F., Stutzki J., Ossenkopf V., 2001, *Astron. & Astrophys.*, 366, 636
- Benzi R., Ciliberto S., Tripicciono R., Baudet C., Massaioli F., Succi S., 1993, *Phys. Rev. E*, 48, R29
- Beresnyak A., Lazarian A., 2009, *Astrophys. J.*, 702, 1190
- Bergin E. A., Tafalla M., 2007, *Ann. Rev. Astron. Astrophys.*, 45, 339
- Bertram E., Glover S. C. O., Clark P. C., Klessen R. S., 2015c, *Mon. Not. R. Astron. Soc.*, 451, 3679
- Bertram E., Glover S. C. O., Clark P. C., Ragan S. E., Klessen R. S., 2015d, *Mon. Not. R. Astron. Soc.*, 455, 3763
- Bertram E., Klessen R. S., Glover S. C. O., 2015b, *Mon. Not. R. Astron. Soc.*, 451, 196
- Bertram E., Konstandin L., Shetty R., Glover S. C. O., Klessen R. S., 2015a, *Mon. Not. R. Astron. Soc.*, 446, 3777

- Bertram E., Shetty R., Glover S. C. O., Klessen R. S., Roman-Duval J., Federrath C., 2014, *Mon. Not. R. Astron. Soc.*, 440, 465
- Beuther H., Ragan S. E., Ossenkopf V., Glover S., Henning T., Linz H., Nielbock M., Krause O., Stutzki J., Schilke P., Güsten R., 2014, *Astron. & Astrophys.*, 571, A53
- Beuther H., Schilke P., Wyrowski F., 2004, *Astrophys. J.*, 615, 832
- Beuther H., Vlemmings W. H. T., Rao R., van der Tak F. F. S., 2010, *Astrophys. J. Let.*, 724, L113
- Bigiel F., Leroy A., Walter F., Brinks E., de Blok W. J. G., Madore B., Thornley M. D., 2008, *The Astron. J.*, 136, 2846
- Birkhoff G. D., 1927, *Dynamical systems*. No. 9 in *Colloquium publications / American Mathematical Society ; 9 ; American Mathematical Society: Colloquium publications*, American Math. Society, Providence, R. I.
- Bisbas T. G., Papadopoulos P. P., Viti S., 2015, *Astrophys. J.*, 803, 37
- Bitran M., Alvarez H., Bronfman L., May J., Thaddeus P., 1997, *Astron. and Astrophys. Sup.*, 125, 99
- Blitz L., Shu F. H., 1980, *Astrophys. J.*, 238, 148
- Bolatto A. D., Leroy A. K., Rosolowsky E., Walter F., Blitz L., 2008, *Astrophys. J.*, 686, 948
- Bolatto A. D., Wolfire M., Leroy A. K., 2013, *Ann. Rev. Astron. Astrophys.*, 51, 207
- Boldyrev S., Nordlund Å., Padoan P., 2002, *Physical Review Letters*, 89, 031102
- Bonnell I. A., Smith R. J., Clark P. C., Bate M. R., 2011, *Mon. Not. R. Astron. Soc.*, 410, 2339
- Bouwens R. J., Illingworth G. D., Labbe I., Oesch P. A., Trenti M., Carollo C. M., van Dokkum P. G., Franx M., Stiavelli M., González V., Magee D., Bradley L., 2011, *Nature*, 469, 504
- Brandenburg A., Sokoloff D., Subramanian K., 2012, *Space Sci. Rev.*, 169, 123
- Brandenburg A., Subramanian K., 2005, *Phys. Rep.*, 417, 1
- Brunt C. M., Heyer M. H., 2002a, *Astrophys. J.*, 566, 276
- Brunt C. M., Heyer M. H., 2002b, *Astrophys. J.*, 566, 289

- Brunt C. M., Heyer M. H., Vázquez-Semadeni E., Pichardo B., 2003, *Astrophys. J.*, 595, 824
- Burgers J. M., 1948, *Adv. Appl. Mech.*, 1, 171
- Burkhart B., Lazarian A., 2012, *Astrophys. J. Let.*, 755, L19
- Burkhart B., Lazarian A., Leão I. C., de Medeiros J. R., Esquivel A., 2014, *Astrophys. J.*, 790, 130
- Burkhart B., Lazarian A., Ossenkopf V., Stutzki J., 2013a, *Astrophys. J.*, 771, 123
- Burkhart B., Ossenkopf V., Lazarian A., Stutzki J., 2013b, *Astrophys. J.*, 771, 122
- Burkhart B., Stanimirović S., Lazarian A., Kowal G., 2010, *Astrophys. J.*, 708, 1204
- Burrows A., Hubbard W., Lunine J., Liebert J., 2001, *Reviews of Modern Physics*, 73, 719
- Burton W. B., Liszt H. S., Gordon M. A., 1978, *J. Phys. F*, 39, 1
- Cappellaro E., Evans R., Turatto M., 1999, *Astron. & Astrophys.*, 351, 459
- Cassen P., Moosman A., 1981, *Icarus*, 48, 353
- Chabrier G., 2003, *Pub. Astron. Soc. Pac.*, 115, 763
- Cho J., Lazarian A., Vishniac E. T., 2002, *The Astrophysical Journal Letters*, 566, L49
- Choudhuri A. R., 1998, *The physics of fluids and plasmas*, 1. publ. edn. Cambridge University Press, Cambridge
- Christopher M., Scoville N., Stolovy S., Yun M. S., 2005, *The Astrophysical Journal*, 622, 346
- Clark P. C., Bonnell I. A., 2004, *Mon. Not. R. Astron. Soc.*, 347, L36
- Clark P. C., Bonnell I. A., Klessen R. S., 2008, *Mon. Not. R. Astron. Soc.*, 386, 3
- Clark P. C., Bonnell I. A., Zinnecker H., Bate M. R., 2005, *Mon. Not. R. Astron. Soc.*, 359, 809
- Clark P. C., Glover S. C. O., 2015, *Mon. Not. R. Astron. Soc.*, 452, 2057
- Clark P. C., Glover S. C. O., Klessen R. S., 2012, *Mon. Not. R. Astron. Soc.*, 420, 745
- Clark P. C., Glover S. C. O., Ragan S. E., Shetty R., Klessen R. S., 2013, *Astrophys. J. Let.*, 768, L34

- Commerçon B., Hennebelle P., Henning T., 2011, *Astrophys. J. Let.*, 742, L9
- Cormier D., Madden S. C., Lebouteiller V., Abel N., Hony S., Galliano F., Rémy-Ruyer A., Bigiel F., Baes M., Boselli A., et al 2015, *Astron. & Astrophys.*, 578, A53
- Crutcher R. M., 1999, *Astrophys. J.*, 520, 706
- Crutcher R. M., 2012, *Ann. Rev. Astron. Astrophys.*, 50, 29
- Crutcher R. M., Troland T. H., 2008, *Astrophys. J.*, 685, 281
- Crutcher R. M., Troland T. H., Goodman A. A., Heiles C., Kazes I., Myers P. C., 1993, *Astrophys. J.*, 407, 175
- Crutcher R. M., Troland T. H., Lazareff B., Paubert G., Kazès I., 1999, *Astrophys. J. Let.*, 514, L121
- Crutcher R. M., Wandelt B., Heiles C., Falgarone E., Troland T. H., 2010, *Astrophys. J.*, 725, 466
- Cummins S. E., Linke R., Thaddeus P., 1986, *The Astrophysical Journal Supplement Series*, 60, 819
- Dale J. E., Bonnell I. A., Clarke C. J., Bate M. R., 2005, *Mon. Not. R. Astron. Soc.*, 358, 291
- Dame T. M., Hartmann D., Thaddeus P., 2001, *Astrophys. J.*, 547, 792
- D’Inverno R., 2009, *Einführung in die Relativitätstheorie*, 2., durchges. und korr. Aufl. edn. *Lehrbuch Physik*, WILEY-VCH, Weinheim
- Dirac P. A. M., 2010, *The principles of quantum mechanics*, 4. ed. (rev.), repr. edn. No. 27 in *International series of monographs on physics* ; 27 ; *International series of monographs on physics*, Clarendon Press, Oxford University Press, Oxford [u.a.]
- Dobler W., Haugen N. E., Yousef T. A., Brandenburg A., 2003, *Phys. Rev. E*, 68, 026304
- Doeleman S. S., Weintroub J., Rogers A. E. E., Plambeck R., Freund R., Tilanus R. P. J., Friberg P., Ziurys L. M., Moran J. M., Corey B., Young K. H., Smythe D. L., et al 2008, *Nature*, 455, 78
- Draine B. T., 1978, *Astrophys. J. Suppl. Ser.*, 36, 595
- Draine B. T., 2003a, *Ann. Rev. Astron. Astrophys.*, 41, 241
- Draine B. T., Lee H. M., 1984, *Astrophys. J.*, 285, 89
- Dubrulle B., 1994, *Phys. Rev. Lett.*, 73, 959

- Dullemond C. P., 2012, *Astrophysics Source Code Library*
- Eisenhauer F., Genzel R., Alexander T., Abuter R., Paumard T., Ott T., Gilbert A., Gillessen S., Horrobin M., Trippe S., Bonnet H., Dumas C., Hubin N., Kaufer A., et al 2005, *Astrophys. J.*, 628, 246
- Eisenhauer F., Schödel R., Genzel R., Ott T., Tecza M., Abuter R., Eckart A., Alexander T., 2003, *Astrophys. J. Let.*, 597, L121
- Elia D., Strafella F., Schneider N., Paladini R., Vavrek R., Maruccia Y., Molinari S., Noriega-Crespo A., Pezzuto S., Rygl K. L. J., Di Giorgio A. M., Traficante A., Schisano E., Calzoletti L., et al 2014, *Astrophys. J.*, 788, 3
- Elmegreen B. G., Scalo J., 2004, *Ann. Rev. Astron. Astrophys.*, 42, 211
- Esquivel A., Lazarian A., 2005, *Astrophys. J.*, 631, 320
- Esquivel A., Lazarian A., Horibe S., Cho J., Ossenkopf V., Stutzki J., 2007, *Mon. Not. R. Astron. Soc.*, 381, 1733
- Evans II N. J., 1999, *Ann. Rev. Astron. Astrophys.*, 37, 311
- Falgarone E., Panis J.-F., Heithausen A., Perault M., Stutzki J., Puget J.-L., Bensch F., 1998, *Astron. & Astrophys.*, 331, 669
- Falkovich G., 1994, *Physics of Fluids*, 6, 1411
- Federrath C., 2013, *Mon. Not. R. Astron. Soc.*, 436, 1245
- Federrath C., 2015a, *Mon. Not. R. Astron. Soc.*, 450, 4035
- Federrath C., 2015b, *Mon. Not. R. Astron. Soc.*, 450, 4035
- Federrath C., Banerjee R., Clark P. C., Klessen R. S., 2010b, *Astrophys. J.*, 713, 269
- Federrath C., Klessen R. S., 2012, *Astrophys. J.*, 761, 156
- Federrath C., Klessen R. S., 2013, *Astrophys. J.*, 763, 51
- Federrath C., Klessen R. S., Schmidt W., 2008, *Astrophys. J. Let.*, 688, L79
- Federrath C., Klessen R. S., Schmidt W., 2009, *Astrophys. J.*, 692, 364
- Federrath C., Roman-Duval J., Klessen R. S., Schmidt W., Mac Low M.-M., 2010, *Astron. & Astrophys.*, 512, A81
- Federrath C., Roman-Duval J., Klessen R. S., Schmidt W., Mac Low M.-M., 2010a, *Astron. & Astrophys.*, 512, A81

- Figer D. F., Kim S. S., Morris M., Serabyn E., Rich R. M., McLean I. S., 1999, *Astrophys. J.*, 525, 750
- Fliessbach T., 2005, *Quantenmechanik*, 4., überarb. Aufl. edn. Spektrum, Akad. Verl., Heidelberg ; Berlin
- Fliessbach T., 2012, *Elektrodynamik*, 6 edn. SpringerLink : Bücher, Spektrum Akademischer Verlag, Heidelberg
- Freeman K., Bland-Hawthorn J., 2002, *Ann. Rev. Astron. Astrophys.*, 40, 487
- Frisch U., Kolmogorov A., 1995, *Turbulence: The Legacy of A.N. Kolmogorov*. Cambridge University Press
- Fryxell B., Olson K., Ricker P., Timmes F. X., Zingale M., Lamb D. Q., MacNeice P., Rosner R., Truran J. W., Tufo H., 2000, *Astrophys. J. Suppl. Ser.*, 131, 273
- Fukui Y., Kawamura A., 2010, *Ann. Rev. Astron. Astrophys.*, 48, 547
- Genzel R., 1989, in , *The Center of the Galaxy*. Springer, pp 393–405
- Genzel R., Eisenhauer F., Gillessen S., 2010, *Reviews of Modern Physics*, 82, 3121
- Genzel R., Thatte N., Krabbe A., Kroker H., Tacconi-Garman L. E., 1996, *Astrophys. J.*, 472, 153
- Genzel R., Townes C., 1987, *Annual review of astronomy and astrophysics*, 25, 377
- Ghez A. M., Duchêne G., Matthews K., Hornstein S. D., Tanner A., Larkin J., Morris M., Becklin E. E., Salim S., Kremenek T., Thompson D., Soifer B. T., Neugebauer G., McLean I., 2003, *Astrophys. J. Let.*, 586, L127
- Gillessen S., Eisenhauer F., Trippe S., Alexander T., Genzel R., Martins F., Ott T., 2009, *Astrophys. J.*, 692, 1075
- Gilmore G., Carswell B., Thanert W., 1989, *Astronomische Nachrichten*, 310, 96
- Ginsburg A., Henkel C., Ao Y., Riquelme D., Kauffmann J., Pillai T., Mills E. A. C., Requena-Torres M. A., Immer K., Testi L., Ott J., Bally J., Battersby C., et al 2015, *ArXiv e-prints*, 1509.01583
- Glover S. C. O., Clark P. C., 2012, *Mon. Not. R. Astron. Soc.*, 421, 116
- Glover S. C. O., Clark P. C., 2012a, *Mon. Not. R. Astron. Soc.*, 421, 9
- Glover S. C. O., Clark P. C., 2012b, *Mon. Not. R. Astron. Soc.*, 421, 116
- Glover S. C. O., Federrath C., Mac Low M.-M., Klessen R. S., 2010, *Mon. Not. R. Astron. Soc.*, 404, 2

- Glover S. C. O., Mac Low M.-M., 2007, *Astrophys. J. Suppl. Ser.*, 169, 239
- Glover S. C. O., Mac Low M.-M., 2011, *Mon. Not. R. Astron. Soc.*, 412, 337
- Goldreich P., Sridhar S., 1995, *Astrophys. J.*, 438, 763
- Goldsmith P. F., Lis D. C., Hills R., Lasenby J., 1990, *Astrophys. J.*, 350, 186
- Goodman A. A., Barranco J. A., Wilner D. J., Heyer M. H., 1998, *Astrophys. J.*, 504, 223
- Goodwin S. P., Nutter D., Kroupa P., Ward-Thompson D., Whitworth A. P., 2008, *Astronomy & Astrophysics*, 477, 823
- Grebel E. K., 2000, in Favata F., Kaas A., Wilson A., eds, *Star Formation from the Small to the Large Scale Vol. 445 of ESA Special Publication, The Star Formation History of the Local Group.* p. 87
- Greif T. H., Springel V., White S. D. M., Glover S. C. O., Clark P. C., Smith R. J., Klessen R. S., Bromm V., 2011, *Astrophys. J.*, 737, 75
- Güsten R., Walmsley C. M., Pauls T., 1981, *Astron. & Astrophys.*, 103, 197
- Habing H. J., 1968, *Bull. Astron. Inst. Netherlands*, 19, 421
- Haugen N. E. L., Brandenburg A., 2004, *Phys. Rev. E*, 70, 026405
- Hayashi C., 1961, *Pub. of the Astron. Soc. of Japan*, 13, 450
- Hayes J. C., Norman M. L., Fiedler R. A., Bordner J. O., Li P. S., Clark S. E., ud-Doula A., Mac Low M.-M., 2006, *Astrophys. J. Suppl. Ser.*, 165, 188
- Heithausen A., Thaddeus P., 1990, *Astrophys. J. Let.*, 353, L49
- Heitsch F., Mac Low M.-M., Klessen R. S., 2001, *Astrophys. J.*, 547, 280
- Hennebelle P., Chabrier G., 2008, *The Astrophysical Journal*, 684, 395
- Hennebelle P., Commerçon B., Joos M., Klessen R. S., Krumholz M., Tan J. C., Teyssier R., 2011, *Astron. & Astrophys.*, 528, A72
- Hennebelle P., Falgarone E., 2012, *Astron. & Astrophys. Rev.*, 20, 55
- Heyer M., Krawczyk C., Duval J., Jackson J. M., 2009, *Astrophys. J.*, 699, 1092
- Heyer M. H., Brunt C. M., 2004, *Astrophys. J. Let.*, 615, L45
- Heyer M. H., Schloerb F. P., 1997, *Astrophys. J.*, 475, 173
- Heyer M. H., Williams J. P., Brunt C. M., 2006, *Astrophys. J.*, 643, 956

- Heyminck S., Graf U. U., Güsten R., Stutzki J., Hübers H. W., Hartogh P., 2012, *Astron. & Astrophys.*, 542, L1
- Hillas A. M., 1984, *Ann. Rev. Astron. Astrophys.*, 22, 425
- Hillenbrand L. A., 1997, *The Astronomical Journal*, 113, 1733
- Hily-Blant P., Falgarone E., Pety J., 2008, *Astron. & Astrophys.*, 481, 367
- Hollenbach D. J., Tielens A. G. G. M., 1997, *Ann. Rev. Astron. Astrophys.*, 35, 179
- Immer K., Menten K. M., Schuller F., Lis D. C., 2012, *Astron. & Astrophys.*, 548, A120
- Indriolo N., Neufeld D. A., Gerin M., Schilke P., Benz A. O., Winkel B., Menten K. M., Chambers E. T., Black J. H., Bruderer S., Falgarone E., Godard B., Goicoechea J. R., Gupta H., et al 2015, *Astrophys. J.*, 800, 40
- Inutsuka S.-I., Miyama S. M., 1992, *Astrophys. J.*, 388, 392
- Jackson J. D., 2014, *Klassische Elektrodynamik*, 5., überarb. Aufl. edn. De Gruyter Studium, De Gruyter, Berlin [u.a.]
- Jappsen A.-K., Klessen R. S., Larson R. B., Li Y., Mac Low M.-M., 2005, *Astron. & Astrophys.*, 435, 611
- Jeans J. H., 1902, *Royal Society of London Philosophical Transactions Series A*, 199, 1
- Johnston K. G., Beuther H., Linz H., Schmiedeke A., Ragan S. E., Henning T., 2014, *Astron. & Astrophys.*, 568, A56
- Juvela M., Harju J., Ysard N., Lunttila T., 2012, *Astron. & Astrophys.*, 538, A133
- Kaneda Y., Ishihara T., Yokokawa M., Itakura K., Uno A., 2003, *Physics of Fluids*, 15, L21
- Kauffmann J., Pillai T., Zhang Q., 2013, *Astrophys. J. Let.*, 765, L35
- Kennicutt R. C., Evans N. J., 2012, *Ann. Rev. Astron. Astrophys.*, 50, 531
- Kennicutt Jr. R. C., 1998a, *Ann. Rev. Astron. Astrophys.*, 36, 189
- Kennicutt Jr. R. C., 1998b, *Astrophys. J.*, 498, 541
- King I., 1962, *The Astronomical Journal*, 67, 471
- King I. R., 1966, *The Astronomical Journal*, 71, 64
- Kirk H., Myers P. C., Bourke T. L., Gutermuth R. A., Hedden A., Wilson G. W., 2013, *Astrophys. J.*, 766, 115

- Klessen R. S., 2000, *Astrophys. J.*, 535, 869
- Klessen R. S., 2000a, *Astrophys. J.*, 535, 869
- Klessen R. S., 2001, *Astrophys. J.*, 556, 837
- Klessen R. S., Glover S. C. O., 2014, ArXiv e-prints, 1412.5182
- Klessen R. S., Heitsch F., Mac Low M.-M., 2000, *Astrophys. J.*, 535, 887
- Klessen R. S., Heitsch F., Mac Low M.-M., 2000b, *Astrophys. J.*, 535, 887
- Kolmogorov A., 1941, *Akademiia Nauk SSSR Doklady*, 30, 301
- Konstandin L., Federrath C., Klessen R. S., Schmidt W., 2012, *Journal of Fluid Mechanics*, 692, 183
- Konstandin L., Girichidis P., Federrath C., Klessen R. S., 2012, *Astrophys. J.*, 761, 149
- Konstandin L., Shetty R., Girichidis P., Klessen R. S., 2015, *Mon. Not. R. Astron. Soc.*, 446, 1775
- Kowal G., Lazarian A., Beresnyak A., 2007, *Astrophys. J.*, 658, 423
- Kritsuk A. G., Norman M. L., Padoan P., Wagner R., 2007a, *Astrophys. J.*, 665, 416
- Kritsuk A. G., Norman M. L., Padoan P., Wagner R., 2007b, *Astrophys. J.*, 665, 416
- Kritsuk A. G., Norman M. L., Wagner R., 2011, *Astrophys. J. Let.*, 727, L20
- Kroupa P., 2001, *Mon. Not. R. Astron. Soc.*, 322, 231
- Kroupa P., 2002, *Science*, 295, 82
- Kruijssen J. M. D., Dale J. E., Longmore S. N., 2015, *Mon. Not. R. Astron. Soc.*, 447, 1059
- Kruijssen J. M. D., Longmore S. N., Elmegreen B. G., Murray N., Bally J., Testi L., Kennicutt R. C., 2014, *Mon. Not. R. Astron. Soc.*, 440, 3370
- Krumholz M. R., Dekel A., McKee C. F., 2012, *Astrophys. J.*, 745, 69
- Krumholz M. R., Klein R. I., McKee C. F., Offner S. S., Cunningham A. J., 2009, *Science*, 323, 754
- Krumholz M. R., Klein R. I., McKee C. F., 2007, *Astrophys. J.*, 656, 959
- Krumholz M. R., Kruijssen J. M. D., 2015, ArXiv e-prints, 1505.07111

- Krumholz M. R., McKee C. F., 2005, *Astrophys. J.*, 630, 250
- Krumholz M. R., Tan J. C., 2007, *Astrophys. J.*, 654, 304
- Lada C. J., 2005, *Progress of Theoretical Physics Supplement*, 158, 1
- Lada C. J., Lada E. A., 2003, *Ann. Rev. Astron. Astrophys.*, 41, 57
- Lada C. J., Lada E. A., Clemens D. P., Bally J., 1994, *Astrophys. J.*, 429, 694
- Landau L. D., Lifshic E. M., 2007, *Hydrodynamik*, korr. nachdr. d. 5., überarb. Aufl. edn. No. 6 in *Lehrbuch der theoretischen Physik* / von L. D. Landau; E. M. Lifschitz ; 6 ; Landau, Lev DavidoviĀD: *Lehrbuch der theoretischen Physik*, Deutsch, Frankfurt am Main
- Larson R. B., 1972, *Monthly Notices of the Royal Astronomical Society*, 156, 437
- Larson R. B., 1981, *Mon. Not. R. Astron. Soc.*, 194, 809
- Larson R. B., 2003, *Reports on Progress in Physics*, 66, 1651
- Lazarian A., Esquivel A., 2003, *Astrophys. J. Let.*, 592, L37
- Lazarian A., Pogosyan D., 2000, *Astrophys. J.*, 537, 720
- Lazarian A., Pogosyan D., 2004, *Astrophys. J.*, 616, 943
- Lazarian A., Pogosyan D., 2006, *Astrophys. J.*, 652, 1348
- Lemaster M. N., Stone J. M., 2008, *Astrophys. J. Let.*, 682, L97
- Leroy A. K., Bolatto A., Gordon K., Sandstrom K., Gratier P., Rosolowsky E., Engelbracht C. W., Mizuno N., Corbelli E., Fukui Y., Kawamura A., 2011, *Astrophys. J.*, 737, 12
- Lilley A. E., 1955, *Astrophys. J.*, 121, 559
- Lis D. C., Menten K. M., 1998, *Astrophys. J.*, 507, 794
- Lis D. C., Menten K. M., Serabyn E., Zylka R., 1994, *Astrophys. J. Let.*, 423, L39
- Lis D. C., Pety J., Phillips T. G., Falgarone E., 1996, *Astrophys. J.*, 463, 623
- Lis D. C., Serabyn E., Zylka R., Li Y., 2001, *Astrophys. J.*, 550, 761
- Liszt H. S., Burton W. B., 1978, *Astrophys. J.*, 226, 790
- Liszt H. S., Pety J., Lucas R., 2010, *Astron. & Astrophys.*, 518, A45
- Lizano S., Heiles C., Rodriguez L. F., Koo B.-C., Shu F. H., Hasegawa T., Hayashi S., Mirabel I. F., 1988, *Astrophys. J.*, 328, 763

- Longmore S. N., Bally J., Testi L., Purcell C. R., Walsh A. J., Bressert E., Pestalozzi M., Molinari S., Ott J., Cortese L., Battersby C., Murray N., Lee E., Kruijssen J. M. D., Schisano E., Elia D., 2013, *Mon. Not. R. Astron. Soc.*, 429, 987
- Longmore S. N., Bally J., Testi L., Purcell C. R., Walsh A. J., Bressert E., Pestalozzi M., Molinari S., Ott J., Cortese L., Battersby C., Murray N., Lee E., Kruijssen J. M. D., Schisano E., Elia D., 2013a, *Mon. Not. R. Astron. Soc.*, 429, 987
- Longmore S. N., Kruijssen J. M. D., Bally J., Ott J., Testi L., Rathborne J., Bastian N., Bressert E., Molinari S., Battersby C., Walsh A. J., 2013b, *Mon. Not. R. Astron. Soc.*, 433, L15
- Longmore S. N., Rathborne J., Bastian N., Alves J., Ascenso J., Bally J., Testi L., Longmore A., Battersby C., Bressert E., Purcell C., Walsh A., Jackson J., Foster J., Molinari S., Meingast S., Amorim A., Lima J., 2012, *Astrophys. J.*, 746, 117
- Mac Low M.-M., 1999, *Astrophys. J.*, 524, 169
- Mac Low M.-M., Klessen R. S., 2004, *Reviews of Modern Physics*, 76, 125
- Mac Low M.-M., Klessen R. S., Burkert A., Smith M. D., 1998a, *Physical Review Letters*, 80, 2754
- Mac Low M.-M., Klessen R. S., Burkert A., Smith M. D., 1998b, *Physical Review Letters*, 80, 2754
- Mac Low M.-M., Ossenkopf V., 2000, *Astron. & Astrophys.*, 353, 339
- Madau P., Dickinson M., 2014, *Ann. Rev. Astron. Astrophys.*, 52, 415
- Madau P., Ferguson H. C., Dickinson M. E., Giavalisco M., Steidel C. C., Fruchter A., 1996, *Monthly Notices of the Royal Astronomical Society*, 283, 1388
- Majewski S. R., 1993, *Ann. Rev. Astron. Astrophys.*, 31, 575
- Martin C. L., Walsh W. M., Xiao K., Lane A. P., Walker C. K., Stark A. A., 2004, *Astrophys. J. Suppl. Ser.*, 150, 239
- Mathis J. S., Mezger P. G., Panagia N., 1983, *Astron. & Astrophys.*, 128, 212
- McKee C. F., 1989, *Astrophys. J.*, 345, 782
- McKee C. F., Ostriker E. C., 2007, *Ann. Rev. Astron. Astrophys.*, 45, 565
- McKee C. F., Zweibel E. G., 1992, *Astrophys. J.*, 399, 551
- Meidt S. E., Hughes A., Dobbs C. L., Pety J., Thompson T. A., García-Burillo S., Leroy A. K., Schinnerer E., Colombo D., Querejeta M., Kramer C., Schuster K. F., Dumas G., 2015, *Astrophys. J.*, 806, 72

- Meyerdierks H., Heithausen A., 1996, *Astron. & Astrophys.*, 313, 929
- Mills E. A. C., Morris M. R., 2013, *Astrophys. J.*, 772, 105
- Miville-Deschênes M.-A., Martin P. G., Abergel A., Bernard J.-P., Boulanger F., Lagache G., Anderson L. D., André P., Arab H., Baluteau J.-P., Blagrove K., Bontemps S., Cohen 2010, *Astron. & Astrophys.*, 518, L104
- Molina F. Z., Glover S. C. O., Federrath C., Klessen R. S., 2012, *Mon. Not. R. Astron. Soc.*, 423, 2680
- Molinari S., Bally J., Noriega-Crespo A., Compiègne M., Bernard J. P., Paradis D., Martin P., Testi L., Barlow M., Moore T., Plume R., Swinyard B., Zavagno A., Calzoletti L., Di Giorgio A. M., Elia 2011, *Astrophys. J. Let.*, 735, L33
- Morris M., Serabyn E., 1996a, *Ann. Rev. Astron. Astrophys.*, 34, 645
- Morris M., Serabyn E., 1996b, *Ann. Rev. Astron. Astrophys.*, 34, 645
- Morris M. R., 2014, ArXiv e-prints, 1406.7859
- Mouschovias T. C., 1991, *The Astrophysical Journal*, 373, 169
- Mouschovias T. C., Tassis K., Kunz M. W., 2006, *The Astrophysical Journal*, 646, 1043
- Murray N., 2011, *Astrophys. J.*, 729, 133
- Nagano M., Teshima M., Matsubara Y., Dai H. Y., Hara T., Hayashida N., Honda M., Ohoka H., Yoshida S., 1992, *Journal of Physics G Nuclear Physics*, 18, 423
- Narayanan D., Hopkins P. F., 2013, *Mon. Not. R. Astron. Soc.*, 433, 1223
- Narayanan D., Krumholz M. R., Ostriker E. C., Hernquist L., 2012, *Mon. Not. R. Astron. Soc.*, 421, 3127
- Nelson R. P., Langer W. D., 1997, *Astrophys. J.*, 482, 796
- Nelson R. P., Langer W. D., 1999, *Astrophys. J.*, 524, 923
- Nolting W., 2012, *Spezielle Relativitätstheorie, Thermodynamik*, 8., aktualisierte aufl. edn. Springer- Lehrbuch, Springer, Berlin ; Heidelberg [u.a.]
- Nolting W., 2015, *Quantenmechanik - Methoden und Anwendungen*, 8. aufl. edn. Springer Lehrbuch, Springer-Spektrum, Berlin ; Heidelberg [u.a.]
- Norman M. L., 2000, in Arthur S. J., Brickhouse N. S., Franco J., eds, *Revista Mexicana de Astronomia y Astrofisica Conference Series Vol. 9 of Revista Mexicana de Astronomia y Astrofisica*, vol. 27, Introducing ZEUS-MP: A 3D, Parallel, Multiphysics Code for Astrophysical Fluid Dynamics. pp 66–71

- Nutter D., Kirk J. M., Stamatellos D., Ward-Thompson D., 2008, *Mon. Not. R. Astron. Soc.*, 384, 755
- Oka T., Hasegawa T., Sato F., Tsuboi M., Miyazaki A., 1998, *Astrophys. J. Suppl. Ser.*, 118, 455
- Oka T., Hasegawa T., Sato F., Tsuboi M., Miyazaki A., Sugimoto M., 2001, *Astrophys. J.*, 562, 348
- O'Shea B. W., Bryan G., Bordner J., Norman M. L., Abel T., Harkness R., Kritsuk A., 2004, *ArXiv Astrophysics e-prints*
- Ossenkopf V., Bensch F., Zielinsky M., 1998, *Interstellar Turbulence*. Cambridge, 252
- Ossenkopf V., Esquivel A., Lazarian A., Stutzki J., 2006, *Astron. & Astrophys.*, 452, 223
- Ossenkopf V., Henning T., 1994, *Astron. & Astrophys.*, 291, 943
- Ossenkopf V., Henning T., Mathis J. S., 1992, *Astron. & Astrophys.*, 261, 567
- Ossenkopf V., Klessen R. S., Heitsch F., 2001, *Astron. & Astrophys.*, 379, 1005
- Ossenkopf V., Krips M., Stutzki J., 2008a, *Astron. & Astrophys.*, 485, 917
- Ossenkopf V., Krips M., Stutzki J., 2008b, *Astron. & Astrophys.*, 485, 719
- Ossenkopf V., Mac Low M.-M., 2002, *Astron. & Astrophys.*, 390, 307
- Ostriker J., Silk J., 1973, *Astrophys. J. Let.*, 184, L113
- Padmanabhan T., 2007, *Astrophysical processes*, repr. edn. Cambridge Univ. Press, Cambridge [u.a.]
- Padoan P., 1995, *Monthly Notices of the Royal Astronomical Society*, 277, 377
- Padoan P., Bally J., Billawala Y., Juvela M., Åke Nordlund 1999, *The Astrophysical Journal*, 525, 318
- Padoan P., Haugbølle T., Nordlund Å., 2012, *Astrophys. J. Let.*, 759, L27
- Padoan P., Jones B. J. T., Åke P. Nordlund 1997, *The Astrophysical Journal*, 474, 730
- Padoan P., Juvela M., Kritsuk A., Norman M. L., 2006, *Astrophys. J. Let.*, 653, L125
- Padoan P., Nordlund Å., 2002, *Astrophys. J.*, 576, 870

- Padoan P., Nordlund Å., 2011, *Astrophys. J.*, 730, 40
- Palla F., Stahler S. W., 1999, *The Astrophysical Journal*, 525, 772
- Pan L., Padoan P., Haugbolle T., Nordlund A., 2015, ArXiv e-prints, arXiv:1510.04742
- Papadopoulos P. P., Thi W.-F., 2013, in Torres D. F., Reimer O., eds, *Cosmic Rays in Star-Forming Environments Vol. 34 of Astrophysics and Space Science Proceedings, The Initial Conditions of Star Formation: Cosmic Rays as the Fundamental Regulators*. p. 41
- Papadopoulos P. P., Thi W.-F., Miniati F., Viti S., 2011, *Mon. Not. R. Astron. Soc.*, 414, 1705
- Paumard T., Genzel R., Martins F., Nayakshin S., Beloborodov A. M., Levin Y., Trippe S., Eisenhauer F., Ott T., Gillessen S., Abuter R., Cuadra J., Alexander T., Sternberg A., 2006, *Astrophys. J.*, 643, 1011
- Paumard T., Maillard J. P., Morris M., Rigaut F., 2001, *Astron. & Astrophys.*, 366, 466
- Peters T., Banerjee R., Klessen R. S., Mac Low M.-M., 2011, *Astrophys. J.*, 729, 72
- Peters T., Banerjee R., Klessen R. S., Mac Low M.-M., Galván-Madrid R., Keto E. R., 2010, *Astrophys. J.*, 711, 1017
- Pillai T., Kauffmann J., Tan J. C., Goldsmith P. F., Carey S. J., Menten K. M., 2015, *Astrophys. J.*, 799, 74
- Pineda J. E., Goodman A. A., Arce H. G., Caselli P., Foster J. B., Myers P. C., Rosolowsky E. W., 2010, *Astrophys. J. Let.*, 712, L116
- Polk K. S., Knapp G. R., Stark A. A., Wilson R. W., 1988, *Astrophys. J.*, 332, 432
- Pope S. B., 2000, *Turbulent flows*, 1. publ. edn. Cambridge University Press, Cambridge [u.a.]
- Pound M. W., 1998, *The Astrophysical Journal Letters*, 493, L113
- Price D. J., Bate M. R., 2007, *Monthly Notices of the Royal Astronomical Society*, 377, 77
- Price D. J., Bate M. R., 2008, *Monthly Notices of the Royal Astronomical Society*, 385, 1820
- Ragan S. E., Henning T., Beuther H., Linz H., Zahorecz S., 2015, *Astron. & Astrophys.*, 573, A119

- Rathborne J. M., Longmore S. N., Jackson J. M., Foster J. B., Contreras Y., Garay G., Testi L., Alves J. F., Bally J., Bastian N., Kruijssen J. M. D., Bressert E., 2014, *Astrophys. J.*, 786, 140
- Rathborne J. M., Longmore S. N., Jackson J. M., Kruijssen J. M. D., Alves J. F., Bally J., Bastian N., Contreras Y., Foster J. B., Garay G., Testi L., Walsh A. J., 2015, *ArXiv e-prints*, arXiv:1501.07368
- Rodríguez-Fernández N. J., Martín-Pintado J., Fuente A., Wilson T. L., 2004, *Astron. & Astrophys.*, 427, 217
- Röllig M., Ossenkopf V., 2013, *Astron. & Astrophys.*, 550, A56
- Roman-Duval J., Federrath C., Brunt C., Heyer M., Jackson J., Klessen R. S., 2011, *Astrophys. J.*, 740, 120
- Roman-Duval J., Jackson J. M., Heyer M., Rathborne J., Simon R., 2010, *Astrophys. J.*, 723, 492
- Rosolowsky E. W., Goodman A. A., Wilner D. J., Williams J. P., 1999, *Astrophys. J.*, 524, 887
- Russeil D., Schneider N., Anderson L. D., Zavagno A., Molinari S., Persi P., Bontemps S., Motte F., Ossenkopf V., André P., Arzoumanian D., Bernard J.-P., Deharveng L., Didelon P., et al 2013, *Astron. & Astrophys.*, 554, A42
- Rybicki G. B., Lightman A. P., 2004, *Radiative processes in astrophysics*. Physics textbook, Wiley-VCH, Weinheim
- Salpeter E. E., 1955, *Astrophys. J.*, 121, 161
- Sandstrom K. M., Leroy A. K., Walter F., Bolatto A. D., Croxall K. V., Draine B. T., Wilson C. D., Wolfire M., Calzetti D., Kennicutt R. C., Aniano G., et al 2013, *Astrophys. J.*, 777, 5
- Scalo J., Elmegreen B. G., 2004, *Ann. Rev. Astron. Astrophys.*, 42, 275
- Schilke P., Mehringer D. M., Menten K. M., 2000, *The Astrophysical Journal Letters*, 528, L37
- Schmidt M., 1959, *Astrophys. J.*, 129, 243
- Schneider N., André P., Könyves V., Bontemps S., Motte F., Federrath C., Ward-Thompson D., Arzoumanian D., Benedettini M., Bressert E., Didelon P., Di Francesco J., Griffin M., Hennemann M., Hill T., 2013, *Astrophys. J. Let.*, 766, L17
- Schneider N., Bontemps S., Simon R., Ossenkopf V., Federrath C., Klessen R. S., Motte F., André P., Stutzki J., Brunt C., 2011, *Astron. & Astrophys.*, 529, A1

- Schneider N., Csengeri T., Hennemann M., Motte F., Didelon P., Federrath C., Bon-temps S., Di Francesco J., Arzoumanian D., Minier V., et al 2012, *Astron. & Astrophys.*, 540, L11
- Schneider S., Elmegreen B. G., 1979, *Astrophys. J. Suppl. Ser.*, 41, 87
- Schober J., Schleicher D., Federrath C., Klessen R., Banerjee R., 2012, *Phys. Rev. E*, 85, 026303
- Schödel R., Ott T., Genzel R., Hofmann R., Lehnert M., Eckart A., Mouawad N., Alexander T., Reid M. J., Lenzen R., Hartung M., Lacombe F., Rouan D., Gendron E., et al 2002, *Nature*, 419, 694
- Schöier F. L., van der Tak F. F. S., van Dishoeck E. F., Black J. H., 2005, *Astron. & Astrophys.*, 432, 369
- Seifried D., Banerjee R., Klessen R., Duffin D., Pudritz R., 2011, *Monthly Notices of the Royal Astronomical Society*, 417, 1054
- Seifried D., Banerjee R., Pudritz R. E., Klessen R. S., 2013, *Mon. Not. R. Astron. Soc.*, 432, 3320
- Seifried D., Pudritz R. E., Banerjee R., Duffin D., Klessen R. S., 2012, *Mon. Not. R. Astron. Soc.*, 422, 347
- Sembach K. R., Howk J. C., Ryans R. S. I., Keenan F. P., 2000, *Astrophys. J.*, 528, 310
- She Z.-S., Leveque E., 1994, *Phys. Rev. Lett.*, 72, 336
- Shetty R., Beaumont C. N., Burton M. G., Kelly B. C., Klessen R. S., 2012, *Mon. Not. R. Astron. Soc.*, 425, 720
- Shetty R., Glover S. C., Dullemond C. P., Klessen R. S., 2011a, *Mon. Not. R. Astron. Soc.*, 412, 1686
- Shetty R., Glover S. C., Dullemond C. P., Ostriker E. C., Harris A. I., Klessen R. S., 2011b, *Mon. Not. R. Astron. Soc.*, 415, 3253
- Shetty R., Kelly B. C., Bigiel F., 2013, *Mon. Not. R. Astron. Soc.*, 430, 288
- Shetty R., Kelly B. C., Rahman N., Bigiel F., Bolatto A. D., Clark P. C., Klessen R. S., Konstandin L. K., 2014, *Mon. Not. R. Astron. Soc.*, 437, L61
- Shu F. H., Adams F. C., Lizano S., 1987, *Annual Review of Astronomy and Astrophysics*, 25, 23
- Smith N., Egan M. P., Carey S., Price S. D., Morse J. A., Price P. A., 2000, *The Astrophysical Journal Letters*, 532, L145

- Smith R. J., Glover S. C. O., Clark P. C., Klessen R. S., Springel V., 2014a, *Mon. Not. R. Astron. Soc.*, 441, 1628
- Smith R. J., Glover S. C. O., Klessen R. S., 2014b, *Mon. Not. R. Astron. Soc.*, 445, 2900
- Smith R. J., Glover S. C. O., Klessen R. S., Fuller G. A., 2015, *ArXiv e-prints*, 1509.03321
- Sobolev V. V., 1957, *SvA*, 1, 678
- Solomon P. M., Rivolo A. R., Barrett J., Yahil A., 1987, *Astrophys. J.*, 319, 730
- Springel V., 2005, *Monthly Notices of the Royal Astronomical Society*, 364, 1105
- Springel V., 2010, *Mon. Not. R. Astron. Soc.*, 401, 791
- Stahler S. W., Palla F., 2006, *The formation of stars*, 1. ed., 1. repr. edn. *Physics textbook*, Wiley-VCH, Weinheim
- Stanimirović S., Lazarian A., 2001, *Astrophys. J. Let.*, 551, L53
- Stutzki J., Bensch F., Heithausen A., Ossenkopf V., Zielinsky M., 1998, *Astron. & Astrophys.*, 336, 697
- Stutzki J., Stacey G., Genzel R., Harris A., Jaffe D., Lugten J., 1988, *The Astrophysical Journal*, 332, 379
- Sun K., Kramer C., Ossenkopf V., Bensch F., Stutzki J., Miller M., 2006, *Astron. & Astrophys.*, 451, 539
- Szűcs L., Glover S. C. O., Klessen R. S., 2014, *ArXiv e-prints*, arXiv:1403.4912
- Takagi S.-i., Murakami H., Koyama K., 2002, *Astrophys. J.*, 573, 275
- Tamblyn P., Rieke G. H., Hanson M. M., Close L. M., McCarthy Jr. D. W., Rieke M. J., 1996, *Astrophys. J.*, 456, 206
- Tan J. C., Krumholz M. R., McKee C. F., 2006, *The Astrophysical Journal Letters*, 641, L121
- Tan J. C., McKee C. F., 2004, *The Astrophysical Journal*, 603, 383
- Tanner A., Figer D. F., Najarro F., Kudritzki R. P., Gilmore D., Morris M., Becklin E. E., McLean I. S., Gilbert A. M., Graham J. R., Larkin J. E., Levenson N. A., Teplitz H. I., 2006, *Astrophys. J.*, 641, 891
- Tassis K., Mouschovias T. C., 2004, *The Astrophysical Journal*, 616, 283

- Tielens A. G. G. M., 2010, *The physics and chemistry of the interstellar medium*, 1. paperback ed. edn. Cambridge University Press, Cambridge [u.a.]
- Toro E. F., 2009, *Riemann solvers and numerical methods for fluid dynamics*, 3. ed. edn. Springer, Berlin ; Heidelberg [u.a.]
- Truelove J. K., Klein R. I., McKee C. F., Holliman II J. H., Howell L. H., Greenough J. A., Woods D. T., 1998, *Astrophys. J.*, 495, 821
- Tsuboi M., Miyazaki A., 2012, *Pub. of the Astron. Soc. of Japan*, 64, 111
- van der Tak F. F. S., van Dishoeck E. F., 2000, *Astron. & Astrophys.*, 358, L79
- van Dishoeck E. F., Blake G. A., 1998, *Ann. Rev. Astron. Astrophys.*, 36, 317
- Vázquez-Semadeni E., Ballesteros-Paredes J., Klessen R. S., 2003, *Astrophys. J. Let.*, 585, L131
- Vázquez-Semadeni E., Banerjee R., Gómez G. C., Hennebelle P., Duffin D., Klessen R. S., 2011, *Monthly Notices of the Royal Astronomical Society*, 414, 2511
- Vázquez-Semadeni E., García N., 2001, *Astrophys. J.*, 557, 727
- Visser R., van Dishoeck E. F., Black J. H., 2009a, *Astron. & Astrophys.*, 503, 323
- Visser R., van Dishoeck E. F., Black J. H., 2009b, *Astron. & Astrophys.*, 503, 323
- Vogelsberger M., Genel S., Springel V., Torrey P., Sijacki D., Xu D., Snyder G., Nelson D., Hernquist L., 2014, *Monthly Notices of the Royal Astronomical Society*, 444, 1518
- Wada K., Meurer G., Norman C. A., 2002, *Astrophys. J.*, 577, 197
- Watson W. D., Anicich V. G., Huntress Jr. W. T., 1976, *Astrophys. J. Let.*, 205, L165
- Weinberg S., 2008, *Cosmology*, 1. publ. edn. Oxford Univ. Press, Oxford [u.a.]
- Weinberg S., 2015, *Lectures on quantum mechanics*, 2. ed. edn. Cambridge Univ. Press, Cambridge [u.a.]
- Weingartner J. C., Draine B. T., 2001, *The Astrophysical Journal Supplement Series*, 134, 263
- Whitworth A. P., Boffin H. M. J., Francis N., 1998, *Mon. Not. R. Astron. Soc.*, 299, 554
- Williams D. A., 2005, *Journal of Physics Conference Series*, 6, 1
- Young J. S., Scoville N. Z., 1991, *Ann. Rev. Astron. Astrophys.*, 29, 581

Yusef-Zadeh F., Wardle M., Roy S., 2007, *Astrophys. J. Let.*, 665, L123

Zeldovich I. B., Ruzmaikin A. A., Sokolov D. D., 1983, in New York, Gordon and Breach Science Publishers (*The Fluid Mechanics of Astrophysics and Geophysics. Volume 3*), 1983, 381 p. Translation. Vol. 3, Magnetic fields in astrophysics

Zernickel A., Schilke P., Smith R., 2013, *Astronomy & Astrophysics*, 554, L2

Ziurys L. M., Turner B. E., 1986, *Astrophys. J. Let.*, 300, L19

Zwart S. P., McMillan S., Gieles M., 2010, arXiv preprint arXiv:1002.1961

Eidesstattliche Erklärung

Ich versichere, dass ich diese Arbeit selbstständig verfasst habe und keine anderen als die angegebenen Quellen und Hilfsmittel benutzt habe.

Heidelberg, den 07. Dezember 2015

Erik Bertram, M.Sc.